Splice Connection for Tubular Section Pultruded Fibre Reinforced Polymer Members in Building Construction

Chengyu Qiu

B.Eng. (Honours)

A thesis submitted for the degree of

Doctor of Philosophy

in February 2020

at Department of Civil Engineering

Monash University, Australia

Copyright Notice

ABSTRACT

Fibre reinforced polymer (FRP) members made from the pultrusion process is a promising candidate for constructing durable and lightweight structures. However, the acceptance of pultruded FRPs as the primary structural members in building construction is hindered by the difficulty in connecting individual members, which is associated with the anisotropic and brittle characteristics of the composite material. This research aims to develop a splice connection to enable the use of tubular section FRP members in structural applications. With the experience gained from previous researches on FRP connections, a splice connection is proposed and conceptualised as consisting of a steel bolted flange joint between two tubular section steel-FRP bonded sleeve joints. The bonded sleeve joints are aimed for high stiffness and strength, while the steel bolted flange joint is to realize convenient assembly & disassembly and ductile failure. Experimental, theoretical and numerical investigations are carried out for the performance of the splice connection under axial, flexural and cyclic loadings.

Investigation of the axial performance of the splice connection begins with a theoretical analysis of the steel-FRP bonded sleeve joint component. A theoretical formulation is developed based on a bilinear elastic-softening bond-slip relation at the adhesive bond. Possible shear stress distributions at elastic limit and ultimate state are formulated, based on which the axial capacities of the bonded sleeve joints are derived. The theoretical analysis is validated by experimental results and finite element (FE) analysis covering a wide range of section geometries and bond lengths.

To investigate the axial performance of the proposed splice connection, experimental testing of the connection components of bonded sleeve joints and bolted flange joints are first conducted individually. Failure of the bonded sleeve joints is brittle within the adhesive layer; the joint capacity increases nonlinearly with the bond length, indicating the existence of an effective bond length. Failure of the bolted flange joints is ductile by yielding of the steel flange-plates. Featuring a bilinear bond-slip relation, FE models are developed and show capability in characterising the behaviour of these component joints. The FE modelling is then utilised to evaluate the axial behaviour of a complete splice connection integrating the component joints. Ductile failure can be realized through brittle failure of the bonded sleeve joint preceded by the yielding of the bolted flange joint.

To investigate the flexural performance of the splice connection, three types of connection specimens, with difference in the bond length or in the bolt arrangement (four or eight bolts), are loaded to failure under four-point bending. All the connection specimens exhibit excellent ductility through yielding of the steel flange-plates. The ultimate failure occurs in the mode of excessive yielding of the flange-plates, web-flange cracking of the connected tubular FRP member, or fracture of the flange-plates near the weld toes. FE modelling, compared to the axial loading scenario, further involves a mixed-mode behaviour for the adhesive bond, considering the presence of both normal and shear stresses in the adhesive. The FE modelling is able to capture the nonlinear moment-rotation behaviours and also the local strain responses in the bonded region and the steel flange-plate. The ultimate failure of web-flange cracking of the FRP member can be predicted by examining the stress state of the FRP against the Tsai-Wu failure criterion.

The cyclic performance of the splice connection is investigated using a cantilever setup to subject the connection to a combined bending-and-shear cyclic loading. Connection specimens are prepared in three configurations as in the flexural loading scenario. The connection specimens experience different levels of yielding in the steel flange-plates, before ultimate failure in mode of web-flange cracking of the FRP member or fracture of the steel flange-plates near the weld toes. Excellent energy dissipation performance is demonstrated in a specimen where plastic deformation of the steel flange-plates is fully developed. The strain responses are analysed to identify damage in the adhesive bond and yielding in the flange-plates. FE modelling, compared to the flexural loading scenario, further incorporates damage accumulation in the adhesive bond and kinematic hardening (after yielding) of the steels, showing satisfactory agreement with the experimental results.

The proposed splice connection is convenient for assembly and disassembly because of the bolted flange joint. Based on the experimental results, satisfactory mechanical performance in terms of stiffness, strength, and ductility is demonstrated for the scenarios of axial, flexural and cyclic loadings. Correspondingly, modelling approaches (theoretical or numerical modelling) are developed to predict and characterise the behaviour of the splice connection.

DELCARATION

I hereby declare that this thesis contains no material which has been accepted for the award of any other degree or diploma at any university or equivalent institution and that, to the best of my knowledge and belief, this thesis contains no material previously published or written by another person, except where due reference is made in the text of the thesis.

Chengyu Qiu

13 May, 2020

PUBLICATIONS DURING ENROLMENT

Peer-reviewed journal papers:

Ding C, Bai Y, **Qiu C**, Wan C, Zhao XL. Steel bolted flanged connections in tension: Effects of stiffener configurations. Thin-Walled Structures. 2020; in-press.

Qiu C, Bai Y, Cai Z, Zhang Z. Cyclic performance of splice connections for hollow section fibre reinforced polymer members. Composite Structures. 2020;243:112222.

Bai Y, **Qiu C**. Load-dependent composite action for beam nonlinear and ductile behavior. Journal of Structural Engineering. 2020;146(4):04020028.

Xie L, Qi Y, Bai Y, **Qiu C**, Wang H, Fang H, Zhao XL. Sandwich assemblies of composites square hollow sections and thin-walled panels in compression. Thin-Walled Structures. 2019;145:106412.

Qiu C, Bai Y, Zhang L, Jin L. Bending performance of splice connections for assembly of tubular section FRP members: Experimental and numerical study. Journal of Composites for Construction. 2019;23(5):04019040.

Qiu C, Ding C, He X, Zhang L, Bai Y. Axial performance of steel splice connection for tubular FRP column members. Composite Structures. 2018;189:498-509.

Qiu C, Feng P, Yang Y, Zhu L, Bai Y. Joint capacity of bonded sleeve connections for tubular fibre reinforced polymer members. Composite Structures. 2017;163:267-79.

Peer-reviewed conference papers:

Qiu C, Bai Y. Splice connection for tubular FRP column members. 9th International Conference on Fibre-Reinforced Polymer (FRP) Composites in Civil Engineering (CICE 2018), Paris, France, 17-19 July 2018.

Qiu C, Bai Y. Axial behaviour of hybrid column-splice connection for tubular GFRP members. The Twenty-Fifth Annual International Conference on Composites/Nano Engineering (ICCE25), Rome, Italy, 16-22 July 2017.

THESIS INCLUDING PUBLISHED WORKS DECLARATION

I hereby declare that this thesis contains no material which has been accepted for the award of any other degree or diploma at any university or equivalent institution and that, to the best of my knowledge and belief, this thesis contains no material previously published or written by another person, except where due reference is made in the text of the thesis.

This thesis includes 4 original papers published in peer-reviewed journals (Chapters 3-6). The core theme of the thesis is Structural Engineering. The ideas, development and writing up of all the papers in the thesis were the principal responsibility of myself, the student, working within the Department of Civil Engineering under the supervision of Prof. Yu Bai.

(The inclusion of co-authors reflects the fact that the work came from active collaboration between researchers and acknowledges input into team-based research.)

In the case of Chapters 3-6 my contribution to the works involved the following:

Ch.	**Publication Title**	**Status**	**Nature and % of student contribution**	**Co-author name(s), nature and % of Co-author's contribution**	**Co-author Monash student**
3	Joint capacity of bonded sleeve connections for tubular fibre reinforced polymer members	Published	Conceptualisation, theoretical derivation, date collection and analysis, numerical modelling, writing-up, revision, 65%	1) P Feng: Review and revision, 5%; 2) Y Yang: Review and revision, 5%; 3) Z Zhu: Review and revision, 5%; 4) Y Bai: Conceptualisation, data analysis, review and revision, financial support, 20%	No
4	Axial performance of steel splice connection for tubular FRP column members	Published	Conceptualisation, methodologies, experimental work, numerical modelling, data analysis, writing-up, revision, 65%	1) C Ding: Experimental work, 5%; 2) X He: Review and revision, 5%; 3) L Zhang: Review and revision, 5%; 4) Y Bai: Conceptualization, methodologies, data analysis, review and revision, financial support, 20%	Yes, C Ding

5	Bending performance of splice connections for assembly of tubular section FRP members: Experimental and numerical study	Published	Conceptualisation, methodologies, experimental work, numerical modelling, data analysis, writing-up, revision, 70%	1) Y Bai: Conceptualization, methodologies, review and revision, financial support, 20%; 2) L Zhang: Review and revision, 5%; 3) L Jin: Review and revision, 5%	No
6	Cyclic performance of splice connections for hollow section fibre reinforced polymer members	Published	Conceptualisation, methodologies, experimental work, numerical modelling, data analysis, writing-up, revision, 70%	1) Y Bai: Conceptualization, methodologies, review and revision, financial support, 15%; 2) Z Cai: Experimental work, 10% 3) Z Zhang: Review and revision, 5%	Yes, Z Cai

I have re-numbered the sections of the published papers in order to generate a consistent presentation style within the thesis.

Student (Chengyu Qiu) signature:

Date:

The undersigned hereby certify that the above declaration correctly reflects the nature and extent of the student's and co-authors' contributions to this work. In instances where I am not the responsible author, I have consulted with the responsible author to agree on the respective contributions of the authors.

Main supervisor (Yu Bai) signature:

Date:

ACKNOWLEDGEMENTS

First of all, I would like to express my sincerest gratitude to my supervisor, Prof. Yu Bai, for his guidance and support throughout the course of my Ph.D. It is not often that one finds a supervisor who always finds the time to listen to and advise on the major and minor problems that unavoidably crop up in the journey of research. His technical and editorial guidance was essential to the completion of this thesis.

I gratefully acknowledge Monash University for providing the scholarships during my Ph.D. candidature, and Australian Research Council and Multiplex Building Innovation Project for supporting the research work.

A large amount of the time devoted to the research work was spent in laboratory. The experimental programs would not have been successful without the skilled assistance and advices from the staffs of the Civil Engineering Laboratory. My thanks also go to the academic and administrative staffs of the Department of Civil Engineering, especially Ms. Min Major and Dr. Fatin Hasan, who continuously provide encouragement and administrative support to the students. Ms. Joan Rosenthal is acknowledged for her editorial assistance in preparing the journal papers.

I give thanks to the fellow students and colleagues in Prof. Yu Bai's research group, in particular Mr. Fujia Luo, for their guidance, help, encouragement and accompany. I appreciate the time spent together with Mr. Dong Guo, whom I have known since the start of my undergraduate study, and the other fellow students sharing the office area. Their accompany is always a source of warmth and joy. I am indebted to my girlfriend Ms. Zhenqi Cai, who is also a colleague in the research group, for making every ordinary day of my life enjoyable and keeping me cheered in time of difficulty.

Most importantly, none of this would have been possible without the unconditional love and support of my mother and father, who have been a constant source of motivation and inspiration for me.

Sincerely,

Chengyu Qiu

May 2020

LIST OF CONTENTS

LIST OF FIGURES

LIST OF TABLES

CHAPTER 1. INTRODUCTION

1.1. Background and Problem

Many commonly used materials in civil engineering construction, such as steel and reinforced concrete, are vulnerable to corrosion in aggressive environments (e.g. in off-shore and industrial applications etc.), resulting in considerable cost for maintenance and rehabilitation. Furthermore, the transportation and erection of structural members made from such heavy materials require intensive labouring and the use of specialised equipment. Under the pressure to produce durable structures that are lighter to transport and quicker to build, the construction industry begins to show interest in innovative construction materials. Fibre reinforced polymer (FRP) composite materials, which have been routinely used in the aerospace and marine industries since the 1970s [1, 2], come up as a promising candidate.

Generally, FRP materials consist of a polymer matrix reinforced by high-strength and stiffness (continuous) fibres. The way the fibres are arranged in the polymer matrix creates an anisotropic composite, where the fibres are mainly responsible for the strength and stiffness while the polymer matrix keeps the fibres aligned and protects them from the environment. Carbon, aramid and glass are the most common types of fibres used in FRPs; among them glass fibres are the least expensive and exhibit relatively low mechanical strength and stiffness. The matrix of FRPs usually is one of the thermosetting polymers of polyester, epoxy, vinylester and phenolic [3]. Compared to conventional construction materials, the key advantages of FRPs are lightness in weight, resistance to corrosion, and other features associated with specific constituents (e.g. minimisation of electro-magnetic interference when glass fibres are used).

In civil engineering, the early use of FRPs mainly involves the strengthening and rehabilitation of existing structures [4], typically through manually laying layers of fibre sheets and impregnating them with a liquid polymer resin that will later cure in place. The potential use of FRPs as the primary load-carrying members is prompted by the mature of the pultrusion manufacturing technique. Pultrusion, patented by Goldsworthy

and Landgraf in 1959 [5], is an automatic process that entails impregnated fibres pulled continuously through a heated die where a thermosetting polymer resin is fed and binds the fibres together as it cures [Figure 1.1 (a)]. The fibre system of a pultruded FRP usually includes unidirectional fibre rovings and multi-directional short fibre mats in symmetric alternating layers [Figure 1.1 (b)]; a layer of surfacing veils is also used when a smooth surface is desired [3].

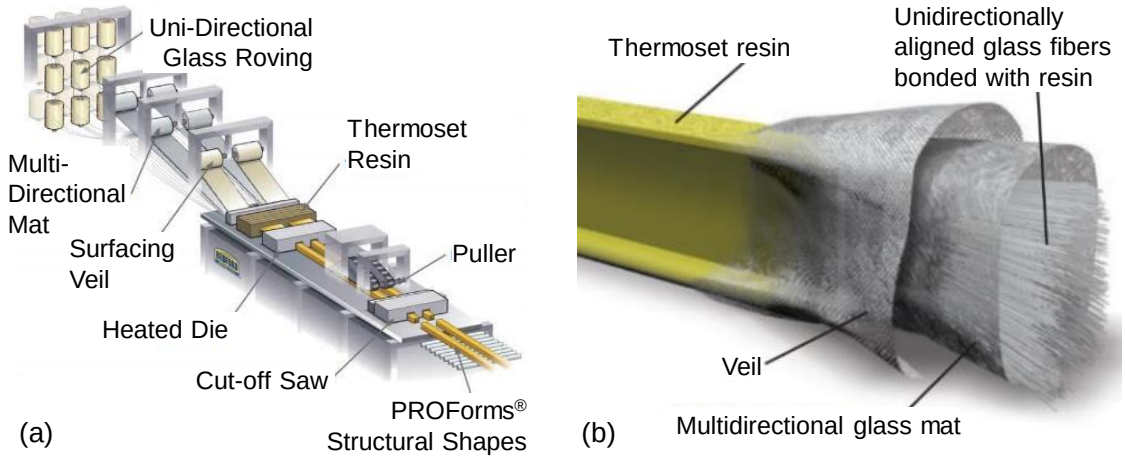

Figure 1.1. Pultruded FRP member: (a) pultrusion process (image courtesy of Bedford Reinforced Plastics) [6]; (b) fibre system (image courtesy of Advantic) [7].

Due to the one-dimensional 'pulling' process, pultruded FRPs mostly are characterised by constant cross-sections and majority of the continuous fibres aligned in the longitudinal direction (thus majority of strength and stiffness in the longitudinal direction). Glass fibres, cheaper than carbon fibres, are frequently used when FRPs are pultruded in large quantities. In the longitudinal direction, pultruded GFRPs (with glass fibres) typically possess strengths comparable to mild steels, but elastic moduli from 1/8 to 1/5 [8]. In the 1980s, GFRPs were pultruded in a range of cross-sections similar to structural steels. Researches have since been carried out in attempt to bring these FRP members from laboratory to implementation in real structures. Later on, the publication of design guide and standard specially for pultruded FRPs [9-11] envisages their prospect as a routine construction material.

In spite of the advantages of FRPs and the advance of manufacturing technique, the application of FRP members in structural construction is challenged by the difficulty to connect individual members. Unlike structural steels, FRPs are anisotropic, brittle, and cannot be welded. These issues complicate the connection behaviour and lead to the difficulty in creating stiff and strong connections. As will be reviewed in Chapter 2, extensive researches have been carried out on the subjects of beam-column and truss connections for FRP members, towards the development of more effective and economical connection designs. Researches on splice connections for FRP members are relatively scarce, especially for tubular sections members. Splice connection are used in building structures to extend the continuity for members of standard or practical length. Adequate stiffness, strength and ductility are required of splice connections, depending on their use in beams, columns or bracings. In steel structures, the typical splice connections entailing bolted lap plates or bolted end plates are shown in Figure 1.2. In reinforced concrete structures, members are spliced by having the reinforcing bars overlapped and bound together as the concrete is cast. For pultruded FRP members, a splice connection should be specially developed to accommodate their unique material properties.

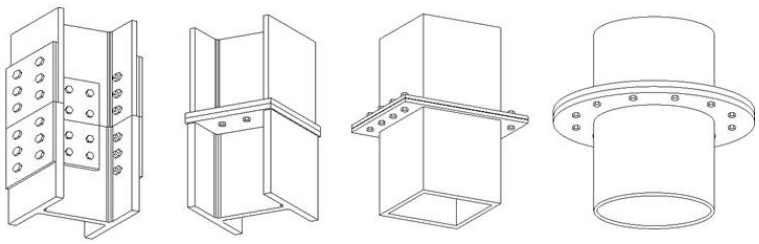

Figure 1.2. Typical splice connections in steel structures (image credit: SteelConstruction.info) [12].

1.2. Aim and Scope of the Research

To address the aforementioned research need, this research project aims to develop a splice connection for tubular section FRP members that is practical and convenient for field application as well as satisfactory in mechanical performance. Firstly, a design of

splice connection is proposed and conceptualised based on the experience gained from a detailed review of past researches on FRP connections. Considering the application in building structures, connection performance under axial, flexural and cyclic loadings is the focus in this project, while the aspects of fire, durability and creep performance may be covered in other literatures or further studies. Following the conceptual design, splice connection specimens with varied geometric parameters are prepared and experimentally examined. Results of overall load-deformation and local strain responses are analysed to evaluate the connection performance. Corresponding theoretical or numerical modelling is performed to predict and characterise the connection behaviour.

1.3. Structure of the Thesis

This thesis is structured into seven chapters.

Chapter 1 firstly presents a background introduction to FRP materials, in particular pultruded FRPs which are economical for use in building construction. The need to develop a splice connection for tubular section FRP member is then identified.

Chapter 2 presents a detailed literature review on the subjects of FRP application in building structures and connections for FRP members. Informed by the findings noted from the review, a design of splice connection is conceptualised which consists of a steel bolted flange joint between two tubular section steel-FRP bonded sleeve joint.

Chapters 3 & **4** concern the study of the proposed splice connection under axial loading. Firstly, in **Chapter 3** a theoretical analysis is conducted on the bonded sleeve joint component of the proposed connection. Results from experimental testing and FE modelling are used to validate the theoretical analysis. The theoretical analysis will aid in understanding the behaviour of the bonded sleeve joint component under other loadings.

Chapter 4 presents the works undertaken to investigate the axial performance of the proposed splice connection. Experimental testing and FE modelling are carried out for the bonded sleeve joint component and bolted flange joint component separately to cover a wider range of parameters. The validated FE modelling approach is then used to

analyse the axial performance of the splice connection integrating the two component joints.

Chapter 5 presents the investigation of the flexural performance of the splice connection. The splice connection is subjected to pure moment loading by way of four-point bending. The corresponding FE modelling, compared to that of **Chapter 4**, features a mixed-mode behaviour for the adhesive bond to account for the presence of normal stress as well as shear stress.

Chapter 6 further investigates the connection performance under cyclic loading. In the experimental program, a cantilever setup is adopted to subject the splice connection to a combined cyclic moment and shear action. The chapter focuses on the stiffness & strength evolution and the energy dissipation of the connection. FE modelling is conducted considering damage accumulation in the adhesive bond and kinematic hardening of the steel components.

Chapter 7, the final chapter of the thesis, presents the conclusions drawn from the investigation of connection performance in the preceding chapters. Possible avenues for future research, on the aspects of improved connection design and characterisation of connection behaviour, are also presented.

1.4. References

1. Irving PE, Soutis C. Polymer Composites in the Aerospace Industry. Woodhead Publishing, 2019.
2. Graham-Jones J, Summerscales J. Marine Applications of Advanced Fibre-Reinforced Composites. Woodhead Publishing, 2015.
3. Bank LC. Chapter 2 Materials and Manufacturing. In: Composites for Construction: Structural Design with FRP Materials. John Wiley & Sons. 2006. p. 40-77.
4. Hollaway LC, Teng JG. Strengthening and Rehabilitation of Civil Infrastructures Using Fibre-Reinforced Polymer (FRP) Composites. Woodhead Publishing, 2008.
5. Goldsworthy BW, Landgraf F. Apparatus for producing elongated articles from fiber-reinforced plastic material. United States patent US2871911A, 1959.

6. Bedford Reinforced Plastics. The Pultrusion Process. 2020. Available: https://bedfordreinforced.com/the-pultrusion-process/ [Accessed 11 February 2020].
7. Advantic. Steel Alternative: Fibre-Reinforced Polymer (FRP). 2020. Available: https://advanticllc.com/technology/#steel [Accessed 17 January 2020].
8. Hollaway L. A review of the present and future utilisation of FRP composites in the civil infrastructure with reference to their important in-service properties. Construction and Building Materials. 2010;24(12):2419-45.
9. CNR – Advisory Committee on Technical Recommendations for Construction. Guide for the Design and Construction of Structures made of FRP Pultruded Elements CNR-DT 205/2007. Rome, Italy: National Research Council of Italy, 2008.
10. ASCE (American Society of Civil Engineers). Pre-Standard for Load & Resistance Factor Design (LRFD) of Pultruded Fiber Reinforced Polymer (FRP) Structures. United States: ASCE, 2010.
11. Ascione L, Caron JF, Godonou P, van IJselmuijden K, Knippers J, Mottram T, Oppe M, Gantriis Sorensen M, Taby J, Tromp L. Prospect for New Guidance in the Design of FRP EUR 27666 EN. Ispra, Italy: Joint Research Centre of the European Commission, 2016.
12. SteelConstruction.info. Simple Connections. 2012. Available: https://www.steelconstruction.info/File:C18-06.png [Accessed 22 January 2020].

CHAPTER 2. LITERATURE REVIEW

2.1. Introduction

Fibre reinforced polymer (FRP) composites, also known as fibre reinforced plastics, or advanced composite materials, have been widely used in the aerospace and marine sectors. In civil engineering the early uses of such composite materials mainly involved the rehabilitation and strengthening of existing reinforced concrete [1] and steel structures [2]. In the late 1950s, the pultrusion manufacturing technique, which was cost-effective for producing high-quality and constant cross-section FRP profiles, was developed in the United States [3]. Since, FRP sheets, stripes and reinforcing bars produced from such method began to be considered for use in reinforced concrete structures [4-6]. Moreover, FRP profiles with cross-sections similar to structural steels were also produced from the pultrusion method, envisaging for use as the primary load-carrying elements in bridge [7] and building structures [8].

Focusing on the application of FRPs in building structures, this chapter begins with a review of existing FRP building structures, i.e. buildings that have the majority of the load-carrying system made of FRPs. From there, the importance and difficulty of connection design is highlighted due to the unique characteristics of FRPs. While the behaviour of FRP connections has been comprehensively researched and reviewed in the basic forms of bolted lap joint [9, 10], bonded lap joint [11-13], and hybrid (bolted-and-bonded) lap joint [14, 15], in this chapter a detailed review is presented on the beam-column, truss, and splice connections for FRP profiles. From the review, the lack of effective splice connections for FRP members with tubular section is identified. Considering the resemblance in structural shape and the versatility of metallic connectors in assembling FRP members, splice connections for steel tubular section members are also briefly reviewed. This chapter concluded with the proposal of a conceptual design of splice connection for tubular section FRP members.

2.2. Existing FRP Building Structures

In this Section, the FRP structures to be reviewed are grouped into three categories based on the manufacturing approaches, forms of structural components and assembly style. These include: free-form structures made from the fibre lay-up and/or resin moulding process, structures assembled using panelised members and snap-fit interlocking connections, and frame structures assembled from linear elements, i.e. beams, columns and bracings etc.

2.2.1. Free-Form Structures Made from the Lay-Up and Moulding Process

In the 1950s the use of FRP composites began to extend from the aerospace and marine industries to the building industry. Similar as in the former two industries, components or entirety of the early-generation FRP buildings were manufactured from the fibre lay-up and resin moulding process. Owing to the flexibility in the fibre architecture and in the overall moulded shape, this type of structures featured a free-form and curved geometry, i.e. the materials of the structure can be easily formed into complex shapes before the resin is cured.

The year of 1957 witnessed the erection of the most famous early-generation FRP building, the *Monsanto House of the Future*, designed jointly by Monsanto, the Massachusetts Institute of Technology, and Walt Disney Imagineering [16, 17]. The structure, as shown in Figure 2.1 (a), featured four symmetric wings cantilevered off a 5×5 m central concrete core. The wings consisted of curved GFRP shells made of glass fibres and polyester resin, and a honeycomb core made of kraft paper. The components of the house were assembled on-site using bolts and epoxy. The tourist attraction, reported as able to withstand earthquakes and strong wind loads, was demolished in 1968.

Another example of early FRP building is the *Futuro* designed by Matti Suuronen. Originally intended as a ski cabin, the *Futuro* house, shown in Figure 2.1 (b), was 4 m in height and 8 m in diameter, and consisted of 16 elements that could be bolted together to form the floor and the roof [18, 19]. The elements were composed of GFRP skins (glass fibres and a polyester resin) sandwiching a polyurethane foam core. Because of the lightweight of the FRP elements, the house could be assembled and disassembled on site

in two days, or even air-lifted in one piece. The house could be placed in a variety of rough terrains as only four concrete piers were required. Thanks to the integrated polyurethane insulation and the electric heating system, the interior temperature of the house could be heated from -29 to 15 °C in half an hour.

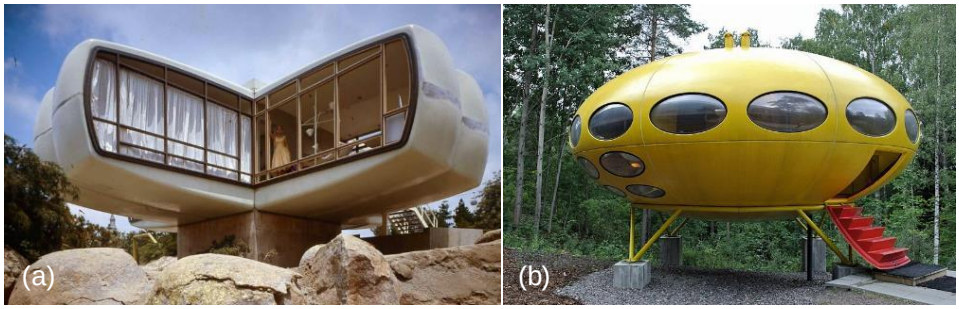

Figure 2.1. Early-generation FRP buildings: (a) the *Mosanto House of the Future* (photo credit: Ralph Crane) [20]; (b) the *Futuro* (photo credit: J-P Kärnä) [21].

By the mid-1970s there were several other free-form type FRP buildings, such as the Rudolf Doernach plastic house (1958) in Germany and the Bakelite Telephone Exchange Room (1962) in the United Kingdom (UK) [22]. The period from mid-1970s to early-2000s saw a decline of this type of FRP structures made from the lay-up and moulding process, perhaps due to the mature of automatic manufacturing methods for FRPs, in particular the pultrusion method [23]. Nevertheless, the lay-up and moulding method retains its unique appeal to architects due to its capability to produce dramatic geometries.

In 1999 the *Millennium Dome* was constructed in London, UK to house the Millennium Experience exhibition. Being the ninth largest building then in the world by usable volume, the *Millennium Dome* [Figure 2.2 (a)] comprised of roof skins supported by a web of 2,600 cables which were suspended by a circle of 12 slightly inclined, almost 100 m-high steel support towers [24]. The roof skins were made of PTFE-coated GFRP for durability and weather resistance. Several complete FRP structures were also housed in the *Millennium Dome*, including the *Rest Zone* [Figure 2.2 (b)] and the *Home Planet* [Figure 2.2 (c)]. Both were assembled on site from FRP sandwich shell panels [25].

Figure 2.2. (a) The *Millennium Dome* (photo courtesy of Mr. Grant Smith http://www.grant-smith.com/); (b) the *Rest Zone* (photo credit: Dick Schmitt) [26]; (c) the *Home Planet* (with permission from Elsevier) [27].

Under the UK government funded project *Future Classrooms*, FRP modular classroom buildings with curved surfaces were designed and constructed [28, 29]. In 2004 this classroom system was pioneered in Grey Court Secondary School and Meadlands Primary School, both in Richmond, Surrey. The modular building was a three-dimensional shell structure [Figure 2.3 (a)] without any internal frames. The complete structure was moulded in factory including internal linings, thereby enabling rapid on-site assembly. Another modular FRP system was the *SpaceBox* developed by Holland Composites [30]. An early client of the system was the Student Housing Service of Delft University. Figure 2.3 (b) shows the erection of a student residential building of the university using the *SpaceBox* modules. The modules could be stacked up to three storeys and, due to lightness in weight, did not required special foundation. Each individual module was completely prefabricated, plumbed, wired, and furbished, such that it could be inhabited within hours of deployment.

Figure 2.3. FRP modular buildings: (a) the *Future Classroom* (image courtesy of Altair HyperWorks) [29]; (b) the *SpaceBox* (image courtesy of Holland Composites) [30].

A more recent example of free-form FRPs in building structure is the carbon fibre reinforced polymer (CFRP) roof of the *Steve Jobs Theatre* which was constructed in 2017 at the Apple Park in Cupertino, California, USA. Shown in Figure 2.4 (a), the lens-shaped roof, 47 m in diameter and 73.2 tons in weight, was supported by a glass cylinder wall 41.1 m in diameter [31,32]. The circular roof consisted of 44 identical radial CFRP panels, each shaped from four layers of 12 mm-thick ply, and a central circular panel. These CFRP panels were manufactured and tested by Premier Composite Technologies in Dubai and shipped to the construction site. On-site, the panels were assembled together [Figure 2.4 (b)] in an adjacent area before lifted in one piece [Figure 2.4 (c)] and installed onto the glass structure.

Figure 2.4. CFRP roof of the *Steve Jobs Theatre* (image credit: Foster + Partners) [31]: (a) in service; (b) assembly; (c) installation.

In most of the free-form FRP structures, a high capability of thermal insultation was integrated into the structural panels through the sandwich construction, i.e. high-

strength and -stiffness FRP skins sandwiching a lightweight core. Besides the architectural appeal, the geometries of this type of structures often had been optimized with respect to the design loadings. However, the creation of these free-form structures involved a costly manufacturing process and was mostly dedicated for highly customised projects, restricting the application of such type of FRP structures in niche markets.

2.2.2. Snap-Fit Panelised Structures

As the pultrusion manufacturing technique developed and matured in the 1970s and 1980s, FRP profiles manufactured through this technique started to show potential as an alternative to conventional structural members. The main motivations were their lightness thus cost saving in transportation and erection, and chemical resistance (including corrosion resistance) thus reduced maintenance in industrial application. To further ease the erection on-site, a type of FRP building system was developed based on standardised building 'panels" or "blocks" and "snap-fit" interlocking connections.

The *Advanced Composite Construction System* (*ACCS*), developed in the 1980s (now named *Composolite*), represents the earliest version of this type of system [33]. Figure 2.5 (a) shows examples of the pultruded multi-cell wall or floor panels; in Figure 2.5 (b) are the pultruded three-way connectors, end-caps and toggle for joining the panels. Adhesive bonding could be applied on the contact surfaces if weatherproof sealing was required. A temporary two-storey site office at Severn Crossing road bridge in Bristol, UK was constructed of the *ACCS* and was later converted to a permanent visitor centre [Figure 2.5 (c)]. In this application the multi-cell panels were infilled with polyurethane foam to enhance thermal insulation [34]. Because of the corrosion resistance of the FRP material, the *ACCS* was also used in a series of industrial applications, including chemical plants walkways, equipment wash houses, odour covers and the outfitting of cooling towers [Figure 2.5 (d)] [33].

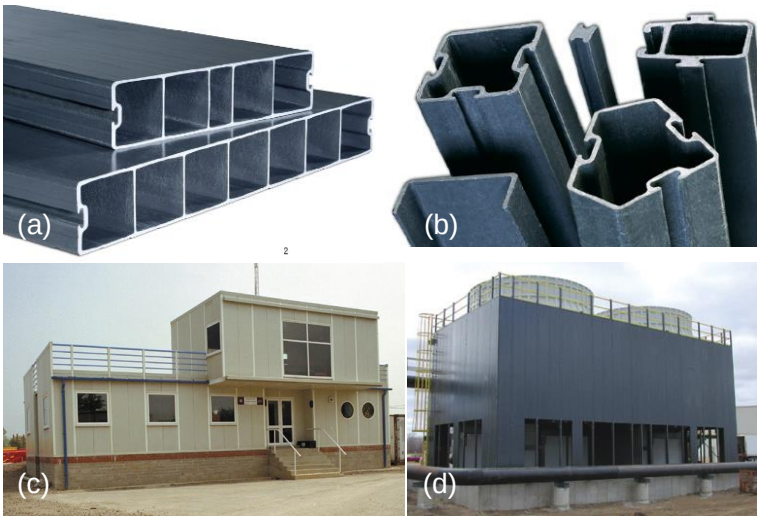

Figure 2.5. The *ACCS/Composolite* (image courtesy of Strongwell) [33]: (a) FRP panel units; (b) FRP connector units; (c) application in site office; (d) application in cooling towers.

A more recent example of this system was the *Startlink* modular FRP building system which was developed in 2004. For design flexibility the system offered a range of 15 open and closed pultruded sections [Figure 2.6 (a)] that could be snap-fit together with rubber seals for weatherproofing [35]. A two-storey demonstration house was built out of the *Startlink* system in Lincolnshire, UK in 2012. The reduced weight of the FRP profiles offered significant saving in transportation and enabled the use of FRP composite piles instead of a concrete foundation [36]. Another example of the snap-fit system was the Hambleside-Danelaw modular building unit [Figure 2.6 (b)] developed as a temporary shelter [28]. The building panels, comprised of pultruded FRP-steel hybrid tubular frames and FRP panels with foam core, could be slid together without the need of mechanical fastener and adhesive bonding.

Figure 2.6. (a) The *Startlink* system – units (image courtesy of Mr. Mark Singleton, Startlink Systems Ltd.) [25] and demonstration house (image courtesy of Larkfleet Group) [36]; (b) the Hambleside-Danelaw modular building (with permission from Elsevier) [28].

This type of snap-fit panel system features an open-building style that may offer certain flexibility in two-dimension; but concerns over the connection reliability limit the application of this system to low-rise structures. Nevertheless, the panelised construction and the snap-fit assembly feature greatly ease the erection of emergency housing and temporary shelter where assembly may have to be quickly carried out by semi-skilled operators.

2.2.3. Frame Structures Assembled from Linear Standard Elements

Through the pultrusion manufacturing process, FRP profiles were produced with standardized sections similar to the structural steel beams and columns. A number of frame structures have been designed and built using these linear FRP beam and column elements. To date, compared to the aforementioned free-form and snap-fit panel systems, this type of FRP building system is perhaps the most popular because of the familiarity with structural engineers and construction practitioners.

The computer and electronics industry appeared to be the first major customer of the FRP frame system, where GFRP profiles were selected to minimise the electro-magnetic interference of the buildings [37,38]. In the 1980s, portal frame structures made of pultruded GFRP profiles were designed and constructed for the testing of computer and electronic equipment of Apple Computer and IBM (Figure 2.7). Like in conventional steel works, these FRP portal frame structures consisted of I-section columns and rafters,

diaphragms, and bracings; the connection of columns and rafters was mainly done by web gussets with bolt fasteners.

Figure 2.7. FRP portal frame structure for the testing of computer and electronic equipment (image courtesy of Strongwell) [38].

Another major customer of the FRP frame system was the cooling tower industry which was seeking a corrosion-proof building solution. Figure 2.8 shows a "stick-built" cooling tower structure developed in the late 1980s [39]. The braced frame structure was constructed of pin-connected tubular and channel sections FRP profiles with an FRP or nonreinforced polymer cladding and flooring system. The structural design and selection of profile size generally followed the then-existing wood designs.

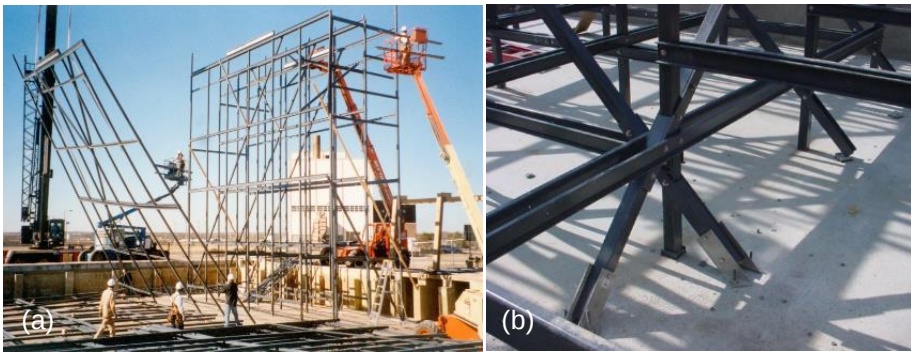

Figure 2.8. FRP stick-built cooling tower (image courtesy of Strongwell): (a) overview at erection; (b) close view of structural elements.

The FRP frame system was also adopted in civil facilities. An example was the 19.2 m-tall stair-tower at the U.S. Army Training Base in Fort Story, Virginia [Figure 2.9 (a)]. Designed by Strongwell, Bristol in the late 1990s, the stair-tower was reported capable of carrying a vertical load of approximately 408 kN and a hurricane wind up to 62 m/s [40]. GFRP profiles were selected as the structural members for quick erection and to resist salt water corrosion from the nearby Chesapeake Bay. The I-section beams, columns and bracings were connected through stainless-steel web angles and bolts [Figure 2.9 (b)].

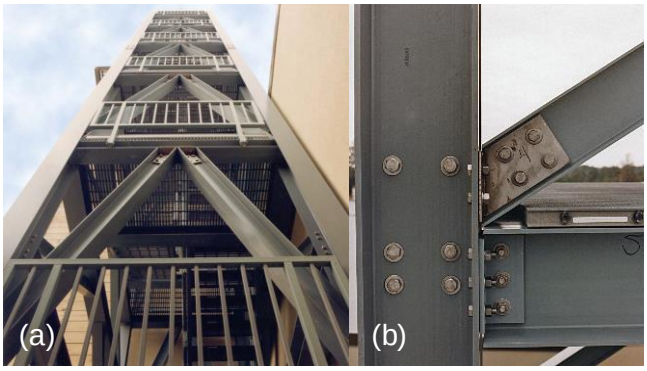

Figure 2.9. FRP stair-tower (image courtesy of Strongwell): (a) overview; (b) close view of connections.

In 1999 the *Eyecatcher* building [Figure 2.10 (a)], five-storey and 15 m-high, was constructed of pultruded FRP profiles by Fiberline A/S. Originally built for the Swissbau exhibition, the structure, with steel bolted connections, was disassembled, transported, and reassembled for use as an office building [Figure 2.10 (b)] [41]. Figure 2.10 (c) shows that I- section profile or flat plates were adhesively bonded with channel section profiles to form more complex built-up members. To enclose the building frame, sandwich walls/facades filled with aerogel were attached to the structural members for thermal insulation.

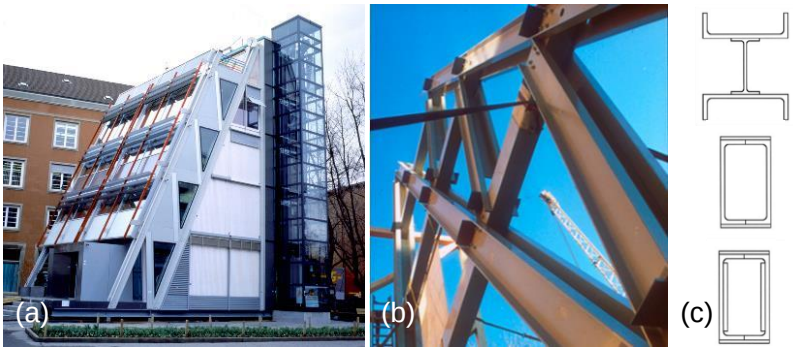

Figure 2.10. The *Eyecatcher* building: (a) overview (image courtesy of Fiberline A/S) [41]; (b) structural frame (with permission from Taylor & Francis) [42]; (c) built-up members [43].

Due to ease of assembly, FRP solutions could benefit the construction of temporary structures. After the partial collapse of the Santa Maria Paganica church in Italy due to the L'Aquila earthquake in 2009, a series of FRP temporary shelter structures were constructed to accommodate restoration activities [44]. Figure 2.11 (a) show one of the shelter structures that measured up to 29.4 m-high and covered an area of 266 m^2. The shelter structures were rectilinear space frames assembled from pultruded FRP elements. Typical primary members consisted of channel or angle pultruded sections joined together with steel bolts. The frame members were connected through bolting to a moulded GFRP gusset web plate as shown in Figure 2.11 (b). The base of the column members was embedded into reinforced concrete pedestals on the ground.

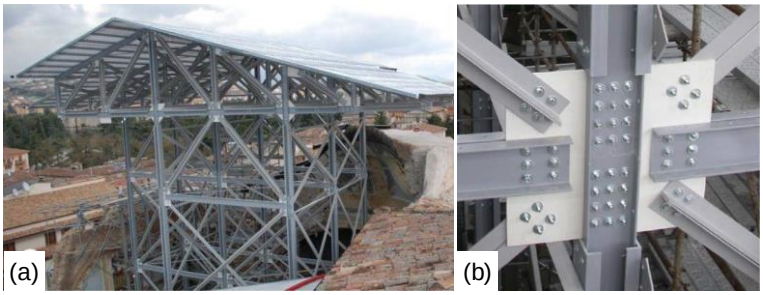

Figure 2.11. FRP shelter structure for the Santa Maria Paganica church (on the courtesy of TOP GLASS Industries S.p.A. www.topglass.com) [44]: (a) overall view; (b) connection between members.

Being lightness in weight, pultruded FRP profiles are ideal structural member in prefabricated systems. In 2014 an FRP prefabricated modular housing system was developed under the *ClickHouse* project [45, 46]. The project aimed to provide prefabricated modular housing system for disaster zones, emergency situations and construction sites. The resulting prototype, shown in Figure 2.12 (a), consisted of two 3×3×3 m modules sharing adjacent beams and columns. The beams and columns were 120×120×10 mm square hollow section pultruded GFRP profiles. Connection between the beam and column was realized by stainless-steel bolted tube connectors inside the hollow section members. To avoid positioning of the fasteners in the closed profiles, bolt nuts were welded onto the inside face of the steel connectors. Sandwich panels with GFRP skins and polyurethane core were adopted for roofs, floors and walls. Water, electricity networks and sanitation facilities etc. would be pre-installed before the house was transported to site.

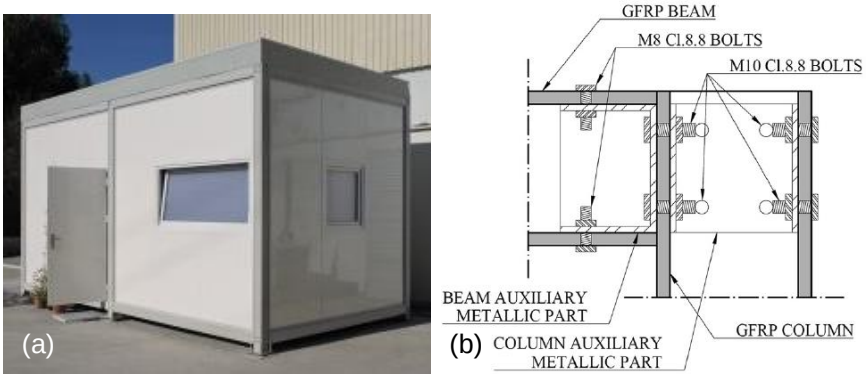

Figure 2.12. The *ClickHouse* modular building: (a) overview (image courtesy of Prof. João Ramôa Correia) [45]; (b) connection details (with permission from Elsevier) [47].

To date, the application of FRP framing systems have been restricted to low-rise or relatively light-load scenarios. The acceptance of FRP profiles as a common structural member is majorly impeded by the difficulty in connecting individual members, associated with the anisotropic and brittle natures of the material. Researches beginning since the 1990s had shown that steel-like connection designs were not the optimized solution for FRP profiles. More researches have been and are going on in search of

economical and effective connection systems. In the context of applying FRP profiles in the framing system, a detailed literature review on the research efforts towards effective connection designs is presented in the following sections.

2.3. Beam-Column Connections for FRP Members

Among the different categories of FRP frame connections, beam-column connections have received early and extensive researches due to its necessity in frame assemblies. A high rotational stiffness is usually sought after in order to compensate for the low flexural stiffness of a GFRP beam member (low elastic modulus in comparison to steel). Along with the high rotational stiffness comes the requirement of moment capacity, as end moment would be incurred in a semi-rigid or rigid beam-column connection. Design of beam-column connections was mainly conducted for I-section open profiles before 1999, and later on also for tubular section profiles.

2.3.1. Connections for I-Section Members

In the early 1990s the first series of beam-column connection design and testing were conducted by Bank et al. [48] using pultruded GFRP I-section members (203×203×9.5 mm), angles and fasteners. The first design, imitating the practice in structural steel, featured bolting the flanges and the web of the beam to the column front flange via angle cleats [Figure 2.13 (a)]. A unique failure mode of pultruded profiles was revealed as tearing of the column flange off the web. To mitigate this failure, in the second design a pair of FRP angles was bolted under the web and flange of the column [Figure 2.13 (b)]. This design shifted the failure to flexural-tension cracking in the GFRP angle cleat at the tension flange of the beam, and enhanced the moment capacity by approximately 40%. Based on the second design, the third design had the top cleat replaced by a bolted built-up gusset angle, and experienced shear-out failure at the gusset angle. Compared to the first design, the initial rotational stiffness was increased by 30% and ultimate moment by 119%. The fourth design in this study, shown in Figure 2.13 (c), consisted of bonded built-up gusset angles at both top and bottom flanges of the beam and through-bolts to engage both flanges of the I-section column. The connection experienced failure in the

adhesive bond in the top built-up gusset angle. Its initial stiffness and ultimate moment were about 273% and 212% higher than those of the first design.

Another early study of beam-column connections was conducted by Bruneau and Walker [49] using 203×103×9.5 mm I-section GFRP profiles. The connection design was similar to that of Figure 2.13 (a) but T-cleats and GFRP web stiffeners were used instead of angles. In addition, adhesive bonding was applied on all contact surfaces besides the GFRP bolts. Probably the first cyclic testing of FRP beam-column assembly was conducted in this study. Failure of the connection occurred as delamination of the T-cleat at the beam flange and also tearing of column flange off the web. The authors concluded that the T-cleats and adhesive bonding were unable to provide a rigid joint, due to the inadequate stiffness and strength of the web-flange junction of the I-section column.

Beam-column connections using similar FRP angle cleats as in [48] were studied by Bass and Mottram [50]. The cross-section of the GFRP profiles was also 203×203×9.5 mm. Similar to the connections of Figure 2.13 (a) and (b), the connections in this study involved adhesive bonding in addition to the bolt fastening. In order to strengthen against failure in the angle cleat, additional angles were included under and stacked onto the tension flange of the beam. It is noteworthy that this study might be the first to undertook minor axis moment-rotation tests on beam-column connections, i.e. the beam was connected to the web of the column. The minor axis tests revealed that, compared to the major axis counterparts, the moment capacities were similar but the initial stiffnesses were 3.2 to 3.4 times. It was noted that the larger rotations of the major axis connections were attributed to the flexibility of the column flange.

Subsequently, specialized connectors were developed for FRP profiles. Wrapped angle connector [Figure 2.13 (d)], fabricated by wrapping glass fibre fabric around a pultruded angle, was developed by Bank et al. [51]. Same I-section profiles (203×203×9.5 mm) and GFRP fasteners were used as in [48]. Moment loading on the beam-column connection resulted in tensile bolt failure (thread striping) at the column. The ultimate moment was 1.92 times of the initial design of Figure 2.13 (a), but the initial stiffness was only 30%. In the shape of a triangular tube as the wrapped angle connector, a moulded multi-cell connector was used in another design. This connection failed by

tensile bolt failure (thread striping) at the beam and exhibited an initial stiffness 75.3% of the initial design of Figure 2.13 (a). Noteworthy is that this connection attained an ultimate moment of 30.5 kNm which was the highest among the connections tested by Bank et al. [48, 51] and was about 5.2 times of the design of Figure 2.13 (a). Nevertheless, the authors recommended the wrapped angle connector considering its simplicity and saving in material.

Based on a parametric finite element (FE) analysis, a so-called universal connector, regarded by the authors as the optimized shape of such element, was developed by Mosallam et al. [52] for joining pultruded FRP profiles with bolts. The universal connector (UC), shown in Figure 2.13 (e), was manufactured from a resin injection process. The I-section beams and columns used in the experimental study were of a cross-section of 102×102×6.4 mm and also incorporated GFRP bolts. It was revealed that the UC specimen, although showing a moment capacity 2.78 times of a control specimen using flange angle cleats, had an initial stiffness only 76%. Another UC specimen was prepared using adhesive bonding as well as bolt fastening. Its initial stiffness was 24.3 times of the control specimen and the ultimate moment was 3.78 times. The bonded-and-bolted UC specimen failed in a much more ductile way through progressive damage in the FRP components. Ultimate failure of both UC specimens occurred mainly as cracking of the gusset plate of the UC and bolts punching through the UC at the column side.

Mottram and Zheng [53] carried out a series of tests on beam-column connections with bolted web angle cleats [Figure 2.13 (a) with only web cleats]. The cross-section of the beam and column profiles was 254×254×12.7 mm. At each side of the beam web a row of three steel bolts were used. The first connection was bolted-only while the second connection was bolted-and-bonded. In both types of connections, the ultimate failure occurred as fracture and delamination of the web cleats under prying action. The addition of adhesive bonding improved the initial stiffness by 350% but improvement in the ultimate moment was marginal. A minor axis connection using bolts only was also tested. The ultimate moment was slightly lower than the corresponding major axis connection and the initial stiffness was 55% higher, which was consistent with the finding by Bass and Mottram [50].

In search of higher moment capacity, Mottram and Zheng [54] conducted another series of tests using flange angle cleats. A smaller cross-section (203×203×9.5 mm) was used in this study and the connections were bolted only. The first connection entailed steel angle cleats at the top and bottom flanges of the beam and steel bolts going though both the front and back flanges of the column. Failure occurred at the tension flange of the beam around the bolt holes. The initial stiffness and ultimate moment were 186% and 480% higher than the best-performing web cleat connection using the same beam and column profile [55]. Another connection was prepared using through-bolts at the beam and a pair of additional angles bolted under the beam flange to inhibit the failure at the beam flange. The top angle cleat was a moulded pre-preg GFRP part and the rest of the cleats were cut from pultruded angles. GFRP bolts were used at the top flange cleat, and steel bolts were used elsewhere. This connection failed through thread stripping of the top GFRP bolts under tension. Compared to the first connection, initial stiffness was improved by 21% and moment capacity by 33%.

Bolted connections using angle cleats (at flange, web, or both) were also tested by Turvey [56]. This study was different in that the GFRP I-section beam (102×102×6.4) was bolted to a rigid steel plate through tight-fitting stainless-steel bolts and angles. With this configuration the failure was majorly restricted to the GFRP beam around the drilled holes. A few other pinned type beam-column connections using bolted web cleats [Figure 2.13 (a) with only web cleats] and steel bolts were conducted by Qureshi and Mottram [57-59]. These studies mainly focused on steel vs. FRP cleats [57], number of bolt rows [58], and characterisation of connection stiffness at different loading stage [59].

A bolted web plate connection was developed for built-up beam and column by Feroldi and Russo [60]. Shown in Figure 2.13 (f), the beam and column were comprised of two back-to-back pultruded GFRP channel section profiles; the beam and column were joined together via a pultruded web gusset plate (fibre direction parallel with the beam) bolted (steel bolts) between the profile webs. Two connections were examined, where the first consisted of 152×43×9.5 mm channel profiles and a 362×230×15 mm web plate and the second of 200×60×10 mm channel profiles and a 433×350×15 mm web plate. The ultimate failure was due to in-plane shear-out of the bolt holes at the web gusset plate. The moment-rotation behaviour showed limited ductility when approaching the ultimate

moment. The larger connection attained an ultimate moment of 21 kNm while the smaller connection's ultimate moment was 12 kNm. A detailed 3-D FE modelling was conducted where damage of the pultruded parts was modelled through an 90% instant stress reduction based on a maximum stress failure criterion. The modelling was able to capture the nonlinear moment-rotation behaviour approaching failure and the ultimate moments.

More recently, to justify the use of adhesive bonding in beam-column connections, fully adhesive bonded GFRP beam-column assemblies were prepared and tested by Ascione et al. [61]. The connection, entailing I-section profiles (200×100×10 mm) and GFRP flange and web angle cleats, was similar to the design of Figure 2.13 (a), except that the bolt-fastening was replaced by adhesive bonding. A reinforced version of the connection was prepared with a pair of GFRP angles bonded under the web-flange junction of the column [similar to Figure 2.13 (b)]. Tested to failure, the connections exhibited linear moment-rotation responses up to brittle failure. The unreinforced connections failed by delamination in the column flange while the reinforced ones failed by surface mat pull-off of the column flange. The reinforced design improved the rotational stiffness by 46-65% and ultimate moment by 31-46%. By comparison to the bolted connections studied by Bank [48], the authors concluded that the fully bonded connections could attain higher or at least same strength as the corresponding bolted connections.

In a continuing study by the authors [62], the benefits of introducing CFRP fabric wrap around the column (and beam) and using steel flange cleat at top of the beam were investigated. The inclusion of CFRP wraps did not improve the stiffness and strength as the CFRP wraps were not engaged until other failure occurred in the connections. The use of top steel flange cleat together with CFRP wraps improved the ultimate moment slightly, but imparted the connection some residual strength after peak moment.

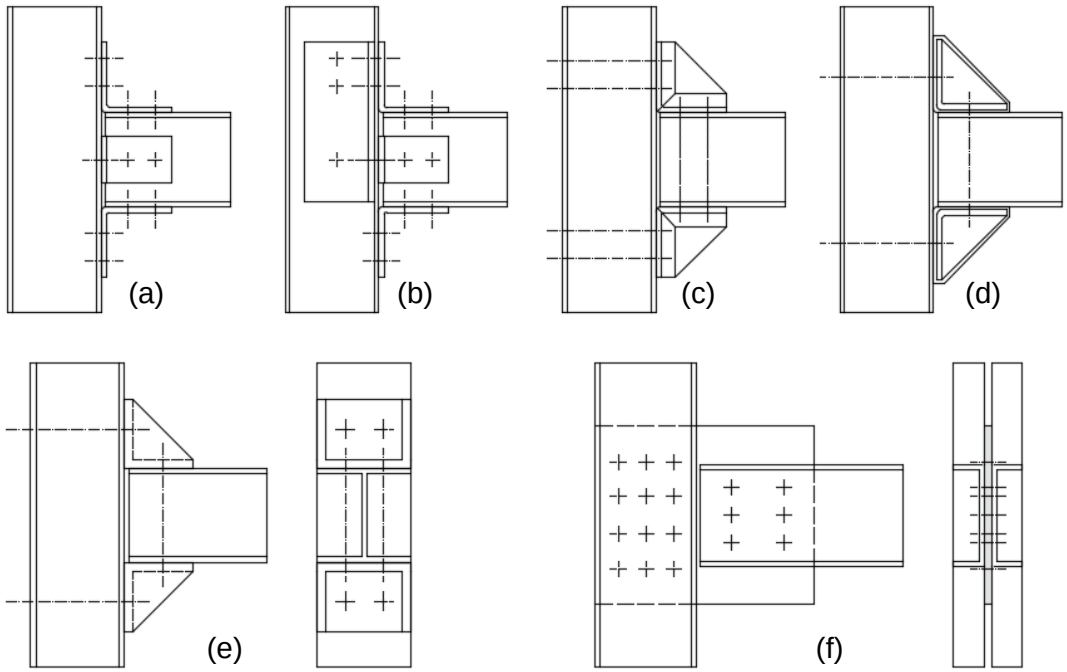

Figure 2.13. Prototypes of I-section FRP beam-column connections: (a) bolted angle cleats at flanges and web [48]; (b) reinforced bolted angle cleats [48]; (c) flange gusset cleats with through-bolts [48]; (d) wrapped angle connector [51]; (e) Universal Connector [52]; (f) bolted web plate for built-up beam and column [60].

2.3.2. Connections for Tubular Section Members

The studies by Smith et al. [63, 64] were the first on beam-column connections for tubular section FRP members. Herein the beam and column members were pultruded GFRP with a rectangular box section of 51×6.4×102×3.2 mm. Generally, the connection elements included flange angle cleats and web plates made of pultruded GFRP or steel. All the elements were bolted and bonded. The first beam-column connection included GFRP flange angle cleats and side plates (fibre direction parallel with the beam) as shown in Figure 2.14 (a). The connection, with an initial stiffness of 430 kNm/rad and ultimate moment of 4.81 kNm, failed through tearing of the side plates. Steel angles and side plates were used in place of the GFRP ones in the second connection, resulting in failure by web-flange separation of column. The initial stiffness was increased by 43% but the ultimate moment was slightly lower. In the third connection, the side plate in the first

connection was replaced by a pair of larger GFRP plates (fibre direction 45° to the beam) gusseting the column as shown in Figure 2.14 (b). Local failure occurred as transverse cracking in the beam web close to the tension flange. Compared to the first connection, the initial stiffness was improved by 33% and the ultimate moment by 21%, respectively. The last connection in this study was a so-called bolted (and bonded) cuff connection as shown in Figure 2.14 (c). The cuff connector was made of a pultruded angle with part of one leg removed so that it could be attached to the column web and at the same time wrapped onto the beam. This connection failed by web-flange separation of the column and exhibited initial stiffness 21% higher than the first connection. The ultimate moment of this cuff connection was the highest in these studies, i.e. 6.2 kNm and 29% higher than the first connection. In [64] the authors also proposed the conceptual design of an idealized bonded cuff connection, which would later be investigated.

Conceptualized in [64], the bonded cuff connection [Figure 2.14 (d)] was materialized by Singamsethi et al. [65]. The cuff connector was manufactured by wrapping layers of unidirectional and ±45° glass fabric onto a mould, followed by a process of vacuum assisted resin transfer moulding. The column and beam were inserted into and bonded to the cuff connector to form a beam-column assembly. Two beam-column connections were prepared and mainly differed in the treatment of the bonded surfaces: hand-abraded or machine-abraded. Cyclic tests were carried out and the moment-rotation responses were mainly linear up to failure. The first connection, with hand-abraded bonded surfaces, failed at approximately 7.8 kNm due to a bond failure between the beam and the cuff, mainly at the adhesive-cuff interface. The second connection failed at 10.2 kNm due to crushing of the beam near the compressive flange as it was pressed against the cuff. No sign of bond failure was observed and the cuff remained mostly intact apart from minor surface cracks. The additional surface treatment clearly improved the bond quality and thus connection strength. Compared to the earlier bolted-and-bonded cuff connection of Figure 2.14 (c) [64], the bonded cuff connections exhibited up to 10% and 64% higher in initial stiffness and moment capacity.

Further experimental investigations on the bonded cuff connections were carried out by Carrion et al [66] using steel beam and columns, aiming to investigate the failure phenomena of the FRP cuff connector. The connections failed in the adhesive bond or in

the cuff depending on the cuff dimensions. The cuff failure, characterised by cracking at the beam-column junction, was more ductile in terms of post-peak behaviour. Another several connections were prepared with pultruded GFRP beam and column, where a pair of C-shaped FRP stiffeners were bonded inside the beam to prevent the beam crushing failure observed in [65]. The resulted cuff failure was deemed favourable, because of the better ductility than the beam crushing failure while the connection strengths were similar. A corresponding detailed FE modelling was carried out in [67] employing elastic material models and Tsai-Wu failure criterion [68] to detect failure initiation in the FRP components. Overall, the modelling satisfactorily captured the connection stiffness and the failure locations of beam crushing and cuff cracking.

A series of experimental tests were conducted on wall stud connections for square tubular section GFRP profiles by Wu et al. [69]. Due to the resemblance in assembly configuration and load application, the wall stud connections are described herein as FRP beam-to-steel column connections. The configuration of bonded sleeve connection featured a steel tube bonded inside the GFRP tubular beam (102×102×9.5 mm in cross-section) and bolted to the steel column through a welded endplate. The bonded sleeve connection failed in a ductile manner due to excessive yielding of the steel endplate and experienced no bolt-hole slipping as observed in the other two connections using bolted steel angles or bolted sleeve connector. The bonded sleeve connection reached an ultimate moment of 19.4 kNm which was at least 60% higher than the other two connections.

The endplate bonded sleeve connection was later adapted for connecting tubular section FRP beam and column (102×102×9.5 mm) as shown in Figure 2.14 (d). Static and cyclic loading studies were carried out. In the static study [70], four types of connections were prepared where the design variables included 80 vs. 160 mm steel-GFRP bond lengths and four vs. eight rows of bolt on the steel endplate [Figure 2.14 (d) shows an example of four rows]. The additional rows of bolts increased the initial stiffness by 7.3-30% and ultimate moment by 11-15%. The connections with 80 mm-bond length failed by cracking in the adhesive and at the web-flange junctions of the GFRP beam. The connections with 160 mm-bond length showed 51-56% higher ultimate moment (at 6.34 kNm and 7.06 kNm) and failed due to web crippling of the GFRP

columns. These two 160 mm-bond length connections failed in a relatively ductile way through yielding of the steel endplate and post-peak progressive failure of the GFRP column. In the cyclic study [71], all the three connections had a 160 mm-bond length and differed in the number of bolt rows (four vs. eight) and thickness of the steel endplate (6 vs. 8 mm). All the connections failed ultimately due to cracking in the adhesive and at the web-flange junctions of the GFRP beam. Satisfactory energy dissipation was demonstrated through yielding of the steel endplate. In these studies, corresponding FE modellings were conducted. The connection initial stiffness and yielding behaviour of the steel endplate could be captured quite accurately. The ultimate failures were predicted by checking the normal stress in the adhesive against its tensile strength, and the stress state of the FRP members against the Tsai-Wu failure criterion [68].

Bolted connections for tubular section GFRP beam and column were developed by Martins et al. [72]. Steel tube connectors were bolted inside the GFRP beam and column (120×120×10 mm in cross-section) as shown in Figure 2.14 (f). Bolt nuts were pre-welded onto the steel connectors to avoid positioning of the nuts inside the closed-section profiles. The steel connector inside the beam had a welded cap plate for bolting to the column. Four types of connection were developed with difference in the bolt arrangement on the beam connector. Figure 2.14 (f) shows the connection with one row of bolts on flange and long bolt edge distance – it had the highest ultimate moment (6.0 kNm) in monotonic testing. The failure of this connection was also the most ductile due to yielding of the steel cap plate and bearing failure of the bolt holes instead of shear-out failure (in the other connections). The ultimate failure was fracture of the steel cap plate and cracking of the column front flange. The connections stiffness and strength were estimated using a component method based on the behaviour of GFRP-steel single lap joints. An accompanying cyclic study [73] was conducted using the same series of connections. The failure modes and connection strengths were consistent with those of the monotonic study. The connection which showed the most ductile failure under monotonic loading also outperformed the others in terms of energy dissipation.

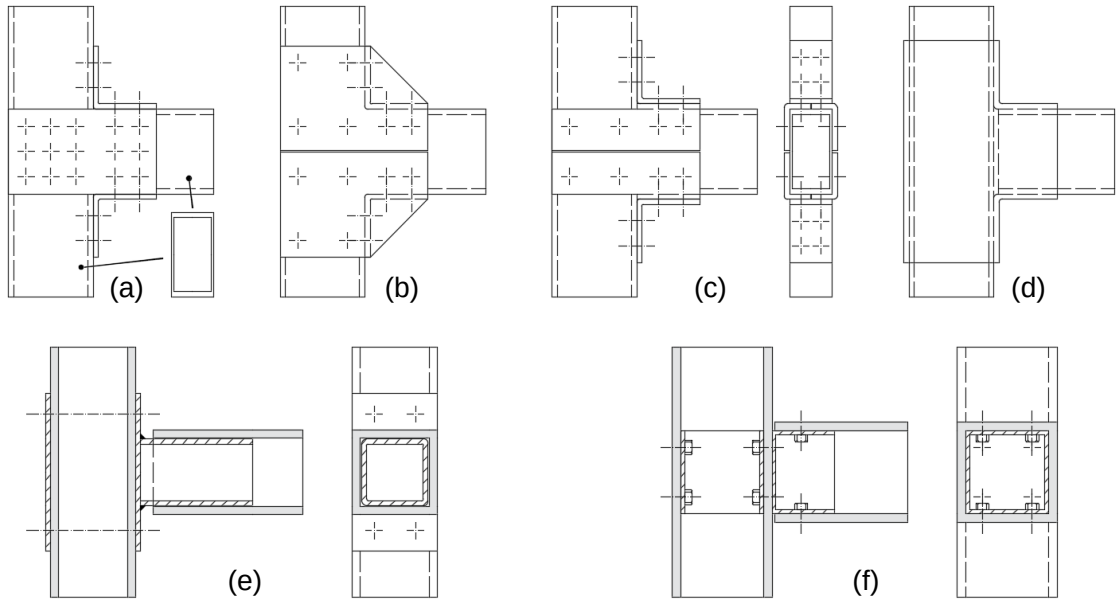

Figure 2.14. Prototypes of tubular section FRP beam-column connections: (a) bolted-and-bonded flange angles and web plates; (b) bolted-and-bonded flange angles and web gusset plates; (c) bolted-and-bonded cuff connection; (d) bonded cuff connection [64]; (e) endplate bonded sleeve connection [70]; (f) bolted steel tube connectors with welded nuts [72].

2.3.2. Comparison of Moment Capacities

Among the above reviewed beam-column connections, the best-performing ones in terms of ultimate moment capacity were presented in Table 2.1. Here, a comparison of connection stiffness was not carried out due to the variety of test setups and methods of rotation measurement, and more importantly, due to the inconsistent or unclear definition of initial stiffness, especially when bolt-hole slipping occurred at the early stage of loading. In Table 2.1 the ultimate moments of the connections (M_u) were normalized with respect to the theoretical section moment capacity of the beam profile ($M_{s,th}$). With a $M_u/M_{s,th}$ ratio of 28.7%, the connection with multi-cell moulded connectors by Bank et al. [51] was the best performing fully bolted connection. But the authors themselves reckoned the fabrication of the multi-cell connector complicated and gave credit to the simplicity of the wrapped angle connector [Figure 2.13 (d)] which had a $M_u/M_{s,th}$ of 10.7%. Overall, the connections for tubular section profiles showed higher strength

performance, because of the increased use of adhesive bonding and the additional web which improved the web-flange junction strength. All of the bolted-and-bonded connections by Smith et al. [64] showed high $M_u/M_{s,th}$ ratio, ranging from 38.7 to 52.1%. The bonded cuff connection had the highest $M_u/M_{s,th}$ of 85.7% among all the reviewed connections. The endplate bonded sleeve connections by Wu et al. [69] and Zhang et al. [71] [Figure 2.14 (e)] were advantageous in that the adhesive bonding could be pre-fabricated and the on-site assembly could be done through bolt fastening. The connection showed a high $M_u/M_{s,th}$ ratio of 63.6% when used to join a FRP beam to steel column [69], and ratio of 24.5% when used in FRP beam-to-FRP column [71].

Table 2.1. The best-performing FRP beam-column connections in terms of strength.

Description of connection	**Beam & column section**	**M_u [a] (kNm)**	**$M_{s,th}$ [b] (kNm)**	**$M_u/M_{s,th}$**	**Reference**
Bolted FRP flange gusset cleats [Figure 2.13 (c)]	203×203×9.5 mm I-section	18.4	106.1	17.3%	[48]
Bolted multi-cell moulded FRP connector		30.5		28.7%	[51]
Bolted FRP web plate [Figure 2.13 (f)]	152×43×9.5 mm channel section back-to-back	12.0	62.6	19.2%	[60]
Bonded reinforced flange and web angle cleats	200×100×10 mm I-section	10.2	55.8	18.2%	[61]
Bolted and bonded [Figure 2.14 (a-c)]	51×6.35×102×3.2 mm rectangular tubular section	6.2	11.9	38.7-52.1%	[64]
Bonded moulded FRP cuff [Figure 2.14 (d)]		10.2		85.7%	[65]
Bonded sleeve with bolted endplate (to steel column)	102×102×9.5 mm square tubular section	19.4	30.5	63.6%	[69]
Bonded sleeve with bolted endplate [Figure 2.14 (e)]		8.04	32.8	24.5%	[71]

[a] ultimate moment of the beam-column connection

[b] theoretical section moment capacity of the beam based on material tensile strength and section elastic modulus

2.4. Connections for FRP Members in Trusses and Space Frames

With majority of the fibres aligned in the axial direction, pultruded FRP members are attractive for use in truss structures where the member forces are mainly transferred in the axial direction. Tubular section members are favoured for their better performance against local and global buckling than open section (e.g. I-section, channel section etc.) members. For the assembly of individual FRP truss members, a widely practiced approach is to fix metallic connectors at the ends of an FRP member. The metallic connector facilitates various connection methods (e.g. bolt-fastening, pinning, welding etc.) to the nodal joints which often are also made of metallic materials such as steel and aluminium. In this section, the review is focused on the connection/joint between the metallic connector and the FRP member.

In an early study of this kind, Green and Phillips [74] developed aluminium alloy tube connectors that were crimped and bonded onto pultruded or rolled FRP circular tubes [Figure 2.15 (a)]. The free end of the aluminium tube connector was flattened for bolting to a nodal joint or another member. FRP tubular members of four cross-sections were studied: 8×1.1 mm (outer dia. × thickness), 8×0.75 mm, 15×1.5 mm and 25.4×2 mm. Joints with multiple overlap lengths were tested under axial tensions. The studied overlap lengths were not explicitly indicated; what could be known from the reference was that 50 to 75 mm overlaps were used for the 8 mm-outer diameter tubes, and that up to 55 mm overlaps were used for the 15 mm- and 25.4 mm-tubes. The joints, loaded in tension, failed through a shear failure in the FRP members. The joints could sustain tensile loads up to 68-92% of the theoretical tensile capacities of the FRP members. It was also reported that the joint capacity increased close to linearly with the overlap length, suggesting in this study a likely constant shear stress distribution along the overlap at failure.

Stainless-steel Mero ball nodes were used by Hagio et al. [75] to assemble a GFRP truss. Stainless-steel tube connectors, to be pinned to the Mero ball node at one end, were fixed inside pultruded GFRP circular tubes (145 × 7.5 mm) via riveting and adhesive bonding. The detailed configuration and dimensions of the rivet and adhesive joint were not reported. Tensile and compressive tests on the joint were performed without description of the failure mode. From the load-displacement plots the joint showed ductile behaviour that was similar under tensile and compressive loads. After the initial linear stage, the zig-zag pattern of the load-displacement behaviour suggested that the joint ductility derived from a series of progressive failures. Under both tension and compression, the tested joints attained ultimate loads of around 300 kN, which amounted to about 29% of the theoretical tensile capacity of the GFRP section.

For the assembly of an FRP truss structure, a pre-tightened teeth joining technique was developed by Zhang et al. to join aluminium tube connectors to FRP circular tubes [76]. With the joint configuration shown in Figure 2.15 (b), the joining process first required grooving well-matched, spiral flat 'teeth' onto the inner and outer surfaces of the aluminium and FRP tubes respectively. The FRP tube was then screwed into the aluminium tube, before another smaller aluminium tube was pressed into the FRP tube using a hydraulic jack, thereby expanding the FRP tube to exert radial normal stress onto the outer aluminium tube, completing the 'pre-tightened' process. Seven and three rows of teeth (8-12 mm in width) were manufactured on the 104×8 mm and 76×6.5 mm FRP tubes. The joints were tested under compression but failure mode and load-displacement response were not reported. The ultimate compressive loads were 730 kN and 320 kN for the larger and smaller joints respectively, which corresponded to 49% and 40% of the theoretical compressive capacities of the FRP tubes.

For easy assembly of tubular section FRP members into space frame structures, bolted sleeve joints with steel tube connector were developed by Luo et al. [77] as shown in Figure 2.15 (c). The bolted sleeve joints were prepared in four configurations, including the design parameters of one vs. two bolts per row, ordinary bolt vs. blind bolt, and member size (GFRP cross-section in 38×38×4 mm vs. 51×51×6.4 mm). Two rows of bolt were used in all joint specimens; Figure 2.15 (c) shows an example of two bolts per row. Both tensile and compressive tests were performed. Under tension, all the joints

failed by shear-out failure in the GFRP. Under compression, the joints showed 29-51% higher compression capacities than under tension as bearing failure became more dominant than shear-out failure. The use of blind bolts, although convenient in cavity fixing, resulted in 15.4% and 26.7% reduction in tensile and compressive capacities, and 30.9% and 44.0% reduction in tensile and compressive stiffness. In this study the bolted sleeve joints could sustain up to 31% and 54% of the tensile and compressive section capacities of the FRP member. An analytical estimate of the joint capacity was carried out based on a 0.57/0.43 load distribution in the first/second bolt row, and shear or compressive strength of the FRP member. By this approach the joint capacity could be estimated to within 20% from the test results.

One of the bolted sleeve joint configurations, the one with two rows of two bolts and a GFRP section of 51×51×6.4 mm, was further studied to investigate its end condition in case of member global buckling [78]. Experimental tests and FE modelling were both carried out. Based on a parametric analysis using the validated FE modelling, the effective length factor was found to converge towards 0.53 as the member slenderness increased, suggesting a desirable rigid end condition. In another study, this joint configuration was tested under flexural loading [79]. Ultimate failure of the joints mainly involved web-flange separation of the GFRP tubular members. The rotational response of the bolted sleeve joint and that of a steel bolted plate nodal joint were obtained for use in the FE analysis of a latticed shell structure.

Bonded sleeve joints were examined by Yang et al. for the assembly of circular GFRP tubes or rods into space frames [80]. The configuration of the bonded sleeve joints involved co-axial coupling and bonding of a steel tube connector to a circular section GFRP member. In this study the unbonded end of the steel tube connector was flattened for bolt fastening to a nodal joint. Bonded sleeve joints of four configurations were prepared: two with steel connectors bonded inside GFRP tubes (38×4 mm and 31×3.2 mm) and two with steel connectors bonded outside GFRP rods (15.5 mm and 25.3 in dia.). Of each configuration, six to eight bond lengths were tested, ranging from 30 to 80 mm. Generally, depending on the bond length, failure occurred as pull-out failure close to the adhesive-FRP interface, or due to yielding and fracture of the steel connector. Among the highest-capacity joints of each configuration, 34-88% of the theoretical

tensile capacity of the GFRP section could be realized. For the joints of the pull-out failure, the calculated average adhesive shear stresses at ultimate load decreased with the bond length, suggesting a non-uniform shear stress distribution. The bonded sleeve joints were also tested under compression. Failure was governed by global buckling of the GFRP member or flexural yielding of the steel connector.

In [81], the bonded sleeve joint was used by the authors to assemble circular GFRP tubes (92×8 mm) into a space frame that measured 8 m in length, 1.6 m in width and 1.13 m in depth. Here the unbonded end of the steel tube connector was slot-welded with a tongue plate for bolt fastening. Testing of individual bonded sleeve joints was carried out. When an 80 mm-bond length was used, pull-out failure occurred in the surface mat layer of the GFRP; using a 120 mm-bond length changed the failure to within the steel connector. During the failure test of the GFRP space frame, in some of the bonded sleeve joints under compression, transverse splitting of the GFRP tube occurred at the bonded end.

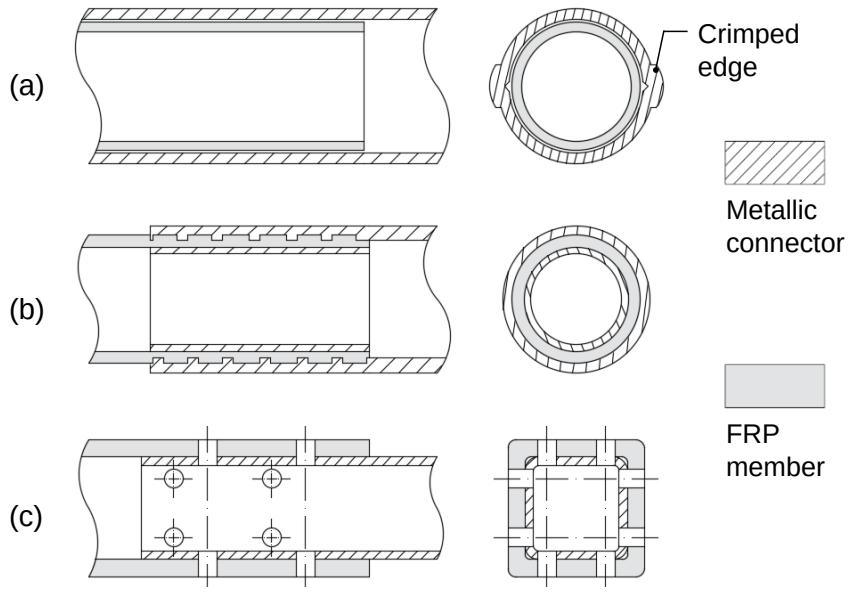

Figure 2.15. Prototypes of joints between FRP truss member and end connector: (a) crimp-bonded joint [74]; (b) pre-tightened teeth joint [76]; (c) bolted sleeve joint [77].

2.5. Splice Connections for FRP Members

Splice connections, as commonly used to create end-to-end continuity for members of standard or practical lengths, have not received much research as beam-column connections in FRP structures. But to enable the use of FRP profiles in long span and multi-storey scenarios, the design of splice connection is necessary. The existing designs of splice connections all involve the use of bolted or/and bonded lap plates and the investigation of flexural behaviour.

In 1998, early studies on flexural performance of splice connections were reported by Nagaraj and Gangarao [82]. The members to be spliced were pultruded GFRP profiles of 102×102×6 mm I- and box sections. Pultruded lap plates 12.7 mm in thickness were bolted and bonded to the eight and four faces of the I- and box sections respectively, as shown in Figure 2.16. Steel bolts were arranged in a staggered pattern but their precise number and location were not indicated. Fatigue tests by three-point bending were first carried out, showing that the splice connections could attain 60-80% fatigue life of a continuous beam for the I-section or 46-60% for the box section. In all connections, fatigue damage first occurred as propagation of cracks in the adhesive layer, followed by the ultimate failure of bolt shear-out at the tension flange of the beams. Monotonic tests revealed that the splice connections could exhibit equal or higher stiffness than the continuous beams. In terms of ultimate capacity, the I-section connection showed 80% capacity of a continuous beam while the box section connection showed a 71% capacity. The high efficiency of the connections in rotational stiffness and moment capacity might be attributed to the low fibre content of the profiles (28% for the box section and 35% for the I-section).

In 2005, Keller and Castro [83] reported the study of two-span spliced and un-spliced pultruded GFRP beams. The GFRP beams, with a square box section of 240×240×12 mm, were supported over two 3.6 m-spans. Two symmetric point loads were applied at 1.2 m from the interior support. One continuous reference beam was prepared as well as three spliced beams with top and bottom bonded lap plates of different lengths [Figure 2.16 (b) without the side lap plates]. Single-span, three-point bending test that corresponded to one half of the two-span beam was also carried out. The aim of this

study was to demonstrate the realization of system ductility through a flexible splice joint where a highly ductile adhesive was used. Although the beams did not show notable difference in terms of nonlinearity in the load-displacement curve, the spliced beam exhibited up to 16% and 23% higher load capacity than the single and two-span un-spliced beam. It was concluded that the flexible splice joint at mid-span resulted in a more balanced distribution of bending moment along the beam, thus improved the load capacity.

Bolted and bolted-and-bonded lap plates were used to splice FRP I-section beams by Manalo and Mutsuyoshi [84]. The I-section beam was 95×14×250×9 mm in cross-section and made of laminated CFRP and GFRP. The splice lap plates, also of hybrid CFRP and GFRP laminates, were bolted (or also bonded) onto eight faces of the I-section [as in Figure 2.16 (a)] with steel bolts. Three beams were tested under four-point bending: a continuous reference beam, a beam spliced at mid-span by bolted lap plates; and a beam spliced at mid-span with the same bolted lap plates and also adhesive bonding. The main finding was that the bolted-and-bonded spliced beam showed stiffness similar to the reference beam without occurrence of bolt-hole slipping which caused stiffness reduction in the bolted-only spliced beam. Failure of the beams occurred in the mode of compressive flange delamination and web buckling outside of the splice connection.

In a continuing study, Hai and Mutsuyoshi [85] conducted flexural tests on the hybrid FRP I-section beam spliced with similar bolted-and-bonded lap plates. Steel instead of FRP lap plates were used in this study. Steel-FRP double lap joints were first tested, and showed that V-notches (about 0.5 mm-deep) engraved on the bonded surfaces could serve as an adhesive thickness controller and delay the initial adhesive damage. The full-scale four-point bending tests included one continuous reference beam and two bolted-and-bonded spliced beams. The two spliced beams differed in the number of bolt rows. All three beams showed similar stiffness and linear load-displacement behaviour prior to failure. Of the first spliced beam (with fewer bolt rows), the load-displacement peaked at 69% of the failure load of the reference beam, and fluctuated as debonding occurred and propagated. The final collapse was due to shear failure of the bolts at the tension flange. The second spliced beam failed outside the splice connection at a similar load as the reference beam.

A series of studies on spliced I-section (152×152×6.4 mm) pultruded GFRP beams were carried out by Turvey and Cerutti [86-88]. The splice connections consisted of bonded or bolted 6 mm-thick pultruded lap plates. Through three- or four-point bending, serviceability level load-unload cycles were applied multiple times to demonstrate the linearity and repeatability of the load-deformation responses. In [86] the splice connections were formed by lap plates bonded onto two faces (top and bottom) or six faces [Figure 2.16 (a) without the web plates] of the I-section flanges. Another parameter was the bonded lap length at each beam, i.e. 100 mm, 200 mm or 300 mm. Minor axis bending, as well as major axis bending was conducted. The test results showed that, for major axis bending the additional four bonded lap plates increased the overall beam flexural stiffness by only 2-6%, but for minor axis bending the increase was 7-12%. It was found that longer bonded overlap increased the flexural stiffness of the beam but not the connection rotational stiffness. Analytical formulae were developed based on transformed sections, method of influence coefficient and shear-deformable beam theory. The connection major axis rotational stiffness could be predicted to within 8% from the test results for the 200 mm and 300 mm bonded overlaps.

In [87], the splice lap plates were bolted onto (with 10 mm-diameter steel bolt) the flanges of the I-section GFRP beams. At each beam there were four bolts (in two rows) on a flange. The investigated parameters were: two (top and bottom) versus six bolted lap plates [Figure 2.16 (a) without the web plates], and three different bolt toques (3, 20 and 30 Nm). Serviceability load level tests revealed that the flexural stiffness of the spliced beams increased linearly with the bolt torque. It was found that the additional four lap plates (six vs. two) raised the flexural stiffness by 17.4-27.9%, where the amplitude of increase (17.4%) reduced as the bolt torque increased.

In [88] again, two or six pultruded splice lap plates were bolted onto the flanges of the I-section beam. One, two or three rows of bolts (10 mm-diameter steel bolts, two bolts per row) were used on each flange at each beam. The bolts were torqued to 3 Nm or 20 Nm. As expected, the flexural stiffness of the spliced beam increased as the number of lap plates and bolt torque increased. These positive effects were most obvious when one row of bolts was used. The flexural stiffness was found to increase linearly with the number of bolt rows. Analytical estimation of the beam flexural stiffness was carried out

based on the transformed section method and Mohr's second theorem. The stiffness could be estimated to within 10%, provided that a correction of rigid-body rotation was applied.

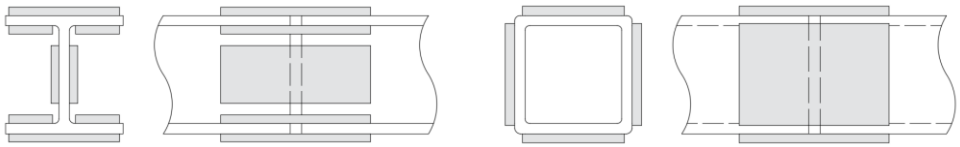

Figure 2.16. Splice connection formed by bolted or/and bonded lap plates: (a) for I-section FRP members; (b) for tubular section FRP members.

2.6. Splice Connections for Tubular Section Steel Members

As reviewed in Section 4 of the chapter, when used in truss and space frame structures, the FRP members were fixed with metallic tube connectors at the ends to enable convenient connection to other components. The fixing of the metallic tube connector to the FRP member could be conducted off-site to minimize fabrication defects. On this basis, a convenient splicing method for the metallic tube connector may be necessary to connect FRP members end-to-end. In steel structures, the bolted flange connections, simple in constitution and excellent in mechanical performance, are widely used for splicing tubular section members. The compressive behaviour of such connections is governed by the connected steel tubular member. The tensile and flexural behaviours of such connections, involving bending of the flange-plate and tensioning of the bolts under prying action, have been extensively studied.

2.6.1. Connections under Tensile Loading

Kato and Hirose [89] carried out theoretical analysis for bolted flange connections joining circular hollow section (CHS) steel members [Figure 2.17 (a)]. In this study, the tensile experiment results of 63 specimens were summarised, covering the dimensional parameters of CHS size, flange outer diameter, flange thickness, and bolt edge distance. Out of the 63 specimens, 40 of them failed ultimately due to excessive flexure of the

flange-plate or fracture of the bolts, while the others failed at the CHS-flange welding or the CHS. The theoretical analysis included four types of yield line patterns on the flange and evaluation of the bolt forces considering the prying effect. Theoretical estimates of the connection ultimate strength were mostly within 20% from the test results. The discrepancy was mainly attributed to the neglect of the fillet weld and the membrane effect associated with the thin flanges in large flexure.

Subsequently, Kato and Mukai [90] conducted analysis on the bolted flange connections with square hollow section (SHS) members. The tested specimens featured one or two bolts at each side of the SHS [Figure 2.17 (b) and (c)]. In each of the configuration the varied design parameters included bolt diameter, flange thickness, and the size of the SHS; while the bolt-edge and the bolt-SHS distances were kept constant. Among the 34 specimens, 28 specimens failed ultimately by bolt failure and the rest failed at the flange. Theoretical analysis similar to the earlier study [89] was carried out, with the assumption of one type of yield line pattern for each of the configurations. The failure modes were correctly predicted for 32 specimens, and the estimates of connection tensile strengths were within 12% from the test results except for one specimen of 20%.

For bolted flange connections with bolts at two opposite sides of the rectangular hollow section (RHS) member [Figure 2.17 (d)], experimental and theoretical analyses were conducted by Packer et al. [91]. Tensile tests were performed on 16 specimens varied in flange thickness, bolt diameter, bolt-edge and bolt-RHS distances, number of bolts (2 vs. 3 at one side of the RHS), and SHS vs. RHS. In each specimen, a “load cell washer” was used to measure the bolt force to quantify the prying effect. An important finding was that the prying effect could be reduced by increase of the bolt-edge distance, decrease of the bolt-RHS distance, and increase of the flange thickness. Theoretical analysis was conducted considering the flange yielded in single or double curvature and the bolts under prying action. Plastic hinges in the flange-plate were allowed to form within the RHS dimension to account for the tensile yielding of thin-walled RHS. The theoretical analysis yielded good agreement with the experimental results in terms of failure mode and ultimate connection strength (within 6%).

The tensile behaviour of bolted flange connections was also studied by Willibald et al. [92], focusing on the bolt failure under prying action. Three types of connection with SHS member were covered: one, or two bolt at each side of the SHS [Figure 2.17 (b) or (c)], and one bolt at each side and also corner of the SHS [Figure 2.17 (d)]. The other design parameters were flange thickness, bolt-edge and bolt-SHS distance, resulting in 16 specimens in total. The eight-bolt configuration of Figure 2.17 (e) was deemed unfavourable, because the bolts were unevenly loaded, leading to an early rupture of the inner bolts. Several then-existing analytical models for similar connection configurations were reviewed and the connection strength predictions were compared to the test results, as well as 10 further test results from [90]. The method by Kato and Mukai [90] was found accurate but reckoned complex for practical application. A slightly adjusted version of the AISC method [93] was recommended due to its simplicity and yet satisfactory accuracy.

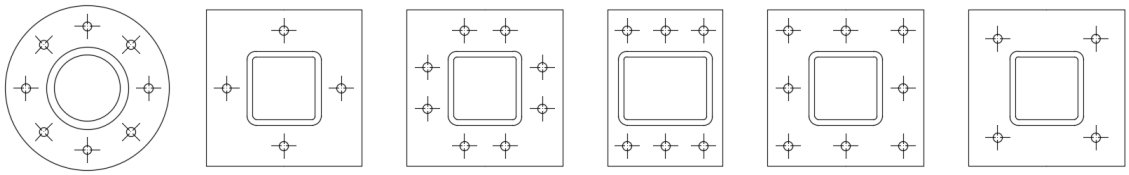

Figure 2.17. Steel bolted flange connections: (a) with CHS member; (b) with one bolt at each side of SHS; (c) with two bolts at each side of RHS/SHS; (d) with bolts at two opposite sides of RHS (two or three bolts at each side); (e) with bolts at four sides and corners of SHS; (f) with one bolt at each corner of RHS/SHS.

2.6.2. Connections under Flexural Loading

Significant works were done by Wheeler et al. on the analysis of RHS bolted flange connections under flexural loading. Their work began with the configuration of four bolts [Figure 2.17 (f)] [94, 95]. 16 connections were experimentally examined under four-point bending, covering the design parameters of flange-plate size, flange thickness, RHS vs. SHS, and positions of the bolts with respect to the RHS. In all specimens, yielding of the

flange-plates was evident before the ultimate failure in mode of bolt fracture or excessive bending of the flanges. Yield line analysis considering three modes of yield line pattern was carried out to estimate the yield moment of the connections. The stud-Tee method that took into account the prying effect was then combined with the proposed yield line patterns to estimate the ultimate moment. The estimates of the yield and ultimate moments were within 12% difference in comparison to the test results.

FE modelling of these four-bolt connections [Figure 2.17 (f)] was conducted in [96]. Material and geometric nonlinearity were incorporated into the modelling, and the contact behaviour between the assembled parts was also defined. The FE models were featured with the inclusion of initial deformation in the flange-plate, which was generated through welding of the flange-plate to the RHS member. As in engineering practice, bolt pre-tensioning was applied in the modelling to close the gaps due to this flange deformation. A parametric study revealed that this initial flange deformation affected the ultimate connection strength minorly, but resulted in higher initial stiffness and lower yield moment. Overall, the FE modelling could accurately capture the moment-rotation responses, producing estimates of the ultimate moment within 10% from the test results.

Later on, the eight-bolt configuration of Figure 2.17 (c) was also studied by Wheeler et al. [97]. Ten connections, with design parameters similar as in the earlier study [94], were tested. Five of the specimens failed ultimately through the RHS teared away from the flange at the toe of weld; three failed in the RHS member; and the other two failed due to bolt fracture. Theoretical analysis was conducted similarly as in [89] but with seven modes of proposed yield line pattern. A corresponding FE modelling of the connections was reported and discussed in [98], using similar approaches as in the earlier FE modelling by the authors [96].

More recently, CHS and SHS bolted flange connections with and without welded stiffeners were studied by Wang et al. [99]. The unstiffened CHS and SHS connections were with eight bolts as in Figure 2.17 (a) and (c). The stiffeners in the CHS connection were welded between the bolts. In the SHS connection, one stiffener was welded between two bolts at each side of the SHS; and another two stiffeners, at right angle to each other, were welded at each corner of the SHS. In total four connections were tested. FE

modelling was performed to visualise the distribution of von Mises stress and the pressure centre, based on which yield line mechanisms were proposed for theoretical estimation of the connection yield moments. The theoretical method generally underestimated the yield moment, but within 11% from test results.

2.7. Concluding Remarks and Proposed Splice Connection Design

Buildings using FRP composites as the load-carrying system had emerged since the 1950s, motivated by their reduced mass, corrosion resistance, low thermal and electro-magnetic conductivity and flexible geometry. The mature of cost-effective automatic manufacturing techniques, in particular pultrusion, opened up greater opportunity for the application of FRPs in building construction. Through the pultrusion method, FRP profiles were produced with a range of standardized sections similar to structural steels. However, connecting individual pultruded FRPs together is a challenging task because of the anisotropic and brittle properties of the material. Furthermore, the low modulus of GFRPs requires connections to be sufficiently stiff. These issues prompted researches into developing effective methods for connecting FRP elements.

Extensive studies have been carried out on the subjects of beam-column connections and truss/space frame connections, with the target towards enhancement in strength, stiffness, and ductility while reduction in cost and labour. Research on splice connections for FRP members is relatively scarce, especially for tubular section members. The splice connections comprised of bonded-and-bolted lap plates [82, 85] demonstrated satisfactory stiffness and strength, but the bonding-and-bolting process requires highly skilled labouring upon field application. Therefore, this research project aims to develop a splice connection for tubular section FRP members that is adequate in mechanical performance as well as practical for use in field application. Before the proposal of a conceptual design, several conclusions are noted from the detailed review in this regard.

1. The web-flange junction (or the nearby region) of pultruded FRP members, particularly single-web I-section members, is vulnerable to failure due to the lack of transverse reinforcing fibres. To avoid significantly stressing the web-flange junction, a

connection should be designed such that both flanges (and better also the webs) are engaged upon loaded.

2. Bolting directly on pultruded FRP members requires hole drilling therefore damages the fibre continuity and causes stress concentration at the bolt-hole contacting region. This, furthermore, exposes the relatively weak in-plane shear strength of pultruded FRPs. Using adhesive bonding on FRPs can improve the connection strength by avoiding or alleviating these issues.

3. Friction-tight bolted connection usually is not attainable for FRP members due to their insufficient transverse strength to sustain a high bolt pre-tension. Using adhesive bonding instead of/in addition to bolt fastening can eliminate bolt-hole slipping upon loaded, resulting in stiffer connections.

4. Despite the superiority in strength and stiffness, adhesive bonding may not be equally convenient when exercised on-site in comparison to bolting. Therefore, bolt-fastening still appears preferable in terms of convenience in assembly and disassembly.

5. Using steel connecting elements with FRP members facilitates a wider range of joining methods (welding, bolting, mechanical fitting etc.). Besides, using steel elements can simplify the potential failure modes of the connection by restricting failure to the FRP components.

6. In the failure process of connections for FRP members, ductility mainly derives from two sources: progressive failure of FRP components, e.g. in [52, 54, 75, 85]; and yielding of metallic components, e.g. in [70, 72, 80]. Where possible, the latter is preferred because the yielding behaviour of isotropic metals is easier to characterise and predict than the damage of brittle and anisotropic composites.

Following the findings noted above, a splice connection for tubular section FRP members is proposed and conceptualized as illustrated in Figure 2.18. The splice connection is comprised of a steel bolted flange joint between two tubular section steel-FRP bonded sleeve joints. The bonded sleeve joint, integrating the steel and FRP tubular members into a monolithic unit, is designed to realize a high joint stiffness and smooth stress transfer to the FRP member. The bonded sleeve joint is intended to be pre-fabricated off-site to minimise fabrication defect. The bolted flange joint, with the flat

flange-plates for parts to be seated before bolted, is designed to enable a convenient on-sit assembly and disassembly. The steel flange-plates, through their yielding in flexure, are also intended to impart ductility to the splice connection. To protect the limited exposed steel parts against corrosion, galvanized steel and stainless-steel parts may be used, or surface coating can be applied.

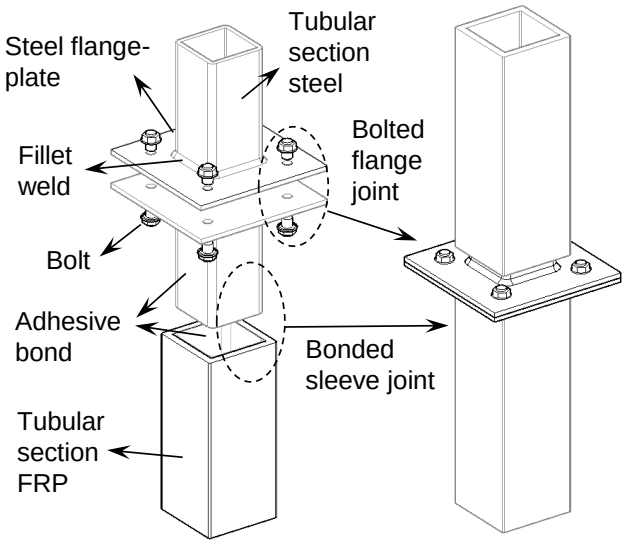

Figure 2.18. Proposed splice connection for tubular section FRP members.

Square tubular section FRP member is selected considering that flat-wall members are preferred for the attachment of other elements in building structures. With a fixed-dimension FRP member, the major design parameter of the bonded sleeve joint is the length of the steel-FRP overlap. Within the appropriate range, a steel section that is close to the FRP section in stiffness is preferred so as to achieve a more uniform stress distribution over the bonded area [100]. Configuration of the bolted flange joint is not restricted to the four-bolt one shown in Figure 2.18. Thickness of the flange-plates, number and position of the bolts etc. can be adjusted to customize the joint behaviour. As reviewed in Section 6, analytical design models and FE modelling are reliable tools to predict the behaviour of such type of joints. In the following four chapters, the mechanical performance of the proposed splice connection will be investigated. Axial performance of the connection will be covered in Chapter 3 and 4 where Chapter 3 will look into the

theoretical aspects of the bonded sleeve joint. Chapter 5 and 6 will investigate the performance of the splice connection under flexural and cyclic loadings.

2.8. References

1. Teng J, Chen J, Smith ST, Lam L. Behaviour and strength of FRP-strengthened RC structures: a state-of-the-art review. Proceedings of the Institution of Civil Engineers-Structures and Buildings. 2003;156(1):51-62.
2. Zhao X-L, Zhang L. State-of-the-art review on FRP strengthened steel structures. Engineering Structures. 2007;29(8):1808-23.
3. Meyer R. Handbook of Pultrusion Technology. Springer Science & Business Media; 2012.
4. Khalifa A, Gold WJ, Nanni A, MI AA. Contribution of externally bonded FRP to shear capacity of RC flexural members. Journal of Composites for Construction. 1998;2(4):195-202.
5. El-Hacha R, Rizkalla SH. Near-surface-mounted fiber-reinforced polymer reinforcements for flexural strengthening of concrete structures. ACI Structural Journal. 2004;101(5):717-26.
6. Benmokrane B, Masmoudi R. Flexural response of concrete beams reinforced with FRP reinforcing bars. ACI Structural Journal. 1996;93(1):46-55.
7. Keller T. Overview of fibre-reinforced polymers in bridge construction. Structural Engineering International. 2002;12(2):66-70.
8. Fang H, Bai Y, Liu W, Qi Y, Wang J. Connections and structural applications of fibre reinforced polymer composites for civil infrastructure in aggressive environments. Composites Part B: Engineering. 2019;164:129-43.
9. Mosallam A. Design Guide for FRP Composite Connections. American Society of Civil Engineers, 2011.

10. Coelho AMG, Mottram JT. A review of the behaviour and analysis of bolted connections and joints in pultruded fibre reinforced polymers. Materials & Design. 2015;74:86-107.
11. Keller T, Vallée T. Adhesively bonded lap joints from pultruded GFRP profiles. Part I: stress–strain analysis and failure modes. Composites Part B: Engineering. 2005;36(4):331-40.
12. Yu T, Fernando D, Teng J, Zhao X. Experimental study on CFRP-to-steel bonded interfaces. Composites Part B: Engineering. 2012;43(5):2279-89.
13. Lu X, Teng J, Ye L, Jiang J. Bond–slip models for FRP sheets/plates bonded to concrete. Engineering structures. 2005;27(6):920-37.
14. Weitzenböck JR, McGeorge D. Science and technology of bolt-adhesive joints. In: Hybrid adhesive joints. Switzerland: Springer, 2011. p. 177-99.
15. Bodjona K, Lessard L. Hybrid bonded-fastened joints and their application in composite structures: A general review. Journal of Reinforced Plastics and Composites. 2016;35(9):764-81.
16. Wikipedia. Monsanto House of the Future. 2018. Available: https://en.wikipedia.org/wiki/Monsanto_House_of_the_Future [accessed 18 October 2019].
17. Mahne KM. Living in the Monsanto House of the Future. Disney Avenue, 2015. Available: http://www.dizavenue.com/2015/05/living-in-monsanto-house-of-future.html [accessed 18 October 2019].
18. Home M, Taanila M, Editors. Futuro: Tomorrow's House from Yesterday. Helsinki: Desura, 2002.
19. Wikipedia. Futuro. 2019. Available: https://en.wikipedia.org/wiki/Futuro [accessed 19 October 2019].
20. Crane R. Monsanto House of the Future - June 12, 1957–December 1967. 2013. Available: https://www.flickr.com/photos/midcentarc/9125148373/ [accessed 09 February 2020].

21. Kärnä J-P. Futuro WeeGee Espoo. Wikimedia Commons, 2013. Available: https://commons.wikimedia.org/wiki/File:Futuro_WeeGee_Espoo.jpg [accessed 19 October 2019].
22. Quarmby A. The plastics architect. London: Pall Mall Press, 1974.
23. Stewart R. Pultrusion industry grows steadily in US. Reinforced Plastics. 2002;46(6):36-9.
24. Rogers Stirk Harbour & Partners. The Millennium Dome. 2010. Available: https://www.rsh-p.com/projects/the-millennium-dome/ [accessed 23 October 2019].
25. Kendall D. Building the future with FRP composites. Reinforced plastics. 2007;51(5):26-33.
26. Fun with Dick and Jane. Dumbing Down the Dome. 2007. Available: https://www.fmschmitt.com/pictures/london/dome.htm [accessed 24 October 2019].
27. BBC News. Picture gallery: Millennium Dome. 1999. Available: http://news.bbc.co.uk/2/hi/uk_news/430031.stm [accessed 25 November 2019].
28. Evernden MC, Mottram JT. A case for houses to be constructed of fibre reinforced polymer components. Proceedings of the Institution of Civil Engineers – Construction Materials. 2012;165(1):3-13.
29. Altair HyperWorks. Using Optimization to Improve the Design of a Reproducible Classroom Environment. Altair Engineering, 2005. Available: https://altairhyperworks.com/ResourceLibrary.aspx?category=Case+Studies&page=3 [accessed 10 January 2020].
30. Holland Composites. SpaceBox. 2008. Available: https://www.hollandcomposites.nl/en/portfolio/temporary-livingspace-unit-spacebox/ [accessed 11 November 2019].
31. Foster & Partners. Steve Jobs Theatre. 2018. Available: https://www.fosterandpartners.com/projects/steve-jobs-theater/ [accessed 28 January 2020].

32. Inside Composites. Largest carbon-fibre roof for Apple HQ. 2017. Available: https://www.insidecomposites.com/largest-carbonfibre-roof-for-apple-hq/ [accessed 28 January 2020].

33. Strongwell. Product brochure – COMPOSOLITE Fibreglass Building Panel Systems. 2019. Available: https://www.strongwell.com/wp-content/uploads/2013/04/COMPOSOLITE-Brochure.pdf [accessed 23 October 2019]

34. Hollaway L, Head P. Applications in advanced polymer composite constructions. In: Advanced Polymer Composites and Polymers in the Civil Infrastructure. Oxford: Elsevier Science Ltd., 2001. p. 221-86.

35. Hutchinson J, Singleton M. Startlink composite housing. In: Proceedings of Advanced Composites in Construction ACIC07 Conference. University of Bath, 2007.

36. Larkfleet Group. PassiveHouse The future of building today. 2014. Available: https://larkfleet.com/larkfleetgroup/assets/img/Downloads/Larkfleet%20Group/New/13-11-PassiveHouse.pdf [accessed 23 October 2019].

37. Bank LC. Composites for Construction: Structural Design with FRP Materials. John Wiley & Sons, 2006.

38. Strongwell. Case Study: Computer Testing Facility Constructed of DURASHIELD® Foam Core Panels & EXTREN®. 2018. Available: https://www.strongwell.com/case-study-computer-testing-facility-constructed-of-durashield-foam-core-panels-extren/ [accessed 13 May 2020].

39. Strongwell. Case Study: Colossal Cooling Towers Rebuilt Using Fiberglass Components. 2018. Available: https://www.strongwell.com/case-study-colossal-cooling-towers-rebuilt-using-fiberglass-components/ [accessed 25 October2019].

40. Strongwell. FRP Stairtower Designed to Meet the Challenge. 2019. Available: https://www.strongwell.com/case-study-frp-stairtower-designed-to-meet-the-challenge/ [accessed 17 November 2019].

41. Fiberline. The Eyecatcher Building. 2019. Available: https://fiberline.com/cases/cases-doors-facades/glass-facades/the-eyecatcher-building/ [accessed 12 October 2019].

42. Keller T. Towards structural forms for composite fibre materials. Structural Engineering International. 1999;9(4):297-300.

43. Bai Y, Keller T, Wu C. Pre-buckling and post-buckling failure at web-flange junction of pultruded GFRP beams. Materials and Structures. 2013;46(7):1143-54.

44. Boscato G, Casalegno C, Russo S. Design of FRP Structures in Seismic Zone. Italy: Manual by Top Glass S.p.A. and IUAV University of Venice, 2015.

45. CORE Group. Applied Projects – The ClickHouse (2015). 2015. Available: http://coregroup.tecnico.ulisboa.pt/~coregroup.daemon/applied-projects/ [accessed 15 December 2019].

46. Abdolpour H, Garzón-Roca J, Escusa G, Sena-Cruz JM, Barros JA, Valente IB. Development of a composite prototype with GFRP profiles and sandwich panels used as a floor module of an emergency house. Composite Structures. 2016;153:81-95.

47. Martins D, Sá MF, Gonilha JA, Correia JR, Silvestre N, Ferreira JG. Experimental and numerical analysis of GFRP frame structures. Part 2: Monotonic and cyclic sway behaviour of plane frames. Composite Structures. 2019;220:194-208.

48. Bank LC, Mosallam AS, McCoy GT. Design and performance of connections for pultruded frame structures. Journal of Reinforced Plastics and Composites. 1994;13(3):199-212.

49. Bruneau M, Walker D. Cyclic testing of pultruded fiber-reinforced plastic beam-column rigid connection. Journal of Structural Engineering. 1994;120(9):2637-52.

50. Bass A, Mottram J. Behaviour of connections in frames of fibre-reinforced-polymer section. The Structural Engineer. 1994;72(17):280-4.

51. Bank LC, Yin J, Moore L, Evans DJ, Allison RW. Experimental and numerical evaluation of beam-to-column connections for pultruded structures. Journal of Reinforced Plastics and Composites. 1996;15(10):1052-67.

52. Mosallam AS, Abdelhamid MK, Conway JH. Performance of pultruded FRP connections under static and dynamic loads. Journal of Reinforced Plastics and Composites. 1994;13(5):386-407.

53. Mottram J, Zheng Y. Further tests on beam-to-column connections for pultruded frames: Web-cleated. Journal of Composites for Construction. 1999;3(1):3-11.

54. Mottram J, Zheng Y. Further tests of beam-to-column connections for pultruded frames: flange-cleated. Journal of Composites for Construction. 1999;3(3):108-16.

55. Mottram J. Tests on nominally pinned connections for pultruded frames. In: Structural Design of Polymer Composites: EUROCOMP Design Code and Handbook. Abingdon: Taylor & Francis, 1996:705-18.

56. Turvey G. Moment–rotation tests on bolted end connections in pultruded GRP beams–tests with stainless steel cleata and an assessment of their performance relative to GRP cleats. In: Proceedings of 9th European Conference on Composite Materials (ECCM 9: From Fundamentals to Exploitation), Brighton, UK, 4-7 June, 2000.

57. Qureshi J, Mottram JT. Response of beam-to-column web cleated joints for FRP pultruded members. Journal of Composites for Construction. 2013;18(2):04013039.

58. Qureshi J, Mottram JT. Behaviour of pultruded beam-to-column joints using steel web cleats. Thin-Walled Structures. 2013;73:48-56.

59. Qureshi J, Mottram JT. Moment-rotation response of nominally pinned beam-to-column joints for frames of pultruded fibre reinforced polymer. Construction and Building Materials. 2015;77:396-403.

60. Feroldi F, Russo S. Structural behavior of all-FRP beam-column plate-bolted joints. Journal of Composites for Construction. 2016;20(4):04016004.

61. Ascione F, Lamberti M, Razaqpur A, Spadea S. Strength and stiffness of adhesively bonded GFRP beam-column moment resisting connections. Composite Structures. 2017;160:1248-57.

62. Ascione F, Lamberti M, Razaqpur A, Spadea S, Malagic M. Pseudo-ductile failure of adhesively joined GFRP beam-column connections: An experimental and numerical investigation. Composite Structures. 2018;200:864-73.

63. Smith S, Parsons I, Hjelmstad K. An experimental study of the behavior of connections for pultruded GFRP I-beams and rectangular tubes. Composite Structures. 1998;42(3):281-90.

64. Smith S, Parsons I, Hjelmstad K. Experimental comparisons of connections for GFRP pultruded frames. Journal of Composites for Construction. 1999;3(1):20-6.

65. Singamsethi S, LaFave J, Hjelmstad K. Fabrication and testing of cuff connections for GFRP box sections. Journal of Composites for Construction. 2005;9(6):536-44.

66. Carrion JE, LaFave JM, Hjelmstad KD. Experimental behavior of monolithic composite cuff connections for fiber reinforced plastic box sections. Composite Structures. 2005;67(3):333-45.

67. Carrion JE, Hjelmstad KD, LaFave JM. Finite element study of composite cuff connections for pultruded box sections. Composite Structures. 2005;70(2):153-69.

68. Tsai SW, Wu EM. A general theory of strength for anisotropic materials. Journal of Composite Materials. 1971;5(1):58-80.

69. Wu C, Zhang Z, Bai Y. Connections of tubular GFRP wall studs to steel beams for building construction. Composites Part B: Engineering. 2016;95:64-75.

70. Zhang ZJ, Bai Y, Xiao X. Bonded Sleeve Connections for Joining Tubular Glass Fiber–Reinforced Polymer Beams and Columns: Experimental and Numerical Studies. Journal of Composites for Construction. 2018;22(4):04018019.

71. Zhang Z, Bai Y, He X, Jin L, Zhu L. Cyclic performance of bonded sleeve beam-column connections for FRP tubular sections. Composites Part B: Engineering. 2018;142:171-82.

72. Martins D, Proença M, Correia JR, Gonilha J, Arruda M, Silvestre N. Development of a novel beam-to-column connection system for pultruded GFRP tubular profiles. Composite Structures. 2017;171:263-76.

73. Martins D, Proença M, Gonilha JA, Sá MF, Correia JR, Silvestre N. Experimental and numerical analysis of GFRP frame structures. Part 1: Cyclic behaviour at the connection level. Composite Structures. 2019;220:304-17.

74. Green A, Phillips L. Crimp-bonded end fittings for use on pultruded composite sections. Composites. 1982;13(3):219-24.

75. Hagio H, Utsumi Y, Kimura K, Takahashi K, Itohiya G, Tazawa H. Development of space truss structure using glass fiber reinforced plastics. Proceedings: Advanced Materials for Construction of Bridges, Buildings, and Other Structures III, Davos, Switzerland, 7-12 September, 2003.

76. Zhang D, Zhao Q, Huang Y, Li F, Chen H, Miao D. Flexural properties of a lightweight hybrid FRP-aluminum modular space truss bridge system. Composite Structures. 2014;108:600-15.

77. Luo FJ, Bai Y, Yang X, Lu Y. Bolted sleeve joints for connecting pultruded FRP tubular components. Journal of Composites for Construction. 2016;20(1):04015024.

78. Luo FJ, Yang X, Bai Y. Member capacity of pultruded GFRP tubular profile with bolted sleeve joints for assembly of latticed structures. Journal of Composites for Construction. 2016;20(3):04015080.

79. Luo FJ, Huang Y, He X, Qi Y, Bai Y. Development of latticed structures with bolted steel sleeve and plate connection and hollow section GFRP members. Thin-Walled Structures. 2019;137:106-16.

80. Yang X, Bai Y, Luo FJ, Zhao X-L, He X-h. Fiber-Reinforced Polymer Composite Members with Adhesive Bonded Sleeve Joints for Space Frame Structures. Journal of Materials in Civil Engineering. 2016:04016208.

81. Yang X, Bai Y, Ding F. Structural performance of a large-scale space frame assembled using pultruded GFRP composites. Composite Structures. 2015;133:986-96.

82. Nagaraj V, Gangarao HV. Fatigue behavior and connection efficiency of pultruded GFRP beams. Journal of Composites for Construction. 1998;2(1):57-65.

83. Keller T, de Castro J. System ductility and redundancy of FRP beam structures with ductile adhesive joints. Composites Part B: Engineering. 2005;36(8):586-96.

84. Manalo A, Mutsuyoshi H. Behavior of fiber-reinforced composite beams with mechanical joints. Journal of Composite Materials. 2012;46(4):483-96.

85. Hai ND, Mutsuyoshi H. Structural behavior of double-lap joints of steel splice plates bolted/bonded to pultruded hybrid CFRP/GFRP laminates. Construction and building Materials. 2012;30:347-59.

86. Turvey G. Experimental and analytical investigation of two-and six-plate bonded splice joints on serviceability limit deformations of pultruded GFRP beams. Composite Structures. 2014;111:426-35.

87. Turvey GJ, Cerutti X. Flexural behaviour of pultruded glass fibre reinforced polymer composite beams with bolted splice joints. Composite Structures. 2015;119:543-50.

88. Turvey GJ, Cerutti X. Effects of splice joint geometry and bolt torque on the serviceability response of pultruded glass fibre reinforced polymer composite beams. Composite Structures. 2015;131:490-500.

89. Kato B, Hirose R. Bolted tension flanges joining circular hollow section members. Journal of Constructional Steel Research. 1985;5(2):79-101.

90. Kato B, Mukai A. Bolted tension flanges joining square hollow section members. Journal of Constructional Steel Research. 1985;5(3):163-77.

91. Packer JA, Bruno L, Birkemoe PC. Limit analysis of bolted RHS flange plate joints. Journal of Structural Engineering. 1989;115(9):2226-42.

92. Willibald S, Packer J, Puthli R. Experimental study of bolted HSS flange-plate connections in axial tension. Journal of Structural Engineering. 2002;128(3):328-36.

93. Packer J, Sherman D, Lecce, M. Design Guide 24: Hollow Structural Section Connections. Chicago, IL: American Institute of Steel Construction (AISC), 1997.

94. Wheeler A, Clarke M, Hancock G, Murray T. Design model for bolted moment end plate connections using rectangular hollow sections. Sydney, Australia: Research Report – Department of Civil Engineering, University of Sydney, 1997.

95. Wheeler A, Clarke M, Hancock G, Murray T. Design model for bolted moment end plate connections joining rectangular hollow sections. Journal of Structural Engineering. 1998;124(2):164-73.

96. Wheeler A, Clarke M, Hancock G. FE modeling of four-bolt, tubular moment end-plate connections. Journal of Structural Engineering. 2000;126(7):816-22.

97. Wheeler A, Clarke M, Hancock G. Design model for bolted moment end plate connections joining rectangular hollow sections using eight bolts. Sydney, Australia: Research Report – Department of Civil Engineering, University of Sdyney, 2003.

98. Wheeler A, Clarke M, Hancock G. Finite Element modelling of eight-bolt rectangular hollow section bolted moment end plate connections. In: Advances in Steel Structures Proceedings of The Second International Conference on Advances in Steel Structures (ICASS'99) 15-17 December 1999, Hong Kong, China: Elsevier, 1999. p. 237-44.

99. Wang Y, Zong L, Shi Y. Bending behavior and design model of bolted flange-plate connection. Journal of Constructional Steel Research. 2013;84:1-16.

100. Hart-Smith LJ. Adhesive-bonded single-lap joints. Langley Research Center, Hampton, VA: NASA, 1973.

CHAPTER 3. THEORETICAL STUDY OF THE BONDED SLEEVE JOINT UNDER AXIAL LOADING

Declaration for the Chapter

Chapter 3 of the thesis presents the following published work in a re-formatted form:

Qiu C, Feng P, Yang Y, Zhu L, Bai Y. Joint capacity of bonded sleeve connections for tubular fibre reinforced polymer members. Composite Structures. 2017;163:267-79. https://doi.org/10.1016/j.compstruct.2016.12.006

Permission has been obtained from the publisher *Elsevier* to include the article, in its published form or in a re-formatted form, in this thesis.

The student's and the co-authors' contribution to the work is listed in the following table:

Name of author	**Nature of contribution**	**Contribution (%)**
C Qiu (the student)	Conceptualisation, theoretical derivation, date collection and analysis, numerical modelling, writing-up and revision	65%
P Feng	Review and revision	5%
Y Yang	Review and revision	5%
L Zhu	Review and revision	5%
Y Bai	Conceptualisation, data analysis, review and revision, financial support	20%

The undersigned hereby certify that the above declaration correctly reflects the nature and extent of the student's and co-authors' contribution to this work.

Student (Chengyu Qiu) signature: Main supervisor (Yu Bai) signature:

Date: Date:

Link of the Published Work to the Thesis

The published work constitutes part of the study of the proposed splice connection (Figure 2.18) under axial loading. While extensive theoretical studies have been conducted for the bolted flange joint component of the splice connection (as reviewed in Section 6 of Chapter 2), this work presents a theoretical study on the bonded sleeve joint component under axial loading. In the theoretical analysis, simplification was made through adopting an axisymmetric circular cross-section for the bonded sleeve joint, which removed the variation of adhesive shear stress in the transverse/circumferential direction.

Abstract

Bonded sleeve joints formed by telescoping a steel tube connector for bolt-fastening are effective means for assembling tubular fibre reinforced polymer (FRP) members into more complex structures such as planar or space frames. A theoretical formulation is developed in this paper to estimate the capacity of such joints in axial loading and the predictions are then validated by experimental results covering various section geometries and bond lengths. The formulation is based on the bilinear bond-slip constitutive relationship considering elastic, softening and debonding behaviour at the adhesive bonding region. Finite element (FE) analysis is also conducted to estimate the joint capacity and to describe shear stress distribution in the adhesive layer, validating the reliability of the theoretical results. The theoretical formulation is therefore further used to study the effects of design parameters including bond length and adherend stiffness ratio, again validated by FE results. An effective bond length can be accurately predicted by the theoretical formulation for the joint capacity at both the elastic limit and the ultimate state. Given a bond length, an optimal adherend stiffness ratio can be identified to achieve the maximum joint capacity at the elastic limit or the ultimate state.

Keywords: Fibre reinforced polymer; Sleeve connection; Adhesive bonding; Shear stress distribution; Joint capacity.

3.1. Introduction

With virtues such as high strength-to-weight ratio, superior corrosion resistance and low maintenance requirements, fibre reinforced polymer (FRP) structural members have gained broad recognition in the construction industry [1,2]. In particular, glass FRP (GFRP) composites, with sufficient strength and stiffness at moderate cost, have received acceptance as construction materials for structural members [3-5]. Aided by the pultrusion manufacturing technique [6,7], mass production of GFRP structural components with constant cross-section has been facilitated at reduced cost and with satisfactory quality control. Such components have been employed as bridge decks [8-11], reinforcements [12], roof structures [13], trusses [14], floor systems [15–17], and components in hybrid members [18–20], in shapes of open or closed sections. However, their application in structural construction still requires the development of reliable and convenient connection approaches, especially for tubular sections.

Early efforts to develop connections for GFRP tubular sections imitated practices in steel structures, for example, using bolted-through web-gusset plates or flange-angle cleats for beam-column connections [21]. Later, a cuff connection for pultruded GFRP tubular sections was proposed and demonstrated enhanced strength and stiffness [22,23]. Recently, the benefits of a sleeve connection formed by telescoping steel and GFRP tubular members have been underlined for applications in space frame structures [24]. The steel sleeve connector not only enables versatile connection forms but also provides ductile failure mode through steel yielding. In such connections, the GFRP-steel telescoping portion or the sleeve portion acts compositely through adhesive bonding [25] or mechanical fastening [26,27]. Although mechanical fastening facilitates convenient in-situ fabrication, its employment in fixing sleeve joints exposes the relatively weak shear strength of anisotropic GFRP materials and such use becomes inapplicable when circular profiles are used. If adhesive bonding is used, a more uniform stress transfer to GFRP materials is achieved. Bonded sleeve connections have also been developed into beam-to-column scenario [28], where pultruded GFRP and steel tubular square members were used. Such bonded sleeve connections have exhibited significant improvement in both stiffness and strength in comparison with traditional steel angle connections and bolted sleeve connections.

Bonded sleeve connections transfer axial loading through shear between the GFRP and steel adherends. As a special type of bonded lap joint, the joint capacity may be determined through the shear mechanism of the adhesive bonding when the adherends (steel and GFRP in this case) are sufficiently strong. Pioneering theoretical works on single and double lap adhesive-bonded joints have been conducted to understand such shear mechanisms where only elastic [29,30] or elastic-plastic [31,32] bonding behaviour was considered. Joint capacity was therefore evaluated against allowable material stress or strain at critical regions. These approaches are limited to identifying possible failure location or initiation.

Fracture mechanics-based approaches were further introduced to understand the full range behaviour of several types of single and double lap joints. This required understanding of the nonlinear bond-slip relationship at the bonded region. Simplification of the nonlinear bond-slip relationship into a bilinear form enabled the development of closed form analytical solutions for joint capacity and shear stress distribution in the adhesive layer. Such a bilinear relationship is characterised by a linearly ascending stage of shear stress with slip, followed by a linear decrease to zero shear stress at the debonding slip (and slip may further increase while shear stress remains zero). This bilinear relationship was adopted by Ranisch [33] to study the post-cracking behaviour of bonded steel-to-concrete single lap joints subjected to axial loading. By incorporating Volkersen's classical stress analysis and the bilinear bond-slip model, analytical solutions for the capacities of a pull-push plate-to-block bonded joint at elastic and ultimate limit states were developed by Brosens and Van Gemert [34]. This work was further expanded in [35], where analytical solutions were developed to identify several stages of the debonding process. Also utilising the bilinear model, Wu et al. [36] analytically derived the expressions for the joint capacity, adhesive shear stress distribution and the debonding processes of pull-pull and pull-push single lap joints. Experimental investigations were also conducted to understand the debonding behaviour of single and double lap joints, such as steel plate-to-concrete block double lap joint in [37], FRP plate-to-steel pull-push joints in [38], single and double lap FRP plate joints for structural rehabilitation in [39], and single and double lap aluminium plate joints in [40]. Such experimental results were able to validate analytical and numerical models that employed the aforementioned

bilinear bond-slip relationship. Furthermore, experimental results of shear stress and slip in the adhesive layer measured from FRP-to-concrete [41,42] and FRP-to-steel bonded lap joints [38,43,44] provided evidence that, when a brittle adhesive was used, the bilinear bond-slip relationship provided a satisfactory approximation to the experimental measurement.

In addition to the bilinear form, several representations of the bond-slip relationships were also proposed to study the behaviour of single and double lap bonded joints. A nonlinear bond-slip curve including softening behaviour was employed by Täljsten [45] for numerical calculation of the capacity of CFRP plate-to-concrete bonded joints; however, it was too sophisticated for analytical derivation, as pointed out by the author. A bond-slip relationship characterised by abrupt failure after the linearly elastic region was adopted by Yuan et al. [35,46]; and a bond-slip relationship with exponential softening behaviour was also considered in the former. For ductile adhesives, bond-slip relationships with trapezoidal shape were considered as more appropriate [44,47]. The load-displacement behaviour of a double lap joint connecting aluminium plates under pull-out test was numerically studied in [48], with consideration of four shapes of bond-slip relationship: bilinear, linear-parabolic, exponential and trapezoidal. It was concluded that, given identical initial stiffness, peak shear stress and fracture energy (as the area under the bond-slip curve) of the bonded interface, the load-displacement behaviour was practically independent of the shape of the bond-slip relationship. It appears that previous analytical and numerical studies have focused mainly on the adhesive shear stress distribution and capacity of adhesive-bonded joints in single or double lap forms. Such responses of a bonded sleeve connection require theoretic understanding and experimental validation to enhance confidence in their application.

This paper therefore formulates theoretical modelling for the joint capacity of a bonded sleeve connection for tubular GFRP members. This theoretical formulation employs the well-accepted bilinear bond-slip relationship. Experimental results of joint capacities were obtained from tension tests conducted on steel/GFRP bonded sleeve connection specimens with various cross-section geometries and bond lengths. Finite element (FE) models were also developed for comparison of the joint capacities and shear stress distribution along the bond length. After validation by experimental and FE results,

the theoretical formulation was further utilised to investigate the effects of major design parameters including bond length and adherend stiffness ratio, i.e. E_sA_s/E_gA_g where E_s or E_g are the Young's modulus of steel or GFRP, and A_s or A_g are cross-section area of the steel or GFRP component.

3.2. Summary of Experimental Results

A series of bonded sleeve joint specimens consisting of a steel tube connector and a GFRP component were prepared and examined, as shown in Figure 3.1 (a-c) [24,25]. Their joint capacities were tested for assembly into planar trusses [49] or space frames with assistance of the Octatube nodal joints [25] [Figure 3.1 (d)]. The tested specimens were categorized into five groups (G1 to G5) based on different cross-sections and geometrical characteristics of steel and GFRP components. Such information is illustrated in Figure 3.2 with relevant dimensions provided in Table 3.1. The material properties of the steel and GFRP components in each group had been measured previously [24,25] and are summarised in Table 3.1. The adhesive used was Araldite 420, a two-component epoxy based structural adhesive. Its tensile strength and Young's modulus were tested to be 28.6 MPa and 1.9 GPa; Poisson ratio of 0.36 was obtained [24].

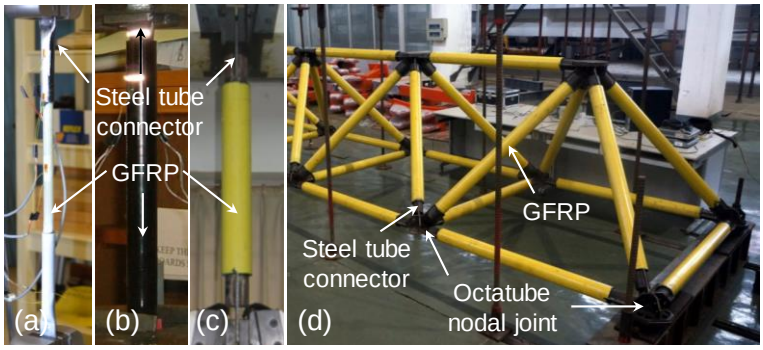

Figure 3.1. Bonded sleeve connections for: (a) specimens G1&G2; (b) specimens G3&G4; (c) specimen G5; and (d) an assembled large-scale space frame.

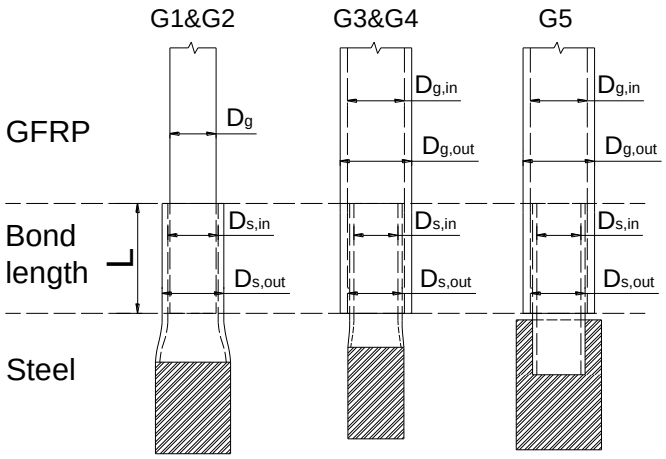

Figure 3.2. Geometries of specimens in different groups (magnitudes of the symbols are given in Table 3.1 for each group).

Table 3.1. Geometry and material properties of specimens.

Group	Description	GFRP dia. $D_{g,out}/D_{g,in}$ (mm)*	Steel dia. $D_{s,out}/D_{s,in}$ (mm)*	Bond length for pull-out failure L (mm)	Young's modulus E (GPa)*	Strength (MPa)*
G1	GFRP rod into steel tube	15.5/-	21.3/17.3	30, 40, 50	51.5/198.3	207.0/487.5
G2		25.3/-	33.7/27.5	30, 40, 50, 60, 70, 80	47.4/209.7	207.0/397.4
G3	Steel tube into GFRP tube	38.0/30.0	26.9/22.3	30, 40	21.6/182.4	240.0/294.7
G4		31.0/24.6	21.3/17.3	30, 40	31.4/198.3	240.0/487.5
G5		92.0/76.0	73.0/65.0	80	39.3/196.8	300.0/451.3

*For GFRP or steel component: outer diameter/inner diameter; for Young's modulus: longitudinal direction of GFRP/steel; for strength: longitudinal tensile strength of GFRP/yield strength of steel.

The bonded sleeve connection specimens in G1 and G2 were formed by GFRP rods inserted into steel tubes; those in G3 to G5 were formed by steel tubes inserted into GFRP tubes (Figure 3.1 and Figure 3.2). These groups of specimens cover possible

scenarios in practice where the GFRP component may be either the outer [25] or inner adherend [49]. The adoption of GFRP rods instead of tubes in G1 and G2 was to increase their cross-section areas thus their axial capacities, preventing potential failure of the GFRP component. In G1 to G4, the free ends of the steel tubes were flattened for clamping or bolt-fastening to nodal joints in structural assembly. With a similar purpose, those in G5 were slot-welded with a steel gusset plate. The specimens were loaded in tension to failure under displacement control. Among all specimens, two types of failure mode were observed, namely pull-out failure [Figure 3.3 (a)] and excessive yielding or fracture of the steel tube connector [Figure 3.3 (b)]. The former failure mode was characterised by adhesive failure close to the inner adherend or interface failure between the adhesive and the inner adherend. Also listed in Table 3.1 are the bond lengths that incurred pull-out failure within each group of specimens. In Table 3.2, these specimens are named following the convention of group index and bond length, together with the experimental results of their ultimate joint capacity $P_{u,E}$.

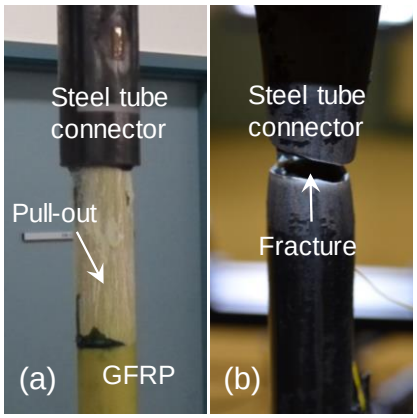

Figure 3.3. Typical failure modes of bonded sleeve connection specimens: (a) pull-out failure; (b) fracture of steel tube connector.

Table 3.2. Ultimate joint capacity (P_u) of specimens with the pull-out failure mode.

Specimen	Experiment $P_{u,E}$ (kN)	Theoretical $P_{u,TH}$ (kN)	$P_{u,E}$ / $P_{u,TH}$	Finite element $P_{u,FE}$ (kN)	$P_{u,E}$ / $P_{u,FE}$
G1-30	40.0	33.8	1.183	34.1	1.172
G1-40	48.0	44.2	1.085	43.3	1.109
G1-50	53.0	53.9	0.983	51.6	1.028
G1-60, 70 and 80 failed by fracture of steel					
G2-30	52.0	54.9	0.947	52.5	0.990
G2-40	72.0	72.3	0.996	69.6	1.035
G2-50	82.0	89.0	0.922	85.7	0.957
G2-60	97.0	104.6	0.927	102.7	0.944
G2-70	111.0	119.1	0.932	114.7	0.968
G2-80	116.0	132.1	0.878	125.5	0.924
G2-90 and 100 failed by excessive yielding of steel					
G3-30	41.0	57.4	0.714	52.9	0.776
G3-40	57.0	73.7	0.773	64.9	0.878
G3-50, 60 and 70 failed by fracture of steel					
G4-30	42.0	46.8	0.897	42.5	0.988
G4-40	56.0	60.7	0.922	55.4	1.012
G4-50, 60 and 70 failed by fracture of steel					
G5-80	362.0	387.6	0.934	378.0	0.958
G5-100 failed by fracture of steel					
Mean			0.935		0.981
Standard deviation			0.114		0.095

3.3. Theoretical Formulation of Joint Capacity

This section starts with formulating the governing differential equation concerning the shear stress (τ) and the relative slip between the adherends (δ), followed by a description of the adopted bond-slip (τ-δ) relationship. The potential types of shear stress distribution

along the bond length at elastic limit and at ultimate state are then identified. For each type of these shear stress distributions, the corresponding joint capacity is solved analytically.

3.3.1. Governing Differential Equations

Differential governing equations are formulated in this section for adhesive shear stress and adherend normal stress based on Volkersen's stress analysis. When a joint is under axial loading (*P*), the adhesive layer is predominantly subjected to shear deformation, as illustrated in Figure 3.4. Here the outer adherend is presumed to be a GFRP tube and the inner adherend a steel tube [Figure 3.4 (a)], though the deduced equilibrium is equally applicable to other materials or to the case in which the inner adherend is a circular rod. Moreover, despite the derivation being based on axial tension, a compression scenario would produce an identical force equilibrium. In this study, *L*, *A* and *b* are the bond length, cross-section area and circular circumference of the bonded face respectively; *r*, *u* and *e* are axial stress, displacement and strain of adherend; *E* is Young's modulus and *s* is shear stress in the adhesive layer; subscripts '*g*' and '*s*' denote the material of GFRP or steel.

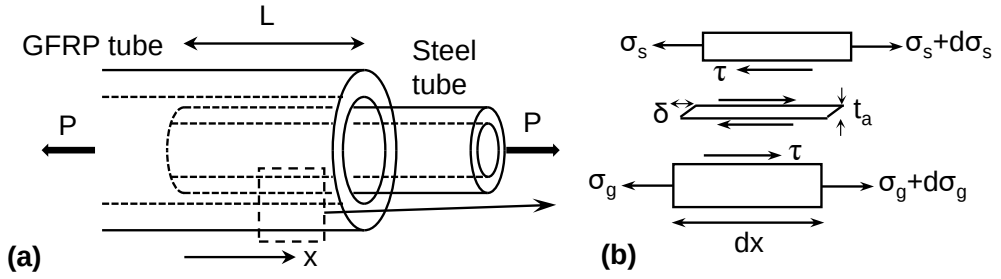

Figure 3.4. A circular bonded sleeve connection under axial tension: (a) overall geometry; (b) typical differential element.

A few assumptions or simplifications are made in the derivation. Adherends are linear elastic thus the formulation is valid before yielding of the steel tube. Normal stress is assumed uniformly distributed over the cross-section of adherends. The adhesive layer is thin compared to the thickness of the adherend; therefore shear stress is considered

uniform through the thickness of adhesive. Cross-sections of adherends and adhesive are constant along the bonded region.

As a result, the slip between adherends δ is defined as the relative displacement between the GFRP and steel components [Figure 3.4 (b)]:

$$\delta = u_s - u_g \tag{3.1}$$

where u_s and u_g are the axial displacement of the steel and GFRP adherend respectively.

Taking derivatives of δ with respect to x gives:

$$\frac{d\delta}{dx} = \frac{du_s}{dx} - \frac{du_g}{dx} = \frac{\sigma_s}{E_s} - \frac{\sigma_g}{E_g} \tag{3.2}$$

$$\frac{d^2\delta}{dx^2} = \frac{d^2u_s}{dx^2} - \frac{d^2u_g}{dx^2} \tag{3.3}$$

For a differential length of the steel tube [Figure 3.4 (b)], the shear stress in the adhesive layer τ and the normal stress in the steel σ_s can be expressed according to force equilibrium in the x direction:

$$\tau b_s dx = A_s d\sigma_s \rightarrow \frac{d\sigma_s}{dx} = \frac{\tau b_s}{A_s} \tag{3.4}$$

$$\sigma_s = E_s \frac{du_s}{dx} \rightarrow \frac{d\sigma_s}{dx} = E_s \frac{d^2u_s}{dx^2} \tag{3.5}$$

Likewise, for a differential length of GFRP tube [Figure 3.4 (b)] shear stress in the adhesive layer τ and normal stress in the GFRP σ_g can be expressed accordingly:

$$\tau b_g dx = -A_g d\sigma_g \rightarrow \frac{d\sigma_g}{dx} = -\frac{\tau b_g}{A_g} \tag{3.6}$$

$$\sigma_g = E_g \frac{du_g}{dx} \rightarrow \frac{d\sigma_g}{dx} = E_g \frac{d^2u_g}{dx^2} \tag{3.7}$$

For a full cross-section within the bond length, the force equilibrium in the axial direction gives:

$$\sigma_s A_s + \sigma_g A_g = P \rightarrow \sigma_s = \frac{P - \sigma_g A_g}{A_s} \tag{3.8}$$

Combining Eqs. (3.3) to (3.7), the governing equation for the shear stress in the adhesive layer τ can be formed as:

$$\frac{d^2\delta}{dx^2} - \left(\frac{b_s}{E_s A_s} + \frac{b_g}{E_g A_g}\right)\tau = 0 \tag{3.9}$$

Because of the thin adhesive layer, in Eq. (3.9) the bonded circumference around the steel b_s is approximately equal to that of the GFRP b_g, and both these values can be considered as the centre line perimeter of the adhesive layer. The governing equation for the normal stress in the GFRP component σ_g can be obtained by substituting Eq. (3.8) into Eq. (3.2):

$$\sigma_g = \frac{1}{\left(\frac{A_g}{A_s}\frac{1}{E_s} + \frac{1}{E_g}\right)}\left(\frac{P}{E_s A_s} - \frac{d\delta}{dx}\right) \tag{3.10}$$

Knowing the normal stress in the GFRP component σ_g from Eq. (3.10), the normal stress in the steel component σ_s can be easily obtained from Eq. (3.8).

Eqs. (3.9) and (3.10) are the governing differential equations for the adhesive shear stress and adherend normal stress of a bonded sleeve joint under axial loading. They are valid regardless of the exact shape of the bond-slip relationship. In the following sections, a bilinear bond-slip relationship is implemented into the governing equations. The stress distributions and corresponding joint capacities are solved under possible cases of boundary conditions.

3.3.2. Bond-Slip Relationship of Adhesive Layer

Figure 3.5 shows the bilinear bond-slip relationship for the adhesive-bonded region. Defined by the origin (0, 0), the peak shear stress point (δ_1, τ_f) and the debonding point (δ_f, 0), such a bilinear curve is commonly described with three stages: elastic, softening and debonding stages, as indicated in Figure 3.5. The area bounded by the curve (i.e. elastic and softening stage) is termed the interface fracture energy (G_f). Eqs. (3.11) and (3.12) were used to determine the peak shear stress τ_f and the debonding slip δ_f, according to the correlations formed in [38]. This is because similar adherend materials (steel and pultruded FRP) and adhesive material (epoxy-based), adhesive thickness (1 to 2 mm) adhesive tensile strength (20 to 30 MPa) and surface preparation of adherends

(sandblasted and cleaned with Acetone) were adopted. With the assumption of uniform shear stress through the thickness of adhesive layer, the slip at peak shear stress δ_1 can be obtained from Eq. (3.13) based on the corresponding shear strain (τ_f/G_a).

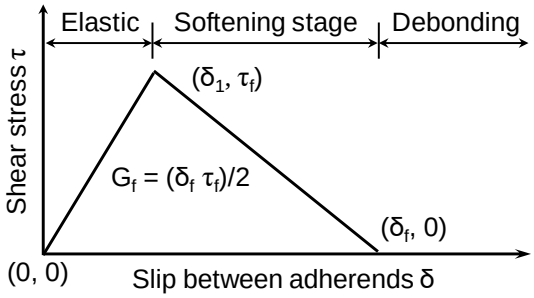

Figure 3.5. Typical bilinear bond-slip relationship for adhesive bonding between steel and GFRP.

$$\tau_f = 0.8 f_{t,a} \tag{3.11}$$

$$\frac{1}{2}\tau_f \delta_f = 31\left(\frac{f_{t,a}}{G_a}\right)^{0.56} t_a^{0.27} \tag{3.12}$$

$$\delta_1 = (\tau_f t_a)/G_a \tag{3.13}$$

where $f_{t,a}$ is the tensile strength of the adhesive; G_a is the shear modulus of the adhesive; and t_a is the thickness of the adhesive layer. In Eq. (3.12), τ_f, $f_{t,a}$ and G_a are in MPa, δ_f and t_a in mm. As a result, the bond-slip relationship is represented in mathematical form as Eq. (3.14)

$$\tau = f(\delta) = \begin{cases} \dfrac{\tau_f}{\delta_1}\delta, & 0 \le \delta \le \delta_1 \\ \dfrac{\tau_f}{\delta_f - \delta_1}\left(\delta_f - \delta\right), & \delta_1 \le \delta \le \delta_f \\ 0, & \delta_f \le \delta \end{cases} \tag{3.14}$$

where τ and δ are the shear stress in the adhesive layer and slip between the adherends.

As the axial load (P) increases, the joint capacity at the elastic limit (P_e) is attained when any location within the bonded area is loaded to completion of the elastic stage, i.e.

when τ reaches τ_f. Further, the joint capacity at the ultimate state is attained when the debonding slip δ_f is reached at either end of the bonded area [35] (i.e. $\delta\ (x = 0\ or\ L) = \delta_f$) with softening of only one end ($P_{u,s1}$) or both ends ($P_{u,s2}$), or when the full bond length is loaded to the softening stage ($P_{u,sf}$, i.e. for $0 \leq x \leq L$ and $\delta_1 \leq \delta < \delta_f$). In what follows, the joint capacities are solved for the elastic limit (P_e) and three different scenarios of the ultimate state ($P_{u,s1}$, $P_{u,s2}$ or $P_{u,sf}$). Finally, the joint capacities can be compared to the capacities of the adherends (steel tube connector or GFRP component) before the critical capacity can be determined accordingly.

3.3.3. Joint Capacity P_e at Elastic Limit

When the applied load P is smaller than the elastic limit P_e, i.e. the slip δ along the bond length is no greater than δ_1, the entire bond length L remains in the elastic region, i.e. $L = L_e$, where L_e denotes the length of the bonded region at the elastic stage. Figure 3.6 presents a typical shear stress distribution along the bond length when $\delta\ (x = 0)$ reaches δ_1, i.e. the applied load P reaches P_e.

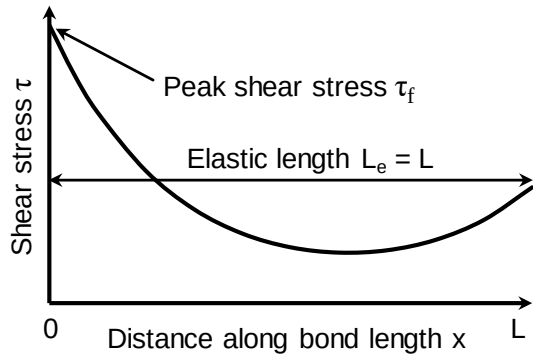

Figure 3.6. Typical shear stress distribution when $P = P_e$.

Since $0 \leq \delta < \delta_1$, the corresponding shear stress expression in Eq. (3.14) can be substituted into Eq. (3.9) as:

$$\frac{d^2\delta}{dx^2} - \left(\frac{b_s}{E_s A_s} + \frac{b_g}{E_g A_g}\right)\frac{\tau_f}{\delta_1}\delta = 0 \tag{3.15}$$

The general solution form of Eq. (3.15) for slip at the elastic stage δ_{el} can be given as

$$\delta_{el}(x) = A_1 cosh(\lambda_1 x) + B_1 sinh(\lambda_1 x) \tag{3.16}$$

where the subscript '*el*' refers to the region of bond length at the elastic stage

Substituting Eq. (3.16) into Eq. (3.10), the normal stress $\sigma_{g,el}$ in the GFRP at the elastic stage of adhesive bonding can be obtained as

$$\sigma_{g,el}(x) = \eta \left[\frac{P}{E_s A_s} - \lambda_1 A_1 sinh(\lambda_1 x) - \lambda_1 B_1 cosh(\lambda_1 x)\right] \tag{3.17}$$

where the constants λ_1 and η are

$$\lambda_1{}^2 = \left(\frac{b_s}{E_s A_s} + \frac{b_g}{E_g A_g}\right)\frac{\tau_f}{\delta_1} \tag{3.18}$$

$$\eta = \frac{1}{\left(\frac{A_g}{A_s}\frac{1}{E_s} + \frac{1}{E_g}\right)} \tag{3.19}$$

By substituting the boundary conditions (Eqs. 3.20 and 3.21) at the two free ends of the bond length

$$\sigma_{g,el}(x = 0) = \frac{P}{A_g} \tag{3.20}$$

$$\sigma_{g,el}(x = L) = 0 \tag{3.21}$$

The unknown constants A_1 and B_1 can be solved as:

$$A_1 = \frac{P}{\lambda_1}\left[\frac{1}{E_s A_s sinh(\lambda_1 L)} - \frac{1}{tanh\,(\lambda_1 L)}\left(\frac{1}{E_s A_s} - \frac{1}{\eta A_g}\right)\right] \tag{3.22}$$

$$B_1 = \frac{P}{\lambda_1}\left(\frac{1}{E_s A_s} - \frac{1}{\eta A_g}\right) \tag{3.23}$$

P_e is then obtained when δ_{el} at either end ($x = 0$ or L) reaches δ_1 and the shear stress along the bond length $\tau(x)$ when $0 \le P \le P_e$ can be obtained as

$$\tau(x) = \frac{\tau_f}{\delta_1}\delta_{el}(x),\ 0 \le x \le L \tag{3.24}$$

3.3.4. Joint capacity $P_{u,\,s1}$ at ultimate state for softening of only one end

A bonded sleeve joint may reach its ultimate capacity $P_{u,s1}$ (the subscript '*s1*' denotes softening of one end) when the debonding slip δ_f is attained at one end while the other remains in the elastic stage (i.e. δ at this end is no greater than δ_1). The full bond length L in this case can be divided into two portions: the softening length L_s where the τ-δ relationship has entered the softening stage, and the elastic length L_e where the τ-δ relationship remains at the elastic stage (Figure 3.7). If the steel component is stiffer than the GFRP component (i.e. $E_sA_s > E_gA_g$), the GFRP end of the bonded area may be subjected to a higher level of slip between adherends [29, 32]. Figure 3.7 depicts a typical shear stress distribution along the bond length when δ reaches δ_f at the GFRP end and the corresponding applied load P therefore reaches the ultimate load $P_{u,\,s1}$.

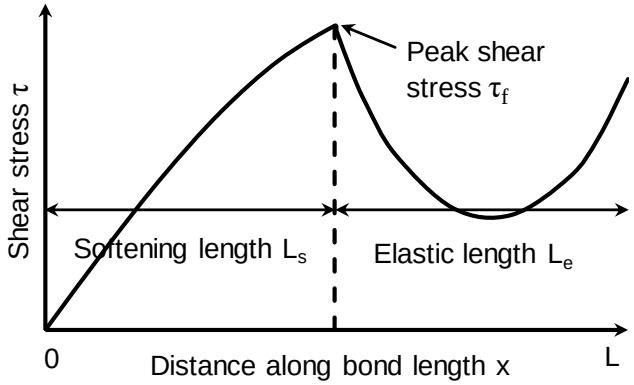

Figure 3.7. Typical shear stress distribution when $P = P_{u,s1}$ (softening of only one end).

Within the elastic length, i.e. $L_s < x \leq L$, and based on Eqs. (3.15) and (3.16), the slip between adherends δ_{el} and normal stress in the GFRP component $\sigma_{g,el}$ can be expressed as:

$$\delta_{el}(x) = A_2 cosh[\lambda_1(x - L_s)] + B_2 sinh[\lambda_1(x - L_s)] \tag{3.25}$$

$$\sigma_{g,el}(x) = \eta\left(\frac{P_{u,s1}}{E_sA_s} - \lambda_1 A_2 sinh[\lambda_1(x - L_s)] - \lambda_1 B_2 cosh[\lambda_1(x - L_s)]\right) \tag{3.26}$$

Within the softening length, i.e. $0 < x \leq L_s$, the corresponding shear stress expression from Eq. (3.14) can be substituted into Eq. (3.9), and Eq. (3.27) can be obtained as:

$$\frac{d^2\delta}{dx^2} - \left(\frac{b_s}{E_s A_s} + \frac{b_g}{E_g A_g}\right)\left(\frac{\tau_f}{\delta_f - \delta_1}\right)\delta = \left(\frac{b_s}{E_s A_s} + \frac{b_g}{E_g A_g}\right)\left(\frac{\tau_f}{\delta_f - \delta_1}\right)\delta_f \tag{3.27}$$

The general solution for δ in Eq. (3.27) can be formed as:

$$\delta_{sl}(x) = C_1 cosh(\lambda_2 x) + D_1 sinh(\lambda_2 x) + \delta_f \tag{3.28}$$

where the subscript '*sl*' refers to the region of bond length at the softening stage, and the constant λ_2 is

$$\lambda_2{}^2 = \left(\frac{b_s}{E_s A_s} + \frac{b_g}{E_g A_g}\right)\left(\frac{\tau_f}{\delta_f - \delta_1}\right) \tag{3.29}$$

Substituting Eq. (3.28) into Eq. (3.10) gives

$$\sigma_{g,sl}(x) = \eta\left[\frac{P_{u,s1}}{E_s A_s} - \lambda_2 C_1 sinh(\lambda_2 x) - \lambda_2 D_1 cosh(\lambda_2 x)\right] \tag{3.30}$$

where the values of A_2, B_2, C_1, D_1, $P_{u,s1}$, L_s can be determined by applying the following six boundary conditions:

$$\delta_{sl}(x = 0) = \delta_f \tag{3.31}$$

$$\delta_{el}(x = L_s) = \delta_1 \tag{3.32}$$

$$\delta_{sl}(x = L_s) = \delta_1 \tag{3.33}$$

$$\sigma_{g,sl}(x = 0) = \frac{P_{u,s1}}{A_g} \tag{3.34}$$

$$\sigma_{g,el}(x = L) = 0 \tag{3.35}$$

$$\sigma_{g,el}(x = L_s) = \sigma_{g,sl}(x = L_s) \tag{3.36}$$

When $P = P_{u,s1}$, the shear stress $\tau(x)$ at a given location x along the bond length can be obtained as:

$$\tau(x) = \begin{cases} \dfrac{\tau_f}{\delta_f - \delta_1}\left[\delta_f - \delta_{sl}(x)\right], & 0 \le x \le L_s \\ \dfrac{\tau_f}{\delta_1}\delta_{el}(x), & L_s < x \le L \end{cases} \tag{3.37}$$

When the applied load P is less than $P_{u,s1}$ (while larger than P_e), the values of A_2, B_2, C_1, D_1 *and* L_s can be obtained by applying Eqs. (3.32) to (3.36), and the shear stress $\tau(x)$ and normal stress $\sigma_{g,el}(x)$ can be solved accordingly using Eqs. (3.25), (3.26), (3.28), (3.30) and (3.37). It is also necessary to check that the steel end is within the elastic stage (i.e. $\delta_{el}(x = L) < \delta_1$) and the softening length is less than the bond length (i.e. $L_s < L$), for the validity of this ultimate state (when $P = P_{u,s1}$), as softening of the bond length occurs only at one end.

3.3.5. Joint Capacity $P_{u,s2}$ at Ultimate State for Softening of Both Ends

This case of the ultimate state represents the scenario when the debonding slip δ_f is attained at one end while the other end is loaded into the softening stage of the bond-slip curve (i.e. $\delta_1 \le \delta < \delta_f$). Therefore, the full bond length L can be divided into three portions: with two softening lengths at two ends (L_{s1} at the GFRP end and L_{s2} at the steel end), a portion of the bond length in between remains in the elastic stage (L_e). Figure 3.8 shows a typical shear stress distribution for this ultimate state and the divisions of bond length, when the applied load P reaches the ultimate load $P_{u,s2}$ (the subscript '*s2*' denotes softening of two ends) for this case.

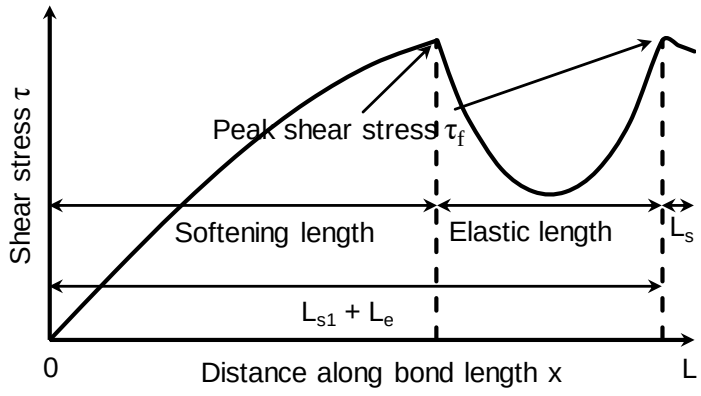

Figure 3.8. Typical shear stress distribution when $P = P_{u,s2}$ (softening of both ends).

Within the elastic length, i.e. $L_{s1} < x \leq L_{s1}+L_e$ (Figure 3.8), and based on Eqs. (3.25) and (3.26), the slip δ_{el} between adherends and normal stress $\sigma_{g,el}$ of the GFRP component can be expressed as:

$$\delta_{el}(x) = A_3 cosh[\lambda_1(x - L_{s1})] + B_3 sinh[\lambda_1(x - L_{s1})] \tag{3.38}$$

$$\sigma_{g,el}(x) = \eta\left(\frac{P_{u,s2}}{E_s A_s} - \lambda_1 A_3 sinh[\lambda_1(x - L_{s1})] + \lambda_1 B_3 cosh[\lambda_1(x - L_{s1})]\right) \tag{3.39}$$

Within the left softening length, i.e. $0 \leq x < L_{s1}$, and based on Eqs. (3.28) and (3.30), the slip δ_{sl1} and normal stress $\sigma_{g,sl1}$ of the GFRP component can be expressed as:

$$\delta_{sl1}(x) = C_2 cosh(\lambda_2 x) + D_2 sinh(\lambda_2 x) + \delta_f \tag{3.40}$$

$$\sigma_{g,sl1}(x) = \eta\left[\frac{P_{u,s2}}{E_s A_s} - \lambda_2 C_2 sinh(\lambda_2 x) - \lambda_2 D_2 cosh(\lambda_2 x)\right] \tag{3.41}$$

where the subscript '*sl1*' refers to the left softening length.

Within the right softening length, i.e. $L_{s1}+L_e < x \leq L$ (Figure 3.8), and also based on Eqs. (3.28) and (3.30), slip δ_{sl2} and normal stress $\sigma_{g,sl2}$ of the GFRP component can be expressed as:

$$\delta_{sl2}(x) = C_3 cosh[\lambda_2(x - L_{s1} - L_e)] + D_3 sinh[\lambda_2(x - L_{s1} - L_e)] + \delta_f \tag{3.42}$$

$$\sigma_{g,sl2}(x) = \eta\left[\frac{P_{u,s2}}{E_s A_s} - \lambda_2 C_3 sinh[\lambda_2(x - L_{s1} - L_e)] - \lambda_2 D_3 cosh[\lambda_2(x - L_{s1} - L_e)]\right] \tag{3.43}$$

where the subscript '*sl2*' refers to the right softening length.

The values of A_3, B_3, C_2, D_2, C_3, D_3, $P_{u,s2}$, L_{s1}, L_e can be determined by applying the following nine boundary conditions:

$$\delta_{sl1}(x = 0) = \delta_f \tag{3.44}$$

$$\delta_{sl1}(x = L_{s1}) = \delta_1 \tag{3.45}$$

$$\delta_{el}(x = L_{s1}) = \delta_1 \tag{3.46}$$

$$\delta_{el}(x = L_{s1} + L_e) = \delta_1 \tag{3.47}$$

$$\delta_{sl2}(x = L_{s1} + L_e) = \delta_1 \tag{3.48}$$

$$\sigma_{g,sl1}(x = 0) = \frac{P_{us,2}}{A_g} \tag{3.49}$$

$$\sigma_{g,sl2}(x = L) = 0 \tag{3.50}$$

$$\sigma_{g,sl1}(x = L_{s1}) = \sigma_{g,el}(x = L_{s1}) \tag{3.51}$$

$$\sigma_{g,el}(x = L_{s1} + L_e) = \sigma_{g,sl2}(x = L_{s1} + L_e) \tag{3.52}$$

When $P = P_{u,s2}$, the resulting shear stress at a given location x along the bond length $\tau(x)$ can be calculated from Eq. (3.53):

$$\tau(x) = \begin{cases} \dfrac{\tau_f}{\delta_f - \delta_1}\left[\delta_f - \delta_{sl1}(x)\right], & 0 \le x \le L_{s1} \\ \dfrac{\tau_f}{\delta_1}\delta_{el}(x), & L_{s1} < x \le L_{s1} + L_e \\ \dfrac{\tau_f}{\delta_f - \delta_1}\left[\delta_f - \delta_{sl2}(x)\right], & L_{s1} + L_e < x \le L \end{cases} \tag{3.53}$$

If the applied load P continuously increases from P_e to the ultimate load $P_{u,s2}$, one end of the bond length (i.e. the GFRP end) starts to soften first, followed by the softening of both ends and then pull-out failure occurs when the debonding slip δ_f is attained at the GFRP end. Thus the form of shear stress distribution changes accordingly, depending on the applied load level. When $P_e < P < P_{u,s2}$, shear stress distribution $\tau(x)$ thus may involve the softening of one or both ends, depending on the load level. It is also necessary to check that at this ultimate state (when $P = P_{u,s2}$), the slip at the steel end is within the softening region (i.e. $\delta_1 < \delta_{sl2}\ (x = L) < \delta_f$), and the softening length at the steel end is positive (i.e. $L_{s2} > 0$).

3.3.6. Joint Capacity $P_{u,sf}$ at Ultimate State for Softening of Full Bond Length

This ultimate state corresponds to the scenario in which the full bond length is loaded into the softening stage of the bilinear bond-slip curve (i.e. $L = L_s$) and the peak shear stress τ_f is achieved within the bond length at a location $x = L_p$, as illustrated by Figure 3.9.

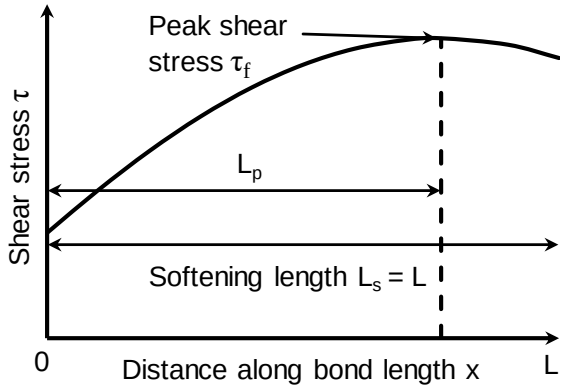

Figure 3.9. Typical shear stress distribution when $P = P_{u,sf}$ (softening of full bond length).

As $L = L_s$ and based on Eqs. (3.28) and (3.30), the slip δ_{sl} and normal stress of the GFRP component $\sigma_{g,sl}$ can be expressed as:

$$\delta_{sl}(x) = C_2 cosh(\lambda_2 x) + D_2 sinh(\lambda_2 x) + \delta_f \tag{3.54}$$

$$\sigma_{g,sl}(x) = \eta \left[\frac{P_{u,sf}}{E_s A_s} - \lambda_2 C_2 sinh(\lambda_2 x) - \lambda_2 D_2 cosh(\lambda_2 x) \right] \tag{3.55}$$

When this ultimate state is attained, i.e. $P = P_{u,sf}$ (the subscript '*sf*' denotes softening of the full bond length), the peak shear stress τ_f appears at the location $x = L_p$, and the values of C_2, D_2, $P_{u,sf}$, L_p can be determined by applying the following four boundary conditions:

$$\delta_{sl}(x = L_p) = \delta_1 \tag{3.56}$$

$$\frac{d\delta_{sl}}{dx}(x = L_p) = 0 \tag{3.57}$$

$$\sigma_{g,sl}(x = 0) = \frac{P_{u,sf}}{A_g} \tag{3.58}$$

$$\sigma_{g,sl}(x = L) = 0 \tag{3.59}$$

The corresponding shear stress distribution $\tau(x)$ can be formed by Eq. (3.60) for this ultimate state.

$$\tau(x) = \frac{\tau_f}{\delta_f - \delta_1}\left[\delta_f - \delta_{sl}(x)\right], \qquad 0 \le x \le L \tag{3.60}$$

When the applied load increases from P_e to $P_{u,sf}$, softening of one end is initiated first (i.e. the GFRP end), followed by softening of the other end, and finally the two softening regions merge into one (i.e. $L_s = L$) and pull-out failure occurs. The forms of shear stress distribution may change accordingly, depending on the applied load level. When $P_e < P < P_{u,s2}$, shear stress distribution $\tau(x)$ thus may involve softening of one or two ends, depending on the load level. Again, it is necessary to validate this ultimate state (when $P = P_{u,sf}$) by checking that the slip at the GFRP end is within the softening stage [i.e. $\delta_1 < \delta_{sl}\ (x = 0) < \delta_f$] and the same condition at the steel end [i.e. $\delta_1 < \delta_{sl}\ (x = L) < \delta_f$].

It should be noted that failure may also occur in the steel or GFRP component if the joint capacity is greater than the axial capacity of the adherend components. In this case, the joint capacity P_s is determined by the steel yielding strength as $A_s f_{sy}$ or by the GFRP tensile strength as $A_g f_{gu}$, where f_{sy} and f_{gu} are the yield strength and ultimate strength of the steel and GFRP component respectively.

3.4. Finite Element Analysis

3.4.1. Geometry and Materials

Finite element (FE) analysis was conducted using the ANSYS package to describe the mechanical response of bonded sleeve joints under axial tension. Figure 3.10 (a) presents an example of the geometry of a bonded sleeve joint connecting steel and GFRP tubes. Focusing on verifying the theoretical results and estimating the experimental pull-out failure load, the FE models were constructed only concerning the bonded regions of the specimens. The material properties of the GFRP, steel and adhesive are provided in Table 3.1. The GFRP was defined as a linearly elastic and transversely isotropic material with its longitudinal direction in alignment with the x-axis [Figure 3.10 (a)]. An isotropic bilinear work hardening material model was employed for the steel component, with Von Mises's yield criterion and flow rule after yielding. The post-yield hardening modulus of the steel was taken 2% of its Young's modulus (2% E_s), an upper limit of practical steel

material as suggested in [50]. The material definition for the adhesive was isotropic and linearly elastic.

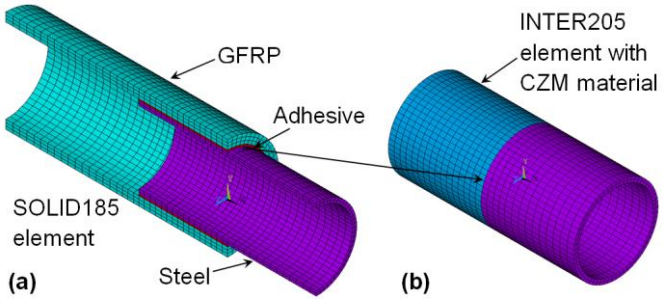

Figure 3.10. FE modelling: (a) overall geometry; (b) interface elements.

3.4.2. Elements

All elements of the GFRP, steel and adhesive components were meshed in ANSYS with SOLID185, a 3-D 8-node element. Three or seven layers of elements were used across the thickness of each GFRP tube or rod, while two layers were used for the steel and one for the adhesive. Success in simulating bonded zone behaviour hinges on correct implementation of the cohesive zone modelling (CZM) technique in ANSYS. In general, the pull-out failure observed from experiments took place in the adhesive layer (near the inner adherend) or at the adhesive-inner adherend interface. This is because of the slightly smaller bonded area associated to the inner adherend, thus larger shear stress on the inner surface of the adhesive layer. Accordingly, INTER205, a planar 3-D 8-node cohesive element, was applied between the adhesive and the inner adherend [Figure 3.10 (b)]. This 8-node element has four pairs of overlapping nodes; each pair is attached to adjacent elements of steel and adhesive or GFRP and adhesive. The overlapping nodes were separated upon loading through a ‘Mode II’ separation, parallel to the bonded interface, as observed from the experiments [Figure 3.3 (a)]. The shear traction–separation relationship was defined with the CZM material property option in ANSYS, and was established in accordance to the bilinear bond-slip relationship presented in Figure 3.5. Mesh studies were performed for specimens in G2 and G5 with respect to the number of

elements along the bond length, ensuring that further refinement resulted in less than 1% change in the ultimate joint capacities. As a result, elements sized at approximately 2 mm in the bond length direction were adopted.

3.4.3. Boundary Conditions

In application of the axial loading, the GFRP end was restrained in all directions before the steel end was displaced in a tensile manner until the ultimate load was attained. The effect of material nonlinearity was accounted for. The displacement was applied in two load steps and solved with the sparse direct equation solver. The first load step was a ramped-load where the displacement was increased uniformly. As the ultimate load was approached, a second load step was introduced for better convergence, in which the automatic time stepping option was activated. This enabled the program to determine the size of displacement increment based on the structural response, and upon convergence failure after a certain number of iterations, to restart with a halved increment size.

3.5. Results and Discussion

3.5.1. Comparison of Ultimate Joint Capacity

Summarised in Table 3.2 are the experimental results of the ultimate joint capacities ($P_{u,E}$), along with theoretical estimates $P_{u,TH}$ (either $P_{u,s1}$, $P_{u,s2}$ or $P_{u,sf}$) and numerical estimates ($P_{u,FE}$) for the specimens observed with the pull-out failure mode. Among these 14 specimens, the average ratio between experimental and theoretical results of joint capacity ($P_{u,E}/P_{u,TH}$) was 0.935 and that between experimental and FE results ($P_{u,E}/P_{u,FE}$) was 0.981, with standard deviations of 0.114 and 0.095 respectively. These indicated good prediction and slight overestimation by the theoretical and FE modelling, which may be attributed to fabrication defects in the bonding zones of the specimens examined in the experiments.

According to the theoretical and FE modelling of all the experimental specimens, their ultimate states were achieved when the full bond length was loaded into the softening stage, i.e. $P = P_{u,sf}$, therefore the resulting shear stress distribution was formulated in Section 3.3.6. Because the same bond-slip relationship was used, it was

anticipated that close values of ultimate joint capacity (i.e. $P_{u,TH}$ vs. $P_{u,FE}$) would be obtained from the theoretical and FE modelling. However, the FE modelling produced slightly lower estimates than the theoretical ones (the average ratio $P_{u,FE}/P_{u,TH}$ was 0.952). This may be attributed to a smaller bonded circumference outside the inner adherend in the FE modelling compared to that defined at the adhesive centreline in the theoretical formulation, i.e. due to the assumption of a thin adhesive layer. Still, a discrepancy to notice is that, besides the yielding of steel, the FE modelling further considered shear deformation of adherends whereas the theoretical formulation did not. The effects of shear deformation of adherends may be taken into account by adopting the improved Volkersen method developed in [51]. Such effects were revealed by trial FE analysis to be insignificant and were thus neglected in the theoretical formulation. It should be noted that FE modelling was also conducted for the same specimens under compression loading. Identical joint capacity and adhesive shear stress distribution were produced as those under tension, which was also in accordance to the theoretical formulation.

3.5.2. Shear Stress Distribution

Verified against the experimental ultimate joint capacities, the theoretical and FE modelling are capable of providing insight into the shear stress distribution, which is difficult to measure from experiments. Figure 3.11 shows examples of three forms of shear stress distribution corresponding to different states of joint capacity through theoretical and FE modelling. Using specimen G1-50 as an example, Figure 3.11 (a) or (b) present the stress distribution when the applied load P reached P_e or $P_{u,sf}$. In Figure 3.11 (a), the full bond length was in the elastic stage (i.e. $\delta \leq \delta_1$ and $L = L_e$) with the peak shear stress τ_f attained at the GFRP end. The FE modelling gave higher estimates of slip δ (or shear stress τ) in the middle portion, resulting in 12.4% overestimation of P_e. For the same specimen, in Figure 3.11 (b), the full bond length was in the softening stage (i.e. $\delta_1 \leq \delta < \delta_f$ and $L = L_s$) corresponding to the joint capacity $P_{u,sf}$ of 53.9 kN by theoretical formulation or 51.6 kN by FE modelling. The peak shear stress τ_f appeared closer to the steel end, indicating that the GFRP end was subjected to higher level of slip. The shear stress distributions provided by theoretical and FE modelling were practically identical.

The section configuration of specimens G2, with a longer bond length of 140 mm, can be used for theoretical and numerical investigation. Figure 3.11 (c) presents the shear stress distribution when $P = P_{u,s2}$, i.e. softening occurred at both ends and the debonding slip δ_f was attained at the GFRP end. In Figure 3.11 (c), the two peaks, representing the peak shear stress τ_f, divide the full bond length into three portions: L_{s1}, L_e and L_{s2} from left to right. This was in accordance with the form of shear stress distribution presented in Figure 3.8. Compared to the theoretical distribution, the FE result exhibited shorter L_{s1} (84.6% of the theoretical result) and longer L_e (130.6% of the theoretical result). In general, however, a satisfactory agreement of joint capacity $P_{u,s2}$ can be found from Figure 3.11 (c). It should be noted that experimentally such a specimen would fail in the steel component because of the joint capacity being greater than the 118.4kN of the steel adherend.

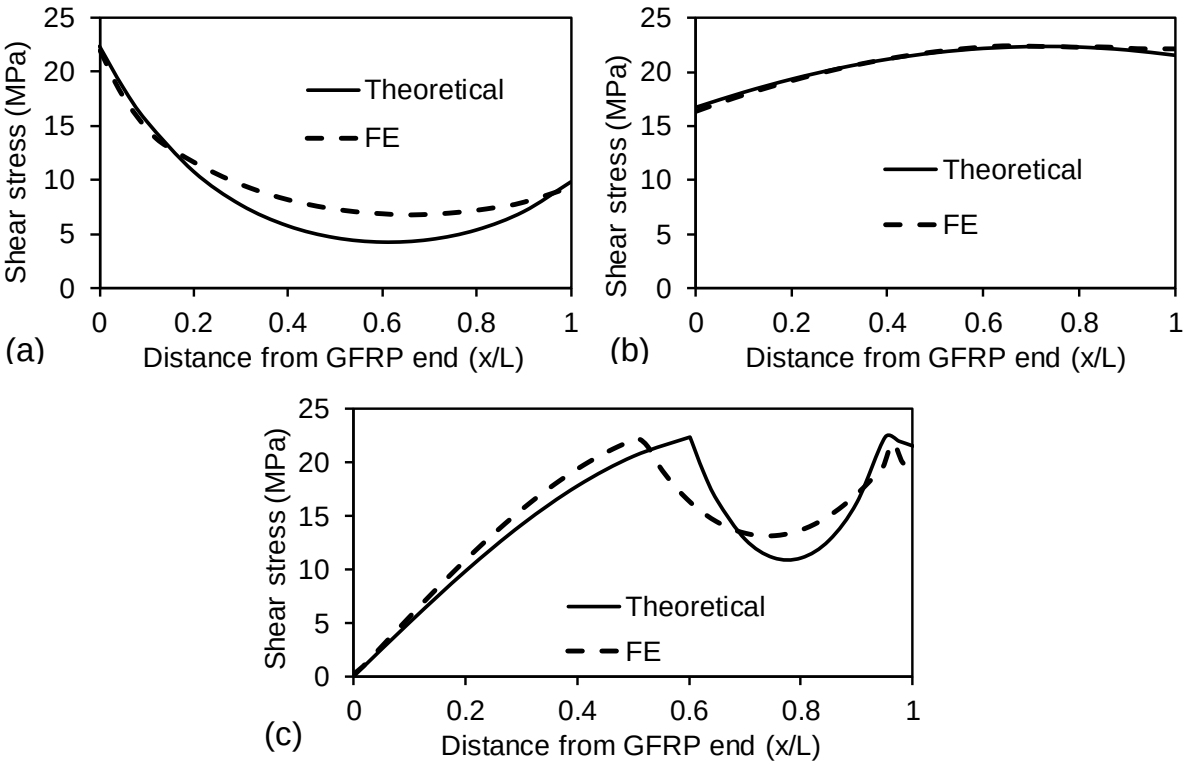

Figure 3.11. Shear stress distribution along bond length: (a) specimen G1-50 when $P = P_e$ (20.9 kN or 23.5 for theoretical or FE modelling); (b) specimen G1-50 when $P = P_{u,sf}$ (53.9 kN or 51.6 kN for theoretical or FE modelling); (c) theoretical and FE example G2-140 when $P = P_{u,s2}$ (167.8 kN or 160.4 kN for theoretical or FE modelling).

Figure 3.12 shows, through FE analysis, the adhesive shear stress distribution at different load levels. For both the specimen G1-50 and the numerical example of G2-140, when the applied load [85% P_e in Figure 3.12 (a) and (b)] was less than P_e, the full bond length remained in the elastic stage and the maximum shear stress appeared at the GFRP end due to its lower stiffness (E_gA_g). As the axial load [85% $P_{u,sf}$ in Figure 3.12 (a) and 85% $P_{u,s2}$ in Figure 3.12 (b)] increased beyond the elastic limit while still below the ultimate state (i.e. $P_e < P < P_{u,sf}$ or $P_{u,s2}$), softening was introduced at the GFRP end, resulting in the peak shear stress (τ_f) appearing and shifting towards the steel end while the rest of bond length remained in the elastic stage. Approaching the ultimate state, specimen G1-50 [see Figure 3.12 (a)] had softening at both ends, and these two regions merged into one when the load increased to 100% $P_{u,sf}$, resulting in softening of the entire bond length. The peak shear stress (τ_f) appeared at the confluence point of the two softening regions, i.e. at the location of L_p in Figure 3.9. In contrast, for the numerical example G2-140 at 100% $P_{u,s2}$ [see Figure 3.12 (b)], where the ultimate state corresponds to softening of both ends, the softening length at the GFRP end extended towards the steel end such that the slip δ *(x/L = 0)* reached δ_f. Meanwhile, softening was also introduced at the steel end [i.e. $\delta_1 < \delta$ *(x/L = 1)* $< \delta_f$]. The peak shear stress (τ_f), appearing at two locations corresponding to those of L_{s1} and $L_{s1}+L_{se}$ (also see Figure 3.8), defines the boundaries of the bond length remaining in the elastic stage.

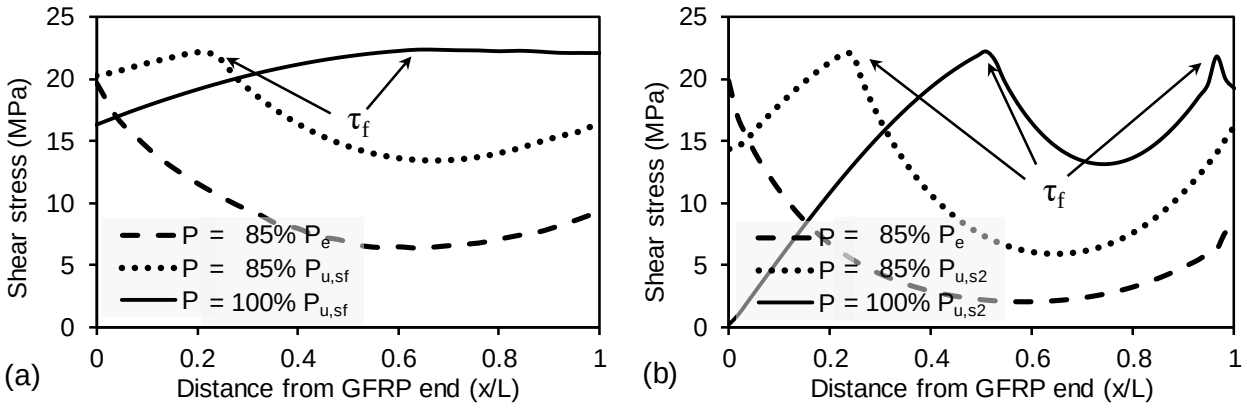

Figure 3.12. Shear stress distribution along bond length from FE modelling at different load level: (a) specimen G1-50; (b) FE example G2-140.

3.5.3. Effect of Bond Length on Joint Capacity

Variation of bond length (L), resulting in different forms of shear stress distribution as illustrated in the theoretical formulation, is believed to have a significant effect on the joint capacity. Figure 3.13 presents the results of a parametric study with respect to bond length (L), using section configuration of specimens G2 (GFRP rod into steel tube as per Table 3.1). Both the theoretical and the FE results in Figure 3.13 indicated that the joint capacity at the elastic limit P_e ceased to improve when the bond length reached a certain level, demonstrating the existence of an effective bond length within the elastic stage, which in this case was around 40 mm. For bond lengths longer than the effective value, the theoretical and FE modelling presented joint capacity P_e around 46 kN and 55 kN respectively.

Clearly, the applied load may be increased beyond the elastic stage. Experimental, theoretical and FE results of the relationship between ultimate joint capacity and bond length are also presented in Figure 3.13. Represented by the black triangles, the experimental results increased almost linearly until a bond length of around 70 mm, after which little improvement in joint capacity was observed, due to yielding of the steel tube connector as observed from experiments. The theoretical and FE results, showing similar patterns, produced close agreement to experimental data. It is worth clarifying that steel yielding was considered in both theoretical and FE calculations, resulting in the joint capacity at 119 kN and 126 kN formed as a horizontal line as the representation of the capacity of the steel tube connector.

Furthermore, in order to investigate the effect of bond length on ultimate joint capacity that is dominated not by adherend capacity (e.g. steel yielding) but by adhesive bonding, theoretical and FE modelling were conducted on a series of specimens with the same cross-section configuration as those in G2 but with the different steel yield strength (f_{sy}) of 580 MPa. Shown in Figure 3.13, the theoretical and FE ultimate joint capacities of such specimens still reached a plateau that was not defined by the capacity of the adherends (steel yielding in this case), corresponding to an effective bond length of around 125 mm at the ultimate state. At and beyond this effective value, the ultimate joint

capacity was calculated as 169 kN from theoretical modelling and 163 kN from FE modelling.

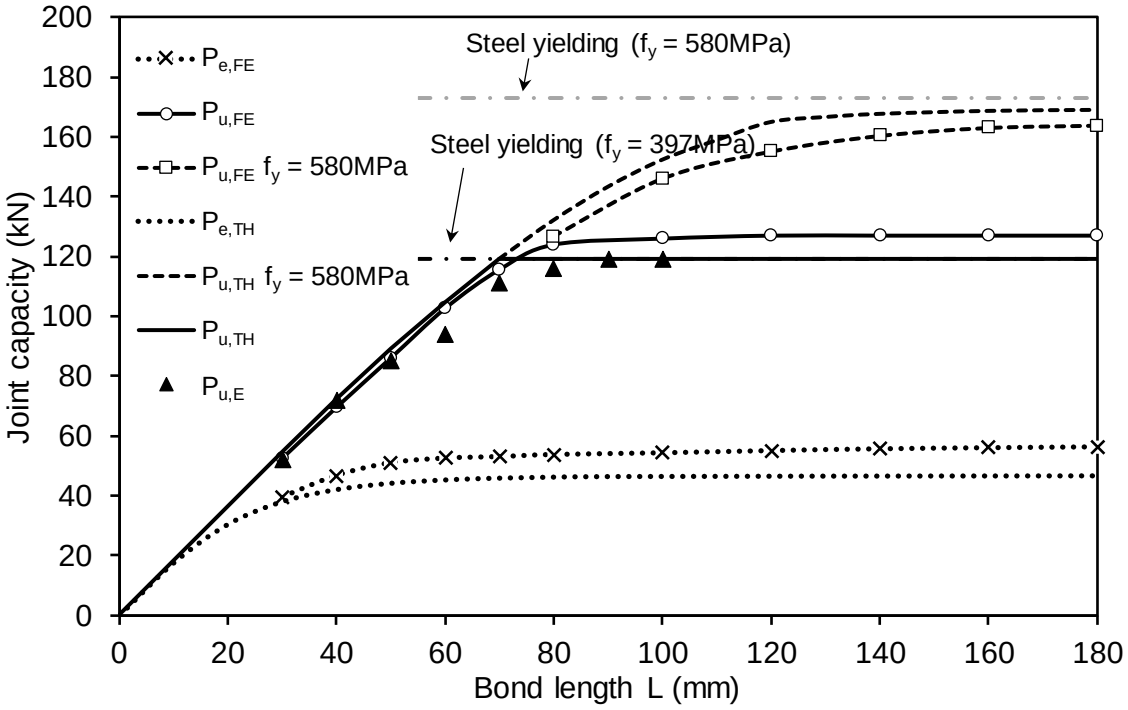

Figure 3.13. Effect of bond length on joint capacity (specimens based on cross-section configuration in G2).

It is also worthwhile to examine the change in the form of shear stress distribution at the ultimate state of adhesive bonding (rather than adherend) when the bond length approached the effective value. For the section configuration G2 with steel yield strength (f_{sy}) of 580 MPa, Figure 3.14 (a) shows that, at the bond length of 100 mm (slightly below the effective value of 125 mm), the type of shear stress distribution at the ultimate state (i.e. $P = P_{u,sf}$) was characterised by softening of the full bond length. In contrast, with a bond length of 120 mm, which was close to the effective value, Figure 3.14 (b) shows the type of distribution when softening occurred at both ends, with the debonding slip δ_f attained at the GFRP end, corresponding to the ultimate state illustrated in Figure 3.8, i.e. $P = P_{u,s2}$. This outcome occurred because, as the bond length became sufficiently long,

the debonding slip δ_f was attained at one end before the two softening ends merged. It should also be noted that as the bond length passed the effective value, other than the change of ultimate state from $P_{u,sf}$ to $P_{u,s2}$ as illustrated above, a change from $P_{u,sf}$ to $P_{u,s1}$ could also occur depending on the section geometries and bond-slip parameters. Similarly, this change was due to the redistribution of shear stress. With a sufficiently long bond length, the debonding slip δ_f might be attained at one end before the other was loaded into the softening stage.

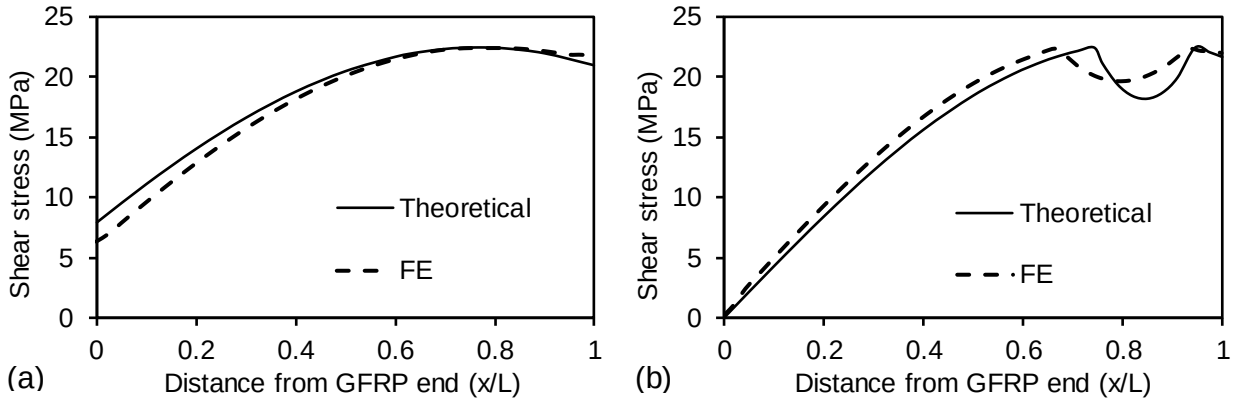

Figure 3.14. Change of shear stress distribution form as bond length approached effective value: (a) G2-100 with elevated adherend strength ($P_{u,sf}$ = 152.4 kN or 145.9 kN for theoretical or FE modelling); (b) G2-120 with elevated adherend strength ($P_{u,s2}$ = 165.1 kN or 155.8 kN for theoretical or FE modelling).

3.5.4. Effect of Stiffness Ratio on Joint Capacities

The stiffness ratio between adherends (i.e. E_sA_s/E_gA_g) is another important parameter to be considered in the design of such bonded sleeve connections. In previous elastic analysis of single or double lap joints, the inequality between E_sA_s and E_gA_g, known as the adherend stiffness imbalance, could cause incapacity of a joint to develop full strength at the elastic stage. This is because the bonded zone at the end with the less stiff adherend could be loaded to its stress limit prior to the other end [32,52,53]. Using the developed theoretical formulation, the effect of this stiffness imbalance on both the elastic and the

ultimate state joint capacity of a bonded sleeve connection is illustrated in Figure 3.15, based on the cross-section configuration of the G5-series specimens. The variation of stiffness ratios was achieved by changing the outer diameter of the GFRP tube or the inner diameter of the steel tube, while maintaining the section geometry of the adhesive layer. This resulted in stiffness ratios E_sA_s/E_gA_g from 0.2 to 4 as shown in Figure 3.15.

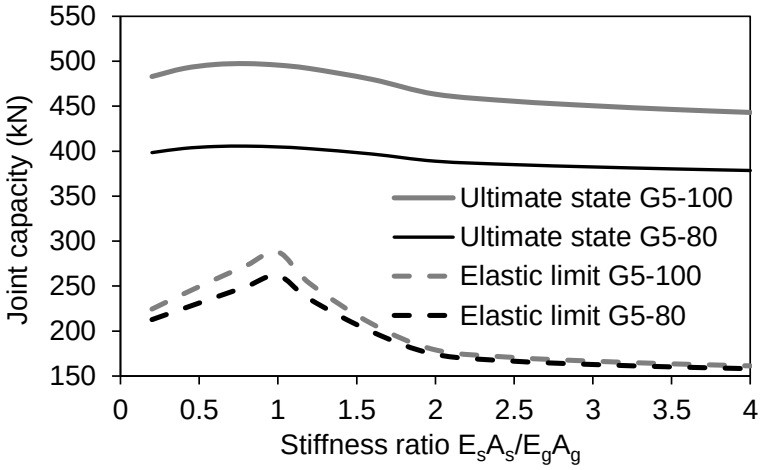

Figure 3.15. Effect of stiffness ratio (E_sA_s/E_gA_g) on joint capacity at elastic limit (P_e) and at ultimate state ($P_{u,sf}$) based on the G5-series specimens.

Figure 3.15 shows that, consistent with the cases of single or double lap joints, the greatest joint capacity at the elastic limit (P_e) of a bonded sleeve connection was achieved when the adherends had equal stiffness i.e. $E_sA_s/E_gA_g = 1$. At the ultimate state (in this case $P_{u,sf}$), the greatest joint capacity was achieved at a stiffness ratio of around 0.8, as shown in Figure 3.15. The variation of joint capacity at the elastic limit (P_e) with the stiffness ratio E_sA_s/E_gA_g was much more significant than that at the ultimate state ($P_{u,sf}$). This finding is attributed to the steeper slope of the bilinear bond-slip relationship at the elastic stage than at the softening stage (see Figure 3.5).

Figure 3.16 shows the shear stress distribution calculated by the theoretical formulation for the configuration of specimen G5-80 with three stiffness ratios. For the elastic limit, i.e. $P = P_e$, Figure 3.16 (a) indicates that the shear stress distribution was symmetrical when $E_sA_s/E_gA_g = 1$, and the peak shear stress was attained simultaneously

at both ends. Otherwise, for the unbalanced stiffness ratios (i.e. E_sA_s/E_gA_g = 0.4 or 2.5), the peak shear stress only appeared at the end of the less stiff adherend. Figure 3.16 (b) presents the shear stress distribution at the ultimate state, i.e. $P = P_{u,sf}$. Likewise, the balanced adherend stiffness (i.e. E_sA_s/E_gA_g = 1) produced a symmetrical shear stress distribution which had the peak shear stress τ_f appear at the middle of the bond length. The unbalanced adherend stiffness resulted in the peak shear stress τ_f being located closer to the end of the stiffer adherend, indicating a higher level of slip δ at the other end.

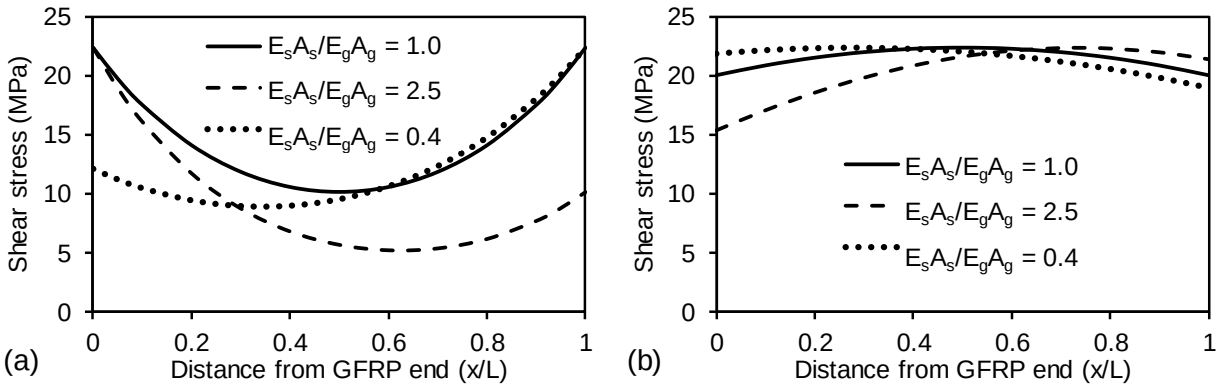

Figure 3.16. Effect of stiffness ratio (E_sA_s/E_gA_g) on shear stress distribution from theoretical modelling based on specimen G5-80: (a) when $P = P_e$; (b) when $P = P_{u,sf}$.

3.6. Conclusions

This paper develops a theoretical formulation to characterise the adhesive shear stress distribution and to predict the joint capacity of bonded sleeve connections. A bilinear bond-slip relationship was implemented in the governing equations to consider the elastic, softening and debonding behaviour of the adhesive bonding. The results of ultimate joint capacity calculated by the theoretical formation were validated by the results from FE modelling and from experiment. Utilising the validated theoretical and FE modelling, the effects of bond length and stiffness ratio on the adhesive shear stress distribution and joint capacity were discussed and clarified for such bonded sleeve

connections. The work presented in this paper allows the following conclusions to be drawn:

1. **Theoretical stress distributions and joint capacities**. Employing the bilinear bond-slip relationship, when the bonded sleeve connection is loaded to elastic limit, the peak shear stress (τ_f) appears at the end of the less stiff adherend. The joint capacity at the ultimate state shows three different scenarios, each corresponding to shear stress distribution that features softening of one end or both ends or along the full length of the bonding region. The theoretical formulation gives satisfactory prediction of the pull-out joint capacities for the experimental specimens; the average test/prediction ratio was obtained as 0.935.

2. **FE modelling of the bonded sleeve joints**. FE modelling can simulate adhesive bonding using the cohesive interface elements associated with Mode II separation and the bilinear bond-slip relationship. The FE modelling produced slightly lower joint capacities compared to the theoretical modelling, which could be explained by the more conservative representation of the actual bond area and the consideration of material nonlinearity in the adherend. The FE modelling yielded accurate prediction of the experimental joint capacities for the pull-out failure mode, with an average test/prediction ratio of 0.981.

3. **Effective bond length**. For cases with no adherend failure, effective bond lengths do exist for the joint capacities at both the elastic limit and the ultimate state. Such effective bond lengths can be well identified by the theoretic formulation and further well validated by the FE modelling results. Attainment of effective bond length may further cause transformation of the type of shear stress distribution at the ultimate state. Finally, taking into account the capacity of adherends, the relationship between bond length and ultimate joint capacity can be developed via theoretical and FE modelling for a specific bonded sleeve connection.

4. **Effect of adherend stiffness**. The maximum joint capacity at the elastic limit (P_e) occurs when the stiffnesses of adherends are balanced (i.e. $E_sA_s/E_gA_g = 1$). Whereas the joint capacity at the ultimate state ($P_{u,s}$) is optimal at the stiffness ratio (E_sA_s/E_gA_g) of around 0.8. The effect of this stiffness ratio on the ultimate joint capacity is much less

obvious in comparison to the effect on the elastic joint capacity. For both the elastic limit and ultimate state, a balanced adherend stiffness generates symmetrical shear stress distribution, while a difference in adherend stiffness leads to more slip (δ) at the end of the less stiff adherend.

3.7. Acknowledgements

The authors gratefully acknowledge the support from the ARC Training Centre for Advanced Manufacturing of Prefabricated Housing (IC150100023) and the National Natural Science Foundation of China (No. 51522807).

3.8. References

1. Bakis C, Bank LC, Brown V, Cosenza E, Davalos J, Lesko J, et al. Fiber-reinforced polymer composites for construction-state-of-the-art review. Journal of Composites for Construction. 2002;6(2):73-87.
2. Hollaway L. A review of the present and future utilisation of FRP composites in the civil infrastructure with reference to their important in-service properties. Construction and Building Materials. 2010;24(12):2419-45.
3. Nagaraj V, GangaRao HV. Static behavior of pultruded GFRP beams. Journal of Composites for Construction. 1997;1(3):120-9.
4. Di Tommaso A, Russo S. Shape influence in buckling of GFRP pultruded columns. Mechanics of Composite Materials. 2003;39(4):329-40.
5. Keller T, Schollmayer M. Plate bending behavior of a pultruded GFRP bridge deck system. Composite Structures. 2004;64(3):285-95.
6. Bank LC. Composites for Construction: Structural Design with FRP Materials. John Wiley & Sons, 2006.
7. Meyer R. Handbook of Pultrusion Technology. Springer Science & Business Media, 2012.
8. Bank LC, Gentry TR, Nuss KH, Hurd SH, Lamanna AJ, Duich SJ, et al. Construction of a pultruded composite structure: Case study. Journal of Composites for Construction. 2000;4(3):112-9.

9. Keller T. Use of fibre reinforced polymers in bridge construction. International Association for Bridge and Structural Engineering (IABSE), Zurich, 2003
10. Turner MK, Harries KA, Petrou MF, Rizos D. In situ structural evaluation of a GFRP bridge deck system. Composite Structures. 2004;65(2):157-65.
11. Zou X, Feng P, Wang J. Perforated FRP ribs for shear connecting of FRP-concrete hybrid beams/decks. Composite Structures. 2016;152:267-76.
12. Benmokrane B, El-Salakawy E, El-Gamal S, Goulet S. Construction and testing of an innovative concrete bridge deck totally reinforced with glass FRP bars: Val-Alain Bridge on Highway 20 East. Journal of Bridge Engineering. 2007;12(5):632-45.
13. Keller T, Haas C, Vallée T. Structural concept, design, and experimental verification of a glass fiber-reinforced polymer sandwich roof structure. Journal of Composites for Construction. 2008;12(4):454-68.
14. Hagio H, Utsumi Y, Kimura K, Takahashi K, Itohiya G, Tazawa H. Development of space truss structure using glass fiber reinforced plastics. Proceedings: Advanced Materials for Construction of Bridges, Buildings, and Other Structures III, Davos, Switzerland, 7-12 September, 2003.
15. Awad ZK, Aravinthan T, Zhuge Y. Experimental and numerical analysis of an innovative GFRP sandwich floor panel under point load. Engineering Structures. 2012;41:126-35.
16. Satasivam S, Bai Y, Zhao X-L. Adhesively bonded modular GFRP web–flange sandwich for building floor construction. Composite Structures. 2014;111:381-92.
17. Satasivam S, Bai Y. Mechanical performance of bolted modular GFRP composite sandwich structures using standard and blind bolts. Composite Structures. 2014;117:59-70.
18. Feng P, Cheng S, Bai Y, et al. Mechanical behavior of concrete-filled square steel tube with FRP-confined concrete core subjected to axial compression. Composite Structures. 2015;123:312–24.
19. Feng P, Zhang Y, Bai Y, Ye L. Combination of Bamboo Filling and FRP Wrapping to Strengthen Steel Members in Compression. Journal of Composites for Construction. 2013;17(3):347-56.

20. Feng P, Zhang Y, Bai Y, Ye L. Strengthening of steel members in compression by mortar-filled FRP tubes. Thin-Walled Structures. 2013;64(64):1-12.
21. Smith S, Parsons I, Hjelmstad K. An experimental study of the behavior of connections for pultruded GFRP I-beams and rectangular tubes. Composite Structures. 1998;42(3):281-90.
22. Smith S, Parsons I, Hjelmstad K. Experimental comparisons of connections for GFRP pultruded frames. Journal of Composites for Construction. 1999;3(1):20-6.
23. Singamsethi S, LaFave J, Hjelmstad K. Fabrication and testing of cuff connections for GFRP box sections. Journal of Composites for Construction. 2005;9(6):536-44.
24. Yang X, Bai Y, Luo FJ, Zhao X-L, He X-h. Fiber-Reinforced Polymer Composite Members with Adhesive Bonded Sleeve Joints for Space Frame Structures. Journal of Materials in Civil Engineering. 2016:04016208.
25. Yang X, Bai Y, Ding F. Structural performance of a large-scale space frame assembled using pultruded GFRP composites. Composite Structures. 2015;133:986-96.
26. Luo FJ, Bai Y, Yang X, Lu Y. Bolted sleeve joints for connecting pultruded FRP tubular components. Journal of Composites for Construction. 2016;20(1):04015024.
27. Luo FJ, Yang X, Bai Y. Member Capacity of Pultruded GFRP Tubular Profile with Bolted Sleeve Joints for Assembly of Latticed Structures. Journal of Composites for Construction. 2016;20(3):04015080.
28. Wu C, Zhang Z, Bai Y. Connections of tubular GFRP wall studs to steel beams for building construction. Composites Part B: Engineering. 2016;95:64-75.
29. Volkersen O. Die Nietkraftverteilung in zugbeanspruchten Nietverbindungen mit konstanten Laschenquerschnitten. Luftfahrtforschung. 1938;15(1/2):41-7.
30. Goland M, Reissner E. The stresses in cemented joints. Journal of Applied Mechanics. 1944;11(1):A17-A27.
31. Hart-Smith L J. Adhesive-bonded single-lap joints. Langley Research Center, Hampton, VA: NASA, 1973.
32. Hart-Smith L J. Adhesive-bonded double-lap joints. Langley Research Center, Hampton, VA: NASA, 1973.

33. Ranisch E-H. Zur Tragfähigkeit von Verklebungen zwischen Baustahl und Beton: geklebte Bewehrung: Inst. für Baustoffe, Massivbau und Brandschutz der Techn. Univ.; 1982.
34. Brosens K, Van Gemert D. Plate end shear design for external CFRP laminates. Fracture Mechanics of Concrete Structures. 1998;3:1793-804.
35. Yuan H, Teng J, Seracino R, Wu Z, Yao J. Full-range behavior of FRP-to-concrete bonded joints. Engineering Structures. 2004;26(5):553-65.
36. Wu Z, Yuan H, Niu H. Stress transfer and fracture propagation in different kinds of adhesive joints. Journal of Engineering Mechanics. 2002;128(5):562-73.
37. Holzenkämpfer P. Ingenieurmodelle des Verbunds geklebter Bewehrung für Betonbauteile. 1997.
38. Xia S, Teng J. Behaviour of FRP-to-steel bonded joints. In: Proceedings of the international symposium on bond behaviour of FRP in structures, International Institute for FRP in Construction; 2005. p. 419-26.
39. Campilho R, De Moura M, Domingues J. Modelling single and double-lap repairs on composite materials. Composites Science and Technology. 2005;65(13):1948-58.
40. Campilho R, Banea MD, Pinto A, da Silva LF, De Jesus A. Strength prediction of single-and double-lap joints by standard and extended finite element modelling. International Journal of Adhesion and Adhesives. 2011;31(5):363-72.
41. Nakaba K, Kanakubo T, Furuta T, Yoshizawa H. Bond behavior between fiber-reinforced polymer laminates and concrete. ACI Structural Journal. 2001;98(3):359-67.
42. Wu Z, Yin J. Fracturing behaviors of FRP-strengthened concrete structures. Engineering Fracture Mechanics. 2003;70(10):1339-55.
43. Fawzia S, Zhao X-L, Al-Mahaidi R. Bond–slip models for double strap joints strengthened by CFRP. Composite Structures. 2010;92(9):2137-45.
44. Yu T, Fernando D, Teng J, Zhao X. Experimental study on CFRP-to-steel bonded interfaces. Composites Part B: Engineering. 2012;43(5):2279-89.
45. Täljsten B. Strengthening of concrete prisms using the plate-bonding technique. International journal of Fracture. 1996;82(3):253-66.

46. Yuan H, Wu ZS, Yoshizawa H. Theoretical solutions on interfacial stress transfer of externally bonded steel/composite laminates. J Struct Mech Earthquake Eng, Japan Society of Civil Engineers, Tokyo 2001(675):27-39.
47. Campilho R, De Moura M, Domingues J. Using a cohesive damage model to predict the tensile behaviour of CFRP single-strap repairs. International Journal of Solids and Structures. 2008;45(5):1497-512.
48. Alfano G. On the influence of the shape of the interface law on the application of cohesive-zone models. Composites Science and Technology. 2006;66(6):723-30.
49. Bai Y, Zhang C. Capacity of nonlinear large deformation for trusses assembled by brittle FRP composites. Composite Structures. 2012;94(11):3347-53.
50. Kadin Y, Kligerman Y, Etsion I. Multiple loading–unloading of an elastic–plastic spherical contact. International Journal of Solids and Structures. 2006;43(22):7119-27.
51. Tsai M, Oplinger D, Morton J. Improved theoretical solutions for adhesive lap joints. International Journal of Solids and Structures. 1998;35(12):1163-85.
52. DoD (USA), Structural behaviour of joints, in: Military Handbook – MIL-HDBK-17-3F: Composite Materials Handbook, Volume 3 – Polymer Matrix Composites Materials Usage, Design, and Analysis, US Dept of Defense, Washington DC, 2002.
53. Al-Shawaf A. Understanding and predicting interfacial stresses in advanced fibre-reinforced polymer (FRP) composites for structural applications. Advanced Fibre-Reinforced Polymer (FRP) Composites for Structural Applications. 2013:255.

CHAPTER 4. PERFORMANCE OF THE SPLICE CONNECTION UNDER AXIAL LOADING

Declaration for the Chapter

Chapter 4 of the thesis presents the following published work in a re-formatted form:

Qiu C, Ding C, He X, Zhang L, Bai Y. Axial performance of steel splice connection for tubular FRP column members. Composite Structures. 2018;189:498-509. https://doi.org/10.1016/j.compstruct.2018.01.100

Permission has been obtained from the publisher *Elsevier* to include the article, in its published form or in a re-formatted form, in this thesis.

The student's and the co-authors' contribution to the work is listed in the following table:

Name of author	**Nature of contribution**	**Contribution (%)**
C Qiu (the student)	Conceptualisation, methodologies, experimental work, numerical modelling, data analysis, writing-up, revision	65%
C Ding	Experimental work	5%
X He	Review and revision	5%
L Zhang	Review and revision	5%
Y Bai	Conceptualization, methodologies, data analysis, review and revision, financial support	20%

The undersigned hereby certify that the above declaration correctly reflects the nature and extent of the student's and co-authors' contribution to this work.

Student (Chengyu Qiu) signature: Main supervisor (Yu Bai) signature:

Date: Date:

Link of the Published Work to the Thesis

The published work presents experimental and numerical studies on the proposed splice connection (Figure 2.18) under axial loading.

Abstract

A splice connection is proposed for connecting tubular fibre reinforced polymer (FRP) members. This connection consists of a steel bolted flange joint (BFJ) and two steel-FRP bonded sleeve joints (BSJs). The BFJ connects two steel hollow sections, each of which is telescoped into the targeted tubular FRP member through adhesive bond, forming a BSJ. To evaluate the performance of the proposed splice connection under axial loadings, BSJs of four different bond lengths and BFJs of two bolt configurations are tested individually. Finite element (FE) models are developed which feature a bilinear bond-slip relation, contact behaviours and bolt pre-tensioning. Comparisons are made between experimental and FE results in terms of load-displacement behaviours, ultimate capacities and strain responses. Besides being capable of identifying an effective bond length for the BSJ and modelling the yielding process of the BFJ, FE analysis provides insight into the distribution of adhesive shear stress over the bond area of the BSJs, and the steel yield line pattern on the flange-plate of the BFJs. Verified by experimental results, the FE modelling technique is then utilised to understand the integrated axial behaviours of a complete splice connection.

Keywords: Fibre reinforced polymer (FRP); Tubular member; Splice connection; Axial loading; Bonded sleeve joint; Bolted flange joint.

4.1. Introduction

Fibre reinforced polymer (FRP) composites are increasingly used in civil engineering structures, thanks to their high specific strength, superior corrosion resistance and availability in various geometries [1-3]. In particular, glass FRP (GFRP) composites are credited with sufficient strength and stiffness at moderate cost. Advances in the pultrusion manufacturing technique [4,5] have enabled mass production of GFRP profiles at reduced

cost with satisfactory quality control, motivating research into their application as bridge decks [6,7], reinforcement [8], roof structure [9], trusses [10–12] and floor systems [13–15]. Compared to open section profiles (i.e. I or channel profiles), closed section profiles (i.e. circular or rectangular tubular profiles) exhibit better resistance against torsional and global buckling [16]. Yet these merits of tubular GFRP members coexist with the difficulty of connecting the members into truss and frame assemblies, due to the material anisotropy and the closed section shape.

Extensive research has been conducted in pursuit of viable connection forms for tubular GFRP members. Imitating practices in steel structures, early efforts to connect GFRP tubular members utilised bolted-through web-gusset plates or flange-angle cleats for beam-column connections [17]. In the development of a connection form for axially loaded tubular GFRP profiles, the benefits of using a steel tubular sleeve connector which was inserted into and bolt-fastened to the tubular GFRP profile were underlined in [18,19]. This steel sleeve connector facilitated versatile connection forms to adjacent members. Despite the convenience of in-situ installation, bolt fastening requires hole-drilling on the composite material, creating problems such as damaged fibre architecture, stress concentration, and exposure of the weak in-plane shear strength of the FRP composites. Adhesive bonding, as an alternative, offers structural integrity, reduced stress concentration and also improved fatigue resistance [20-22]. Combining the benefits of the adhesive bond and the steel sleeve connector, bonded sleeve connections for joining circular GFRP truss members to nodal joints were proposed and examined in [11,12]. In an experimental investigation by Wu et al. [23] and the accompanying numerical study [24], the FRP-steel tubular bonded sleeve connection concept was utilised in FRP beam to steel column configurations. Such connections exhibited significant improvement in both rotational strength and stiffness over steel angle connections and bolted sleeve connections.

Despite the aforementioned works, research into developing a column-splice connection for FRP tubular members remains scarce. In steel structures, a widely used splice connection for rectangular/square hollow sections (RHS/SHS) is the bolted flange joint (BFJ), which possesses the benefits of simple constitution and convenient in-situ installation [25]. Combining the FRP-steel bonded sleeve joint and the steel hollow

section bolted flange joint, a column-splice connection for GFRP tubular members is proposed as illustrated in Figure 4.1. This steel-GFRP connection system consists of two components: a bonded sleeve joint (BSJ) coupling GFRP and steel tubes adhesively, and a bolted flange joint (BFJ) connecting two steel SHSs through fillet weld. The BSJ reduces stress concentration in the GFRP compared to bolt fastening, while the BFJ enables convenient installation and imparts ductility to the system (through steel yielding).

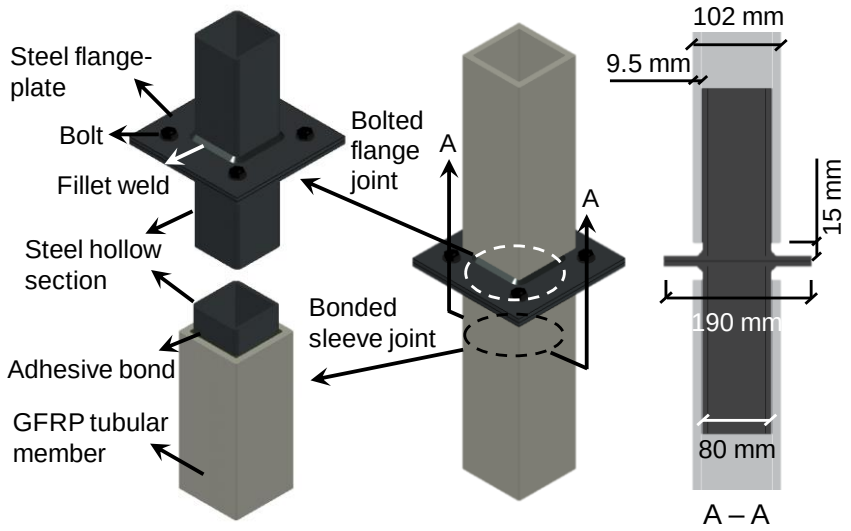

Figure 4.1. Proposed column-splice connection for tubular GFRP members.

As presented in Figure 4.1, for a pultruded FRP box section of 102×102×9.5 mm, a steel SHS of outer dimension of 80×80mm is selected in this study to achieve an adhesive thickness of 1.5mm for practical assembly. To accommodate the fillet weld and to remove rotational constraint, a gap of 15mm exists between the GFRP tubular member and the steel flange-plate. Steel flange-plate of 190×190mm is selected for practical installation of the fastener (M12 bolt) and to fulfil the requirements for the edge distances of the fastener according to AS4100 [26]. Steel is used in the present study because of its wide availability, good weldability and moderate cost. Aluminium can be used for the BFJ when further weight-saving and corrosion resistance is required. Different loading scenarios may be found for the proposed splice connection depending on its potential

applications. When used as a column splice, the connection is mainly subjected to a combination of axial (as a combination of tension and compression) and flexural loadings. When used as a beam splice, it would be under flexural and shear loadings. This paper focuses on investigating the performance of the proposed connection under axial loadings for column application.

Axial loading on the BSJ is resisted by shear between the GFRP and the steel adherends. Such a load transfer mechanism has been extensively studied in the form of single or double lap joints. A bilinear relationship has been widely utilised to model the bond-slip behaviour due to its simple constitution and hence convenient analytical and numerical implementation. This bilinear relationship is characterised by a linearly ascending stage between the adhesive shear stress and relative slip between the adherends, followed by a linear decrease to zero shear stress at the debonding slip.

Early analytical study took advantage of this relationship to solve for the axial capacities of single lap joints in several configurations [27,28] and also to identify the shear stress distribution [29,30] and debonding process [31]. Experiments were carried out to measure the shear stress-slip relationship along the bond line in FRP-concrete [32,33] and FRP-steel bonded lap joints [34-36], verifying that the bond-slip curves resembled a bilinear shape when brittle adhesives were used. For ductile adhesives, meanwhile, a trapezoidal shape was found suitable [36,37]. The bilinear bond-slip relationship was incorporated into numerical analyses through the technique of cohesive zone modelling [38-40], in which a crack interface was pre-defined for the bond area and the tangential traction-slip relationship was defined as the bilinear shape. In light of previous work on single and double lap joints, an analytical solution, verified by experiments and FE analysis, was recently developed for the joint capacity of bonded sleeve connections consisting of circular steel and FRP tubular members [41]. In contrast to the earlier studies where adhesive shear stress was uniform in the transverse direction of single/double lap joints or in the circumferential direction of a circular section, the proposed connection, involving square or rectangular tubular adherends (Figure 4.1), is distinguished by varying shear stress distribution in the transverse direction.

The failure mechanism of the bolted flange joint (BFJ) in axial loading of tension (more critical than in compression) is governed by a yield line mechanism in the steel flange-plate or/and tensile failure of the bolts under prying action. Taking into account both types of failure, design models were developed in [42] for configurations where one or two bolts were positioned at each side of the SHS. A similar design approach was later employed to solve for the layout with bolts at two sides of the RHS [43]. Focusing on the bolt failure under tensile loading, well-instrumented experiments were conducted to investigate the prying action on the bolts [44], before a modified AISC design procedure [45] was formulated. Design method is provided in Section 6 of Eurocode 3 Part 1–8 [46] to calculate the moment resistance of bolted flange splices or beam-column connections. Three modes of local yield lines are considered around the bolt holes at the tensile flange. Although this method is intended for I or H sections under bending loading, adaptation can be made as suggested in [47] by mirroring the yielding lines at the tensile flange to calculate the tensile resistance of RHS/SHS bolted flange joints with bolts at two sides of the hollow section. The aforementioned experimental and analytical studies centred on the ultimate load-carrying capacities, and very limited description was presented of stiffness, failure processes and strain responses. Finite element (FE) methods were successfully utilised to understand the bending behaviour of these BFJ with [48] and without stiffeners [49]. Yet modelling results for the tensile behaviour of BFJs are still limited.

The remainder of this paper experimentally and numerically investigates the mechanical performance of the proposed column-splice connection in axial loadings. Design parameters for the specimens include four different bond lengths and two types of bolt configuration (four and eight bolts). The detailed three-dimensional FE models feature utilising the bilinear bond-slip relationship for bond behaviour, contact between assembled parts and bolt pre-tensioning. Experimental results are then discussed and compared with FE modelling with respect to load-displacement behaviours, strain data, effect of bond length and yield line patterns of the connections. Finally, design recommendations are provided for optimising the performance of the proposed column-splice connection.

4.2. Experimental Program

4.2.1. Specimens

As the proposed connection consisted of bonded sleeve joints (BSJs) and bolted flange joint (BFJ) in series as described in Figure 4.1, experiments were conducted individually on each component. Considering shear failure within the adhesive layer (cohesive failure) as the failure mode of interest for the BSJs, tensile and compressive loadings would theoretically induce identical adhesive shear stress distribution along the bond length and thus identical joint behaviour [41]; therefore, only compression tests were conducted on the BSJ specimens. For the BFJs, compressive failure would be preceded by member failure of the connected steel hollow section member, for which reason only the tensile behaviours of the BFJs were investigated.

Each of the BSJ specimens, illustrated in Figure 4.2, was fabricated from a pultruded GFRP square tube (102×102×9.5 mm), a grade 355 steel square hollow section (SHS, 80×80×6 mm) and Sikadur-30, a two-component epoxy-based structural adhesive. The BSJs were coded '*BSJ-x-y*' where '*x*' represents the bond length in mm (*x= 50, 100, 140 or 180*) and '*y*' refers to the index of the repeating specimen in each bond length (*y= 1 or 2*). Bonded surfaces of the steel and GFRP were pre-treated by a procedure of 'degreasing – sandblasting – acetone cleaning' before adhesive was applied, as recommended in [50]. Consistent thickness of the adhesive layer was controlled by 1.5 mm-diameter spacers pre-bonded onto the steel SHS. To minimise the air voids in the adhesive layer, excessive adhesive was applied onto the bonded surfaces before squeezed out as the steel SHS was forced into the GFRP tube. Fabrication of the specimens was followed by a 2-week curing under room temperature before testing.

Two types of bolt configuration were adopted for the BFJs, with their geometries shown in Figure 4.3. These two configurations were doubly symmetric and were efficient in resisting both tensile and bending actions. The BFJs were coded '*BFJ-a-b*' where '*a*' represents the bolt number (*a = 4 or 8*) and '*b*' the index of the repeating specimen (*b = 1or 2*). BFJ-4 and BFJ-8 specimens shared the same geometries except for the number of bolts and their positions. Fillet welds of approximately 6 mm joined the steel SHS (80×80×6 mm, same as those in the BSJs) to the 6 mm-thick grade 250 steel flange-plate

as shown in Figure 4.3. During the welding, the flange-plate was clamped firmly against a rigid flat base to prevent likely deformation caused by heat distortion. A gusset plate was slot-welded into each steel SHS to enable application of tensile loading through gripping [Figure 4.3 (a)]. The bolts were M12 grade 8.8 hex bolts with washers and nuts, pre-tensioned to around 52 kN (70% of the nominal proof load of the bolt) by a torque wrench before testing according to [45].

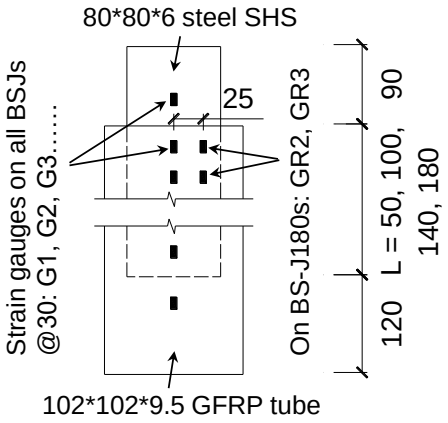

Figure 4.2. Geometries of bonded sleeve joint specimens BSJ-50 to 180 and positions of strain gauges (all units in mm).

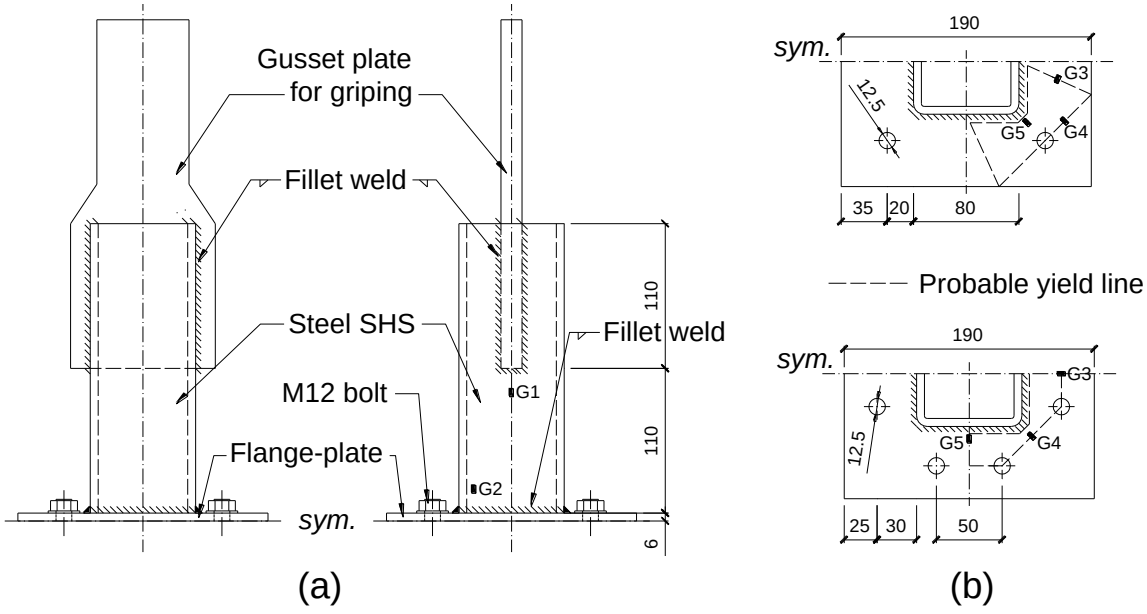

Figure 4.3. (a) Front and side view of a BFJ-4 specimen; (b) plan views of BFJ-4 and BSJ-8 and positions of strain gauges (all units in mm).

4.2.2. Material Properties

The pultruded GFRP square tubes were composed of a polyester matrix (volume fraction 53.3%) and E-glass fibres (volume fraction 46.7%) [51]. The strength and elastic modulus properties of the GFRP material were determined in [51,52] according to relevant standard methods [53-55] as summarised in Table 4.1. The material properties of the steel SHS and flange-plate, tested from tensile coupons in accordance with ASTM A370-16 [56] [1], are summarised in Table 4.2. The M12 bolt was reported to have a yield strength of 1043 MPa and Young's modulus of 235 GPa [24]. The Sikadur-30 adhesive, tested in [36] in accordance with ASTM D638-10 [57], exhibited linear brittle behaviour with tensile strength of 22.3 MPa and elastic modulus of 11.3 GPa.

Table 4.1. Strength and stiffness of the GFRP material [56].

Orientation and component	**Strength (MPa)**	**Stiffness (GPa)**	**Method**
Longitudinal tensile	306.5 ± 18.0	30.2 ± 1.4	ASTM D3039 [53]
Transverse tensile	-	5.5 ± 0.7	ASTM D3039 [53]
Interlaminar shear	26.7 ± 0.2	-	ASTM D2344 [54]
In-plane shear	14.9 ± 1.3	3.5 ± 0.7	10° off-axis tensile test [55]

Table 4.2. Strength and stiffness of the steel materials.

Steel component	**Yield strength (MPa)**	**Ultimate strength (MPa)**	**Young's modulus (GPa)**	**Poisson's ratio**
80*80*6mm SHS [a]	420.1 ± 5.9 [b]	519.4 ± 8.4	209.5 ± 3.9	0.277 ± 0.07
6mm-thick flange	313.6 ± 1.0	458.5 ± 0.0	200.6 ± 2.2	0.277 ± 0.01

[a] Tensile coupons cut from walls of the tube;

[b] 0.2 % offset yield strength.

[1] More information of the material testing of the steel flange-plates is provided in Section A.1.2 of Appendix.

4.2.3. Instrumentation and Experimental Setup

Compressive loading on the BSJ specimens was implemented by a 500 kN Amsler machine under displacement control at 0.4 mm/min loading rate [Figure 4.4 (a)]. Axial shortening of the specimens was measured by two linear variable differential transducers (LVDT). As shown in Figure 4.2 (a), strain gauges were installed on the surface of the GFRPs along the centre bond line at 30mm intervals; two additional strain gauges were installed on the BSJ-180s offset 25mm from the centre bond line, as indicated. The BSJs were each loaded past their peak load.

Tensile loading on the BFJ specimens was carried out by a 500 kN Baldwin machine at a 0.5 mm/min loading rate [Figure 4.4 (b)]. A laser extensometer was used to gauge axial elongation of the specimens. Besides strain gauges G1 and G2 on the steel SHS [Figure 4.3 (a)], strain gauges G3 to G5 were installed on the flange-plate where, from trial FE analysis, yield lines were likely to form [Figure 4.3 (b)]. The BFJs were each loaded until substantial yielding deformation of the steel was observed in the load-displacement curve.

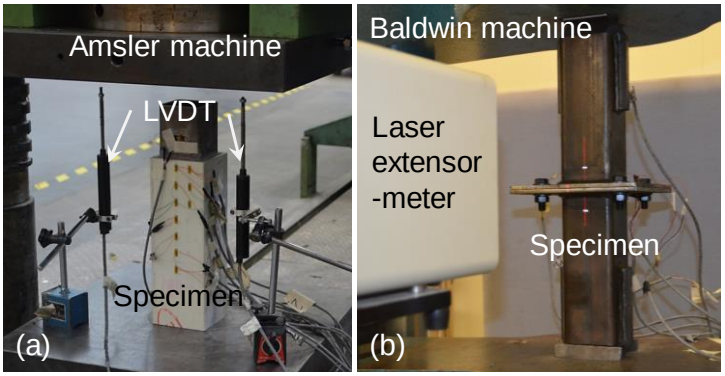

Figure 4.4. Experimental test setup: (a) compression test on BSJs; (b) tension test on BFJs.

4.3. Finite Element Modelling

4.3.1. Geometries, Materials and Elements

FE modelling of the specimens under axial loadings was performed using the commercial software ANSYS. Figure 4.5 shows representative meshed models of the BSJ and BFJ specimens, for each of which half of the geometry was constructed due to symmetry. All the GFRP and steel components were meshed with SOLID185, a 3-D 8-node element in ANSYS. The GFRP was modelled as an orthotropic linear elastic material whose longitudinal direction aligned with the X-axis shown in Figure 4.5 (a). The walls of the tubular GFRP members were idealised as transversely isotropic composite laminates, resulting in identical interlaminar and in-plane shear modulus (Table 4.1). The longitudinal and transverse elastic modulus of the GFRP were defined according to the values in Table 4.1. The steel SHS and flange-plate were modelled as isotropic multilinear work-hardening materials, representing the stress-strain curves measured from the tensile coupon tests. The fillet welds were considered to be the same material as the steel flange-plate.

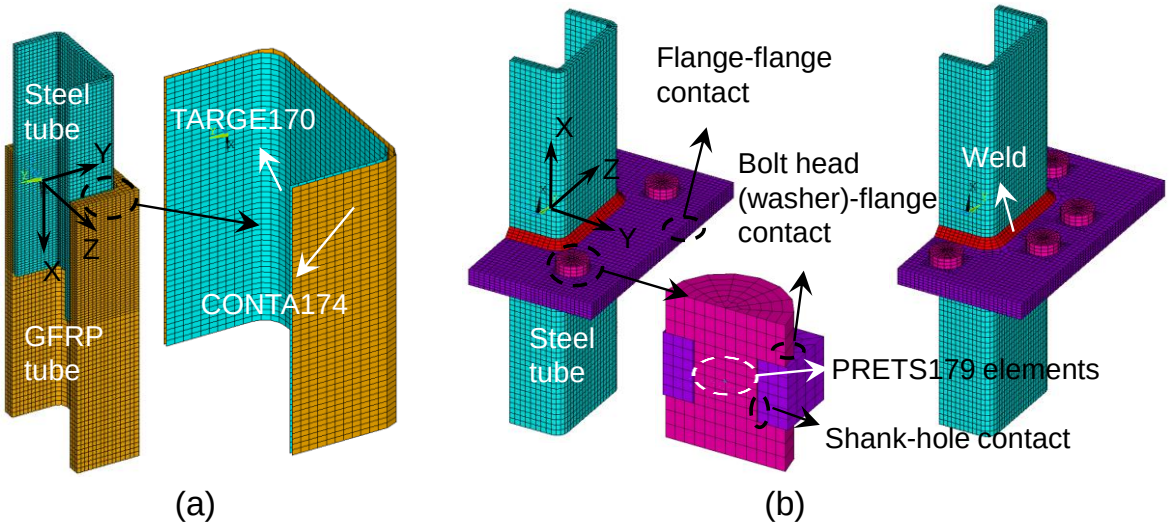

Figure 4.5. Meshed FE models: (a) BSJ specimens; (b) BFJ-4 and BFJ-8 specimens.

4.3.2. Modelling Bond Behaviour in BSJs

Bond behaviour in the FE analysis was established through the cohesive zone modelling (CZM) approach. This was enforced by a contact pair on the bonded surfaces, i.e.

CONTA174 and TARGE170, a pair of 3-D 8-node surface-to-surface contact elements, applied on the bonded surface of the GFRP and steel respectively [Figure 4.5 (a)]. A 1.5 mm-gap existed between the contact surfaces, representing the thickness of the adhesive layer. The normal stiffness of the contact interaction (both opening and closing) was input as the product of the elastic modulus and the thickness of the adhesive. The tangential traction between the contact surfaces was modelled as a bilinear function of the shear slip between the contact pair, as shown in Figure 4.6. This bilinear bond-slip relationship, consisting of a linear ascending elastic stage, a linear descending softening stage and also a debonding stage with zero shear stress, has been deemed appropriate for modelling cohesive failures in bonded lap joints when brittle adhesives are used [34-36]. It should be noted that, in the CZM approach, the distribution of shear stress was considered uniform through the thickness of the adhesive layer.

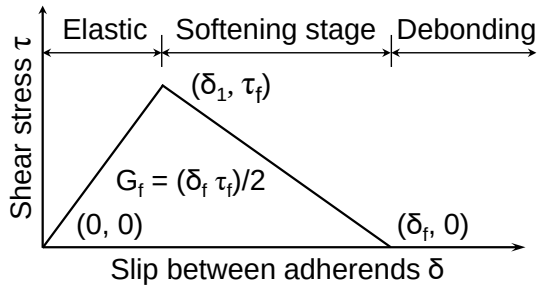

Figure 4.6. Bilinear bond-slip relationship for GFRP-steel bond.

To define this bilinear relationship in ANSYS, three material parameters were required – the peak shear stress (τ_f), the stiffness of the elastic stage ($K_a = \tau_f/\delta_1$) and the critical fracture energy ($G_f = \tau_f\delta_f/2$). For the same adhesive (Sikadur-30) with identical layer thickness ($t_a = 1.5\ mm$), the peak shear stress ($\tau_f = 18.4\ MPa$) and critical fracture energy ($G_f = 1.25\ N/mm$) had been determined in a previous experimental investigation of steel-FRP single lap joints [36]. Assuming uniform shear stress thus shear strain through the thickness of the adhesive layer, the stiffness K_a was calculated by:

$$K_a = G_a t_a \tag{4.1}$$

where G_a is the adhesive shear modulus calculated from the elastic modulus with a Poisson's ratio of 0.3, and t_a is the thickness of the adhesive layer

Before applying the axial loading, the GFRP end was constrained in all directions and symmetric constraint was applied on the longitudinal cut plane [XZ plane in Figure 4.5 (a)]. A load step which displaced the steel end in tension or compression was solved with automatic time-stepping for better convergence. It was further confirmed that tensile and compressive loadings generated identical load-displacement behaviour and shear stress distribution between the bonded surfaces.

4.3.3. Modelling Contact and Pre-tension in BFJs

In the modelling of the BFJs, contact between the assembled steel components was considered by the contact pair CONTA174 and TARGE170, with a steel-to-steel friction coefficient of 0.44 [58]. Three contact pairs were identified as shown in Figure 4.5 (b), i.e. those between the two flange-plates, between the bolt washer and flange-plate, and between the bolt shank and hole. Bolt pretension was applied via PRETS179 elements defined at the midsection of each bolt shank [Figure 4.5 (b)]. In terms of boundary conditions, one end of the specimen was constrained in all directions and symmetry constraint was applied on the longitudinal cut plane [XZ plane in Figure 4.5 (b)]. Application of the bolt pre-tension was solved in a first load step before a second load step axially displaced the free end of the specimen in the tensile direction.

4.4. Results and Discussion: Bonded Sleeve Joint (BSJ) Specimens

4.4.1. Failure Modes and Load-Displacement Responses

Experiments revealed brittle cohesive failure within the adhesive layer of all the BSJs. Figure 4.7 shows typical load-displacement curves of the BSJs, characterised by a linear increase to peak load before brittle failure. Post-failure residual strength, provided by friction on the fracture surfaces, was recorded between 10 and 45 kN among specimens. Likewise, as also shown in Figure 4.7, linear brittle load-displacement behaviours were produced by FE modelling, except that the experimental residual strength could not be captured. Of all the BSJ specimens, discrepancy in the stiffness is found no more than

18% between experiment and FE modelling. When the peak load was imminent, cracking in the adhesive layer was observed as shown in Figure 4.8 (a). In BSJ-100-1 and BSJ-140-1, post-failure loading resulted in cracks at the web-flange junction of the GFRPs, as indicated in Figure 4.8 (b), possibly due to the confining pressure generated through sliding of the adherends over the uneven crack surface. Figure 4.8 (c), representative of all BSJs, shows the separated adherends and the crack surface where bond failure occurred; the attachment of adhesive to both the steel and GFRP indicates cohesive failure located within the adhesive layer but closer to the GFRP.

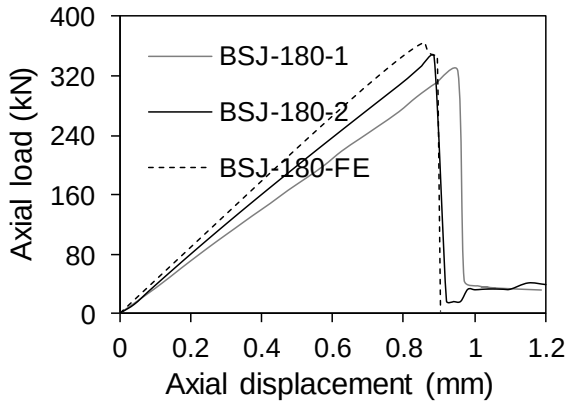

Figure 4.7. Typical experimental and FE load-displacement curves of BSJs [1].

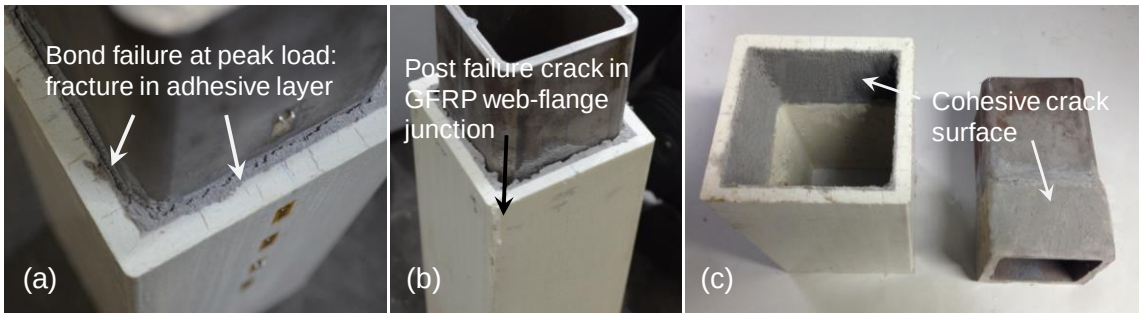

Figure 4.8. Failure modes of BSJs: (a) adhesive failure at peak load; (b) cracking of GFRP after peak load (BSJ-100-1 and BSJ-140-1); (c) bond failure surface.

[1] Load-displacement curves of all BSJs are provided in Section A.1.2 of Appendix.

4.4.2. Joint capacity versus bond length

Table 4.3 summarises the experimental joint capacities ($P_{u,E}$) of all BSJs and the corresponding FE estimates ($P_{u,FE}$). Except for the BSJ-50 specimens (where $P_{u,E}/P_{u,FE}$ = 0.761), the FE modelling compared well to the experimental results with differences less than 13%. For all BSJs, the overestimation by FE modelling may be due to the fact that the bilinear bond-slip relationship adopted in the FE analysis was derived from a plate-to-block single lap joint configuration [36], while the square tubular geometry of the BSJs imposed higher levels of through-thickness stress within the adhesive layer. This complex stress state in the adhesive, although dominated by shear stress, may advance expected bond failure. To account for the existence of the through-thickness stress in addition to the shear stress in the adhesive layer, application of a mixed-mode (mode I and mode II) bilinear bond behaviour in the numerical modelling [59] may represent the experiment scenario more accurately. However, this requires determination of the cohesive parameters of both mode I and mode II [60]; while further experimental calibration is needed to acquire the mode I parameters for this study. It should also be noted that implementation of the mixed-mode model in the contact behaviour often encounters with convergence difficulty for the 3-D modelling as in this study although such mixed-mode bond behaviour was successfully applied in 2-D FE modelling [59]. The overestimation of joint capacities can also be attributed to the thicker adhesive layer at the corners (due to the round corners of the steel SHS) where local bond strength may be compromised. Joint capacities $P_{u,E}$ and $P_{u,FE}$ versus bond length (L) are plotted in Figure 4.9. The increase in $P_{u,E}$ with L slowed dramatically after around $L = 100$ *mm*, which was successfully captured by the FE modelling, indicating an effective bond length of 100 mm.

Table 4.3. Comparison of experimental and FE joint capacity of BSJs.

Bond length	**Experimental joint capacity $P_{u,E}$ (kN)**			**FE joint capacity**	**Accuracy**
***L* (mm)**	1	2	Average	**$P_{u,FE}$ (kN)**	**($P_{u,E}/P_{u,FE}$)**
50	155	166	160.5 (± 3.4%)	211	0.761
100	303	266	284.5 (± 6.5%)	323	0.881
140	327	278	302.5 (± 8.1%)	346	0.875
180	326	346	336.0 (± 3.0%)	350	0.960

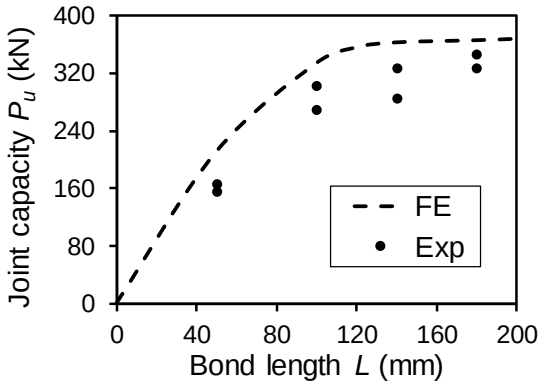

Figure 4.9. Experimental and FE results of axial joint capacity versus bond length.

4.4.3. Strain Responses

The specimen BSJ-180-2 sustained the greatest axial load of all the BSJs. Its load-strain responses recorded by strain gauges outside the bond region (G1 and G8) are plotted in Figure 4.10. The linear responses and the strain values indicated that both the steel and the GFRP adherends were within elastic range. From the same specimen, axial strains on the outer surface of the GFRP along the centre bond line, at four different load levels from FE modelling as well as experiment, are plotted in Figure 4.11. It is evident that the axial strain distribution at mid-portion of the bond length features a flatter gradient, revealing lower levels of shear stress in this region than at the ends of the bond length. In general, the axial strain distribution near the GFRP end of the bond length ($x = 180$ *mm*) exhibits a steeper gradient than at the steel end ($x = 0$ *mm*), matching anticipation that greater shear slip (δ) would occur near the more flexible adherend (GFRP in this case).

Also noteworthy is that in Figure 4.11 (d) (corresponding to 100% P_u) the strain distribution flattens near the GFRP end, indicating a drop of adhesive shear stress as a result of the GFRP end being loaded into the softening stage (see Figure 4.6). The discrepancy between the experimental and FE strain data derives from two main sources. One is approximation of the true bond-slip relationship into a bilinear shape; the other source is that the GFRP was approximated as uniform through its wall thickness, instead of its actual mat-roving-mat layered structure.

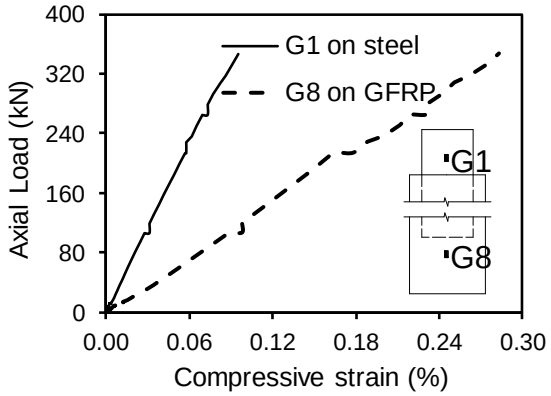

Figure 4.10. Load-strain behaviour from strain gauges installed outside bond area (BSJ-180-2).

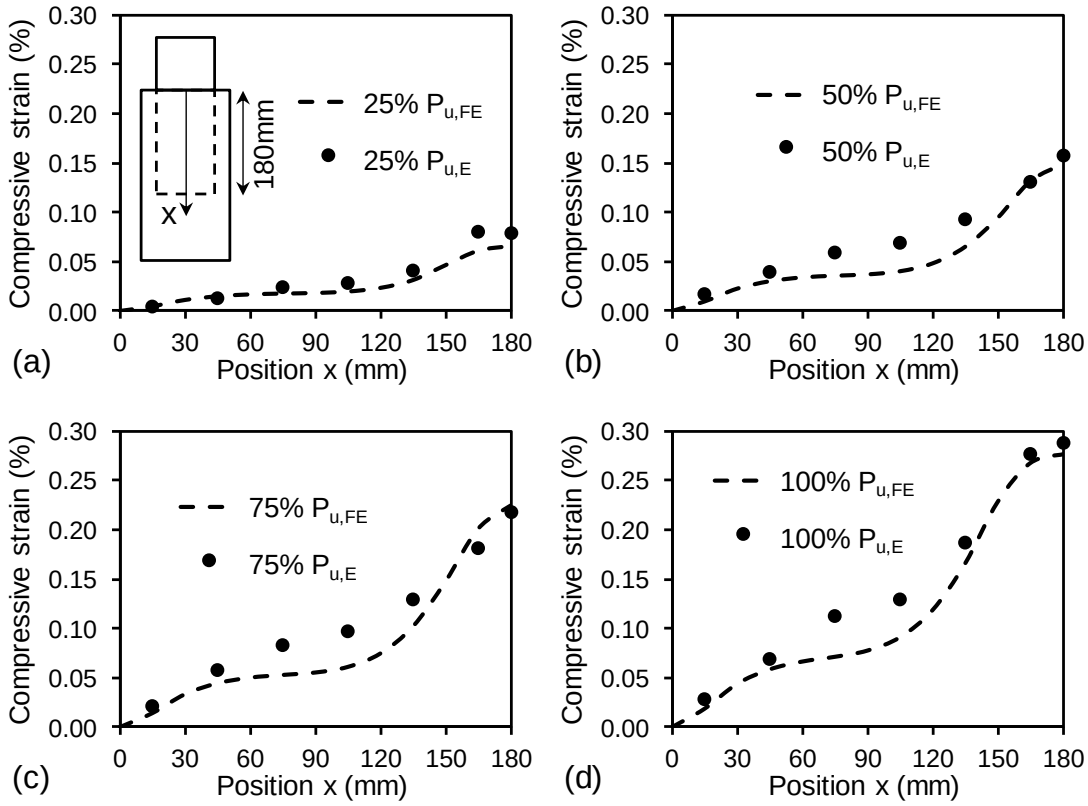

Figure 4.11. Experimental and FE results of axial strains on the outer surface of the GFRP along centre bond line (BSJ-180-2, positions of strain gauges indicated in Figure 4.2) at (a) 25% P_u; (b) 50% P_u; (c) 75% P_u; (d) 100% P_u.

4.4.4. Adhesive shear stress distribution

Figure 4.12 shows, from FE analysis, the distribution of adhesive shear stress along the centre bond line at four different load levels of BSJ-180 as a representation for all the BSJs. At 25% and 50% P_u, the full bond length is within the elastic stage of the bilinear bond-slip curve (Figure 4.6); the majority of the shear resistance is provided near the two ends of the bond line and the maximum shear stress (τ_f) appears at the GFRP end (x = *180 mm*, as the more flexible adherend). The increase of load from 50% to 75% P_u introduces a drop in shear stress near the GFRP end, due to its moving past the peak shear stress point (δ_1, τ_f) in the bilinear curve before entering the softening stage. As P increases further to 100% P_u, the softening length at the GFRP side extends inwards while the rest of bond length remains in the elastic stage.

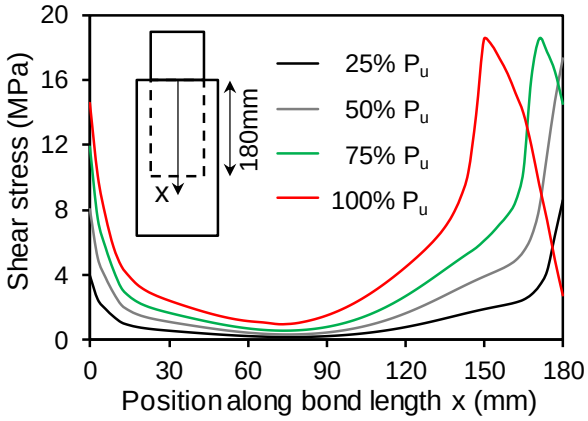

Figure 4.12. FE results of shear stress distribution along centre bond line at different load levels of BSJ-180.

Figure 4.13 presents, at peak loads, the FE results of shear stress distribution over the entire bond area for all the BSJs. In contrast to single/double lap joints or circular bonded sleeve joints, non-uniform adhesive shear stress in the BSJs is found in the transverse direction (z direction). Generally, higher shear slip (δ) is induced further from the centre bond line, due to the greater rigidity at the corners of the tubular adherends than in the flat wall regions. The gradient of the transverse variation is flatter near the two longitudinal ends ($x = 0$ *mm* and *180 mm*) and steeper inwards. The transverse variation of shear stress is implicitly evidenced by the experimental load-strain curves (BSJ-180-1) shown in Figure 4.14; consistent with the FE output, the GFRP axial strains closer to the transverse corner of the adherend (GR2 and GR3) are greater than those along the centre bond line (G2 and G3).

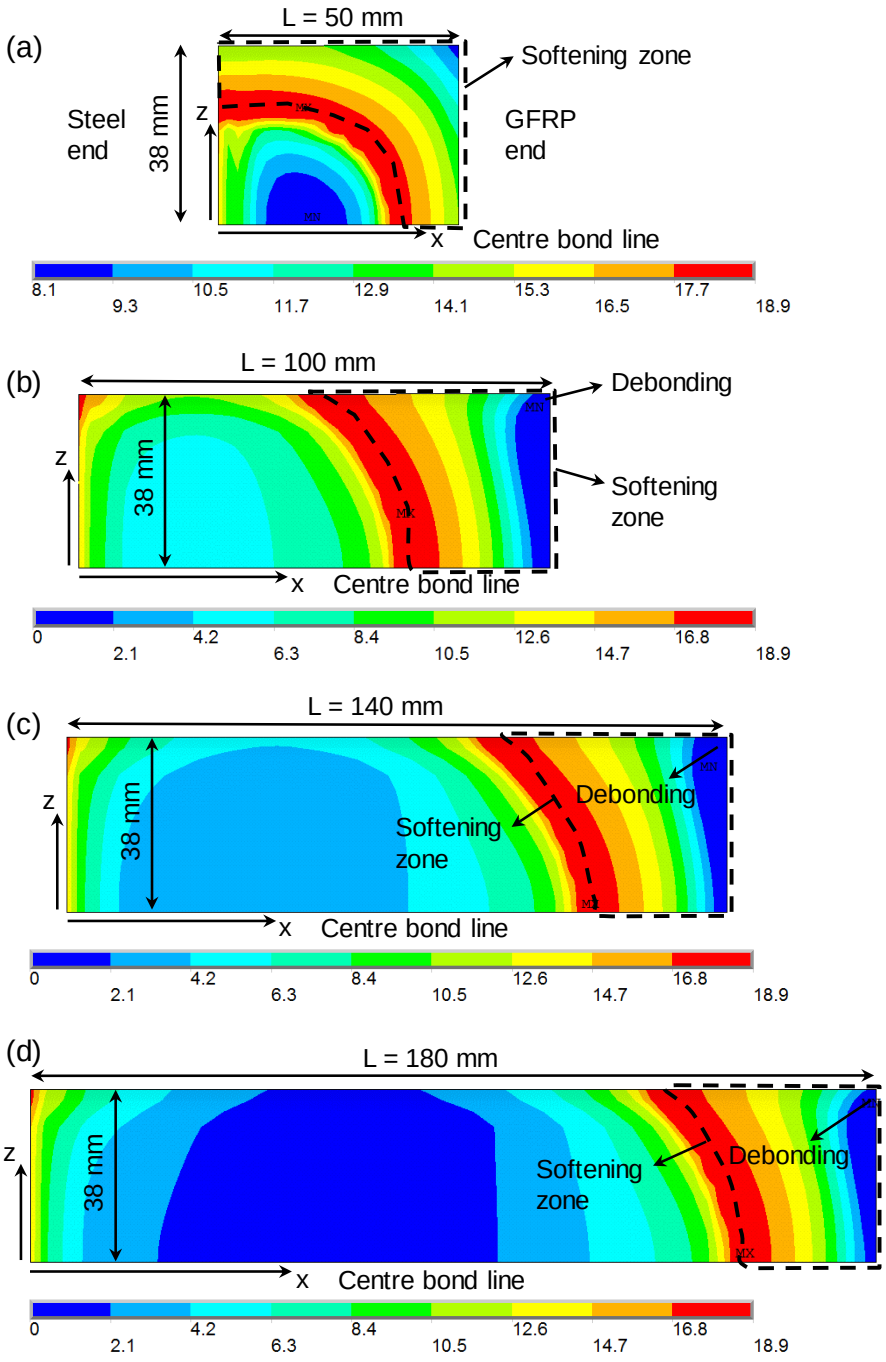

Figure 4.13. Adhesive shear stress distribution from FE modelling at peak load: (a) BSJ-50; (b) BSJ-100; (c) BSJ-140; (d) BSJ-180.

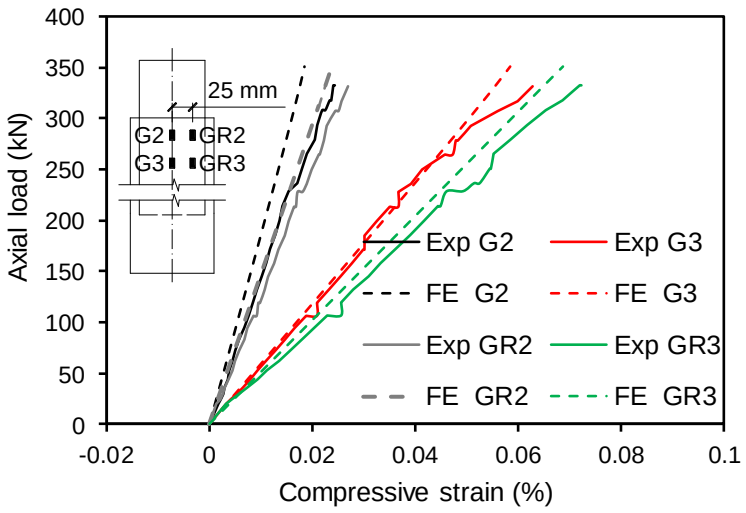

Figure 4.14. Comparison of strain responses from 25 mm-offset and centre strain gauges (BSJ-180-1).

In consideration of the shear stress distribution at peak load (100% P_u), the bond areas of the four BSJs could each be divided into two regions: a softening zone as highlighted in Figure 4.13 and the remaining elastic zone, the boundary between the regions being defined by a line of the peak shear stress τ_f. Figure 4.13 (a) presents a typical shear stress distribution at peak load with a short bond length (BSJ-50). Near the location where $z = 38\ mm$ (the adherend transverse corner), the full bond length is loaded into the softening stage of the bilinear curve. Figure 4.13 (b-d) share typical stress distributions for longer bond lengths (BSJ-100, 140, 180). Stress distribution along the x direction can generally be characterised by an elastic zone near the steel side and a softening zone near the GFRP side, with the debonding point of the bilinear curve (δ_f, *0*) attained at the GFRP end close to the transverse corners of the steel SHS (i.e. $z = 38\ mm$). In Figure 4.13 (b), (c), and (d), as the bond length increases, the softening zone does not exhibit notable change whereas the low-stress region in the elastic zone expands markedly. This observation signifies an inefficient increase in bond strength, thus implying the existence of an effective bond length.

4.5. Results and Discussion: Bolted Flange Joint (BFJ) Specimens

4.5.1. Failure Modes and Load-Displacement Behaviours

All the BFJ specimens failed through steel yielding with notable deformation of the flange-plates; no bolt deformation was visible but the nuts were found to loosen after loading. As shown in Figure 4.15, elongation of BFJ-4 (i.e. BFJ with four bolts) resulted in opening gaps between the two flange-plates in the region away from the bolts; while in BFJ-8, the flange-plates were bent outwards near the location welded with the SHS. Figure 4.16 presents the tensile load-displacement behaviours of the BFJs. After steel yielding, the load-displacement curves kept increasing gradually at near constant slopes until the loading process was ceased at 9mm elongation for the BFJ-4s or at 8mm for the BFJ-8s.

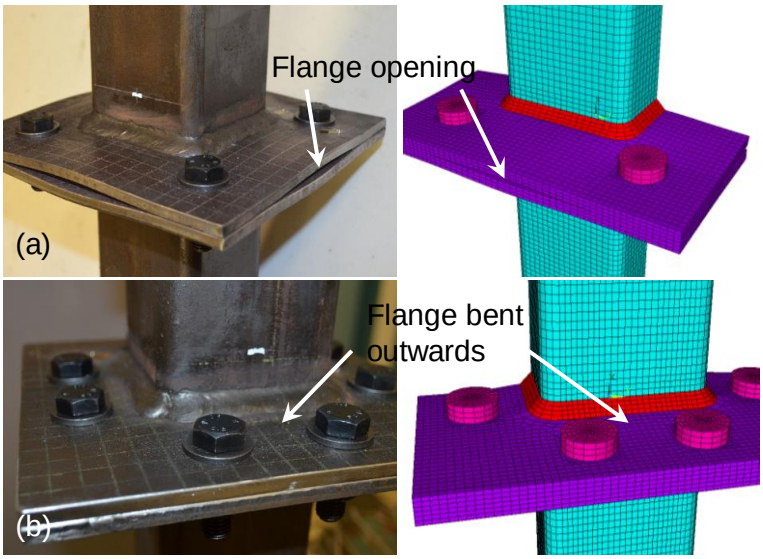

Figure 4.15. Experimental and FE deformed shapes of BFJ specimens (a) BFJ-4 at 6mm extension; (b) BFJ-8 at 5mm extension.

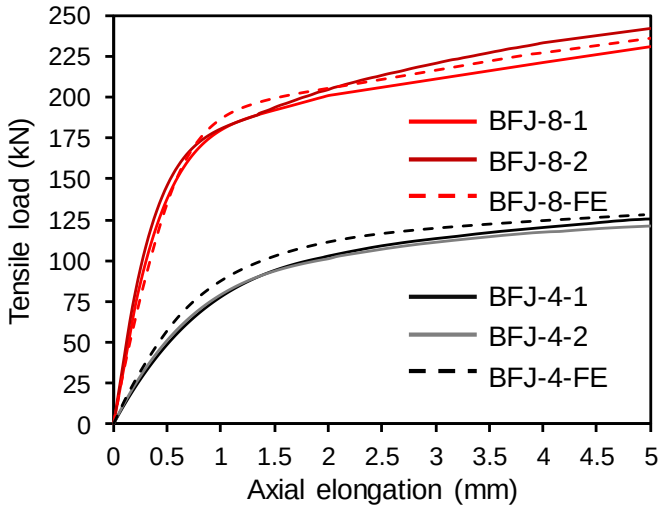

Figure 4.16. Experimental and FE tensile load-displacement behaviours of (a) BFJ-4 and (b) BFJ-8.

The initial stiffness of the BFJs (S_i) is defined as the slope of the linear stage of the load-displacement curves, and yield capacity (P_y) is determined by the intersection of the elastic and post-yield tangent lines. Both experimental and FE values of S_i and P_y are summarised in Table 4.4. From BFJ-4 to BFJ-8, an increase of four bolts improved the experimental stiffness ($S_{i,E}$) by 233% and the yield capacity ($P_{y,E}$) by 77%. Comparison between the FE and experimental results, presented in Figure 4.15 and Figure 4.16, shows that both the deformed shapes and the load-displacement behaviours were accurately captured by the FE modelling. As presented in Table 4.4, the FE results of stiffness ($S_{i,FE}$) are within 16% from experimental values, and the FE yield capacities ($P_{y,FE}$) within 8%. The slightly higher yield capacities obtained from the FE modelling may be a consequence of welding residual stress in the flange-plates of the experimental specimens.

Table 4.4. Comparison of yield capacity (P_y) and initial stiffness (S_i) of BFJs from experiment and FE modelling.

Specimen	$P_{y,E}$ (kN) [a, b]	$P_{y,FE}$ (kN) [b]	$P_{y,E}/P_{y,FE}$	$S_{i,E}$ (kN/mm) [a, c]	$S_{i,FE}$ (kN/mm) [c]	$S_{i,E}$ / $S_{i,FE}$
BFJ-4	104	113	0.920	104	117	0.889
BFJ-8	184	192	0.958	346	305	1.134

[a] Average value of the two repeating specimens

[b] intersection point of the load-displacement curve's elastic and post-yield tangent lines

[c] slope of the initial linear part of the load-displacement curve

4.5.2. Stress Distribution and Load-Strain Responses

Figure 4.17 depicts from FE modelling the distributions of stress state ratio (defined as the ratio of von Mises stress to yield stress) for BFJ-4 at 114 kN and BFJ-8 at 198 kN, where a ratio larger than 1.0 indicates yielding of steel at the position. These stress distributions reveal that, as the loads increased beyond the yield capacities of the BFJs, the high stress areas formed into a pattern, allowing continuous yielding and thereby causing large elongation deformation of the specimens. Figure 4.17 also presents the stress state of the bolts, indicating that the bolts were subjected to a combination of bending and tensile action, due to the prying effect from the deformed flange-plates. The bolts of BFJ-4 were found to be under greater stresses than those of BFJ-8, yet yielding was limited to less than 16% of the cross-section area of the bolt shank.

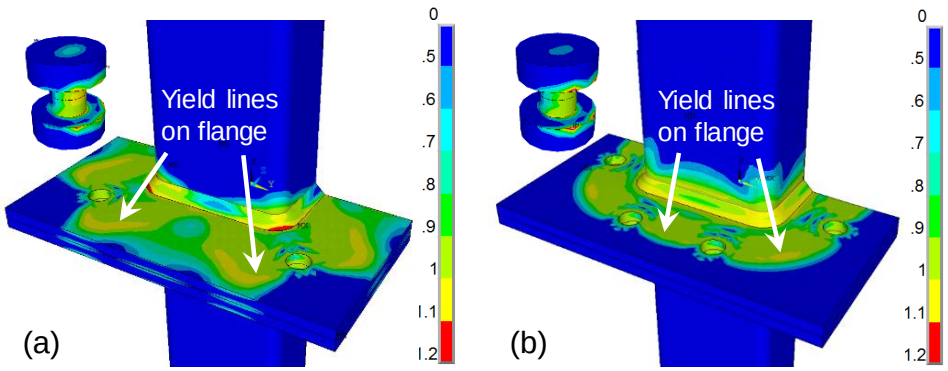

Figure 4.17. Von-Mises stress state (a) BFJ-4 at 114 kN; (b) BFJ-8 at 198 kN.

Both experimental and FE load-strain curves are plotted in Figure 4.18. As the strain gauges G3 to G5 were installed at highly stressed locations and orientations, their readings can indicate the yield initiation of the specimens. For BFJ-4 [Figure 4.18 (a)], the experimental G3 curve deviates from initial linearity at around 50 kN tensile load, which resembles the beginning of nonlinearity in the load-displacement curve [Figure 4.16 (a)]. Likewise for the BFJ-8, both the experimental G3 curve [Figure 4.18 (b)] and load-displacement curve [Figure 4.16 (b)] begin to exhibit nonlinearity at around 86 kN tensile load. The linear behaviour of G2 shown in Figure 4.18 (b) demonstrates that the SHS was within the elastic range for all the BFJs. Further, the experimental and FE load-strain curves show satisfactory agreement, especially when steel yielding has occurred.

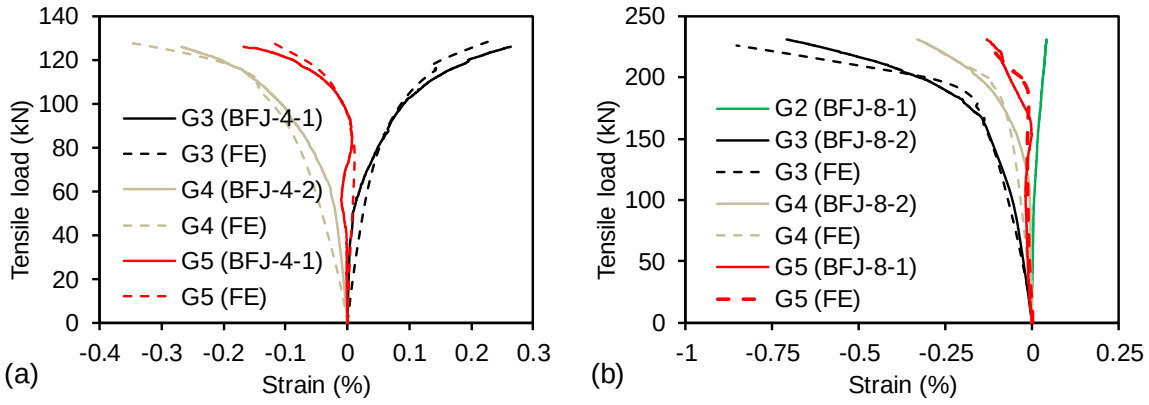

Figure 4.18. Experimental and FE load-strain responses of (a) BFJ-4 and (b) BFJ-8 (refer to Figure 4.3 for positions of strain gauges).

4.6. Integrated Performance of Proposed Splice Connection

Given the bonded sleeve joint (BSJ) and bolted flange joint (BFJ) investigated in prior sections, the experiment-validated FE modelling approaches can aid understanding of the performance of the proposed splice connection as an integration of BSJ and BFJ under axial loadings. Figure 4.19 presents the meshed FE model of a design example SC-180-8, namely a splice connection using 180 mm bond length and the BFJ-8 bolt configuration. The FE model of SC-180-8 incorporates all the features and details of BSJ-

180 and BFJ-8 described in Section 4.3, i.e. geometries (with the 15 mm-gap distance between the GFRP tube and steel flange-plate as described in Figure 4.1), element types, material properties and contact behaviours. The load-carrying performances of SC-180-8 in both tension and compression are also indicated in Figure 4.19.

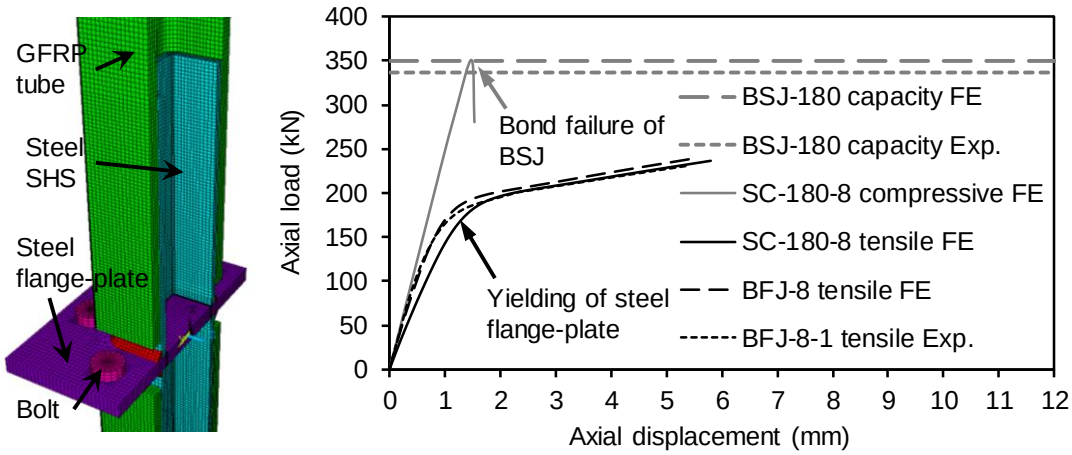

Figure 4.19. Meshed FE model of a tubular FRP splice connection SC-180-8 and indication of its axial load-carrying performance.

The tensile load-displacement behaviour of the design connection SC-180-8 is plotted as the black curve in Figure 4.19. It is confirmed that the yielding and the subsequent hardening behaviour of SC-180-8 coincide with those of BFJ-8 (FE shown as the black dashed curve and experimental as the black dotted curve), due to the same failure mode of flange-plate yielding. The initial stiffness of SC-180-8 differs from that of BFJ-8 due to the inclusion of the GFRP tube. With a gauged length of 640mm used in Figure 4.19, SC-180-8 exhibits slightly lower initial stiffness than BFJ-8. The ultimate load capacities of SC-180-8, both in tension and compression, are bounded by the axial joint capacity of BSJ-180, which is presented in Figure 4.19 as the horizontal dashed line from FE modelling and the horizontal dotted line from the experimental result. Generally, for other bond lengths and bolt configurations used with the splice connection, the tensile performance may show either brittle or ductile responses. The former happens when axial capacity of the BSJ is attained before yielding of the BFJ; and the resulting load-

displacement curve of the splice connection develops linearly before the brittle failure of the BSJ component. The latter takes place when yielding of the BFJ precedes failure of the BSJ as in the case of SC-180-8. In this case, the load-displacement curve flattens upon yielding of the BFJ component, and continues to develop at reduced stiffness until axial capacity of the BSJ is attained.

Behaviour of the connection SC-180-8 under compression loading is presented as the solid grey line in Figure 4.19. The compressive load-displacement curve ascends linearly until the axial capacity of BSJ-180 is reached, where the bond failure of the BSJ component occurs. Furthermore, design of the compressive performance of FRP tubular members with such a connection may also involve buckling of the FRP member or yielding of the steel SHS, depending on their geometries and material properties. The tensile behaviour of the designed splice connection, which is governed by that of BFJ-8, as discussed above, utilises yielding of the steel component, and therefore ductile performance before brittle bond failure is achieved. In this particular design, the yield load of BFJ-8 was approximately 55% of the ultimate load of BSJ-180, resulting in a ductility index of over 6.0 and a safety factor of 1.82. Nevertheless, further design could be optimized by adjusting the geometric parameters such as the bond length and position & number of the bolts, to better utilize the load capacity of the BSJ component.

4.7. Conclusions

A steel splice connection was developed to join tubular FRP members and its axial performance was investigated through experimental study and FE modelling. The two components of the splice connection, namely the bonded sleeve joint (BSJ) and bolted flange joint (BFJ), were first experimentally examined. FE modelling was performed to study and understand the failure modes, load-displacement behaviours and strain responses. Verified by experimental results, the FE modelling technique was applied to understand the axial performance of the proposed splice connection integrated by the BSJ and BFJ. From the present study, the following conclusions can be drawn:

1. **Failure and capacities of the BSJs**. Under axial loading, the BSJs failed in a brittle manner within the adhesive layer. Their load-displacement behaviour was linear

up to the peak load, followed by a sudden drop. Among the four bond length groups (50, 100, 140 and 180 mm), FE analysis employing the bilinear bond-slip relationship produced estimates of joint capacity mostly within 15%. An effective bond length of around 100mm was identified both experimentally and numerically for this joint configuration.

2. **Strain and stress distribution in the BSJs**. For the BSJ specimens, strain distribution on the GFRP surface indicated softening of the bond length at the GFRP end as the load increased and transverse variation of adhesive shear stress. The consistency between experimental and FE results for strain distribution further validated the FE modelling approach. Therefore the FE analysis provided insights into the adhesive shear stress distribution over the bond area. At peak loads, two types of shear stress distribution were identified. In the BSJ specimen with 50mm bond length (BSJ-50), the entire bond length near the adherend transverse corner was loaded into the softening stage. In other specimens with longer bond lengths (BSJ-100, 140 and 180), softening occurred near the GFRP side and the transverse corner of the GFRP end was loaded to the debonding point of the bilinear bond-slip relationship.

3. **Failure, capacities and stress distribution in the BSJs**. Failure of the BFJs was ductile through yielding of the flange-plates. The load-displacement responses could all be characterised as a 'linear ascending – yielding – linear hardening' process. The eight-bolt configuration (BFJ-4), compared to the four-bolt one (BFJ-4), improved the initial stiffness by 225% and the yield capacity by 82%. The FE modelling successfully captured the deformed shapes and produced load-displacement and load-strain responses that were in good comparison with experimental ones. The FE estimates of initial stiffness were within 14% of the experimental ones and those of yield capacity were within 8% of the experimental estimates. From review of the FE von Mises stress distributions on the flange-plates, the improvement in stiffness and yield capacity from BFJ-4 to BFJ-8 was revealed to be associated with a more optimal yield line mechanism which involved an enlarged yielding area.

4. **Behaviour of a complete splice connection**. The axial behaviours of a complete splice connection, integrating the BSJ and BFJ, could be studied through the

experiment-validated FE modelling approach. A FE model of a splice connection, integrating the BSJ with 180 mm bond length and the BFJ with eight bolts (SC-180-8), was developed, with its load-carrying performance verified by experimental data. The tensile behaviour of SC-180-8, involving yielding of the BFJ below the ultimate load of the BSJ, demonstrated that ductile failure could be achieved by utilising the yielding of the steel component.

4.8. Acknowledgements

The authors wish to acknowledge the support from the Australian Research Council through the Discovery scheme (DP180102208) and the project of innovation driven plan in Central South University, China (2015CX006). Thanks are also given to Mr Fujia Luo, and Mr Long Goh in the Civil Engineering Laboratory of Monash University, for their technical supports.

4.9. References

1. Keller T. Recent all-composite and hybrid fibre-reinforced polymer bridges and buildings. Progress in Structural Engineering and Materials. 2001;3(2):132-40.
2. Bakis C, Bank LC, Brown V, Cosenza E, Davalos J, Lesko J, et al. Fiber-reinforced polymer composites for construction-state-of-the-art review. Journal of Composites for Construction. 2002;6(2):73-87.
3. Hollaway L. A review of the present and future utilisation of FRP composites in the civil infrastructure with reference to their important in-service properties. Construction and Building Materials. 2010;24(12):2419-45.
4. Bank LC. Composites for Construction: Structural Design with FRP Materials. John Wiley & Sons, 2006.
5. Meyer R. Handbook of Pultrusion Technology. Springer Science & Business Media, 2012.
6. Bank LC, Gentry TR, Nuss KH, Hurd SH, Lamanna AJ, Duich SJ, et al. Construction of a pultruded composite structure: Case study. Journal of Composites for Construction. 2000;4(3):112-9.

7. Keller T. Use of fibre reinforced polymers in bridge construction. Zurich: International Association for Bridge and Structural Engineering (IABSE); 2003.
8. Benmokrane B, El-Salakawy E, El-Gamal S, Goulet S. Construction and testing of an innovative concrete bridge deck totally reinforced with glass FRP bars: Val-Alain Bridge on Highway 20 East. Journal of Bridge Engineering. 2007;12(5):632-45.
9. Keller T, Haas C, Vallée T. Structural concept, design, and experimental verification of a glass fiber-reinforced polymer sandwich roof structure. Journal of Composites for Construction. 2008;12(4):454-68.
10. Hagio H, Utsumi Y, Kimura K, Takahashi K, Itohiya G, Tazawa H. Development of space truss structure using glass fiber reinforced plastics. Proceedings: Advanced Materials for Construction of Bridges, Buildings, and Other Structures III, Davos, Switzerland, 2003.
11. Bai Y, Zhang C. Capacity of nonlinear large deformation for trusses assembled by brittle FRP composites. Composite Structures. 2012;94(11):3347-53.
12. Yang X, Bai Y, Ding F. Structural performance of a large-scale space frame assembled using pultruded GFRP composites. Composite Structures. 2015;133:986-96.
13. Awad ZK, Aravinthan T, Zhuge Y. Experimental and numerical analysis of an innovative GFRP sandwich floor panel under point load. Engineering Structures. 2012;41:126-35.
14. Satasivam S, Bai Y, Zhao X-L. Adhesively bonded modular GFRP web–flange sandwich for building floor construction. Composite Structures. 2014;111:381-92.
15. Satasivam S, Bai Y. Mechanical performance of bolted modular GFRP composite sandwich structures using standard and blind bolts. Composite Structures. 2014;117:59-70.
16. Wardenier J, Packer J, Zhao X, Van der Vegte G. Hollow Sections in Structural Applications. Netherlands: Cidect Zoetermeer, 2010.
17. Smith S, Parsons I, Hjelmstad K. Experimental comparisons of connections for GFRP pultruded frames. Journal of Composites for Construction. 1999;3(1):20-6.
18. Luo FJ, Bai Y, Yang X, Lu Y. Bolted Sleeve Joints for Connecting Pultruded FRP Tubular Components. Journal of Composites for Construction. 2016:04015024.

19. Luo FJ, Yang X, Bai Y. Member Capacity of Pultruded GFRP Tubular Profile with Bolted Sleeve Joints for Assembly of Latticed Structures. Journal of Composites for Construction. 2016;20(3):04015080.
20. Kwakernaak A, Hofstede J. Adhesive bonding: providing improved fatigue resistance and damage tolerance at lower costs. SAMPE Journal. 2008;44(5):6-15.
21. Keller T, Gürtler H. Quasi-static and fatigue performance of a cellular FRP bridge deck adhesively bonded to steel girders. Composite Structures. 2005;70(4):484-96.
22. Zhang Y, Vassilopoulos AP, Keller T. Stiffness degradation and fatigue life prediction of adhesively-bonded joints for fiber-reinforced polymer composites. International Journal of Fatigue. 2008;30(10):1813-20.
23. Wu C, Zhang Z, Bai Y. Connections of tubular GFRP wall studs to steel beams for building construction. Composites Part B: Engineering. 2016;95:64-75.
24. Zhang Z, Wu C, Nie X, Bai Y, Zhu L. Bonded sleeve connections for joining tubular GFRP beam to steel member: Numerical investigation with experimental validation. Composite Structures. 2016;157:51-61.
25. Kurobane Y. Design Guide for Structural Hollow Section Column Connections. Verlag TUV Rheinland, 2004.
26. Standards Australia. AS4100 steel structures. Sydney (SA); 1998.
27. Ranisch E-H. Zur Tragfähigkeit von Verklebungen zwischen Baustahl und Beton: geklebte Bewehrung: Inst. für Baustoffe, Massivbau und Brandschutz der Techn. Univ.; 1982.
28. Brosens K, Van Gemert D. Plate end shear design for external CFRP laminates. AEDIFICATIO Publishers, Fracture Mechanics of Concrete Structures. 1998;3:1793-804.
29. Yuan H, Wu ZS, Yoshizawa H. Theoretical solutions on interfacial stress transfer of externally bonded steel/composite laminates. J Struct Mech Earthquake Eng, Japan Society of Civil Engineers, Tokyo. 2001(675):27-39.
30. Wu Z, Yuan H, Niu H. Stress transfer and fracture propagation in different kinds of adhesive joints. Journal of Engineering Mechanics. 2002;128(5):562-73.
31. Yuan H, Teng J, Seracino R, Wu Z, Yao J. Full-range behavior of FRP-to-concrete bonded joints. Engineering Structures. 2004;26(5):553-65.

32. Nakaba K, Kanakubo T, Furuta T, Yoshizawa H. Bond behavior between fiber-reinforced polymer laminates and concrete. ACI Structural Journal. 2001;98(3):359-67.
33. Wu Z, Yin J. Fracturing behaviors of FRP-strengthened concrete structures. Engineering Fracture Mechanics. 2003;70(10):1339-55.
34. Xia S, Teng J. Behaviour of FRP-to-steel bonded joints. Proceedings of the international symposium on bond behaviour of FRP in structures. International Institute for FRP in Construction, 2005. p. 419-26.
35. Fawzia S, Zhao X-L, Al-Mahaidi R. Bond–slip models for double strap joints strengthened by CFRP. Composite Structures. 2010;92(9):2137-45.
36. Yu T, Fernando D, Teng J, Zhao X. Experimental study on CFRP-to-steel bonded interfaces. Composites Part B: Engineering. 2012;43(5):2279-89.
37. Campilho R, De Moura M, Domingues J. Using a cohesive damage model to predict the tensile behaviour of CFRP single-strap repairs. International Journal of Solids and Structures. 2008;45(5):1497-512.
38. Alfano G, Crisfield M. Finite element interface models for the delamination analysis of laminated composites: mechanical and computational issues. International Journal for Numerical Methods in Engineering. 2001;50(7):1701-36.
39. Alfano G. On the influence of the shape of the interface law on the application of cohesive-zone models. Composites Science and Technology. 2006;66(6):723-30.
40. Campilho R, Banea MD, Pinto A, da Silva LF, De Jesus A. Strength prediction of single-and double-lap joints by standard and extended finite element modelling. International Journal of Adhesion and Adhesives. 2011;31(5):363-72.
41. Qiu C, Feng P, Yang Y, Zhu L, Bai Y. Joint capacity of bonded sleeve connections for tubular fibre reinforced polymer members. Composite Structures. 2017;163:267-79.
42. Kato B, Mukai A. Bolted tension flanges joining square hollow section members. Journal of Constructional Steel Research. 1985;5(3):163-77.
43. Packer JA, Bruno L, Birkemoe PC. Limit analysis of bolted RHS flange plate joints. Journal of Structural Engineering. 1989;115(9):2226-42.

44. Willibald S, Packer J, Puthli R. Experimental study of bolted HSS flange-plate connections in axial tension. Journal of Structural Engineering. 2002;128(3):328-36.
45. Packer J, Sherman D, Lecce, M. Design Guide 24: Hollow Structural Section Connections. Chicago, IL: American Institute of Steel Construction (AISC), 1997.
46. EN 1993-1-8. Eurocode 3: design of steel structures, part 1-8: design of joints. Bryssels: CEN; 2005.
47. Heinisuo M, Ronni H, Perttola H, Aalto A, Tiainen T. End and base plate joints with corner bolts for rectangular tubular member. Journal of Constructional Steel Research. 2012;75:85-92.
48. Wang Y, Zong L, Shi Y. Bending behavior and design model of bolted flange-plate connection. Journal of Constructional Steel Research. 2013;84:1-16.
49. Wheeler A, Clarke M, Hancock G. FE modeling of four-bolt, tubular moment end-plate connections. Journal of Structural Engineering. 2000;126(7):816-22.
50. Teng J, Fernando D, Yu T, Zhao X. Treatment of steel surfaces for effective adhesive bonding. In: Advances in FRP Composites in Civil Engineering. Springer, 2011. p. 865-8.
51. Satasivam S, Bai Y, Yang Y, Zhu L, Zhao X-L. Mechanical performance of two-way modular FRP sandwich slabs. Composite Structures. 2018;184:904–16.
52. Xie L, Bai Y, Qi Y, Caprani C, Wang H. Effect of width–thickness ratio on capacity of pultruded square hollow polymer columns. Proceedings of the Institution of Civil Engineers - Structures and Buildings. 2018;171(11):842-854.
53. ASTM International. Standard Test Method for Tensile Properties of Polymer Matrix Composite Materials. ASTM D3039. West Conshohocken, PA.2014.
54. ASTM International. Standard Test Method for Short-Beam Strength of Polymer Matrix Composite Materials and Their Laminates. ASTM D2344. West Conshohocken, PA.2016.
55. Lee S, Munro M, Scott R. Evaluation of three in-plane shear test methods for advanced composite materials. Composites. 1990;21(6):495-502.
56. ASTM International. Standard Test Methods and Definitions for Mechanical Testing of Steel Products. ASTM A370-16. West Conshohocken, PA. 2016.

57. ASTM International. Standard Test Method for Tensile Properties of Plastics. ASTM D638-10. West Conshohocken, PA. 2010.
58. Trahair N, Bradford M. The Behaviour and Design of Steel Structures to AS 4100. Third Edition. Taylor & Francis; 1998.
59. Da Silva LF, Campilho RD. Advances in numerical modelling of adhesive joints. Advances in Numerical Modeling of Adhesive Joints: Springer; 2012. p. 1-93.
60. Lee MJ, Cho TM, Kim WS, Lee BC, Lee JJ. Determination of cohesive parameters for a mixed-mode cohesive zone model. International Journal of Adhesion and Adhesives. 2010;30(5):322-8.

CHAPTER 5. PERFORMANCE OF THE SPLICE CONNECTION UNDER FLEXURAL LOADING

Declaration for the Chapter

Chapter 5 of the thesis presents the following published work in a re-formatted form:

Qiu C, Bai Y, Zhang L, Jin L. Bending performance of splice connections for assembly of tubular section FRP members: Experimental and numerical study. Journal of Composites for Construction. 2019;23(5):04019040. https://doi.org/10.1061/(ASCE)CC.1943-5614.0000964

Permission has been obtained from the publisher *American Society of Civil Engineers (ASCE)* to include the article, in its published form or in a re-formatted form, in this thesis.

The student's and the co-authors' contribution to the work is listed in the following table:

Name of author	Nature of contribution	Contribution (%)
C Qiu (the student)	Conceptualisation, methodologies, experimental work, numerical modelling, data analysis, writing-up, revision	70%
Y Bai	Conceptualization, methodologies, review and revision, financial support	20%
L Zhang	Review and revision	5%
L Jin	Review and revision	5%

The undersigned hereby certify that the above declaration correctly reflects the nature and extent of the student's and co-authors' contribution to this work.

Student (Chengyu Qiu) signature: Main supervisor (Yu Bai) signature:

Date: Date:

Link of the Published Work to the Thesis

The published work presents experimental and numerical studies on the proposed splice connection (Figure 2.18) under flexural loading.

Abstract

This paper presents experimental and numerical investigations of the bending performance of innovative splice connections developed for tubular section FRP members. Each of the splice connections consists of a steel bolted flange joint between two tubular steel-FRP bonded sleeve joints. Three connection specimens with different bolt configurations or bond lengths are prepared and tested under four-point bending. Finite element (FE) models are developed featuring a mixed-mode bilinear traction-separation relation for the adhesive bond, the Tsai-Wu failure criterion for the FRP, and yielding of the steel components. The contact behaviour and bolt pre-tensioning are also modelled in detail. All of the connection specimens exhibit excellent ductility through yielding of the steel flange-plate before ultimate failure. The FE modelling, validated by the experimental failure mode, moment-rotation behaviour, and strain response, provides insight into the adhesive stress distribution and the yielding mechanism of the steel flange-plates. According to Eurocode 3 for steel structures, the connection specimens are all classified as semirigid and partial-strength connections. The results also show that under flexural loading, the splice connections, which have ductility indices between 5.7 and 8.4, are able to impart ductility to a structure made of brittle FRP members.

Keywords: Fibre reinforced polymer (FRP); Tubular section member; Splice connection; Bolted flange joint; Bonded sleeve joint; Ductility.

5.1. Introduction

The past two decades have seen increasing application of fibre reinforced polymer (FRP) composites in civil engineering structures. These lightweight and corrosion-proof materials have gained recognition worldwide through applications in the rehabilitation and strengthening of existing structures [1, 2]. Due to the moderate cost of glass fibres

and advances in the pultrusion manufacturing technique [3], FRP composites also have a great potential as load-bearing members in new construction. Examples include bridge decks [4], beams [5], columns [6], and floor systems [7]. Connection designs for these members should consider the brittle and anisotropic nature of FRP materials. Mosallam [8] provided major references for FRP composite connections, primarily for plates and I-section members. Additional studies may be needed for tubular section members which have the added advantage of efficient resistance against torsional and global buckling [9].

The closed section shape of tubular members poses an additional challenge for connection design; regardless, several connection methods have been proposed and studied. Various types of bolted connections have been developed and compared for FRP beam-to-column assemblies with tubular sections [10]. To assemble tubular FRP members into space lattice structures, a steel-FRP bolted sleeve joint configuration was proposed and tested under axial loading [11]. These bolt-fastening methods caused stress concentrations around the drilled holes and exposed the weak in-plane shear strength of the FRP members. In contrast, adhesive bonds maintain the integrity of the FRP composites (without drilling holes), alleviate the stress concentrations and adapt well to curved surfaces. In a recent study by Ascione et al. [12], full adhesive FRP beam-column connections were shown to be more advantageous in stiffness and moment capacity than bolted connections. Smith et al. [10] proposed a cuff connector for tubular section members that integrated the FRP beam and column into a monolithic unit with adhesive bond. An experimental study of these bonded cuff connections [13] revealed up to 57% increase in the moment capacity compared with connections with bolted cuffs. Subsequently, a bonded sleeve connection with a steel endplate was designed to join tubular FRP beams to steel columns [14]. Improved rotational stiffness, moment capacity, and ductility were demonstrated over steel seated angle connections and bolted sleeve connections. This bonded sleeve connection was later adapted for all FRP beam-to-column assemblies and evaluated under static [15] and cyclic [16] loadings. The tubular FRP-steel bonded sleeve connection was also adopted in spatial trusses to connect circular FRP tubes to steel Octatube nodal joints [17].

The steel-FRP bonded sleeve joint (BSJ) can be adapted to provide a splicing solution that is needed to apply tubular section FRP members in building structures and

in long-span scenarios. Previous studies of adhesively bonded FRP-steel [18-20] and FRP-FRP joints [21] could be useful references to gain an understanding of the bond behaviour in BSJs. To integrate BSJs into a splice connection, the bolted flange joint (BFJ) offers a solution for splicing the steel tubular members. The axial and flexural behaviours of BFJs have been subjects of extensive research. For tensile scenarios, yield line mechanisms were proposed by Kato and Mukai [22] to derive the load capacities of BFJs with one or two bolts on each side of the square hollow section (SHS). BFJs of similar configurations were also studied under tension [23] but with a focus on bolt failure. Focusing on bending performance, yield line mechanisms were developed to derive the moment capacities of four-bolt (one at each corner) [24] and eight-bolt (two at each side of the SHS) [25] configurations. The effect of stiffeners on the eight-bolt configuration was studied by Wang et al. [26] using experimental testing and FE modeling, based on which simplified yield line method was proposed.

To date, splice connections for FRP members, especially those with tubular sections, have been the focus of limited research. Beam splices formed by bonded or bolted lap plates have been developed for I-sections [27-29] and square tubular section members [30]. However, these studies primarily focused on the serviceability or fatigue behaviour; the ultimate capacities and corresponding failure modes were not clearly understood. To address this research need, a splice connection for tubular FRP members [Figure 5.1 (a)] that integrates two BSJs and a BFJ was proposed [31]. The stress concentration in the FRP members is reduced by the bonded joints (compared with bolt-fastening), and convenient on-site assembly and ductile failure can be realized by the BFJ. In this configuration, limited steel parts are exposed (the flange-plates and the bolts); to protect against corrosion galvanized parts can be used or surface coating can be easily applied. In addition to a general column or beam splice to extend the member continuity, another potential application of the splice connection is to enable the assembly of FRP modular building units [Figure 5.1 (b)]. As in modular steel construction [32], the ceiling and floor beams (where partition walls may be attached) of two adjacent stories are connected, respectively, to the lower and upper columns spliced by the connection. The research gap and the potential applications of this splice connection require understanding of its stiffness, strength, and ductility under flexural loading.

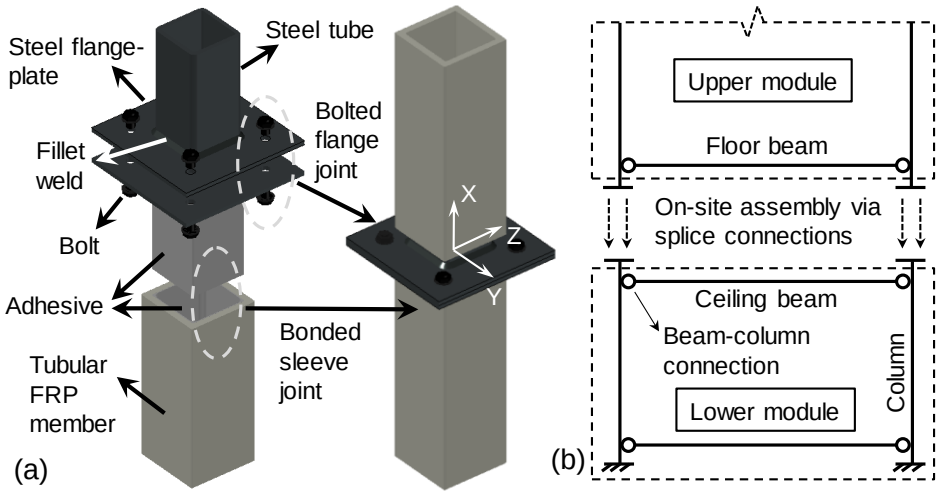

Figure 5.1. (a) Proposed splice connection for tubular section FRP members; and (b) potential application to FRP modular buildings.

Therefore, this paper presents experimental and numerical investigations of the bending performance of the splice connection described in Figure 5.1. Three specimens with different bolt configurations or bond lengths are tested under four-point bending. Detailed three-dimensional FE modelling is also conducted. The experimental results are discussed and compared with the FE modelling in terms of the failure mode, moment-rotation behaviour, and local strain response. Finally, the performance of the splice connection specimens is discussed respecting the rotational stiffness, moment capacity, and ductility.

5.2 Experiment

5.2.1. Specimens

The splice connection specimens were indexed in the format *B-x-y*, where the first letter *B* refers to the bending loading; *x* denotes the bond length of the steel-FRP bonded sleeve joint in mm; and *y* is the number of bolts. Three types of connection specimens, with one specimen per type, were prepared: B-170-4, B-170-8, and B-120-8. The configuration

and dimensions of each specimen are illustrated in Figure 5.2 and Figure 5.3. A grade 355 steel square tube (80×80×6 mm) was joined to a 6-mm-thick grade 250 steel flange-plate (Figure 5.3) by fillet welds with a leg length of approximately 6 mm. The other end of the steel tube was coaxially coupled into and bonded to a pultruded glass fibre reinforced polymer (GFRP) square tube (102×102×9.5 mm) with Sikadur-330, a two-component epoxy-based adhesive. To achieve optimal bonding, the surface treatment of the steel and GFRP followed a procedure of degreasing, grit-blasting, and solvent cleaning before the adhesive was applied. The bonded assembly was cured for 2 weeks at room temperature. Before the experimental testing, two of the bonded assemblies were fastened together at the steel flange-plates with M12 grade 8.8 bolts (with washers and nuts), each of which was pretensioned to approximately 65 kN by a torque wrench to qualify as tension-tight according to AS1998 [33].

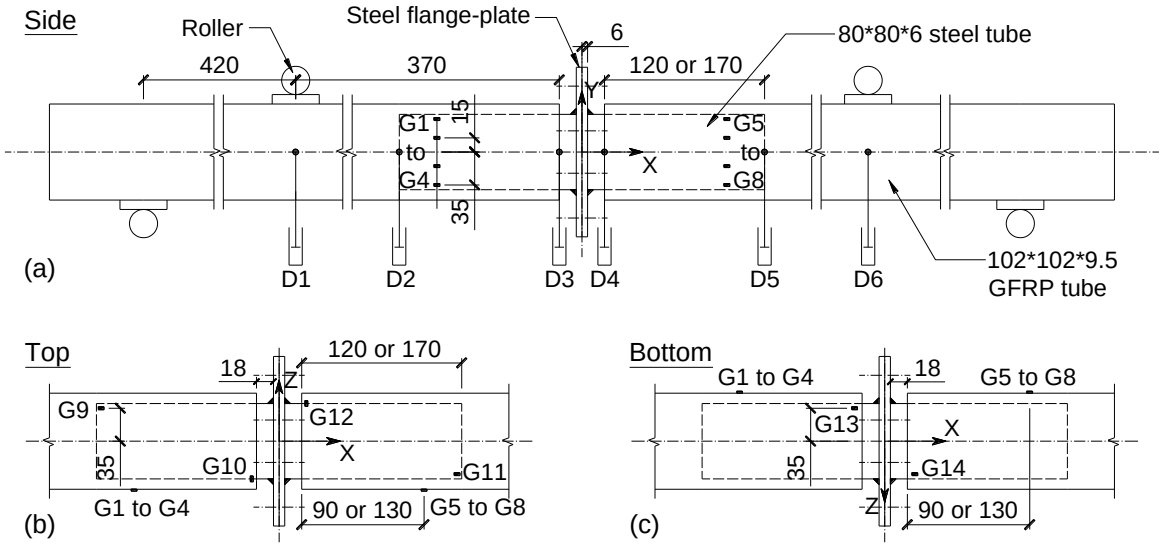

Figure 5.2. Dimensions of specimens and instrumentation: (a) side view; (b) top view; and (c) bottom view (all dimensions in mm).

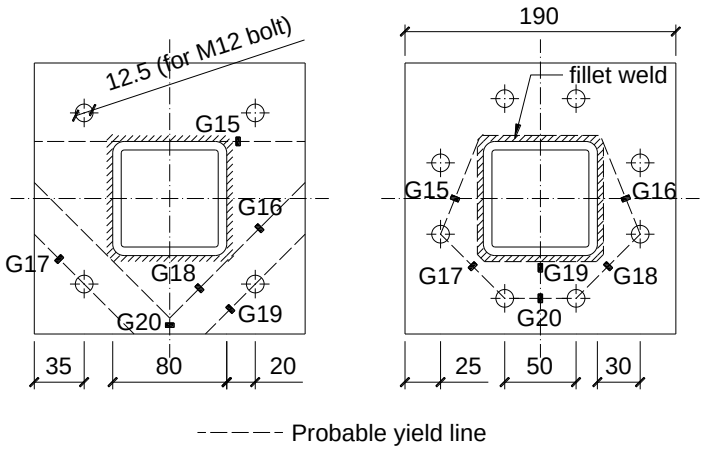

Figure 5.3. Dimensions of steel flange-plates with four (B-170-4) and eight (B-120-8 and B-170-8) bolts and the positions of the strain gauges (all dimensions in mm).

5.2.2. Material Properties

The pultruded GFRP square tubes, supplied by EXEL Composites, consist of E-glass fibres embedded in a polyester matrix. The strength and modulus properties of the GFRP are summarized in Table 5.1, and the corresponding test methods [34-37] are referenced in the fourth column [1]. The material properties of the steel tube and flange-plate, summarized in Table 5.2, were determined from tensile coupon tests following ASTM A370 [38][2]. The M12 bolt had a yield strength of 1,043 MPa and a Young's modulus of 235 GPa, as reported in an earlier study [39]. Under the tensile test in accordance with ASTM D638 [40], the Sikadur-330 adhesive exhibited a linear load-displacement behaviour. The average tensile strength ($f_{t,a}$) was recorded as 32.2 MPa with an elastic modulus (E_a) of 4.25 GPa and a Poisson's ratio (v_a) of 0.28 [3]. Notched beam specimens of the Sikadur-330 adhesive, which were tested under three-point bending as per ASTM D5045 [41], showed an average mode I fracture energy (G_I^{cr}) of 0.887 kN/m[4]. To accurately represent the material properties, the tensile and notched beam specimens of

[1] More information of the material testing of the GFRP is provided in Section A.2.1 – A.2.4 of Appendix.
[2] More information of the material testing of the steel flange-plate is provided in Section A.2.5 of Appendix.
[3] More information of the tensile testing of the adhesive is provided in Section A.2.6 of Appendix.
[4] More information regarding the determination of the fracture energy is provided in Section A.2.7 of Appendix.

the adhesive were cured in the same environment for the same period of time as the connection specimens.

Table 5.1. Strengths and moduli of the GFRP material.

Orientation and component	**Strength (MPa)**	**Modulus (GPa)**	**Test method**
Longitudinal tensile	330.6 ± 19.4	25.2 ± 1.3	ASTM D3039 [34]
Longitudinal compressive	330.6	-	Taken equal to the longitudinal tensile
Transverse flexural	88.5 ± 6.5	6.2 ± 1.2	ASTM D7264 [35]
Transverse tensile	88.5	-	Taken equal to the transverse flexural [a]
Transverse compressive	103.0	-	From the manufacturer's datasheet
Interlaminar shear	31.2 ± 1.9	-	ASTM D2344 [36]
In-plane shear	27.6 ± 1.7	3.0 ± 0.3	10° off-axis tensile test [37]

[a] Transverse samples too short for tensile testing.

Table 5.2. Strengths and moduli of the steel materials.

Steel component	**Yield strength (MPa)**	**Ultimate strength (MPa)**	**Young's modulus (GPa)**	**Poisson's ratio**
80×80×6 mm SHS [a]	420.1 ± 5.9 [b]	519.4 ± 8.4	209.5 ± 3.9	0.28 ± 0.1
6-mm-thick flange	311.8 ± 1.7	455.2 ± 2.0	201.2 ± 2.1	0.28 ± 0.1

[a] Tensile coupon samples cut from walls of the tube.

[b] 0.2% offset yield strength.

5.2.3. Loading Setup and Instrumentation

To specifically characterize the rotational stiffness and moment capacity, a four-point bending setup (Figure 5.2 and Figure 5.4) was adopted which subjected the splice connection to pure and uniform moment loading. For each specimen, 14 strain gauges

(G1–G14) were attached on the GFRP tubes as shown in Figure 5.2. The other six strain gauges (G15–G20) on the steel flange-plates (Figure 5.3) were positioned and oriented across the probable yield lines based on the FE analysis. Six displacement gauges (D1–D6, linear variable differential transducers or string pots) were deployed at the positions shown in Figure 5.2 to measure the deflection of the specimens. Using a 200 kN-capacity Amsler machine, four-point bending of the specimens was applied by locking the two uppers rollers while lifting the two lower ones at a rate of 1.5 mm/min (Figure 5.4).

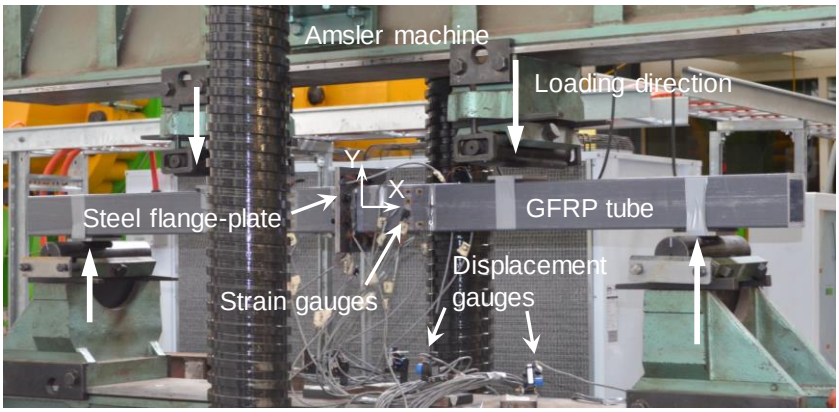

Figure 5.4. Four-point bending experiment setup for all specimens.

5.3. Finite Element Modelling

5.3.1. Geometries, Element Types, and Material Models

The finite element (FE) modelling was performed using the ANSYS Mechanical APDL package. A representative meshed model is presented in Figure 5.5 (a), where half of the geometry was constructed due to symmetry about the XZ plane. Three-dimensional eight-node solid elements (SOLID185) were used to mesh the GFRP and the steel components. The GFRP was defined as an orthotropic linear elastic material with its longitudinal direction aligned with the X axis [Figure 5.5 (a)]. The longitudinal, transverse, and shear moduli shown in Table 5.1 were employed to define the GFRP material. The steel components were modelled with isotropic multilinear hardening properties to simulate

the stress-strain curves obtained from the tensile coupon tests. The fillet weld that joined the steel tube to the flange-plate was assumed to be the same material as the latter.

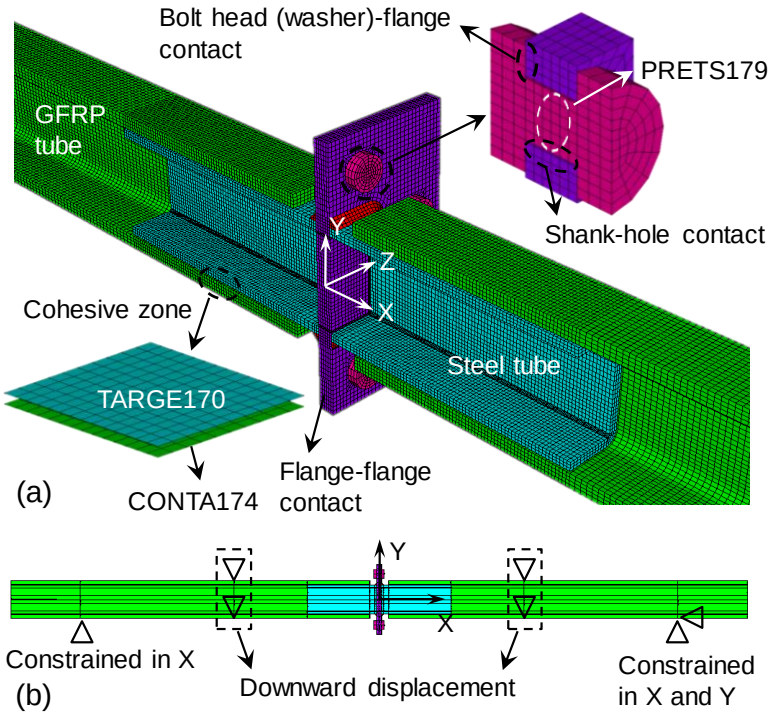

Figure 5.5. Detailed FE modelling: (a) representative meshed model (B-170-8) with cohesive zone modelling and contact behaviour; and (b) boundary conditions to simulate four-point bending.

The contact between the bolt-fastened parts (the flange-plates and the bolts) was modelled by a pair of four-node surface-to-surface contact elements, CONTA174 and TARGE170, applied to the potential contact surfaces. Three pairs of potential contacts were included and are highlighted in Figure 5.5 (a): between the flange-plates, between the bolt shank and the flange-plate, and between the bolt head (washer) and the flange-plate. A steel-to-steel friction coefficient of 0.44 was adopted [42]. Pre-tension in the bolts was applied through PRETS179 elements defined at the midsections of the bolt shanks [Figure 5.5 (a)]. The boundary conditions that simulate a four-point bending scenario are indicated in Figure 5.5 (b) except for the symmetric constraint applied on the

XZ cut plane. Pre-tensioning of the bolts was solved in the first load step before the four-point bending in the second load step.

5.3.2. Bond Behaviour between Steel and FRP

The bond behaviour between the steel and the GFRP was defined through the cohesive zone modelling (CZM) that utilizes both strength and energy criteria to characterize the debonding process on a pre-defined path or plane [43]. A pair of 3D four-node surface-to-surface contact elements, CONTA174 and TARGE170, was superposed on the bonded surface of the steel and GFRP, respectively [Figure 5.5 (a)]. Deformation and cracking of the adhesive layer was modelled by the interaction between the contact pair. Representing the thickness of the adhesive layer, the pair of contact elements was initially separated by 1.5 mm but with enforcement of contact interaction. Because the flexural loading on the bonded sleeve joint presents a combination of shear and normal stresses on the adhesive layer, the interaction between the contact pair was defined with mixed-mode softening initiation and propagation. Mode I behaviour of the adhesive layer was modelled by a normal traction-separation relation between the contact pair, whereas modes II and III, which are both represented by the tangential separation between the contact pair, were modelled by the traction-separation relation referred to as mode II or tangential in this study. As depicted in Figure 5.6, in each pure mode (mode I or II), the traction-separation relation between the contact pair followed a bilinear elastic-softening curve, which has been used for brittle adhesives with sufficient accuracy [18]. The bilinear curve of each pure mode is defined by three parameters: the critical peel or shear stress (σ_I^{cr} or σ_{II}^{cr}), the corresponding separation (δ_I^{cr} or δ_{II}^{cr}), and the debonding separation (δ_I^f or δ_{II}^f). The critical fracture energy of each mode is G_I^{cr} or G_{II}^{cr}, which is calculated as the area under the bilinear curve. Initiation of the mixed-mode softening was triggered by a quadratic combination of the pure mode scenarios, which is expressed as

$$\left(\frac{\langle\sigma_I\rangle}{\sigma_I^{cr}}\right)^2 + \left(\frac{\sigma_{II}}{\sigma_{II}^{cr}}\right)^2 = 1 \tag{5.1}$$

where σ_I and σ_{II} represent the normal and shear stress, respectively; and the bracket $\langle\rangle$ implies that compressive stress does not contribute to the initiation of softening.

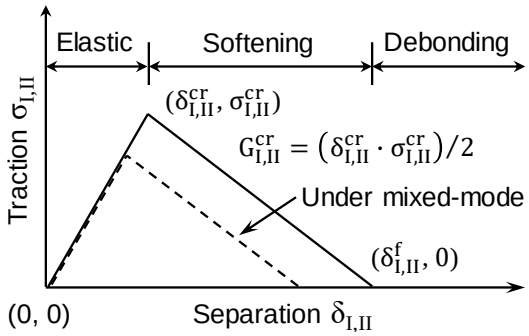

Figure 5.6. Bilinear traction-separation relation for the GFRP-steel bond.

Under mixed-mode conditions, linear softening occurs in modes I and II as represented by the dashed line in Figure 5.6. Debonding under the mixed-mode conditions is predicted by the following quadratic energy criterion [44, 45]:

$$\left(\frac{G_I}{G_I^{cr}}\right)^2 + \left(\frac{G_{II}}{G_{II}^{cr}}\right)^2 = 1 \tag{5.2}$$

where G_I and G_{II} are the work done by the peel (σ_I) and shear (σ_{II}) stress with the corresponding separation (δ_I and δ_{II}), respectively.

The mode I critical stress takes the value of the tensile strength of the adhesive ($\sigma_I^{cr} = f_{t,a}$ = 32.2 MPa). The critical fracture energy takes the value determined from the bulk adhesive notched beam test (G_I^{cr} = 0.887 kN/m), for testing of the bulk brittle epoxy adhesive was reported to produce a similar value of G_I^{cr} compared to joints with an adhesive layer thicker than 1.5 mm [46, 47]. The separation (δ_I^{cr}) at the critical stress is calculated by

$$\delta_I^{cr} = \frac{\sigma_I^{cr}}{E_a} \cdot t_a \tag{5.3}$$

where E_a = 4.25 GPa is the elastic modulus of the adhesive; and t_a = 1.5 mm is the thickness of the adhesive layer.

For mode II conditions, the critical stress (σ_{II}^{cr} = 25.8 MPa) and the critical fracture energy (G_{II}^{cr} = 3.80 kN/m) were obtained based on the empirical correlation [Eqs.

(5.4) and (5.5)] developed by Xia and Teng [48], where similar adherends (steel and FRP), adhesive type (linear brittle epoxy) and adhesive thickness (1-2 mm) were used. The shear displacement (δ_{II}^{cr}) at the critical stress is determined by Eq. (5.6).

$$\sigma_{II}^{cr} = 0.8 f_{t,a} \tag{5.4}$$

$$G_{II}^{cr} = 31\left(\frac{f_{t,a}}{G_a}\right)^{0.56} t_a^{0.27} \tag{5.5}$$

$$\delta_{II}^{cr} = \frac{\sigma_{II}^{cr}}{G_a} \cdot t_a \tag{5.6}$$

where $f_{t,a}$ = 32.2 MPa is the tensile strength of the adhesive; and G_a is the shear modulus of the adhesive, which is calculated from the elastic modulus (E_a = 4.25 GPa) and Poisson's ratio (v_a = 0.28) by

$$G_a = \frac{E_a}{2(1+v_a)} \tag{5.7}$$

5.3.3. Failure Criterion for the FRP Members

Although the FRP members were defined with a linear elastic material model, a failure criterion can be applied based on the computed stresses to identify damage initiation. The Tsai-Wu failure criterion [49], which has been successfully applied to detect damage initiation in pultruded FRP members [50, 51], was adopted in this study. An inverse Tsai-Wu failure index (I_F), calculated by Eq. (5.8), was used to evaluate the stress state of the FRP material, where I_F > 1.0 indicates material failure at the location:

$$I_F = 1\Big/\left(-\frac{B}{2A} + \sqrt{(B/2A)^2 + (1.0/A)}\right) \tag{5.8}$$

with

$$\begin{aligned} A = &-\frac{\sigma_x^2}{\sigma_{xt}^f \sigma_{xc}^f} - \frac{\sigma_y^2}{\sigma_{yt}^f \sigma_{yc}^f} - \frac{\sigma_z^2}{\sigma_{zt}^f \sigma_{zc}^f} + \frac{\sigma_{xy}^2}{\left(\sigma_{xy}^f\right)^2} + \frac{\sigma_{yz}^2}{\left(\sigma_{yz}^f\right)^2} + \frac{\sigma_{xz}^2}{\left(\sigma_{xz}^f\right)^2} \\ &+ \frac{C_{xy}\sigma_x\sigma_y}{\sqrt{\sigma_{xt}^f \sigma_{xc}^f \sigma_{yt}^f \sigma_{yc}^f}} + \frac{C_{yz}\sigma_y\sigma_z}{\sqrt{\sigma_{yt}^f \sigma_{yc}^f \sigma_{zt}^f \sigma_{zc}^f}} + \frac{C_{xz}\sigma_x\sigma_z}{\sqrt{\sigma_{xt}^f \sigma_{xc}^f \sigma_{zt}^f \sigma_{zc}^f}} \end{aligned} \tag{5.9}$$

$$B = \left(\frac{1}{\sigma_{xt}^{f}} + \frac{1}{\sigma_{xc}^{f}}\right)\sigma_x + \left(\frac{1}{\sigma_{yt}^{f}} + \frac{1}{\sigma_{yc}^{f}}\right)\sigma_y + \left(\frac{1}{\sigma_{zt}^{f}} + \frac{1}{\sigma_{zc}^{f}}\right)\sigma_z \quad (5.10)$$

where σ_i and σ_{ij} are the stress components in the *i* and *ij* directions, respectively;σ_{xt}^{f} and σ_{xc}^{f} = the longitudinal tensile and compressive strengths, respectively, of the GFRP member = 330.6 MPa; $\sigma_{yt}^{f} = \sigma_{zt}^{f}$ = transverse tensile strengths = 88.5 MPa; $\sigma_{yc}^{f} = \sigma_{zc}^{f}$ = transverse compressive strengths = 103.0 MPa; $\sigma_{xy}^{f} = \sigma_{yz}^{f} = \sigma_{xz}^{f}$ = shear strengths = 27.6 MPa (in-plane shear strength); and $C_{xy} = C_{yz} = C_{xz}$ = coupling coefficients for the Tsai-Wu theory = -1.0 [52].

5.4. Results and Discussion

5.4.1. Failure Modes and Moment-Rotation Behaviour

All three specimens exhibited considerable ductility through yielding of the steel flange-plate before their ultimate loads were reached, as reflected in the moment-rotation (*M*-θ) curves (Figure 5.7). The rotation angle θ, illustrated in Figure 5.8 (a) which indicates the overall deformation of the specimen, is calculated by Eq. (5.11):

$$\theta = \frac{D_2 - D_1}{L_{1,2}} + \frac{D_5 - D_6}{L_{5,6}} \quad (5.11)$$

where D_i is the displacement measured by displacement gauge *i*; and $L_{i,j}$ is the distance between displacement gauges *i* and *j*.

The *M*-θ curve of B-170-4 (Figure 5.7) shows that nonlinearity began to develop at approximately 3.4 kNm and was caused by yielding of the steel flange-plate. The flange deformation of B-170-4 [Figure 5.8 (b)] was characterized by the opening of gaps at the sides and bottom. The bending of B-170-4 continued until its moment resistance ceased to increase after *M* = 8.4 kNm. Specimens B-170-8 and B-120-8 experienced similar nonlinearity in the *M*-θ curves, which started at approximately 5.7 kNm and was again triggered by yielding of the steel flange-plate. As highlighted in Figure 5.8 (c), the steel flanges were bent outward between the steel tube and the tensile bolts. In B-170-8, the moment resistance continued to increase at a reduced rotational stiffness until *M* = 15.4

kNm, when the steel flange-plate fractured near the weld line on the tensile side of the steel tube [Figure 5.8 (d)]. In B-120-8, which had a shorter bond length of 120 mm, the peak bending moment was attained at M = 13.9 kNm and was marked by brittle failure due to cracking at the top flange of the GFRP tube near the web-flange junctions [Figure 5.8 (e)]. This was instantly followed by debonding of the GFRP from the steel tube at the side and bottom faces. Figure 5.8 (f) shows the debonded steel and GFRP tube of B-120-8, where the adhesive remaining on the surfaces of the steel and the GFRP indicates a cohesive failure.

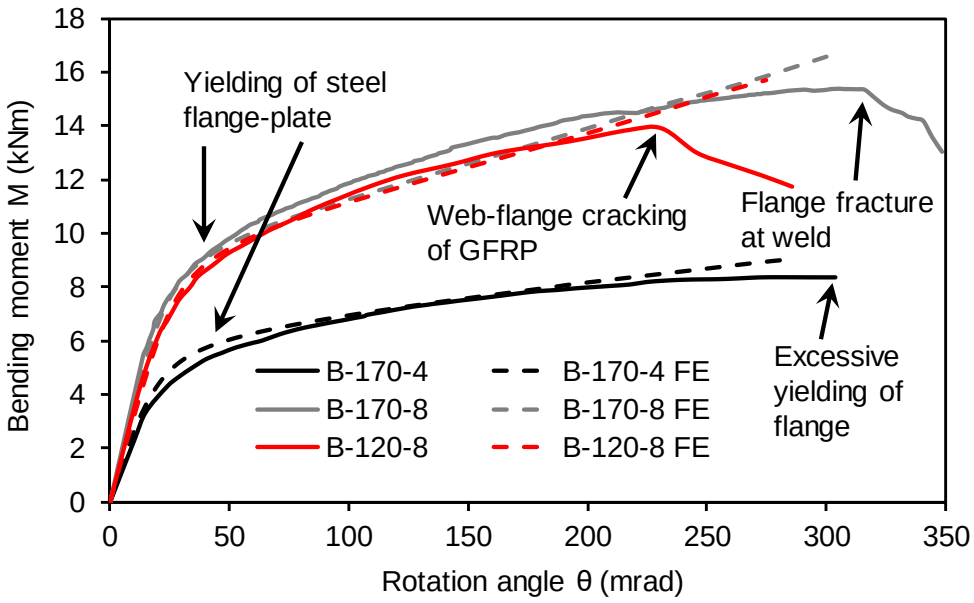

Figure 5.7. Moment-rotation (*M*-θ) curves for all specimens from the experiments and FE modelling.

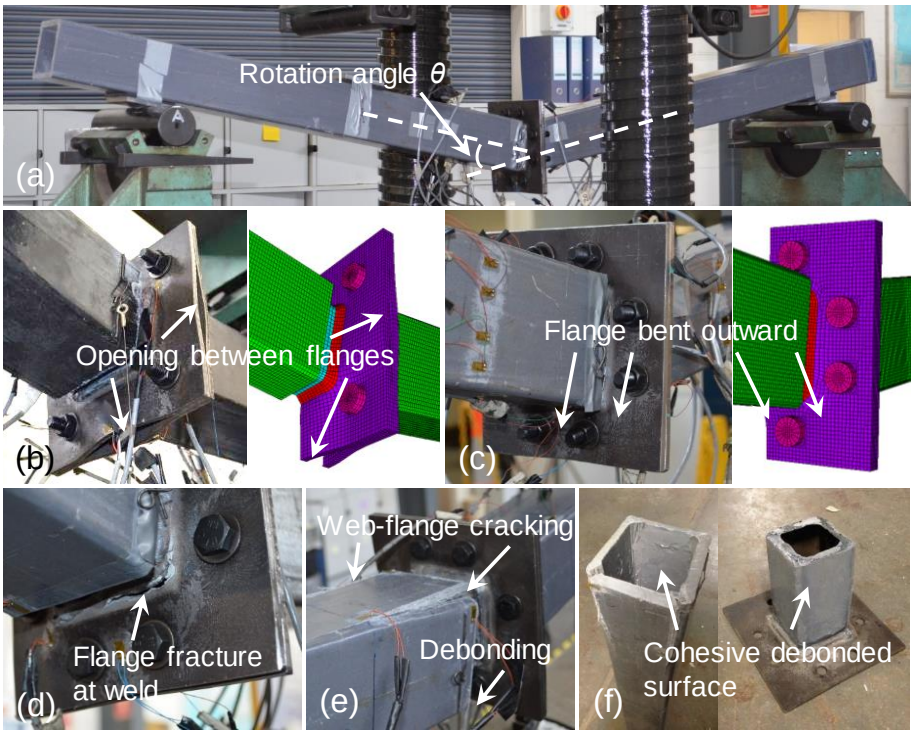

Figure 5.8. Deformations and failure modes: (a) typical overall deformation; (b) experimental and FE deformation of steel flange-plate B-170-4; (c) experimental and FE deformation of steel flange-plate B-170-8; (d) ultimate failure of B-170-8 by steel fracturing; (e) ultimate failure of B-120-8 by GFRP web-flange cracking; and (f) debonded failure surface of B-120-8.

The initial rotational stiffnesses and moment capacities of the specimens are summarized in Table 5.3. A comparison of B-170-4 and B-170-8 shows that the change of the flange-plate configuration from the four-bolt to eight-bolt design increases the rotational stiffness (S_E) by 64% (from 225 to 369 kNm/rad) and the yield moment ($M_{y,E}$) by 75% (from 5.6 to 9.8 kNm). The ultimate bending moment ($M_{u,E}$) also increases by 83% from 8.4 to 15.4 kNm. A comparison of B-120-8 and B-170-8 shows that the increase of the bond length improves S_E slightly from 324 to 369 kNm/rad; the recorded values of $M_{y,E}$ were 8.6 kNm for B-120-8 and 9.8 kNm for B-170-8. The increased bond length also shifts the ultimate failure from the GFRP web-flange cracking (B-120-8) to fracturing of the steel flange-plate (B-170-8), enhancing the ultimate moment ($M_{u,E}$) from 13.9 to 15.4 kNm.

Table 5.3. Rotational stiffnesses and moment capacities of all specimens.

Specimen	**Rotational stiffness, S [a, c] (kNm/rad)**			**Yield moment, M_y [b, c] (kNm)**			**Ultimate moment, M_u [c] (kNm)**		**Ductility index, DI [d]**
	S_E	**S_{FE}**	**S_E/S_{FE}**	**$M_{y,E}$**	**$M_{y,FE}$**	**$M_{y,E}/M_{y,FE}$**	**$M_{u,E}$**	**$M_{u,FE}$**	
B-170-4	225	244	0.922	5.6	5.9	0.949	8.4	9.0	8.4
B-170-8	369	342	1.078	9.8	9.4	1.043	15.4	16.6	6.1
B-120-8	324	310	1.045	8.6	9.3	0.925	13.9	15.3	5.7

[a] Slope of the initial linear part of the moment-rotation (M-θ) curve.

[b] Intersection point of the elastic and post-yield tangent lines of the M-θ curve.

[c] The subscript *E* refers to experimental results, and *FE* refers to FE results.

[d] $DI = \theta_u/\theta_y$, where θ_y is the rotation angle θ at $M_{y,E}$, and θ_u is θ at $M_{u,E}$.

The M-θ results from the FE modelling are plotted as the dashed lines alongside the experimental results in Figure 5.7 and show a good match of the initial stiffnesses and the yielding behaviours. The validity of the modelling is reinforced by the consistent deformations of the steel flange-plates produced by the experiments and FE modelling [Figure 5.8 (c) and (d)]. As shown in Table 5.3, the rotational stiffnesses from the FE modelling (S_{FE}) are within 7.8% of the experimental values (S_E), and the yield moments from the FE modelling ($M_{y,FE}$) are within 7.6% of $M_{y,E}$. In Figure 5.7, the M-θ curves of B-170-4 and B-170-8 from the FE modelling are plotted up to attainment of the steel ultimate strain in the flange-plates, and the corresponding ultimate moments ($M_{u,FE}$) are listed in Table 5.3. The $M_{u,FE}$ of B-120-8 is deemed to attain in the FE modelling when damage is detected in the GFRP tube based on the Tsai-Wu failure criterion, as discussed in further detail in Section 5.4.3 “Failure Prediction of GFRP”.

5.4.2. Strain and Stress Responses of Steel-GFRP Bonding

For specimens B-120-8 and B-170-8, the axial strains on the side surfaces of the steel-GFRP bonded sections are plotted along the section depth at different load levels (Figure 5.9). In both Figure 5.9 (a) and (b), the strain distribution deviates from linearity at 100%

M_u, which implies a loss of full composite action between the steel and GFRP tube in the later stage of the loading process. The load-strain curves from these strain gauges (G1–G4) are presented in Figure 5.10. For both B-120-8 [Figure 5.10 (a)] and B-170-8 [Figure 5.10 (b)], a linear load-strain behaviour up to the ultimate load is observed from G3 and G4, whereas nonlinearity appears in the curves of G1 and G2. These nonlinear load-strain behaviours most likely stem from the adhesive bond being loaded into the softening stage (Figure 5.6), resulting in an incomplete stress transfer between the steel and the GFRP tube. The observation that the G1 and G2 curves exhibit nonlinearity compared with the G3 and G4 curves suggests that the softening may be more significant closer to the top face of the adhesive layer.

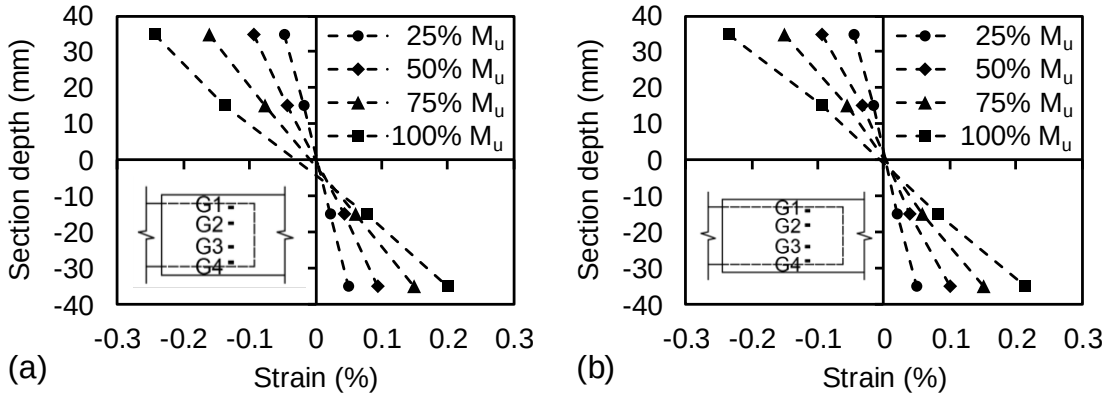

Figure 5.9. Experimental axial strain distributions along the depth of the steel-GFRP bonded sections: (a) B-120-8; and (b) B-170-8.

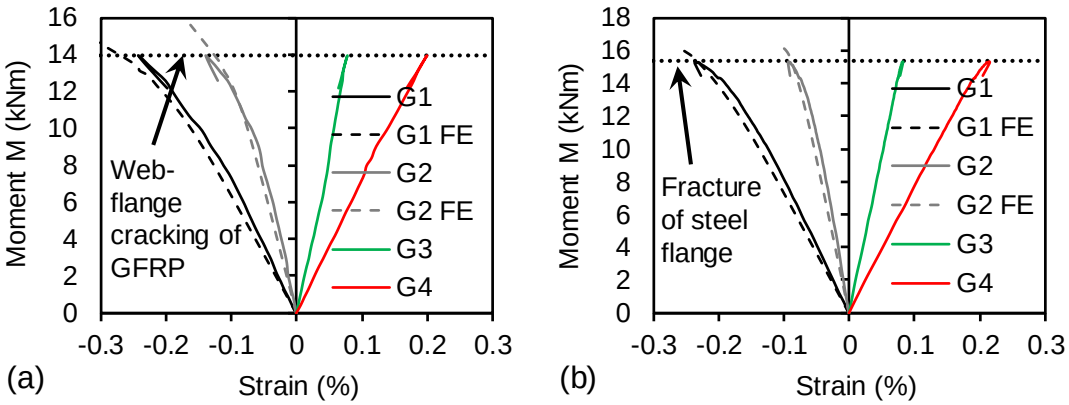

Figure 5.10. Experimental and FE load-strain responses from the strain gauges along the depth of the steel-GFRP bonded sections: (a) B-120-8; and (b) B-170-8.

The load-strain curves from the FE modelling, also plotted in Figure 5.10, successfully capture the nonlinear behaviour. The nonlinearity in the experimental G1 and G2 curves initiates at approximately 7.9 kNm for B-120-8 and 9.7 kNm for B-170-8. Correspondingly, the FE curves begin to exhibit nonlinearity at approximately 9.3 and 11.0 kNm, respectively. Softening of the adhesive bond is further evidenced by the nonlinear load-strain response (G13 or G14) shown in Figure 5.11. Similar to Figure 5.10, the FE modelling predicts a later appearance of nonlinearity, at 9.3 kNm for B-120-8 and 11.2 kNm for B-170-8, than the experimental values of 7.7 and 9.6 kNm, respectively. The discrepancy (within 17%) between the experimental and FE curves in Figure 5.10 and Figure 5.11 implies that FE modelling predicts the occurrence of bond softening at larger load levels than the experiments. A likely reason is that the FE models assume a perfect adhesive bond, whereas defects and geometric imperfections inevitably exist in the fabricated specimens, causing premature bond softening.

With the FE modelling validated by the load-strain behaviours, the interaction stress between the CZM contact pair is computed and presented in Figure 5.12 to provide insight into the distribution of the adhesive stress. As the vector sum of the normal and shear stresses between the contact pair, the total contact stress shown in Figure 5.12 is able to indicate softening and debonding of the adhesive under mixed-mode conditions. It is revealed that the top, bottom, and side faces of the adhesive layer are all subjected to shear stresses between the GFRP and steel. Compressive stresses are incurred on the top face near the steel end (X = 0) and on the bottom face near the GFRP end (X = 120 or 170), whereas tensile (peeling) stresses are induced on the top face near the GFRP end and on bottom face near the steel end. Figure 5.12 shows that the loading on the adhesive layer is primarily sustained near the steel and GFRP ends and especially the GFRP end, which corresponds to the more flexible adherend. Softening first occurs near the adherend corners at the GFRP end before extending inward transversely (in the Z direction) and longitudinally (in the X direction) as the load increases.

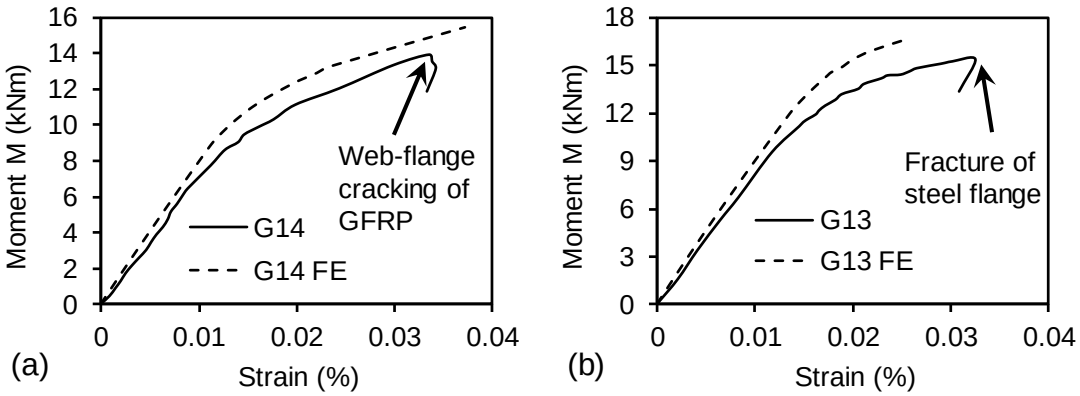

Figure 5.11. Experimental and FE load-strain responses from strain gauges G13 or G14: (a) B-120-8; and (b) B-170-8.

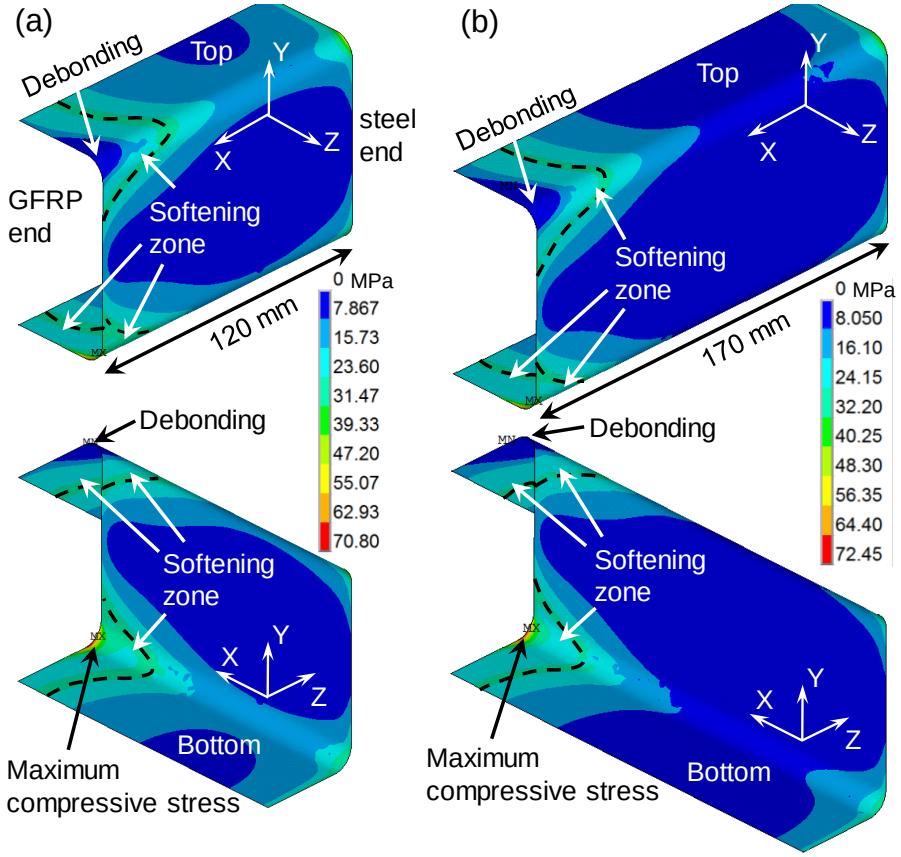

Figure 5.12. Distributions of the CZM total contact stress over the bonded area from the FE modelling at $M_{u,FE}$: (a) B-120-8 at 15.3 kNm; and (b) B-170-8 at 16.6 kNm.

The boundary between the softening zone and the remaining elastic zone, which is highlighted by the dashed lines in Figure 5.12, is marked by lines of critical stress (a combination of shear and peeling stresses that initiates softening of the adhesive bond). The results show that the softening is more significant on the top face compared with the bottom and side faces, because the top adhesive layer at the GFRP end is subjected to, besides shear stress, peeling stress which contributes to softening of the adhesive. At the GFRP end, the observation that softening is more significant on the top face than on the bottom face echoes the load-strain behaviours of G1 and G4 in Figure 5.10; i.e., the load-strain curve of G1 (near the top of the section) exhibits apparent nonlinearity, whereas the curve of G4 (near the bottom of the section) is almost linear. On the top face of the adhesive at the GFRP end, debonding is identified near the adherend corner, indicated in Figure 5.12 (a) and (b) as the region with zero contact stress. The maximum compressive stress in the adhesive is found on the bottom face at the GFRP end near the adherend corner [Figure 5.12 (a) and (b)]. A comparison of Figure 5.12 (a) and (b), which are at similar load levels, shows that the increase of the bond length from 120 to 170 mm does not result in a notable change of the softening zone but rather a larger area of the low-stress zone in the elastic stage. This observation suggests that increasing the bond length beyond 120 mm is not efficient in reducing the softening of the adhesive bond.

5.4.3. Failure Prediction of GFRP

The B-120-8 specimen ultimately failed by cracking in the GFRP tube at the top flange near the web-flange junctions [Figure 5.8 (e)]. The Tsai-Wu failure criterion was applied in the FE model to predict the initiation of this failure. Figure 5.13 presents the distributions of the Tsai-Wu failure index (I_F) for B-120-8 and B-170-8 at the ultimate loads ($M_{u,FE}$), where $I_F > 1.0$ indicates exceedance of the failure criterion. Figure 5.13 (a) shows that the FE modelling indicated failure at the top flange near the web, which correlated well with the position where the GFRP cracking shown in Figure 5.8 (e) initiated. Because the ultimate failure of B-120-8 (cracking of the GFRP) occurred in a rather brittle manner without signs of prior local damage, its $M_{u,FE}$ was considered to be reached when I_F became larger than 1.0. Beyond this load, the modelling would no longer be valid because post-damage behaviour was not defined for the GFRP material. The FE

modelling gave a satisfactory prediction for B-120-8 as $M_{u,FE}$ = 15.3 kNm, in comparison with the experimental result of $M_{u,E}$ = 13.9 kNm. The distribution of I_F for B-170-8 is also presented [Figure 5.13 (b)]; this specimen ultimately failed by fracturing of the steel flange-plate. As indicated, the critical region is also at the top flange near the web, but with no occurrence of GFRP damage (i.e., I_F < 1.0).

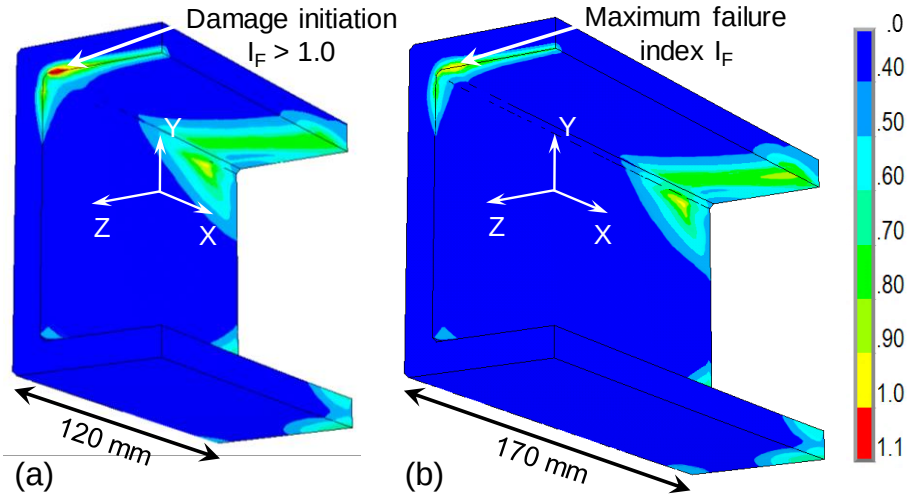

Figure 5.13. Distribution of the Tsai-Wu failure index (I_F) on the GFRP from the FE modelling at $M_{u,FE}$: (a) B-120-8 at 15.3 kNm; and (b) B-170-8 at 16.6 kNm.

5.4.4. Strain and Stress Responses of Steel Flange-Plates

The load-strain responses from the strain gauges on the steel flange-plates are plotted in Figure 5.14 with the FE results. Because the strain gauges were positioned and oriented across the probable yield lines, their readings provide indications of the initiation of yielding and further validation of the FE modelling. For B-170-4 [Figure 5.14 (a)], G16 is the first experimental curve to exhibit nonlinearity, which signals the beginning of yielding, at approximately 2.5 kNm. For B-170-8, the initiation of yielding can be identified from the G16 and G19 experimental curves, which deviate from initial linearity at approximately 4.9 kNm. The load-strain curves from the FE modelling, shown as the dashed lines in Figure 5.14, correlate well with the corresponding experimental curves, especially in the nonlinear stages.

The FE modelling, which was validated by the moment-rotation and load-strain behaviours, is able to visualize the stress distributions of the steel flange-plates (B-170-4 and B-170-8) as presented in Figure 5.15. The stress state ratio, defined as the ratio of the von-Mises stress to the yield stress, is shown; thus, a value larger than 1.0 indicates yielding of the steel. At bending moments of 6.8 kNm [B-170-4, Figure 5.15 (a)] and 11.2 kNm [B-170-8, Figure 5.15(b)], where substantial yielding had occurred, the yielded areas of the flange-plate connected to continuous patterns that enabled plastic rotation of the specimen. Notably, the yielding mechanism of B-170-8, compared with that of B-170-4, involves larger yielded areas thus engage more internal work as the flange-plate deforms, which results in the enhanced stiffness and moment capacities. Figure 5.15 also shows the stress state of the bottom bolts, which were the most critically stressed in each specimen. The bottom bolts were subjected to a combined tensile and bending loading due to the prying action exerted by the deformed flange-plate. In the FE models, minor yielding is observed in the middle of the bolt shank but over less than 20% of the cross section.

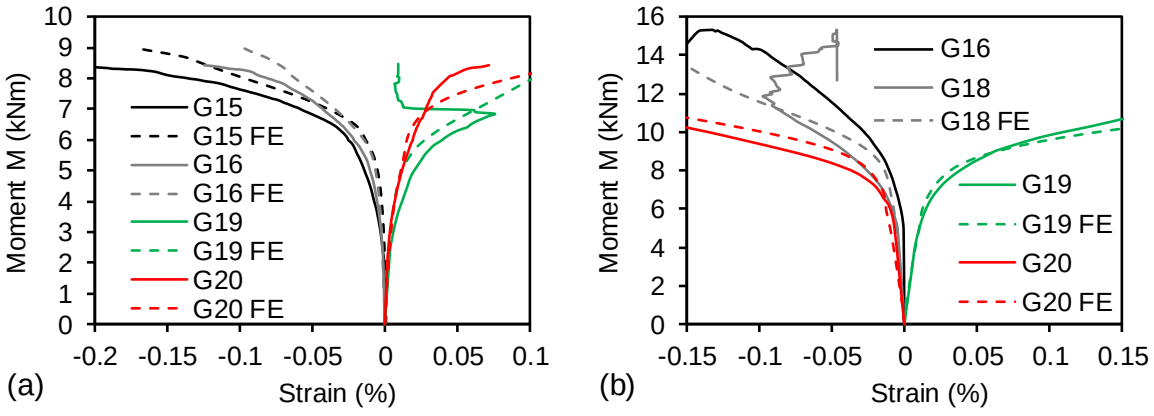

Figure 5.14. Experimental and FE load-strain responses from the strain gauges on the steel flange-plates: (a) B-170-4; and (b) B-170-8.

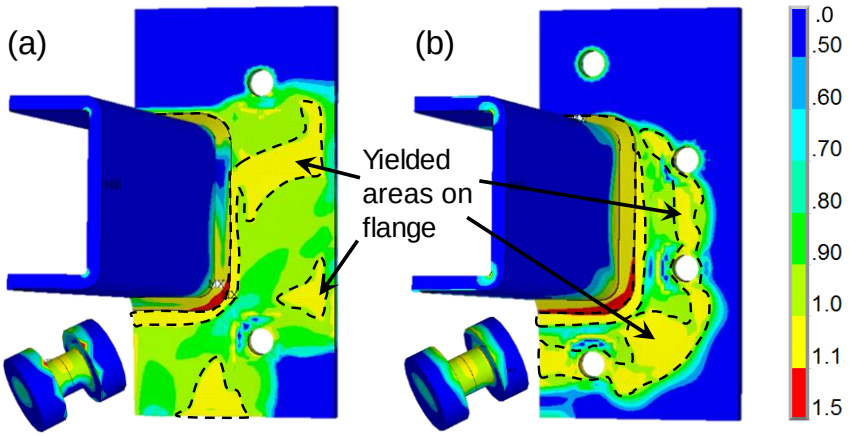

Figure 5.15. Distributions of the von-Mises stress state on the steel components from the FE modelling: (a) B-170-4 at 6.8 kNm; and (b) B-170-8 at 11.2 kNm.

5.5. Stiffness, Strength, and Ductility of the Connections

As design guidelines for FRP frame structures are not yet available, Eurocode 3 [53], which concerns the design of steel structures, is often referred to for classification of FRP beam-column connections [54, 55]. Eurocode 3 is also followed in this study to classify the splice connections in terms of their stiffness and strength. Table 5.4 presents the classification adapted to the GFRP member in this study. In Table 5.4, E, I_s, and L_s are the longitudinal modulus, second moment of area, and length of the connected GFRP members, respectively, and M_s is the section moment capacity of the GFRP member calculated according to its section geometries and tensile strength. The member length (L_s) takes a value of 3.5 m based on the proposed splice connection for column applications and typical story heights. A comparison between the connection specimens (S_E and $M_{u,E}$ in Table 5.3) and the classification boundaries in Table 5.4 shows that all three specimens are classified as semirigid and partial-strength connections. Having the highest moment capacity among the specimens, B-170-8 achieved an ultimate moment of 47%M_s.

Table 5.4. Classification of the splice connections according to Eurocode 3 [53].

Category	**Classification**	**Equation** *	**Requirement**
Stiffness (S)	Rigid	$S \geq 25EI_s/L_s$	$S \geq 911$ kNm/rad
	Semi-rigid	$0.5EI_s/L_s < S < 25EI_s/L_s$	18 kN m/rad < S < 911 kNm/rad
	Nominally pinned	$S \leq 0.5EI_s/L_s$	$S \leq 18$ kNm/rad
Strength (M_u)	Full-strength	$M_u \geq M_s$	$M_u \geq 32.8$ kNm
	Partial-strength	$0.25M_s < M_u < M_s$	8.2 kNm < M_u < 32.8 kNm
	Nominally pinned	$M_u \leq 0.25M_s$	$M_u \leq 8.2$ kNm

* *E, I_s L_s and M_s* are the longitudinal modulus, second moment of area, length and section moment capacity of the connected GFRP members, respectively; L_s = 3.5 m based on column application and typical story heights.

The three specimens demonstrate excellent ductility through yielding of the steel flange-plate prior to ultimate failure. The ductility index (*DI*), defined by Eq. (5.12), is calculated for each specimen and presented in Table 5.3.

$$DI = \theta_u/\theta_y \tag{5.12}$$

where θ_y is the rotation angle θ at the yield moment $M_{y,E}$; and θ_u is θ at the ultimate moment $M_{u,E}$.

Of the specimens, B-170-4 has the highest *DI* value of 8.4, whereas B-170-8, which has the highest rotational stiffness (S_E) and moment capacities ($M_{y,E}$ and $M_{u,E}$), has a lower *DI* of 6.1. For a structure made of brittle FRP members, the proposed splice connection should be able to provide adequate pre-failure warning and substantial energy dissipation before collapse of the structure.

5.6. Conclusions

This paper investigated the bending performance of splice connections developed to assemble tubular section FRP members. Each of the splice connections was composed of a steel bolted flange joint between two tubular steel-GFRP bonded sleeve joints. Based

on the results from experimental testing and FE modelling, the following conclusions are drawn:

1. Under flexural loading, all the splice connection specimens exhibited favourable ductile moment-rotation responses through yielding of the steel flange-plates. The ultimate failure occurred as excessive yielding or fracturing of the flange-plate or web-flange cracking of the GFRP tube. According to Eurocode 3, all of the connection specimens could be classified as semirigid and partial-strength connections. The ductility indices of the connection specimens ranged from 5.7 to 8.4.

2. The FE modelling produced deformed shapes and moment-rotation responses that were consistent with the experimental results. The differences between the rotational stiffnesses from the modelling (S_{FE}) and from the experiments (S_E) were within 7.8%, and those between the yield moments ($M_{y,FE}$ and $M_{y,E}$) were within 7.6%.

3. For the GFRP-steel bonded sections, the loss of full composite action was identified before the ultimate load. This was associated with softening of the adhesive bond, which was evidenced by the nonlinear load-strain responses produced consistently by both the experiments and FE models.

4. Regarding the ultimate failure by web-flange cracking of the GFRP tube (specimen B-120-8), using the Tsai-Wu failure criterion the FE modelling was able to predict the location where failure initiated. The FE bending moment at the initiation of failure ($M_{u,FE}$ = 15.3 kNm) was in good agreement with the ultimate moment in the experiment ($M_{u,E}$ = 13.9 kNm).

5. The eight-bolt configuration (B-170-8) of the steel bolted flange joint component, compared with the four-bolt configuration (B-170-4), improved the rotational stiffness (S_E) by 64% and the yield moment ($M_{y,E}$) by 75%. These improvements were associated with a yielding mechanism that involved more internal work as the flange-plate deformed.

5.7. Acknowledgments

The authors acknowledge the support from the Australian Research Council through the Discovery project (DP180102208) and the Multiplex Building Innovation Project. Thanks are extended to the staff of the Civil Engineering Laboratory of Monash University, particularly Mr. Philip Warnes, for their assistance in the experimental program.

5.8. References

1. Teng J, Chen J, Smith ST, Lam L. Behaviour and strength of FRP-strengthened RC structures: a state-of-the-art review. Proceedings of the Institution of Civil Engineers − Structures and Buildings. 2003;156(1):51-62.
2. Zhao X-L, Zhang L. State-of-the-art review on FRP strengthened steel structures. Engineering Structures. 2007;29(8):1808-23.
3. Meyer R. Handbook of Pultrusion Technology. Springer Science & Business Media, 2012.
4. Turner MK, Harries KA, Petrou MF, Rizos D. In situ structural evaluation of a GFRP bridge deck system. Composite Structures. 2004;65(2):157-65.
5. Bank LC. Flexural and shear moduli of full-section fiber reinforced plastic (FRP) pultruded beams. Journal of Testing and Evaluation. 1989;17(1):40-5.
6. Tomblin J, Barbero E. Local buckling experiments on FRP columns. Thin-Walled Structures. 1994;18(2):97-116.
7. Satasivam S, Bai Y, Zhao X-L. Adhesively bonded modular GFRP web–flange sandwich for building floor construction. Composite Structures. 2014;111:381-92.
8. Mosallam A. Design Guide for FRP Composite Connections. American Society of Civil Engineers (ASCE), 2011.
9. Xie L, Bai Y, Qi Y, Caprani C, Wang H. Effect of width–thickness ratio on capacity of pultruded square hollow polymer columns. Proceedings of the Institution of Civil Engineers − Structures and Buildings. 2018:1-13.
10. Smith S, Parsons I, Hjelmstad K. Experimental comparisons of connections for GFRP pultruded frames. Journal of Composites for Construction. 1999;3(1):20-6.
11. 11 Luo FJ, Bai Y, Yang X, Lu Y. Bolted sleeve joints for connecting pultruded FRP tubular components. Journal of Composites for Construction. 2016;20(1):04015024.
12. Ascione F, Lamberti M, Razaqpur A, Spadea S. Strength and stiffness of adhesively bonded GFRP beam-column moment resisting connections. Composite Structures. 2017;160:1248-57.

13. Singamsethi S, LaFave J, Hjelmstad K. Fabrication and testing of cuff connections for GFRP box sections. Journal of Composites for Construction. 2005;9(6):536-44.
14. Wu C, Zhang Z, Bai Y. Connections of tubular GFRP wall studs to steel beams for building construction. Composites Part B: Engineering. 2016;95:64-75.
15. Zhang ZJ, Bai Y, Xiao X. Bonded sleeve connections for joining tubular glass fiber–reinforced polymer beams and columns: Experimental and numerical studies. Journal of Composites for Construction. 2018;22(4):04018019.
16. Zhang Z, Bai Y, He X, Jin L, Zhu L. Cyclic performance of bonded sleeve beam-column connections for FRP tubular sections. Composites Part B: Engineering. 2018;142:171-82.
17. Yang X, Bai Y, Ding F. Structural performance of a large-scale space frame assembled using pultruded GFRP composites. Composite Structures. 2015;133:986-96.
18. Yu T, Fernando D, Teng J, Zhao X. Experimental study on CFRP-to-steel bonded interfaces. Composites Part B: Engineering. 2012;43(5):2279-89.
19. Fernando D, Yu T, Teng J-G. Behavior of CFRP laminates bonded to a steel substrate using a ductile adhesive. Journal of Composites for Construction. 2013;18(2):04013040.
20. Qiu C, Feng P, Yang Y, Zhu L, Bai Y. Joint capacity of bonded sleeve connections for tubular fibre reinforced polymer members. Composite Structures. 2017;163:267-79.
21. Keller T, Vallée T. Adhesively bonded lap joints from pultruded GFRP profiles. Part I: stress–strain analysis and failure modes. Composites Part B: Engineering. 2005;36(4):331-40.
22. Kato B, Mukai A. Bolted tension flanges joining square hollow section members. Journal of Constructional Steel Research. 1985;5(3):163-77.
23. Willibald S, Packer J, Puthli R. Experimental study of bolted HSS flange-plate connections in axial tension. Journal of Structural Engineering. 2002;128(3):328-36.
24. Wheeler A, Clarke M, Hancock G, Murray T. Design model for bolted moment end plate connections joining rectangular hollow sections. Journal of Structural Engineering. 1998;124(2):164-73.
25. Wheeler A, Clarke M, Hancock G. Design model for bolted moment end plate connections joining rectangular hollow sections using eight bolts. Research Rep. No. R827. Sydney, Australia: Department of Civil Engineering, University of Sdyney; 2003.
26. Wang Y, Zong L, Shi Y. Bending behavior and design model of bolted flange-plate connection. Journal of Constructional Steel Research. 2013;84:1-16.
27. Hai ND, Mutsuyoshi H. Structural behavior of double-lap joints of steel splice plates bolted/bonded to pultruded hybrid CFRP/GFRP laminates. Construction and Building Materials. 2012;30:347-59.

28. Turvey G. Experimental and analytical investigation of two-and six-plate bonded splice joints on serviceability limit deformations of pultruded GFRP beams. Composite Structures. 2014;111:426-35.

29. Turvey GJ, Cerutti X. Flexural behaviour of pultruded glass fibre reinforced polymer composite beams with bolted splice joints. Composite Structures. 2015;119:543-50.

30. Nagaraj V, Gangarao HV. Fatigue behavior and connection efficiency of pultruded GFRP beams. Journal of Composites for Construction. 1998;2(1):57-65.

31. Qiu C, Ding C, He X, Zhang L, Bai Y. Axial performance of steel splice connection for tubular FRP column members. Composite Structures. 2018;189:498-509.

32. Deng E-F, Zong L, Ding Y, Dai X-M, Lou N, Chen Y. Monotonic and cyclic response of bolted connections with welded cover plate for modular steel construction. Engineering Structures. 2018;167:407-19.

33. Standard Australia. AS4100 Steel Structures. Sydney, Australia, 1998.

34. ASTM International. Standard Test Method for Tensile Properties of Polymer Matrix Composite Materials. ASTM D3039. West Conshohocken, PA., 2014.

35. ASTM International. Standard Test Method for Flexural Properties of Polymer Matrix Composite Materials. ASTM D7264. West Conshohocken, PA., 2015.

36. ASTM International. Standard Test Method for Short-Beam Strength of Polymer Matrix Composite Materials and Their Laminates. ASTM D2344. West Conshohocken, PA., 2016.

37. Lee S, Munro M, Scott R. Evaluation of three in-plane shear test methods for advanced composite materials. Composites. 1990;21(6):495-502.

38. ASTM International. Standard Test Methods and Definitions for Mechanical Testing of Steel Products. ASTM A370-16. West Conshohocken, PA., 2016.

39. Zhang Z, Wu C, Nie X, Bai Y, Zhu L. Bonded sleeve connections for joining tubular GFRP beam to steel member: Numerical investigation with experimental validation. Composite Structures. 2016;157:51-61.

40. ASTM International. Standard Test Method for Tensile Properties of Plastics. ASTM D638-10. West Conshohocken, PA., 2010.

41. ASTM International. Standard Test Methods for Plane-Strain Fracture Toughness and Strain Energy Release Rate of Plastic Materials. ASTM D5045-99. West Conshohocken, PA., 2007.

42. Trahair N, Bradford M. The Behaviour and Design of Steel Structures to AS 4100. Third Edition ed. Taylor & Francis, 1998.

43. Campilho RD, Banea MD, Neto J, da Silva LF. Modelling adhesive joints with cohesive zone models: effect of the cohesive law shape of the adhesive layer. International Journal of Adhesion and Adhesives. 2013;44:48-56.

44. Da Silva LF, Campilho RD. Advances in numerical modelling of adhesive joints. In: Advances in Numerical Modeling of Adhesive Joints. Springer, 2012. p. 1-93.

45. ANSYS 16.1. ANSYS Mechanical APDL Theory Reference. Canonsburg, PA: ANSYS, 2016.
46. Bascom W, Cottington R, Jones R, Peyser P. The fracture of epoxy-and elastomer-modified epoxy polymers in bulk and as adhesives. Journal of Applied Polymer Science. 1975;19(9):2545-62.
47. Lee D-B, Ikeda T, Miyazaki N, Choi N-S. Effect of bond thickness on the fracture toughness of adhesive joints. Journal of Engineering Materials and Technology. 2004;126(1):14-8.
48. Xia S, Teng J. Behaviour of FRP-to-steel bonded joints. In: Proceedings of the international symposium on bond behaviour of FRP in structures. International Institute for FRP in Construction, 2005. p. 419-26.
49. Tsai SW, Wu EM. A general theory of strength for anisotropic materials. Journal of Composite Materials. 1971;5(1):58-80.
50. Carrion JE, Hjelmstad KD, LaFave JM. Finite element study of composite cuff connections for pultruded box sections. Composite Structures. 2005;70(2):153-69.
51. Luo FJ, Yang X, Bai Y. Member Capacity of Pultruded GFRP Tubular Profile with Bolted Sleeve Joints for Assembly of Latticed Structures. Journal of Composites for Construction. 2016;20(3):04015080.
52. Barbero EJ. Finite Element Analysis of Composite Materials Using ANSYS®: CRC press, 2013.
53. CEN (European Committee for Standardization). Eurocode 3: Design of Steel Structures, Part 1-8: Design of Joints. Brussels, Belgium, 2005.
54. Martins D, Proença M, Correia JR, Gonilha J, Arruda M, Silvestre N. Development of a novel beam-to-column connection system for pultruded GFRP tubular profiles. Composite Structures. 2017;171:263-76.
55. Ascione F, Lamberti M, Razaqpur A, Spadea S, Malagic M. Pseudo-ductile failure of adhesively joined GFRP beam-column connections: An experimental and numerical investigation. Composite Structures. 2018;200:864-73.

CHAPTER 6. PERFORMANCE OF THE SPLICE CONNECTION UNDER CYCLIC LOADING

Declaration for the Chapter

Chapter 6 of the thesis presents the following published work in a re-formatted form:

Qiu C, Bai Y, Cai Z, Zhang Z. Cyclic performance of splice connections for hollow section fibre reinforced polymer members. Composite Structures. 2020;243:112222. https://doi.org/10.1016/j.compstruct.2020.112222

Permission has been obtained from the publisher *Elsevier* to include the article, in its published form or in a re-formatted form, in this thesis.

The student's and the co-authors' contribution to the work is listed in the following table:

Name of author	**Nature of contribution**	**Contribution (%)**
C Qiu (the student)	Conceptualisation, methodologies, experimental work, numerical modelling, data analysis, writing-up, revision	70%
Y Bai	Conceptualization, methodologies, review and revision, financial support	15%
Z Cai	Experimental work	10%
Z Zhang	Review and revision	5%

The undersigned hereby certify that the above declaration correctly reflects the nature and extent of the student's and co-authors' contribution to this work.

Student (Chengyu Qiu) signature: Main supervisor (Yu Bai) signature:

Date: Date:

Link of the Manuscript to the Thesis

The manuscript presents experimental and numerical studies on the proposed splice connection (Figure 2.18) under combined shear-and-moment cyclic loading.

Abstract

This study investigates the cyclic performance of splice connections developed for hollow section fibre reinforced polymer (FRP) members. Splice connection specimens, each consisting of a steel bolted flange joint between two hollow section steel-FRP bonded sleeve joints, are prepared in three configurations with difference in bolt arrangement or bond length. Correspondingly, detailed finite element (FE) models are constructed with consideration of yielding of the steels, damage in the adhesive bond, pre-tensioning of the bolts and contact between the bolt-fastened parts. Tested under a cyclic flexural loading, the specimens experience different levels of yielding in the steel flange-plates before ultimate failure in the FRP member or in the steel flange-plate. Excellent ductility and energy dissipation capacity are demonstrated in a specimen where plastic deformation of the steel flange-plates is fully developed. The strain responses are also analysed to identify damage in the adhesive bond and yielding in the flange-plates. The FE modelling agrees well with the experimental results in terms of moment-rotation and load-strain responses, and can also predict the initiation of the ultimate failure in the FRP using the Tsai-Wu failure criterion.

Keywords: Fibre reinforced polymer (FRP); Hollow section member; Splice connection; Bonded sleeve joint; Cyclic performance.

6.1. Introduction

Fibre reinforced polymer (FRP) composites, compared to traditional construction materials, have unique features such as high strength-to-weight ratio and corrosion resistance. Majorly used in rehabilitation and strengthening of concrete [1] and steel structures [2], they are also finding applications in new constructions thanks to development of the pultrusion manufacturing technique [3] and the moderate cost of

FRPs with glass fibres (GFRPs). Examples of field applications and laboratory studies include bridges decks [4, 5], space trusses [6, 7], floor slabs [8, 9] and wall panels [10]. In attempts to exploit the advantages of pultruded FRPs in frame structures, structural connections have been developed to accommodate the brittle and anisotropic characteristics of the material.

In frame structures, the beam-column and splice connections are two fundamental connections to facilitate the assembly. To date, beam-column connections of FRP structures have received extensive study. Bank et al. conducted pioneering works in which FRP bolts, seated angles and web cleats were used to connect FRP I-section beam and column similar as in steel structures [11, 12]. Unique failure modes of pultruded FRP composites were revealed such as web-flange separation and delamination of the seated angles. To mitigate these types of failure, through-bolts that engaged both flanges of the I-section were examined [11], before universal connector [13] and wrapped connector [14] were developed. Further works were conducted in [15-17] to explore the effect of bolt arrangements, angle cleats positions and the materials of connectors (i.e. steel vs. FRP). Later on, beam-column connections were developed for hollow section members where steel bolts, adhesive, flange angles and web plates were used [18]. In search of further improvement in strength, a cuff connector that integrated a hollow section FRP beam and column into a monolithic unit using adhesive bond was studied [19, 20]. The ultimate moment capacity was increased by up to 57% compared to specimen with bolted cuff. More recently, bonded sleeve connection with extended steel endplate was developed into stud connection [21] and beam-column connection [22] for hollow section FRP members. In this configuration, the extended endplate enabled easy assembly with bolts and ductile failure through steel yielding. In another recent work, innovative steel tube connectors with welded bolt nuts were designed inside rectangular hollow section FRP members for easy connection of beam and column, and to impart ductility by yielding of these steel connectors [23].

Apart from the aforementioned works which focused on the monotonic behaviour of beam-column connections, the cyclic performance was also investigated in a few studies. Early cyclic studies were conducted on connections consisting of FRP angle and T-shaped connectors [24] or universal connectors [25] that were bonded and/or bolted to

I-section beams and columns. The bonded cuff connection for hollow section members was also examined under cyclic loading [20, 26]. These cyclic studies revealed limited ductility and energy dissipation due to brittle fracture or delamination of the connector elements at the beam flanges. In the more recent cyclic studies, i.e. the bonded sleeve connection with extended endplate [27] and the connection comprised of steel tubular connectors bolted inside the hollow section beam and column [28, 29], improved energy dissipation capacities were demonstrated through yielding of steel components and also bearing failure of bolted joints in FRP instead of shear-out failure [30].

In comparison, splice connections for FRP members have received far less research. Splice connections are often used in beams or columns to enable their continuity over long span or multiple storeys. In one of the earliest studies, beam splices formed by bolted and bonded FRP lap plates were applied to wide flange I-sections and square hollow sections [31]. This study focused on the fatigue performance and reported the realization of 60-80% (I-section) and 46-60% (hollow section) of the intact beam fatigue life. Hybrid FRP I-beams with double lap splice joints at midspan were tested in [32] where bonded and bolted joints proved enhanced stiffness compared to bolted-only joints. In another similar work, steel splice plates were used instead of FRP plates, and the effect of bolt row number was investigated [33]. Later, the serviceability behaviour of beam splices formed by bonded-only [34] and bolted-only [35, 36] lap plates for pultruded wide flange I-section was investigated, while the behaviour at ultimate state was not reported.

Among the aforementioned works of splice connections, few was conducted for hollow section FRP members. Therefore, a splice connection was proposed in [37] consisting of a steel bolted flange joint between two hollow section steel-FRP bonded sleeve joints (Figure 6.1). The bonded sleeve joint, formed by a steel square hollow section (SHS) member coupled into an FRP SHS member with a high-strength adhesive, was intended to be prefabricated off-site to attain manufacturing accuracy. The bonded sleeve joint, by integrating the FRP and steel member into a monolithic unit, provided a high degree of interaction between the two components and a reduced stress concentration in the FRP member (compared to bolt-fastening). A rotational stiffness up to 114% of a continuous member was realized, and an ultimate moment capacity of 47% of the FRP section could be attained [38]. The steel flange-plate, designed for easy on-

site assembly, also enabled ductile failure by steel yielding [38], suggesting promising energy dissipation performance of the splice connection under cyclic loading. To protect the exposed steel parts (the flange-plates and the bolts) against corrosion, galvanized or stainless-steel parts can be used instead, or surface coating can be easily applied.

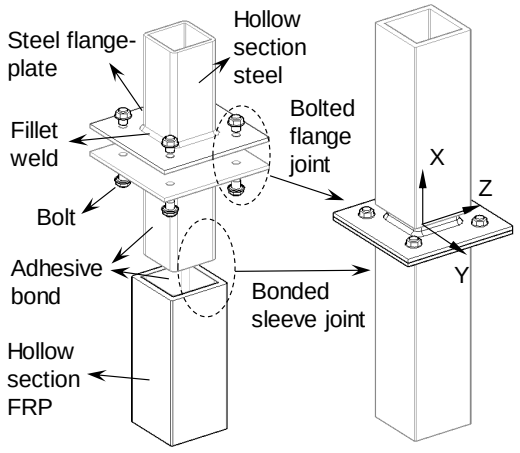

Figure 6.1. Configuration of the proposed splice connection for hollow section FRP member.

In multi-storey FRP frame structures, the energy dissipation capacity of the splice connections will be of important concern under seismic loading. Therefore, this paper investigates the cyclic performance of the splice connection, by both full-scale experimental testing and finite element (FE) modelling. Splice connection specimens with difference in bolt arrangement or bond length are studied under cyclic flexural loading to reveal their failure modes, moment-rotation behaviours and cyclic performances. Local strain responses that indicate the interaction between the bonded members and yield status of the steel components are also reported and discussed.

6.2. Experimental Program

6.2.1. Specimens and Fabrication

The overall configuration and dimensions of the splice connection specimens are illustrated in Figure 6.2 (a). The connection specimens were prepared in three configurations, namely C-170-8, C-120-8 and C-170-4. The first letter "C" refers to the cyclic loading; the first number (170 or 120) denotes the steel-FRP coupling bond length in mm [Figure 6.2 (b-d)]; and the second number (4 or 8) represents the number of bolts on the steel flange-plate [Figure 6.2 (e)]. One specimen per configuration was prepared considering the large scale and verification from FE modelling. Fabrication of the specimens started with welding a 6 mm-thick steel flange-plate to one end of a steel SHS (80×80×6 mm) member by fillet weld approximately 6 mm in leg length. The other end of the steel SHS member was co-axially coupled into and bonded to a pultruded GFRP member with a hollow section of 102×102×9.5 mm. Before the adhesive was applied, the to-be-bonded surfaces of the steel and GFRP members were treated following a procedure of degreasing, grit blasting for steel/sandpaper abrading for GFRP, air nozzle blow-off cleaning, and solvent cleaning. Each of the bonded assembly was cured for two weeks under room temperature, before a pair of them was bolted together at the flange-plates with grade 8.8 M12 bolts and nuts with washers. The fasteners were pre-tensioned to around 65 kN by a torque wrench to meet the specification of "tension tight" according to AS4100 [39].

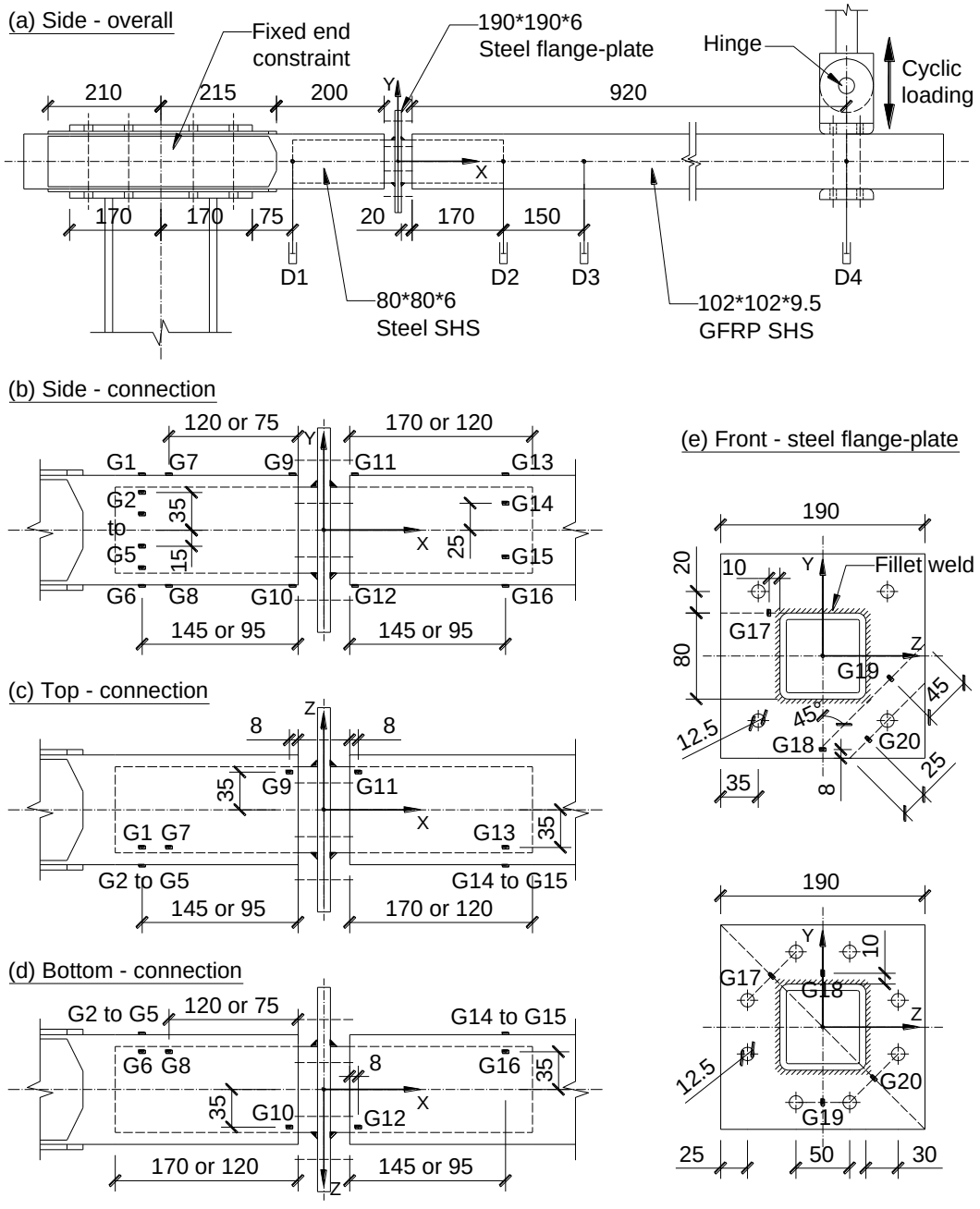

Figure 6.2. Dimensions of the splice connection specimens (all units in mm; G1 to G20: strain gauges; D1 to D4: displacement gauges): (a) overall side view; (b) side view of the connection; (c) top view of the connection; (d) bottom view of the connection; (e) front view of the flange-plates with four and eight bolts.

6.2.2. Material Properties

The pultruded GFRP SHS member was comprised of E-glass fibres embedded in a polyester resin matrix. The strengths and moduli of the GFRP material are summarised in Table 6.1 where the relevant test methods [40-44] are also provided[1]. The stress-strain behaviours of the steel SHS and flange-plate were characterised from tensile coupon tests following ASTM A370-16 [45] [2]; the key strength and modulus properties are summarised in Table 6.2. Reported in an earlier study [46], the grade 8.8 M12 bolts had a yield strength of 1043 MPa and Young's modulus of 235 GPa. The adhesive used to bond the steel and GFRP members was Sikadur-330, a two-component epoxy-based adhesive. Tested under tensile loading as per ASTM D638-10 [47], the Sikadur-330 adhesive showed a linear stress-strain behaviour up to an average ultimate strength of 33.7 MPa[3]; the elastic modulus was recorded as 4.09 GPa and the Poisson's ratio as 0.28.

Table 6.1. Strengths and moduli of the GFRP material.

Component of properties	**Modulus (GPa)**	**Strength (MPa)**	**Test method**
Longitudinal tensile	25.18 ± 12.80 [a]	330.6 ± 19.4 [b]	ASTM D3039 [40]
Longitudinal compressive	23.77 ± 5.46	307.7 ± 4.3 [b]	ASTM D695 [41]
Transverse flexural	6.24 ± 1.18 [a]	88.5 ± 6.5	ASTM D7264 [42]
Transverse tensile	5.52	48.3 [b]	From manufacturer's datasheet [c]
Transverse compressive	8.78 ± 2.37	127.9 ± 7.6 [b]	ASTM D695 [41]
Interlaminar shear	-	31.2 ± 1.9	ASTM D2344 [43]
In-plane shear	3.02 ± 0.31 [a]	27.6 ± 1.7 [b]	10° off-axis tensile test [44]

[a] Adopted as the elastic moduli in the FE modelling.

[b] Adopted as the strength parameters in the Tsai-Wu failure criterion.

[c] Transverse sample too short for tensile testing.

[1] More information of the material testing of the GFRP is provided in Section A.3.1 of Appendix.
[2] More information of the material testing of the steel flange-plate is provided in Section A.3.2 of Appendix.
[3] More information of the tensile testing of the adhesive is provided in Section A.3.3 of Appendix.

Table 6.2. Strengths and moduli of the steel materials.

Steel material	Yield strength (MPa)	Ultimate strength (MPa)	Young's modulus (GPa)	Poisson's ratio
6mm-thick flange	372.8 ± 4.0	467.2 ± 3.1	205.1 ± 2.0	0.243 ± 0.08
80×80×6mm SHS	420.1 ± 5.9 [a]	519.4 ± 8.4	209.5 ± 3.9	0.277 ± 0.07

[a] 0.2% offset yield strength

6.2.3. Test Setup and Instrumentation

A cantilever flexural setup was adopted as shown in Figure 6.2 (a) where the cyclic loading was applied vertically at the free end of the specimen. The test setup, designed to subject the splice connection to a combination of shear and moment cyclic loading, simulates the load scenario of a beam or column splice when a building frame is under seismic or other lateral sway loadings. To approximate a fixed boundary condition, the constrained end of the specimen was clamped over a 340 mm-length to a short steel column which was anchored to the strong floor [Figure 6.2 (a) and Figure 6.3]. The clamped area of the GFRP member was strengthened against failure by externally bonded steel plates. The cyclic loading was applied by an Instron hydraulic actuator with a jack stroke limit of ±125 mm and a load cell of ±250 kN capacity. Shown in Figure 6.3, a spread plate with a hinge joint was used at the loaded end of the specimen to ensure freedom of rotation and verticality of the load. In each specimen, sixteen strain gauges (G1 to G16) were attached on the GFRP member [Figure 6.2 (b-d)] to evaluate the interaction between the bonded steel and GFRP members. Four strain gauges (G17 to G20) were attached on the steel flange-plate [Figure 6.2 (d)] in positions and orientations where yielding would initiate according to FE analysis. Four displacement gauges (D1 to D4, string potentiometers) were deployed along the specimen to measure vertical deflections.

6.2.4. Cyclic Loading Sequence

In the absence of a cyclic loading protocol for FRP structures, the ATC-24 protocol [48] for components of steel structures was selected in this study. The loading sequence,

illustrated in Figure 6.4, used the yield displacement (δ_y) as the reference to increase the amplitude of cycles. The magnitude of δ_y, defined as the loaded end displacement when yielding of the steel flange-plate began, was estimated by FE modelling. For a direct comparison of cyclic performance among specimens, the δ_y value of 25 mm from specimen C-170-4 was adopted for all cyclic testings. The loading sequence, applied in a displacement-control mode (12 mm/min), consisted of nine elastic cycles (amplitude ≤ δ_y) followed by a series of cycle pairs with amplitude increment of 0.5δ_y. In a cyclic testing, the loading sequence was implemented until a complete failure of the specimen, i.e. sudden drop in load resistance, or until the stroke limit of the hydraulic jack (±125 mm) was reached.

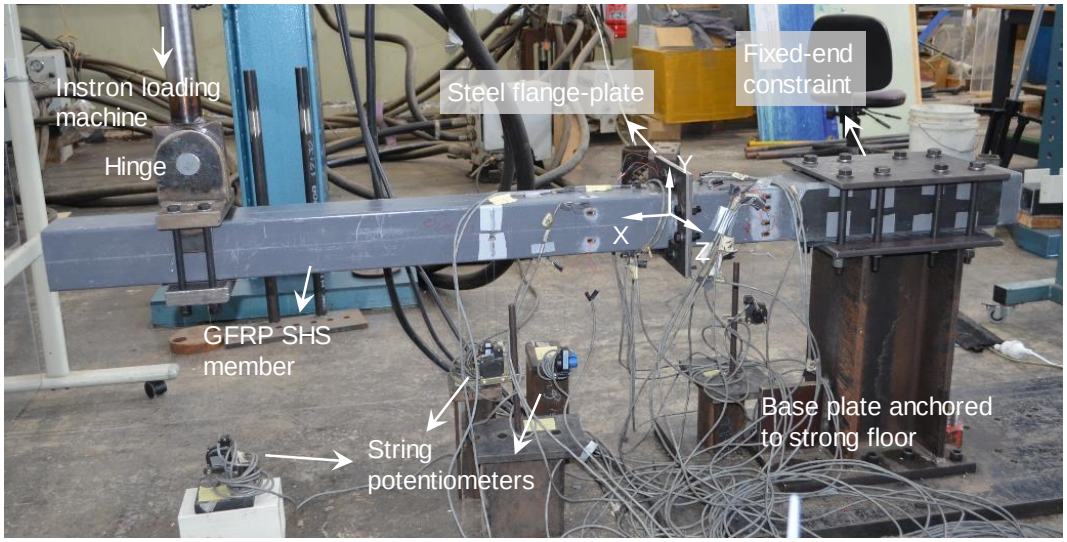

Figure 6.3. Experiment cyclic test setup.

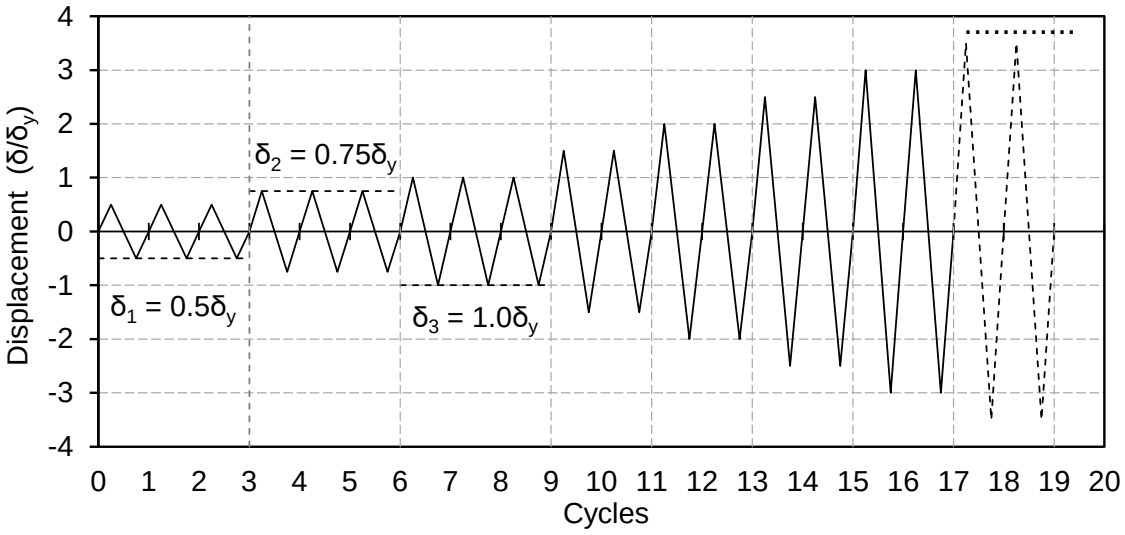

Figure 6.4. Cyclic loading sequence applied to the specimens.

6.3. Finite Element Modelling

6.3.1. Geometries, Element Types, Material Models and Boundary Conditions

Finite element (FE) modelling of the specimens was conducted in the ANSYS 19.2 Mechanical APDL package. The geometry of the model was constructed with symmetric simplification about the XY-plane [Figure 6.5 (a)]. The steel and GFRP components were meshed by a 3D 8-node hexagonal element (SOLID185). The GFRPs were modelled as an orthotropic elastic member with the longitudinal direction aligned parallel to the X-axis. The elastic material properties of the GFRP (longitudinal, transverse and shear moduli) were input as those obtained from the material characterisation tests (Table 6.1). In the post-processing, the Tsai-Wu failure criterion [49] was applied to evaluate the stress status of the GFRP member, and the strength parameters adopted to define the Tsai-Wu criterion (Eqs. 5.8-5.10) are highlighted in Table 6.1. For the steel components, material models with the von-Mises yield criterion and kinematic multi-linear hardening behaviour were adopted; the stress-strain hysteresis behaviour was defined by fitting its envelop to the stress-strain curve obtained from the tensile coupon tests (Section 6.2.2).

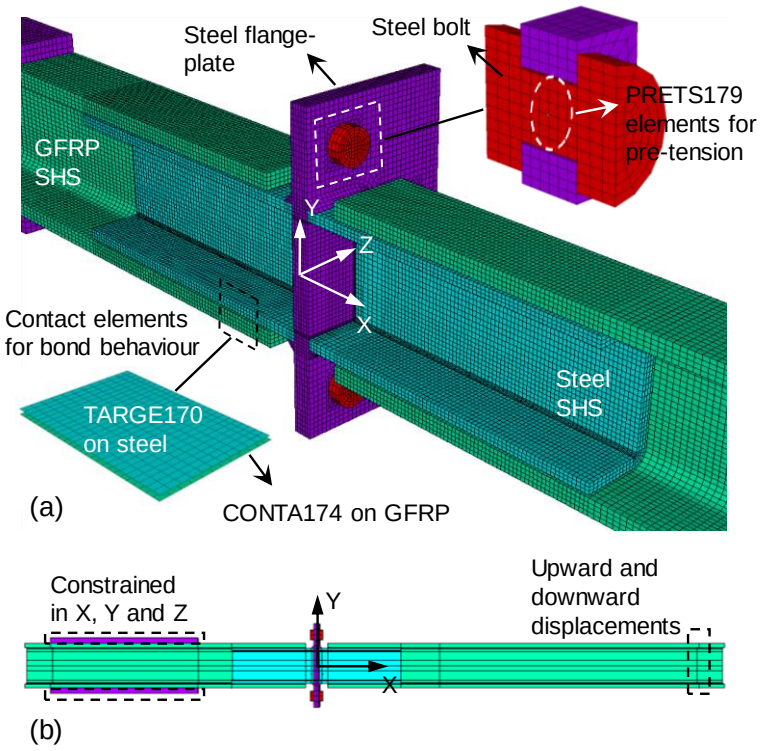

Figure 6.5. FE modelling of the splice connection specimens: (a) a typical meshed model; (b) boundary conditions.

Contact between the bolted parts was considered by defining a pair of 4-node surface-to-surface contact elements (CONTA173 and TARGE170) onto the potential contact surfaces. Three pairs of contact were included: between the flange-plates, between the bolt shank and the flange-plate, and between the bolt head (washer) and the flange-plate. For the contact interaction, free separation was allowed in the normal direction. While in compression the contact behaviour was governed by the augmented Lagrange algorithm where the contact pressure would be adjusted during equilibrium iterations to keep the penetration below an allowable tolerance. The tolerance was defined as 10% of the underlying element depth considering a balance between accuracy and computation time. In trial FE analysis with monotonic loading, the 10% tolerance did not result in a distinguishable difference in specimen load-deflection response compared to a 5% tolerance. Contact behaviour in the tangential direction was governed by a friction coefficient of 0.44 between the steel surfaces [50]. Pre-tensioning of the bolts was modelled by defining PRETS179 elements at the mid-section of the bolt shanks.

In terms of boundary conditions, a symmetric constraint was applied on the XY cut plane of the specimen models. The top and bottom nodes at one end of the models were constrained from translation to simulate the fixed end condition [Figure 6.5 (b)], while the nodes at the other end were displaced upwards and downwards to simulate the cyclic loading. To solve for the mechanical response, pre-tensioning of the bolts was applied in the first load step, before the cyclic displacements were applied in the subsequent load steps.

6.3.2. Modelling of the Steel-GFRP Bond

In adhesive bonded joints, local damage could be initiated in the high stress regions of the bonded area, while this does not necessarily lead to an immediate loss of load-carrying capacity. To account for the damage initiation and propagation in the steel-GFRP bonded sleeve joint of the connection specimens, the bond behaviour was modelled through the interaction between a pair of contact elements. As indicated in Figure 6.5 (a), the adhesive layer was not represented by solid elements; instead, CONTA174 and TARGE170, a pair of 8-node surface-to-surface contact elements, were superposed onto the bonded surface of the steel and the GFRP respectively. Because of the thickness of the adhesive layer (and thus the distance between the steel and GFRP surfaces), the pair of contact elements were 1.5 mm apart from each other initially but with contact interaction.

Considering the presence of both shear and normal stresses on the adhesive layer when the bonded sleeve joint was under flexural loading, damage in the adhesive bond was defined to be initiated when

$$\left(\frac{\sigma_p}{\sigma_p^{cr}}\right)^2 + \left(\frac{\sigma_t}{\sigma_t^{cr}}\right)^2 = 1 \qquad (6.1)$$

where σ_p or σ_t is the peel or tangential stress between the contact pair; σ_p^{cr} or σ_t^{cr} is the corresponding critical stress that would lead to damage initiation in the state of pure peel or tangential stress. Compressive damage was not included in the modelling as the Sikadur-330 adhesive exhibited a 115% higher strength in compression than in tension [51], and also considering that compressive stress could still be transferred when debonded adherends were in contact. As illustrated in Figure 6.6, once damage was

initiated, the stress-separation (σ-δ) relation of the contact pair entered the debonded stage in a brittle manner, ideally with a $\delta_{p,t}^{f}/\delta_{p,t}^{cr}$ ratio of 1.0. However, in the numerical implementation, a debonding slope was defined ($\delta_{p,t}^{f}/\delta_{p,t}^{cr} > 1.0$) to overcome convergence difficulty. From trial FE analyses, a $\delta_{p,t}^{f}/\delta_{p,t}^{cr}$ ratio of 1.15 was found to allow substantial propagation of the adhesive bond damage, and was therefore adopted. To complete the definition of the bond behaviour, the state of ($\delta_{p,t}^{f}$, *0*) in Figure 6.6 was reached when

$$\frac{G_p}{G_p^{cr}} + \frac{G_t}{G_t^{cr}} = 1 \tag{6.2}$$

where G_p or G_t is the work done by the peel (σ_p) or tangential (σ_t) stress with the corresponding separation (δ_p or δ_t); G_p^{cr} or G_t^{cr}, as the area under the corresponding σ-δ curve, was calculated by Eq. (6.3) or (6.4).

$$G_p^{cr} = \sigma_p^{cr}\delta_p^{f}/2 \tag{6.3}$$

$$G_t^{cr} = \sigma_t^{cr}\delta_t^{f}/2 \tag{6.4}$$

It should be noted that under cyclic loading, damage in the adhesive bond was deemed to be cumulative that any unloading and reloading beyond the elastic stage would occur with a reduced slope as shown in Figure 6.6. Moreover, at damaged regions, compressive normal stress could still be transferred with the initial stiffness.

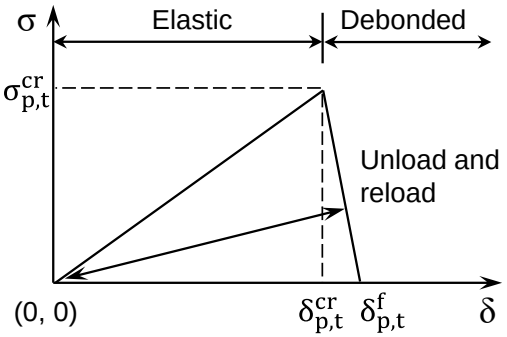

Figure 6.6. Stress-separation (σ-δ) relation for steel-GFRP adhesive bond.

The critical peel stress (σ_p^{cr}) was input as the tensile strength of the adhesive, i.e. $f_{t,a}$ = 33.7 MPa. The critical tangential stress (σ_t^{cr}) was input as the shear strength of the adhesive, i.e. $\tau_a = 0.8 f_{t,a}$ = 27.0 MPa based on the empirical correlation concluded in [52] where the shear-slip behaviour of steel-FRP bonded joints was investigated using linear brittle epoxy adhesives 1-2 mm in thickness. Between the contact pair, the contact stiffness in the normal ($\sigma_p^{cr}/\delta_p^{cr}$ and σ_c/δ_c) and tangential ($\sigma_t^{cr}/\delta_t^{cr}$) directions were calculated based on a linear elastic and isotropic deformation of the adhesive layer:

$$\sigma_p^{cr}/\delta_p^{cr} = \sigma_c/\delta_c = E_a/t_a \tag{6.5}$$

$$\sigma_t^{cr}/\delta_t^{cr} = G_a/t_a \tag{6.6}$$

$$G_a = \frac{E_a}{2(1+v_a)} \tag{6.7}$$

where σ_c and δ_c are the stress and relative displacement between the contact pair in the normal compressive direction; t_a (1.5 mm) is the thickness of the adhesive; G_a is the shear modulus of the adhesive; E_a (4.09 GPa) and v_a (0.28) are the elastic modulus and Poison's ratio.

6.4. Results and Discussion

6.4.1. Moment-Rotation Responses and Failure Modes

The moment-rotation (M-θ) hysteresis responses of all the specimens are presented in Figure 6.7 where the bending moment M was calculated considering a lever arm of 946 mm measured horizontally from the loading position to the centre of the steel flange-plates. The rotation angle θ was derived from the vertical deflections measured by the displacement gauges [Figure 6.2 (a)]:

$$\theta = \frac{D_3 - D_2}{L_{2,3}} - \frac{D_1}{L_1} \tag{6.8}$$

where D_i = deflection measured by displacement gauge i, $L_{2,3}$ = 150 mm, and L_1 = 75 mm

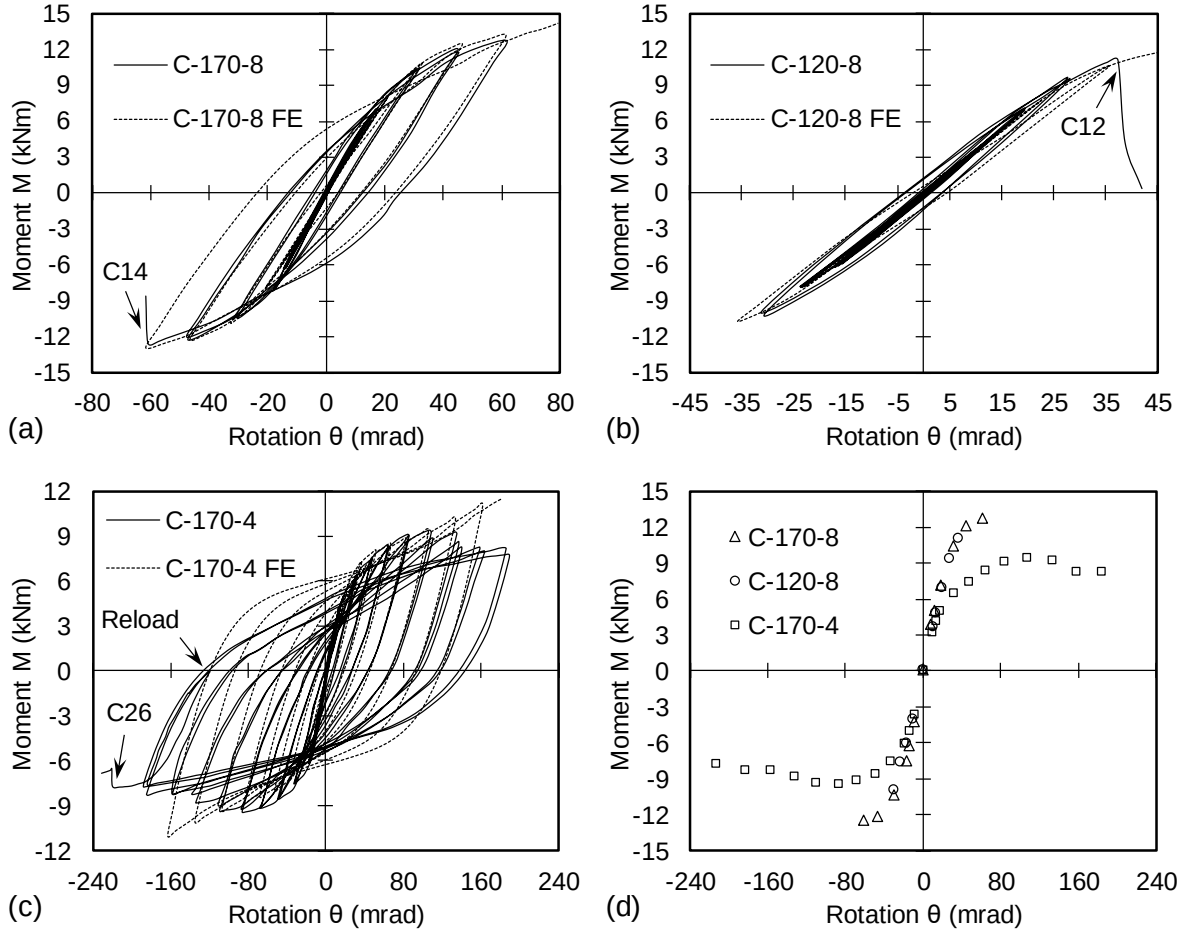

Figure 6.7. Moment-rotation (*M-θ*) responses: (a) specimen C-170-8; (b) C-120-8; (c) C-170-4; (d) envelop curves of all specimens.

The *M-θ* curve of specimen C-170-8 [Figure 6.7 (a)] started to show identifiable nonlinearity and residual rotation (upon unloading to 0 kNm) in the 10th cycle (C10). The nonlinearity, due to yielding of the steel-flange plate (to be discussed in Section 6.4.3), continued to develop as the cycle amplitude increased. In the upward excursion of C14, the specimen attained its peak bending moment (M_u) of +12.74 kNm; in the downward excursion of the same cycle ultimate failure occurred at −12.49 kNm as cracking happened near the lower web-flange junctions of the GFRP SHS member [Figure 6.8 (a)], which was instantly followed by debonding between the steel and the GFRP SHS member at the upper face. Similar to in C-170-8 and because of the same bolt configuration, the

M-θ curve of C-120-8 started its nonlinearity in C10 due to yielding of the steel flange-plate. But with a shorter bond length of 120 mm, C-120-8 was unable to withstand C12 and failed in the upward excursion at M_u of +11.04 kNm. The failure mode of C-120-8, shown in Figure 6.8 (b), was similar to that of C-170-8, except that the GFRP web-flange cracking and the debonding occurred at the reversed sides compared to in C-170-8. Presented in Figure 6.7 (c), specimen C-170-4 exhibited the most ductile *M*-θ hysteresis response because it experienced the most substantial yielding in the steel flange-plate, as visualised by the opening between the flange-plates highlighted in Figure 6.8 (c). In Figure 6.7 (c), C-170-4 started to develop residual rotation in C10, and in the downward excursion of C16 reached its peak bending moment (M_u) of −9.47 kNm. After that the peak *M* in each cycle started to gradually deteriorate. After C25 during which the stroke limit of the hydraulic jack (±125 mm) was attained, an extension bar was attached to the jack and C-170-4 was reloaded downwards until occurrence of ultimate failure at rotation $\theta = -220.5$ mrad. The ultimate failure was highlighted in Figure 6.8 (c) as the fracture of the steel flange-plates near the corner welding of the steel SHS.

The envelops of the *M*-θ responses of the three specimens are plotted together in Figure 6.7 (d) with the key performance results summarised in Table 6.3. A comparison of C-170-8 and C-120-8 shows that the increase of bond length from 120 mm to 170 mm improved the initial rotational stiffness S_i (defined as the average secant stiffness of the first 3 cycles) by 12.9% (from 404 to 456 kNm/rad) and the peak moment capacity M_u by 15.4 % (from 11.04 to 12.74 kNm). Comparing C-170-8 and C-170-4, the change of bolt arrangement (from the 8-bolt to 4-bolt) resulted in 22.1% decrease in S_i (from 456 to 355 kNm/rad) and 25.7% decrease in M_u (from 12.74 to 9.47 KNm), but prevented the brittle failure of GFRP cracking and better utilized the yielding of steel, improving the ultimate rotation from 60.8 to 220.5 mrad.

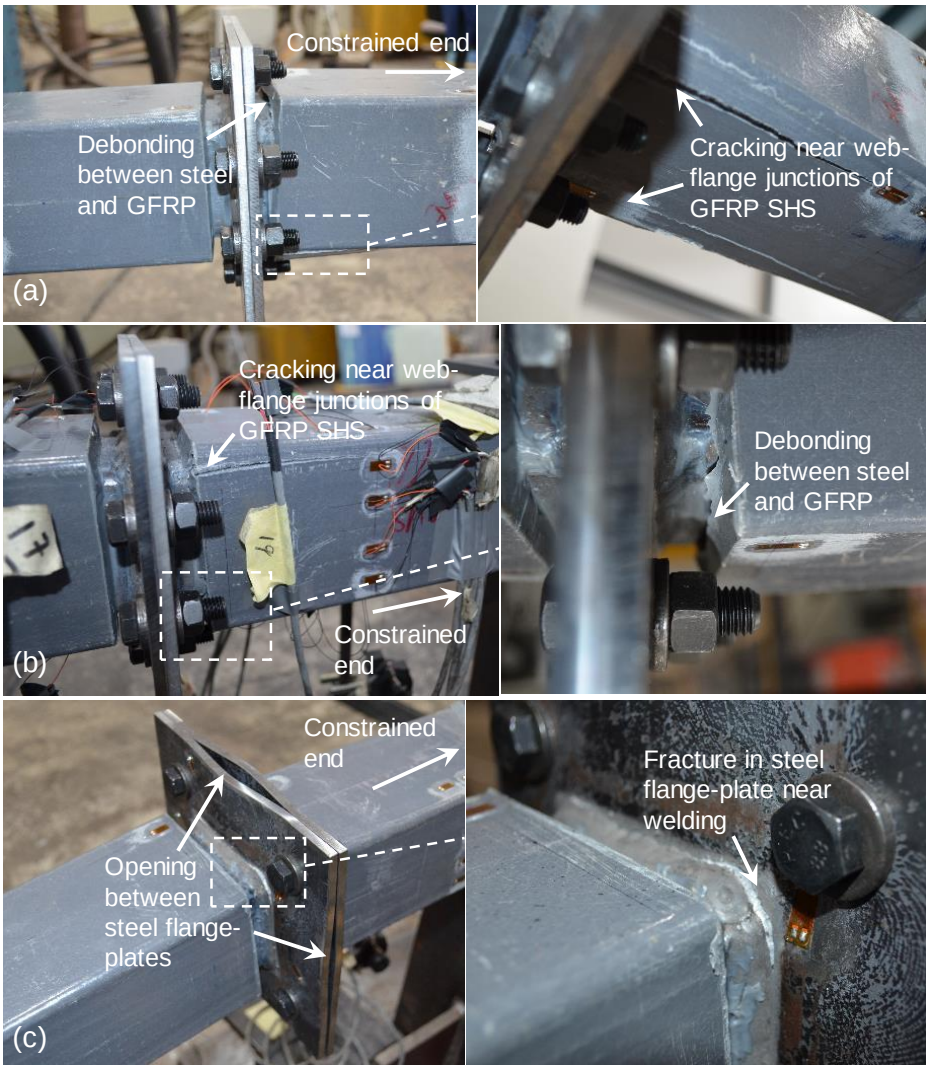

Figure 6.8. Failure modes: (a) specimen C-170-8; (b) C-120-8; (c) C-170-4.

Table 6.3. Mechanical performance of all specimens under cyclic loading.

Specimen	**Rotational stiffness (kNm/rad)** [a, b]		**Peak moment (kNm)** [b, c]		**Failure cycle**	**Ultimate rotation (mrad)** [c]	**Accumulated dissipated energy (kJ)**
	S_i	$S_{i,FE}$	M_u	$M_{u,FE}$			
C-170-8	456	425	12.74 (+)	14.45 (+)	14	60.8 (−)	2.36
C-120-8	404	385	11.04 (+)	12.93 (+)	12	37.3 (+)	0.57
C-170-4	355	333	9.47 (−)	11.35 (+)	26	220.5 (−)	21.85

[a] Average secant stiffness of the first 3 cycles.

[b] Subscript 'FE' means result from FE modelling.

[c] '+' means in the upward excursion, '−' means downward.

The *M-θ* responses from the FE modelling are also plotted in Figure 6.7 (a-c) alongside the experimental results. Overall, the FE modelling is able to well capture the hysteresis responses in terms of the nonlinear behaviours and residual rotations. More detailed comparisons of stiffness and strength evolution are presented in the following section. For C-170-8 and C-120-8, the peak moment from FE modelling ($M_{u,FE}$) was determined by checking the stress state of the GFRP member against the Tsai-Wu failure criterion, as further discussed in Section 6.4.4. For C-170-4, from C20 onwards the FE *M-θ* curve started to show evident deviation from the experimental curve with overestimation of the bending moment. This happened because fracture might have been initiated in the steel flange-plates in the experimental scenario but such steel fracture was not considered in the FE modelling. In FE modelling, the ultimate failure and $M_{u,FE}$ of C-170-4 (Table 6.3) was deemed to be attained when the von-Mises stress in the steel flange-plate reached the steel ultimate strength of 467.2 MPa.

6.4.2. Cyclic Performance

In this study the cyclic performance of the specimens is evaluated in regard to their stiffness and strength evolutions and energy dissipation capacities. The evolutions of stiffness and strength versus the loading cycles are plotted in Figure 6.9 (a) and (b) respectively. Herein the stiffness and strength of each cycle are the secant stiffness (S_s) and bending moment (M) when the loading displacement reversed in direction. Of each cycle the average values (S_s and M) of the upward and downward excursions were adopted, considering the reasonable symmetry of the *M-θ* responses (Figure 6.7). In Figure 6.9 (a), generally for all the specimens, the stiffness fluctuated slightly in C1 to C6 before declining continuously afterwards as yielding developed in the steel flange-plate. The most notable drop in stiffness occurred between C9 and C10, where the cycle amplitude increased from $1.0\delta_y$ to $1.5\delta_y$ (Figure 6.4). Comparing the stiffness evolution of specimens C-170-8 (presented as black triangles) and C-120-8 (red circles) which had the same bolt arrangement, C-120-8 showed slightly lower stiffness in C1 to C9 because of the shorter bond length. However, as the stiffness degraded further (yielding of the

steel flange-plates became more substantial) the stiffness of the two specimens converged towards each other. Compared to C-170-8 and C-120-8, the overall lower S_s of C-170-4 (green squares) shows that the bolt arrangement has a greater effect on the stiffness than the bond length. Among the specimens, C-170-4 sustained the most extended stiffness degradation because of the most substantial steel yielding before ultimate failure. In Figure 6.9 (b) which presents the strength evolution, the bending moment (M) sustained by C-170-8 (black triangles) and C-120-8 (red circles) shows steady increase with the cycle amplitude, until the brittle ultimate failure of GFRP. In contrast, the M of C-170-4 stabilized and deteriorated slowly after peaking at C16, because the brittle GFRP failure was preceded by substantial yielding of the steel flange-plates.

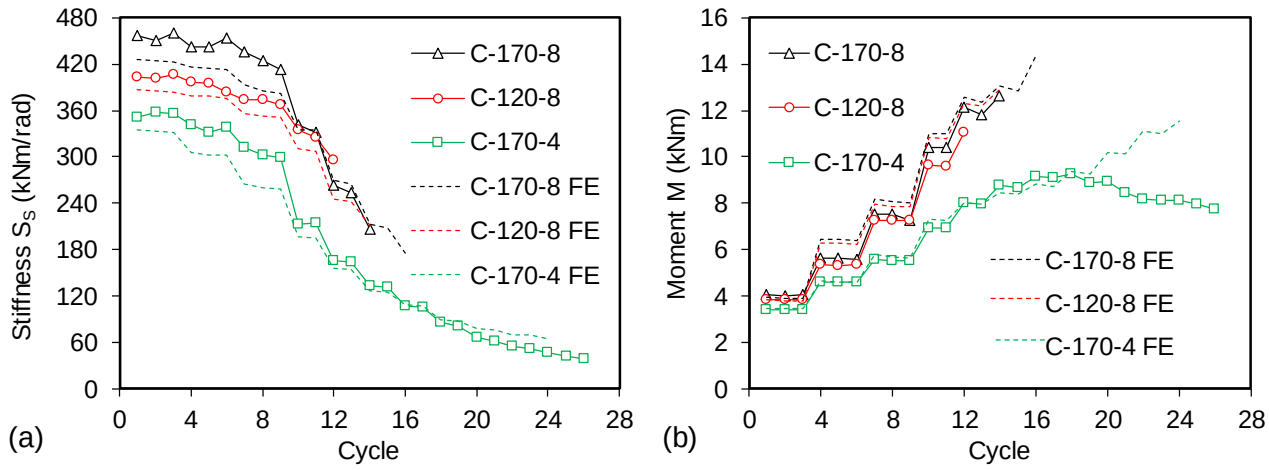

Figure 6.9. Evolution of (a) stiffness (S_s) and (b) strength (M) of the specimens.

The evolutions of stiffness and strength from FE modelling are also plotted in Figure 6.9 (a) and (b) as the dashed lines. In Figure 6.9 (a), the FE modelling was able to capture the stiffness degradation, although the stiffness in the first nine cycles was underestimated (within 15%). The underestimation may be attributed to the neglect of the minor initial bowing deformation of the steel flange-plates induced through welding to the steel SHS member. This deformation resulted in minor gaps between the steel flange-plates which were subsequently closed when the bolts were pre-tensioned. The initial deformation of the flange-plates was shown in [53] to slightly increase the initial flexural

stiffness of the bolted flange joint. The strength evolution produced by FE modelling [Figure 6.9 (b)] also agreed well with the experimental results (difference within 13%) before occurrence of ultimate failure or strength deterioration. The overestimation of the ultimate strength of C-170-8 and C-120-8 is to be discussed in Section 6.4.4. In C-170-4, while the experimental result of strength stabilized and deteriorated after C16, due to excessive yielding and possibly fracture in the steel flange-plates, the FE results kept increasing steadily. This was, again, due to the absence of a fracture behaviour for the steel material in the FE modelling.

The energy dissipation performance of the specimens is shown in Figure 6.10 as the accumulated dissipated energy versus the loading cycles. In each cycle the dissipated energy was calculated as the area enclosed by the M-θ hysteresis loop. For all the specimens, energy dissipation was hardly visible until C10 where a notable drop in stiffness happened compared to C9 [Figure 6.9 (a)]. Up to C14 where its ultimate failure occurred, C-170-8 dissipated the most energy due to its highest stiffness (highest bending moment at similar imposed rotation). Beyond C14, C-170-4 obviously outperformed the others with a total dissipated energy of 21.85 kJ as it withstood the most loading cycles by full utilization of the plastic deformation of the steel flange-plates. In comparison to C-170-8, C-120-8 exhibited inferior cyclic performance with 12.9% lower rotational stiffness (first 3 cycles S_i), 15.4% lower peak moment (M_u) and 75.8% lower energy dissipation. C-170-4 presented a remarkable 825.8% higher energy dissipation than C-170-8, while was 22.1% and 25.7% lower in S_i and M_u respectively. Nevertheless, C-170-4 still had a S_i that amounted to 109.1% of a continuous member (considering a connection length of 392 mm as per Figure 6.2) and a M_u equal to 28.8% of the theoretical elastic moment capacity of the connected section. For the configuration of C-170-4, the excellent energy dissipation capacity, along with the satisfactory rotational stiffness and strength, suggests its potential for application in seismic regions with brittle pultruded FRP members.

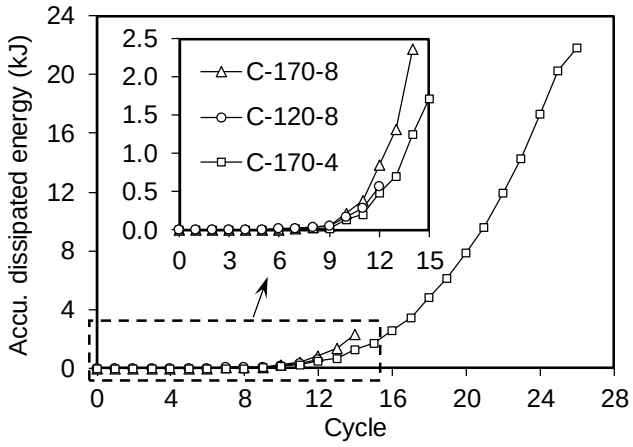

Figure 6.10. Accumulated energy dissipation of the specimens.

6.4.3. Local-Strain Responses

Mechanical responses that are not distinguishable in the *M*-θ results may be reflected in the strain responses. To indicate the interaction between the bonded steel and GFRP SHS members, the strain profiles of the bonded section are plotted at the maximum positive *M* of different cycles in Figure 6.11, based on the measurement of strain gauges G1 to G6 installed on the surface of the GFRP member [Figure 6.2 (b-d)]. In specimen C-170-8 [Figure 6.11 (a)], the strain profile was close to linear in the early cycles (e.g. C6, C9 and C11) but showed apparent nonlinearity at C13 and C14, implying a degradation in the interaction between the steel and the GFRP sections and thus possible damage in the adhesive bond in later stage of the cyclic loading. In C-120-8 with a shorter bond length [Figure 6.11 (b)], the deviation of strain profile from linearity could be identified at C11 and C12.

For strain gauges G1, G2, G5 and G6, the load-strain responses are plotted in Figure 6.12. In both C-170-8 and C-120-8, in the first nine cycles (C1 to C9) the load-strain responses were almost linear. In C-170-8 [Figure 6.12 (a)] the first appearance of nonlinearity was observed in the G5 and G6 curves at −9.13 kNm of C10; then at +10.07 kNm of C12, nonlinear responses also occurred in the G1 and G2 curves. Likewise, in C-120-8 [Figure 6.12 (b)] similar nonlinearity first appeared in the G5 and G6 curves at −8.51 kNm of C10 before in the G1 and G2 curves at +8.36 kNm of C12. These

nonlinearities in the load-strain responses, most likely caused by damage in the adhesive bond, were all initiated at or near the compression flange (negative strain). The strain gauges in Figure 6.12 (G1, G2, G5 and G6) were positioned near the GFRP end of the bonded region, where the compression flange was characterised with an adhesive stress state of peel-and-shear while the tension flange was characterised with a state of compressive-and-shear. The initiation of the load-strain nonlinearities at the compression flange suggested that damage in the adhesive bond was more likely to be induced by a stress state of peel-and-shear than compressive-and-shear. This finding was consistent with the damage criterion of Eq. (6.1) adopted in the FE modelling. The load-strain responses of G6 by FE modelling are also presented in Figure 6.12 as the dashed curves. It can be seen that, with the modelling of debonding behaviour, the FE results were able to capture the nonlinear responses, although at a relatively later stage, i.e. at −10.52 kNm of C12 for C-170-8 and at −9.17 kNm of C10 for C-120-8.

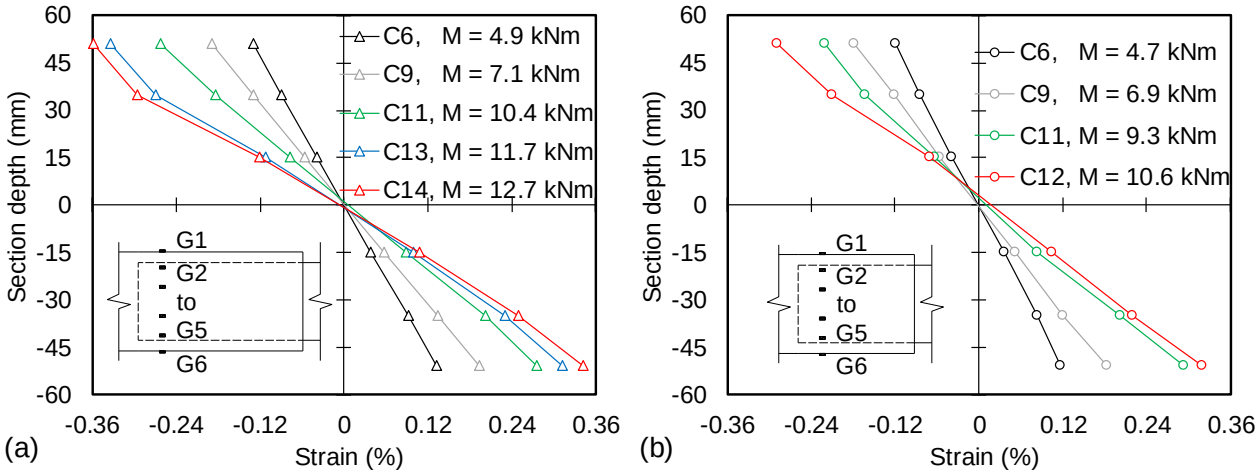

Figure 6.11. Strain profiles of the steel-GFRP bonded section at different cycles: (a) C-170-8; (b) C-120-8.

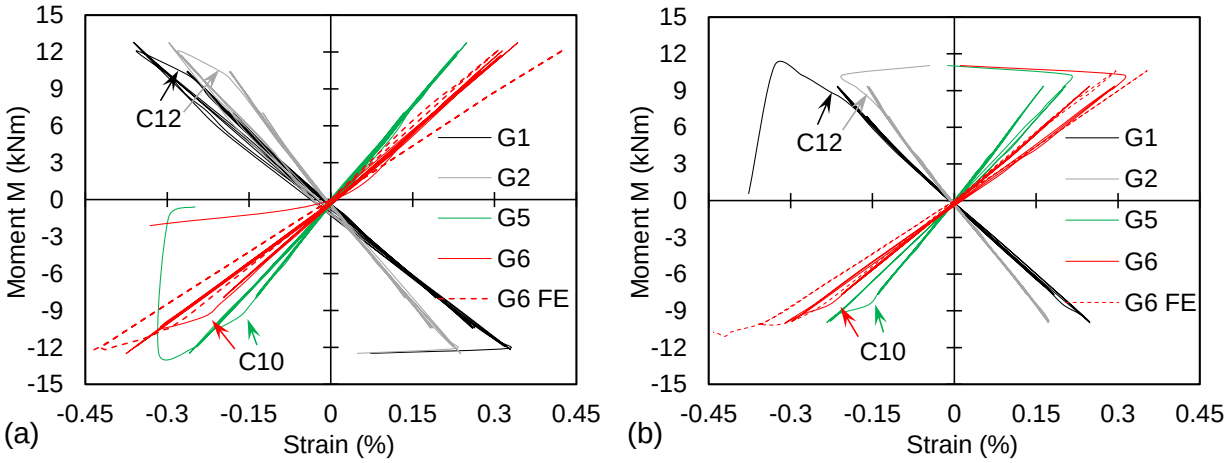

Figure 6.12. Load-strain responses from strain gauges G1, G2, G5 and G6: (a) C-170-8; (b) C-120-8.

The damage in adhesive bond was further evidenced by the load-strain responses from G9 as presented in Figure 6.13. In C10 the tensile strain in both C-170-8 and C-120-8 experienced a release when the bending moment increased beyond −9.52 kNm and −8.71 kNm respectively. This response, also captured in the FE modelling at −10.9 kNm of C12 for C-170-8 and at −8.40 kNm of C10 for C-120-8, was associated with the onset of debonding at the position as exemplified in Figure 6.14 for C-120-8. Figure 6.14 presents the total contact stress, as the vector sum of the normal and tangential stresses, over the steel-GFRP bonded area, at the load level where the strain release (G9) was captured in the FE modelling. The highlighted debonded areas, representing the regions where the contact status was loaded into the debonded stage (Figure 6.6), mainly appeared at the GFRP end because of its smaller stiffness than the steel member [54]. Also noteworthy is that at this load level the debonded area appeared and expanded over the projected position of G9, resulting in the release of tensile strain in the detached region of the GFRP. Total contact stress beyond a trivial level was noted in the debonded areas. This may be resulted from i) the existence of normal compressive stress which could still be transferred in the debonded regions; and ii) the debonding slope defined for the stress-separation behaviour (Figure 6.6) to overcome convergence difficulty (Section 6.3.2), resulting in a quick reduction but not immediate loss of the peel and tangential stresses.

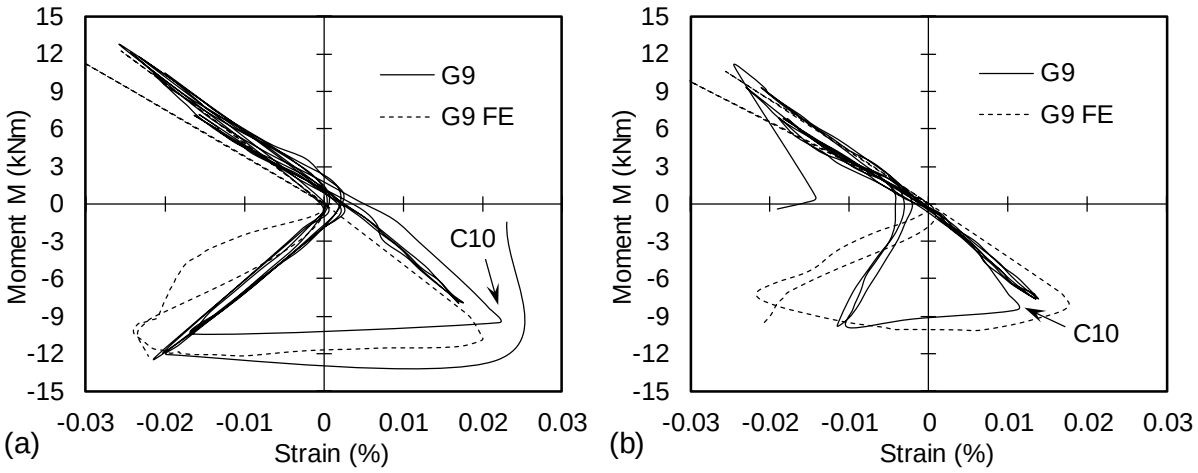

Figure 6.13. Load-strain responses from strain gauges G9: (a) C-170-8; (b) C-120-8.

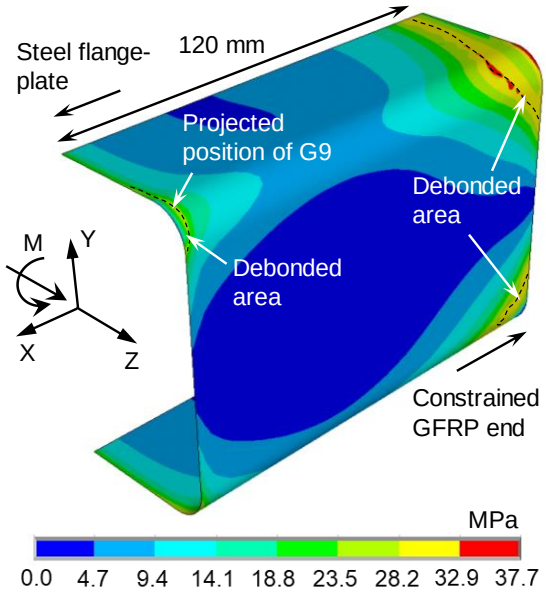

Figure 6.14. Distribution of total contact stress over the bonded area from FE modelling (C-120-8 at $M = -8.40$ kNm of C10).

The strain data from the strain gauges on the steel flange-plates [G17 to G20 in Figure 6.2 (e)] can provide a direct indication of steel yielding, as a verification of the failure modes and M-θ responses. The envelop curves of the load-strain responses are plotted in Figure 6.15 with indication of the steel yield strain (0.182%). In both C-170-8 [Figure 6.15 (a)] and C-170-4 [Figure 6.15 (b)], the yield strain was first attained in C10,

at +8.28 kNm (G19) and at +6.02 kNm (G18) respectively, echoing the observation of residual rotations in C10 from the *M-θ* responses. For C-170-8 where the deformation of the steel flange-plate was difficult to visually notice, the strain responses presented in Figure 6.15 (a) can evidence the yielding of the steel flange-plate. Figure 6.15 (b) shows that the yielding in C-170-4 was more substantial. Besides this, in the curve of G17 which was positioned near the ultimate steel fracture, the envelop strain of C22, compared to that of C21, experienced a decrease although with an increased cycle displacement amplitude, signalling possible initiation of the steel fracture.

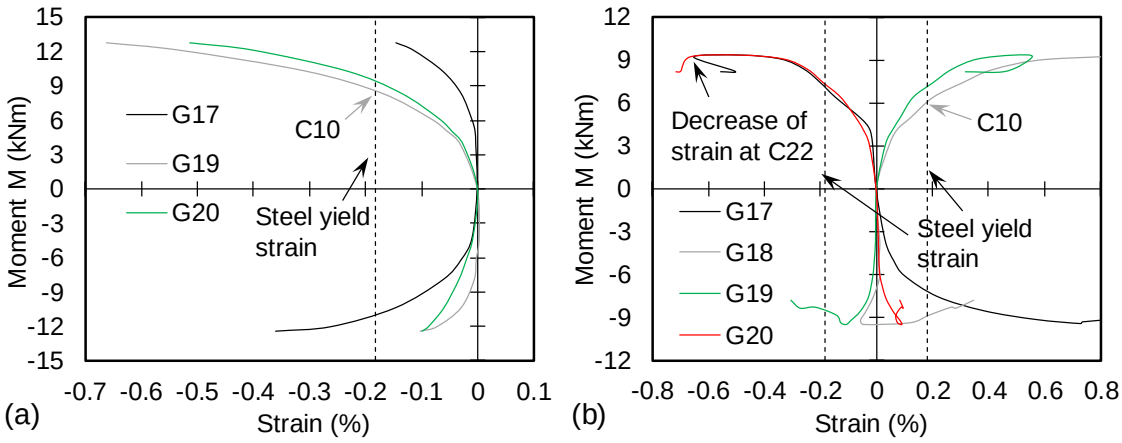

Figure 6.15. Envelop curves of load-strain response from strain gauges on the steel flange-plates: (a) C-170-8; (b) C-170-4.

6.4.4. GFRP Failure

The ultimate failure of specimens C-170-8 and C-120-8, i.e. cracking of the GFRP SHS member near the web-flange junctions, was predicted in the FE modelling by detecting the exceedance of Tsai-Wu failure criterion. For these two specimens, the distributions of Tsai-Wu failure index (I_F) on the GFRP members (at the constrained side) are presented in Figure 6.16 where $I_F > 1.0$ indicates exceedance of the failure criterion. Due to the brittle failure mode, in FE modelling the ultimate bending moments ($M_{u,FE}$) of C-170-8 and C-120-8 were deemed to be reached when $I_F > 1.0$. As shown in Figure 6.16 (a) and (b), $M_{u,FE}$ of both C-170-8 and C-120-8 was reached in an upward loading

excursion as failure was initiated (I_F > 1.0) at the inside of the upper web-flange junctions. This failure initiation signalled an imminent cracking of the GFRP member near the web-flange junctions as observed in the experiments. As the crack development of the GFRP was not modelled, the major debonding [Figure 6.8 (a-b)] that instantly followed was not reflected in the modelling either. The ultimate bending moments of C-170-8 and C-120-8 from experimental testing (M_u) and FE modelling ($M_{u,FE}$) are listed in Table 6.3. The FE modelling overestimated the ultimate moment by less than 18%, resulting in the occurrence of failure one cycle later than the experimental result for C-170-8 and two cycles later for C-120-8. A possible reason for the overestimation is that pultruded FRP members usually exhibit weaker strength at or near the web-flange junctions than in the flanges or webs [55, 56].

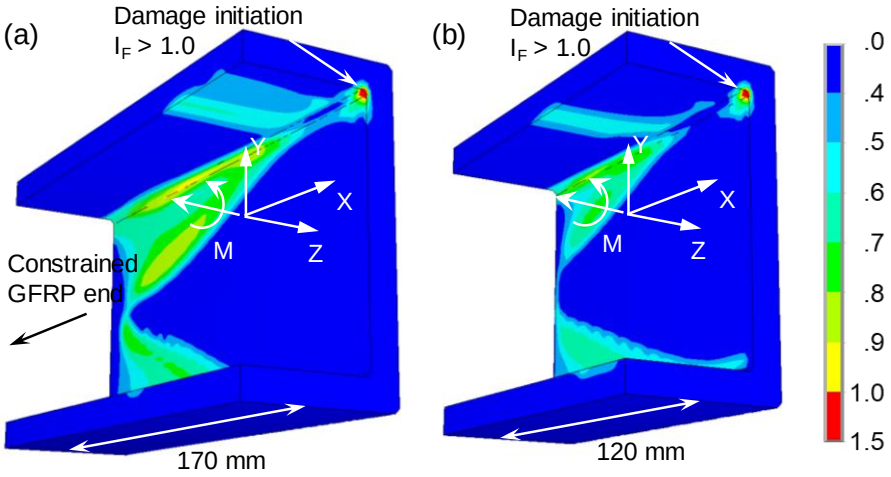

Figure 6.16. Distribution of Tsai-Wu failure index (I_F) on the GFRP from FE modelling: (a) C-170-8 at $M_{u,FE}$ = +14.45 kNm; (b) C-120-8 at $M_{u,FE}$ = +12.93 kNm.

6.5. Conclusions

This paper investigated the cyclic flexural performance of splice connections developed for hollow section FRP members. The splice connection specimens, each comprised of a steel bolted flange joint between two hollow section steel-GFRP bonded sleeve joints, were prepared in three configurations with difference in bond length or bolt arrangement.

Based on the results from the experiments and the corresponding FE modelling, the following conclusions can be drawn:

1. Under the cyclic flexural loading, the specimens experienced different levels of yielding in the steel flange-plates before ultimate failure in the mode of GFRP cracking near the web-flange junctions, i.e. in C-170-8 (the specimen with 170 mm steel-GFRP bond length and eight bolts at the steel flange-plate) and C-120-8, or fracture in the steel flange-plate, i.e. in C-170-4. Specimen C-170-8 exhibited the highest rotational stiffness (456 kNm/rad) and ultimate moment capacity (12.74 kNm); while C-170-4 presented the most ductile moment-rotation behaviour and the highest rotation capacity (220.5 mrad).

2. In terms of cyclic performance, through yielding of the steel flange-plate, the specimens began to show energy dissipation as their cycle secant stiffness underwent a steady degradation. The energy dissipation capacity of C-170-8 (with 170 mm-bond length and eight bolts) and C-120-8 was limited by the brittle failure of GFRP cracking prior to substantial yielding in the steel flange-plate. C-170-4, without significant compromise in the rotational stiffness (22.2% lower than C-170-8) and peak bending moment (25.7% lower), showed remarkably improved total energy dissipation (825.8% higher) by fully exploiting the plastic deformation of the steel flange-plate before failure in the GFRP.

3. In the steel-GFRP bonded sleeve joint of the splice connection, damage in the adhesive bond could be identified from the nonlinear strain profile of the bonded section, and further evidenced from the nonlinearity and strain release in the load-strain responses. The strain data of the steel flange-plate was able to indicate steel yielding which may be difficult to identify from the deformations and moment-rotation responses; from the steel strain data of specimen C-170-4 (with 170 mm-bond length and four bolts), the decrease of cycle envelope strain may signal the initiation of the ultimate steel fracture.

4. The FE modelling produced moment-rotation responses that agreed well with the experimental results. Before failure or deterioration of strength, for all the specimens the difference in stiffness evolution was within 15% and that in strength evolution was within 13%. With the definition of a debonding behaviour, the FE modelling was able to capture the nonlinear load-strain responses in the steel-GFRP bonded sleeve joint. The

ultimate failure of web-flange cracking in the GFRP member (in C-170-8 and C-120-8 with eight bolts but different bond length) was predicted by examining the GFRP stress state against the Tsai-Wu failure criterion. Using this modelling approach, the location of failure initiation could be satisfactorily predicted, and the ultimate moments were overestimated within 18%.

The ductility and energy dissipation capacity are important considerations in the design of a frame structure, especially one with brittle FRP members. The cyclic performance of specimen C-170-4 demonstrated the possibility of substantial energy dissipation at connection level using the developed splice connection. To realize this favourable performance, it is important that the splice connection is designed with a strength governed by the plastic deformation of the steel flange-plates, thereby delaying or preventing the brittle FRP web-flange junction cracking during the course of a seismic loading. The geometries of the flange-plates (e.g. thickness, number and position of bolts etc.) and the steel-FRP bond length are design variables that could be modified to fulfill the objective of energy dissipation as well as other design requirements such as connection stiffness and strength.

6.6. Acknowledgements

This work was supported by the Australian Research Council through Discovery Project DP180102208. The authors are grateful to the staffs of the Civil Engineering Laboratory of Monash University for their support during the experiment program.

6.7. References

1. Teng J, Chen J, Smith ST, Lam L. Behaviour and strength of FRP-strengthened RC structures: a state-of-the-art review. Proceedings of the Institution of Civil Engineers − Structures and Buildings. 2003;156(1):51-62.
2. Zhao X-L, Zhang L. State-of-the-art review on FRP strengthened steel structures. Engineering Structures. 2007;29(8):1808-23.
3. Meyer R. Handbook of Pultrusion Technology. Springer Science & Business Media, 2012.

4. Kumar P, Chandrashekhara K, Nanni A. Structural performance of a FRP bridge deck. Construction and Building Materials. 2004;18(1):35-47.
5. Hayes MD, Ohanehi D, Lesko JJ, Cousins TE, Witcher D. Performance of tube and plate fiberglass composite bridge deck. Journal of Composites for Construction. 2000;4(2):48-55.
6. Zhang D, Zhao Q, Huang Y, Li F, Chen H, Miao D. Flexural properties of a lightweight hybrid FRP-aluminum modular space truss bridge system. Composite Structures. 2014;108:600-15.
7. Yang X, Bai Y, Ding F. Structural performance of a large-scale space frame assembled using pultruded GFRP composites. Composite Structures. 2015;133:986-96.
8. Satasivam S, Bai Y, Zhao X-L. Adhesively bonded modular GFRP web–flange sandwich for building floor construction. Composite Structures. 2014;111:381-92.
9. Satasivam S, Bai Y, Yang Y, Zhu L, Zhao X-L. Mechanical performance of two-way modular FRP sandwich slabs. Composite Structures. 2018;184:904-16.
10. Xie L, Qi Y, Bai Y, Qiu C, Wang H, Fang H, et al. Sandwich assemblies of composites square hollow sections and thin-walled panels in compression. Thin-Walled Structures. 2019;145:106412.
11. Bank LC, Mosallam AS, McCoy GT. Design and performance of connections for pultruded frame structures. Journal of Reinforced Plastics and Composites. 1994;13(3):199-212.
12. Bank L, Mosallam A, Gonsior H. Beam-to-column connections for pultruded FRP structures. In: Serviceability and Durability of Construction Materials, ASCE, 1990. p.804-13.
13. Mosallam AS, Abdelhamid MK, Conway JH. Performance of pultruded FRP connections under static and dynamic loads. Journal of Reinforced Plastics and Composites. 1994;13(5):386-407.
14. Bank LC, Yin J, Moore L, Evans DJ, Allison RW. Experimental and numerical evaluation of beam-to-column connections for pultruded structures. Journal of Reinforced Plastics and Composites. 1996;15(10):1052-67.

15. Smith S, Parsons I, Hjelmstad K. An experimental study of the behavior of connections for pultruded GFRP I-beams and rectangular tubes. Composite Structures. 1998;42(3):281-90.
16. Mottram J, Zheng Y. Further tests on beam-to-column connections for pultruded frames: Web-cleated. Journal of Composites for Construction. 1999;3(1):3-11.
17. Mottram J, Zheng Y. Further tests of beam-to-column connections for pultruded frames: flange-cleated. Journal of Composites for Construction. 1999;3(3):108-16.
18. Mottram J, Turvey GJ. Physical test data for the appraisal of design procedures for bolted joints in pultruded FRP structural shapes and systems. Progress in Structural Engineering and Materials. 2003;5(4):195-222.
19. Smith S, Parsons I, Hjelmstad K. Experimental comparisons of connections for GFRP pultruded frames. Journal of Composites for Construction. 1999;3(1):20-6.
20. Singamsethi S, LaFave J, Hjelmstad K. Fabrication and testing of cuff connections for GFRP box sections. Journal of Composites for Construction. 2005;9(6):536-44.
21. Wu C, Zhang Z, Bai Y. Connections of tubular GFRP wall studs to steel beams for building construction. Composites Part B: Engineering. 2016;95:64-75.
22. Zhang ZJ, Bai Y, Xiao X. Bonded Sleeve Connections for Joining Tubular Glass Fiber–Reinforced Polymer Beams and Columns: Experimental and Numerical Studies. Journal of Composites for Construction. 2018;22(4):04018019.
23. Martins D, Proença M, Correia JR, Gonilha J, Arruda M, Silvestre N. Development of a novel beam-to-column connection system for pultruded GFRP tubular profiles. Composite Structures. 2017;171:263-76.
24. Bruneau M, Walker D. Cyclic testing of pultruded fiber-reinforced plastic beam-column rigid connection. Journal of Structural Engineering. 1994;120(9):2637-52.
25. Mosallam A. Design Considerations for Pultruded Composite Beam-to-Column Connections Subjected to Cyclic and Sustained Loading Conditions. Marketing Technical Regulatory Sessions of the Composites Institutes International Composites Expo. 1997:14-B.
26. Carrion JE, LaFave JM, Hjelmstad KD. Experimental behavior of monolithic composite cuff connections for fiber reinforced plastic box sections. Composite Structures. 2005;67(3):333-45.

27. Zhang Z, Bai Y, He X, Jin L, Zhu L. Cyclic performance of bonded sleeve beam-column connections for FRP tubular sections. Composites Part B: Engineering. 2018;142:171-82.
28. Martins D, Proença M, Gonilha JA, Sá MF, Correia JR, Silvestre N. Experimental and numerical analysis of GFRP frame structures. Part 1: Cyclic behaviour at the connection level. Composite Structures. 2019;220:304-17.
29. Martins D, Sá MF, Gonilha JA, Correia JR, Silvestre N, Ferreira JG. Experimental and numerical analysis of GFRP frame structures. Part 2: Monotonic and cyclic sway behaviour of plane frames. Composite Structures. 2019;220:194-208.
30. Bank LC. Progressive failure and ductility of FRP composites for construction. Journal of Composites for Construction. 2012;17(3):406-19.
31. Nagaraj V, Gangarao HV. Fatigue behavior and connection efficiency of pultruded GFRP beams. Journal of Composites for Construction. 1998;2(1):57-65.
32. Manalo A, Mutsuyoshi H. Behavior of fiber-reinforced composite beams with mechanical joints. Journal of Composite Materials. 2012;46(4):483-96.
33. Hai ND, Mutsuyoshi H. Structural behavior of double-lap joints of steel splice plates bolted/bonded to pultruded hybrid CFRP/GFRP laminates. Construction and Building Materials. 2012;30:347-59.
34. Turvey G. Experimental and analytical investigation of two-and six-plate bonded splice joints on serviceability limit deformations of pultruded GFRP beams. Composite Structures. 2014;111:426-35.
35. Turvey GJ, Cerutti X. Flexural behaviour of pultruded glass fibre reinforced polymer composite beams with bolted splice joints. Composite Structures. 2015;119:543-50.
36. Turvey GJ, Cerutti X. Effects of splice joint geometry and bolt torque on the serviceability response of pultruded glass fibre reinforced polymer composite beams. Composite Structures. 2015;131:490-500.
37. Qiu C, Ding C, He X, Zhang L, Bai Y. Axial performance of steel splice connection for tubular FRP column members. Composite Structures. 2018;189:498-509.
38. Qiu C, Bai Y, Zhang L, Jin L. Bending Performance of Splice Connections for Assembly of Tubular Section FRP Members: Experimental and Numerical Study. Journal of Composites for Construction. 2019;23(5):04019040.

39. Standards Australia. AS4100 steel structures. Sydney, Australia, 1998.
40. ASTM International. Standard Test Method for Tensile Properties of Polymer Matrix Composite Materials. ASTM D3039. West Conshohocken, PA., 2014.
41. ASTM International. Standard Test Method for Compressive Properties of Rigid Plastics. ASTM D695-15. West Conshohocken, PA., 2015.
42. ASTM International. Standard Test Method for Flexural Properties of Polymer Matrix Composite Materials. ASTM D7264. West Conshohocken, PA., 2015.
43. ASTM International. Standard Test Method for Short-Beam Strength of Polymer Matrix Composite Materials and Their Laminates. ASTM D2344. West Conshohocken, PA., 2016.
44. Lee S, Munro M, Scott R. Evaluation of three in-plane shear test methods for advanced composite materials. Composites. 1990;21(6):495-502.
45. ASTM International. Standard Test Methods and Definitions for Mechanical Testing of Steel Products. ASTM A370-10. West Conshohocken, PA., 2010.
46. Zhang Z, Wu C, Nie X, Bai Y, Zhu L. Bonded sleeve connections for joining tubular GFRP beam to steel member: Numerical investigation with experimental validation. Composite Structures. 2016;157:51-61.
47. ASTM International. Standard Test Method for Tensile Properties of Plastics. ASTM D638-10. West Conshohocken, PA., 2010.
48. Krawinkler H. Guidelines for Cyclic Seismic Testing of Components of Steel Structures. Applied Technology Council, 1992.
49. Tsai SW, Wu EM. A general theory of strength for anisotropic materials. Journal of Composite Materials. 1971;5(1):58-80.
50. Trahair N, Bradford M. The Behaviour and Design of Steel Structures to AS 4100. Third Edition ed. Taylor & Francis, 1998.
51. de Castro J, Keller T. Ductile double-lap joints from brittle GFRP laminates and ductile adhesives, Part I: Experimental investigation. Composites Part B: Engineering. 2008;39(2):271-281.
52. Xia S, Teng J. Behaviour of FRP-to-steel bonded joints. In: Proceedings of the International Symposium on Bond Behaviour of FRP in Structures: International Institute for FRP in Construction, 2005. p.419-26.

53. Wheeler AT, Clarke MJ, Hancock GJ. FE modeling of four-bolt, tubular moment end-plate connections. Journal of Structural Engineering. 2000;126(7):816-822.
54. Qiu C, Feng P, Yang Y, Zhu L, Bai Y. Joint capacity of bonded sleeve connections for tubular fibre reinforced polymer members. Composite Structures. 2017;163:267-79.
55. Turvey GJ, Zhang Y. Tearing failure of web–flange junctions in pultruded GRP profiles. Composites Part A: Applied Science and Manufacturing. 2005;36(2):309-17.
56. Turvey GJ, Zhang Y. Shear failure strength of web–flange junctions in pultruded GRP WF profiles. Construction and Building Materials. 2006;20(1-2):81-9.

CHAPTER 7. CONCLUSIONS AND FUTURE WORKS

7.1. Conclusions

This research developed a splice connection for joining tubular section FRP members in building structures. The developed splice connection consisted of two types of component joints: a steel bolted flange joint and two steel-FRP bonded sleeve joints. Welded with a flange-plate at one end, a hollow section steel member was telescoped into and bonded to the targeted tubular section FRP member, forming a steel-FRP bonded sleeve joint; two such assemblies were then bolted together through the steel flange-plates, i.e. the steel bolted flange joint, to form a splice connection. Based on this conceptual design, splice connections with different bond length and bolt configuration were prepared and studied under axial, flexural and cyclic loadings. Overall, based on the results from experimental testing, the splice connection exhibited satisfactory stiffness and strength, and was able to impart ductility to brittle FRP members. Correspondingly, theoretical and numerical analyses were carried out and showed the capability in predicting and characterising the connection mechanical behaviours. More detailed conclusions drawn from this work are summarised as following.

7.1.1. From the Theoretical Study of the Bonded Sleeve Joint under Axial Loading

For the cohesive failure of the bonded sleeve joint under axial loading, a theoretical analysis was conducted with the employment of an elastic-softening bilinear bond-slip relation. One or three possible types of adhesive shear stress distribution, for the joint at elastic limit or ultimate state respectively, were theoretically formulated. Based on the shear stress distribution, the ultimate capacity of the joint was derived, showing good agreement with the test results of 14 joints, with the discrepancy between the theory and the tests less than 7%.

The shear stress distributions obtained from the theoretical analysis agreed well with the FE analysis using the same bilinear bond-slip relation, demonstrating the correctness of the theoretical analysis. For cases of cohesive failure, the theoretical and

FE analyses indicated the existence of effective bond length for the joint capacities at both the elastic limit and ultimate state, which was essentially related to the uneven shear stress distribution. With regard to the effect of adherend stiffness (*EA*) ratio (i.e. stiffness of the steel member to the FRP member), the joint capacity at elastic limit was optimised at a stiffness ratio of 1. In comparison, the stiffness ratio had trivial effect on the joint capacity at ultimate state, because of the much more gradual slope of the bond-slip relation at the softening stage than at the elastic stage.

In the theoretical study, simplification was made through adopting an axisymmetric circular cross-section for the bonded sleeve joint, i.e. without the consideration of the variation of adhesive shear stress in the transverse (or circumferential) direction.

7.1.2. From the Experimental and Numerical Studies of the Splice Connection under Axial Loading

Under axial loading, the bonded sleeve joint component of the splice connection failed in a brittle manner within the adhesive layer. The joint capacity showed nonlinear increase with the bond length, thus suggesting the existence of an effective bond length as well. Strain measurement along the bond length indicated damage in the adhesive bond before ultimate failure. For the square tubular section bonded sleeve joints, in contrast to the circular sections in the theoretical study, uneven shear stress in the transverse direction was identified from the strain measurement.

Failure of the steel bolted flange joint component of the splice connection was ductile through yielding of the steel flange-plates. The eight-bolt configuration exhibited 225% higher initial stiffness and 82% higher yield capacity than the four-bolt configuration. Ductile failure of a splice connection could be realized through brittle failure of the bonded sleeve joint preceded by the yielding of the bolted flange joint.

FE modelling featuring a bilinear bond-slip relation produced estimates of the capacity of the bonded sleeve joints within 15% from the experimental results. The effective bond length and the strain responses in the bonded region could also be captured. The validated FE modelling was used to visualise the shear stress distribution over the bonded area, revealing that the existence of effective bond length was associated

with an extended low-stress area when a long bond length was employed. As for the steel bolted flange joints, their load-deformation and strain responses could be accurately characterised by the FE modelling where yielding of steels, contact behaviour and bolt pre-tensioning were defined.

7.1.3. From the Experimental and Numerical Studies of the Splice Connection under Flexural Loading

Three configurations of splice connection, with difference in the bond length or the bolt arrangement, were studied under flexural loading. All the splice connections exhibited ductile moment-rotation response through yielding of the steel flange-plates. The ultimate failure occurred in the mode of excessive yielding of the flange-plates, web-flange cracking of the connected tubular FRP member, or fracture of the flange-plates near the weld toes.

The eight-bolt bolted flange joint, compared to the four-bolt configuration, improved the rotational stiffness and yield moment of the splice connection by 64% and 75%, respectively. The increased bond length of the bonded sleeve joint (170 vs. 120 mm) changed the ultimate failure from web-flange cracking of the FRP member to fracture of the flange-plates, and raised the ultimate moment by 11%. The increased bond length also delayed the damage in the adhesive bond, which was evidenced by the nonlinearity in the load-strain responses in the steel-FRP bonded region.

The initial stiffness and yielding behaviours of the splice connection, mainly controlled by the steel bolted flange joint, were accurately characterised by the FE modelling. Compared to in the axial loading scenario, the FE modelling further incorporated a mixed mode damage behaviour for the adhesive bond, due to the presence of normal stress as well as shear stress between the adherends. By this approach the nonlinear load-strain responses in the bonded sleeve joint could be captured. The web-flange cracking of the FRP member was predicted in the modelling by examining the stress state against the Tsai-Wu failure criterion; the failure location could be well captured and the failure moment was overestimated by within 12%.

7.1.4 From the Experimental and Numerical Studies of the Splice Connection under Cyclic Loading

Under a shear-and-moment cyclic loading, the three splice connections (same geometric parameters as in the flexural loading) experienced different levels of yielding in the steel flange-plates, before the ultimate failure in the mode of web-flange cracking of the FRP member or fracture of the flange-plate near the weld toes. Over the course of cyclic loading, the splice connections began to show energy dissipation as their cycle secant stiffness underwent a steady degradation due to yielding of the flange-plates. Excellent energy dissipation performance was demonstrated in a splice connection by full utilisation of the plastic deformation of the steel flange-plates.

FE modelling for the cyclic loading, compared to that for the monotonic flexural loading, further accounted for damage accumulation in the adhesive bond and kinematic hardening (after yielding) of the steel materials. Satisfactory agreement between the experimental testing and the modelling was achieved in terms of both moment-rotation hysteresis response and local strain response.

7.2. Proposed Future Works

7.2.1. On the Bonded Sleeve Joint Configuration

The bonded sleeve joint is a versatile configuration for assembling tubular section FRP members. Besides the use in the current splice connection, it can also be adapted to form other FRP connections, e.g. beam-to-column, truss-to-node, stud/column base etc. In the current splice connection, it has been shown that the behaviour of the steel bolted flange joint can be accurately characterised through analytical and numerical modelling. The bonded sleeve joint configuration, in contrast, may be of further research interest in terms of improved design and characterisation of mechanical behaviour, such as for the adhesive bonding and the web-flange junction of the connected FRP member.

In the current study the bonded sleeve joint was intended to realize a smooth stress transfer to the FRP member. Nonetheless, FE analysis (Chapters 3 to 6) revealed notably uneven stress distribution over the bonded area. In planar bonded lap joints, using a softer

adhesive has been shown to result in a more even stress distribution than a stiffer adhesive. Another recommendation in planar bonded joints is the use of a ductile adhesive, such that at ultimate state the full strength of the adhesive can be mobilized over an extended bonded area, compared to when a brittle adhesive is used. Considering the availability of adhesives of various characteristics, the effect of adhesive properties (e.g. stiff vs. soft, brittle vs. ductile etc.) on the performance of the bonded sleeve joint may be worth investigation.

The confidence in structural application of the bonded sleeve joint configuration requires an accurate and reliable prediction of the joint behaviours, which in turn requires a precise characterisation of the local bond behaviour. To date, there exist a variety of test methods for characterising the bond behaviours using relatively elemental joint configurations. Validation tests data of these methods are available but the tests mostly were also conducted with simple configurations. To this end, a systematic study may be needed to investigate the applicability and reliability of such charactering methods in predicting the behaviour of more complex bonded joints (e.g. the bonded sleeve joint).

The web-flange junctions have been identified a weak spot in pultruded FRP members. In Chapter 5 & 6, the ultimate failure of the splice connection was governed by the web-flange junctions of the FRP member. To strengthen against this type of failure, fibre fabrics or metallic parts may be bonded onto the FRP member, wrapping around the web-flange junctions. Another approach is to explore the use of FRP members made from the pull-winding process, which further incorporates crosswise fibres compared to the pultrusion process. Pull-wound FRP members are available in circular and square tubular sections, where the crosswise fibres will no doubt enhance the transvers and the web-flange junction strength. Comparing FRP members made from the pull--winding method against those from pultrusion, the extent of improvement in connection performance and the combined effect with compromised member longitudinal strength and stiffness (due to reduced 0-degree fibres) may be subjects worth investigation.

In Chapters 5 & 6 of the thesis, the failure loads governed by the web-flange junction of the FRP member were consistently overestimated by the FE modelling. It is

believed that in rectangular tubular section pultruded FRP members, the web-flange junctions exhibit weaker strength than the inner wall elements. Research may be needed to develop simple and effective methods for characterising the web-flange junction properties of pultruded FRP members. Preferably, for FRP members a correlation should be established between the web-flange junction properties and other commonly characterised material properties (e.g. tensile strength, fibre volume etc.).

7.2.2. On Incorporating the Connection in FRP Structures

The current thesis limits itself to the study of the splice connection under relatively basic loading scenarios. More complex or combined loading scenarios are expected if the splice connection is to be used in FRP structures. Further experimental studies may be required to understand the behaviour of the connection under combined loadings. Since experimental testing cannot be conducted to encompass every possible loading scenario and geometric variation, more reliable modelling methods, especially for the steel-FRP bonded sleeve joint, are also needed. The works in this thesis have focused on the short-term behaviour of the splice connection. To enable the application in actual structures, the creep and other long-term behaviours are also important areas of investigation.

In steel flexural members, splice connections are typically deployed in at locations of low bending moment. Simple adoption of this practice may not be the optimal approach for FRP members. Unlike steels with inherent ductility, FRPs are brittle. The study in Chapter 5 has shown that the developed splice connection is able to impart flexural ductility to the brittle FRP member. Research may be worth carrying out to investigate the effect of splice location on the performance of FRP structures, in order to realize an optimal combination of system strength and ductility.

With the axial, flexural and cyclic behaviours characterised in the current study, the splice connection, along with other available beam-column connections, can be incorporated into the structural analysis of FRP frame structures. By doing so, the influence of the connections stiffnesses and strengths on the deformation and load-carrying capacity of the frame structure can be evaluated. Furthermore, the energy dissipation capacity of structures under seismic loadings can be more realistically characterised. In addition, in FRP frame structures, effective and economical designs

should also be developed for secondary connections, such as beam-to-girder, slab/wall-to-beam, and purlin-to-rafter connections.

Finally, further works are underway to design a lightweight pultruded FRP frame structure using the current splice connection as well as the beam-column connection, roof connection and FRP sandwich floor system in the research team. The structural frame has been conceptualised and is being materialised into an FE model incorporating the connection behaviours. Structural analysis will be carried out using the FE modelling for load cases devised following relevant building codes. The deformation, stability and strength of the structure will be checked against the corresponding requirements stipulated in available pultruded FRP design guides and building codes. Following a finalised design, works will be commenced towards the erection of a demonstration structure made of pultruded FRPs.

APPENDIX

A.1. Supplementary Information for Chapter 4

A.1.1. Material Properties of Steel Flange-Plates

The material properties of the steel flange-plates were obtained following the guidance of ASTM A370-10 [A1]. The nominal dimensions of the dog bone-shape tensile samples are provided in Figure A.1 (nominal thickness was 6 mm as the steel flange-plates). The actual dimensions were measured using a digital calliper. The tensile tests were performed on an Instron machine with a 50 kN-capacity load cell. Tensile displacement was applied at a crosshead speed of 1mm/min. A laser extensometer was used to gauge the elongation of the sample. Two strain gauges were attached on each sample as shown in Figure A.1: one along the tensile direction and the other along the transverse direction. The strain data of these two strain gauges was used to calculate the Young's modulus and Poisson's ratio. A representative tensile stress-strain curve of the samples is presented in Figure A.1. Three samples were tested to obtain the material properties summarised in Table 4.2.

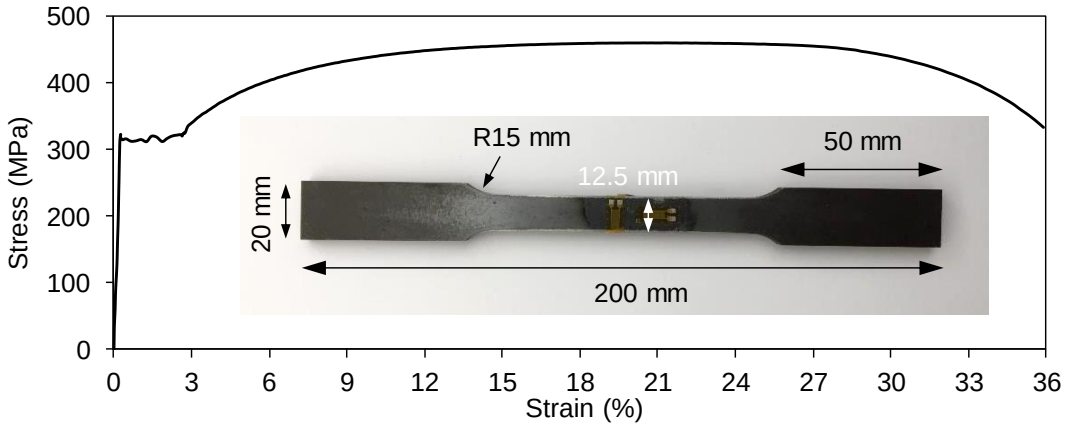

Figure A.1. Nominal dimensions and a representative tensile stress-strain curve of samples from the steel flange-plate (Chapter 4).

A.1.2. Load-Displacement Curves of Bonded Sleeve Joint Specimens

In Section 4.1 of Chapter 4, Figure 4.7 presents the compressive load-displacement curves of BSJ-180s (experiment and FE) as representative examples of the bonded sleeve joint (BSJ) specimens. Figure A.2 here presents the load-displacement curves of all the BSJ specimens.

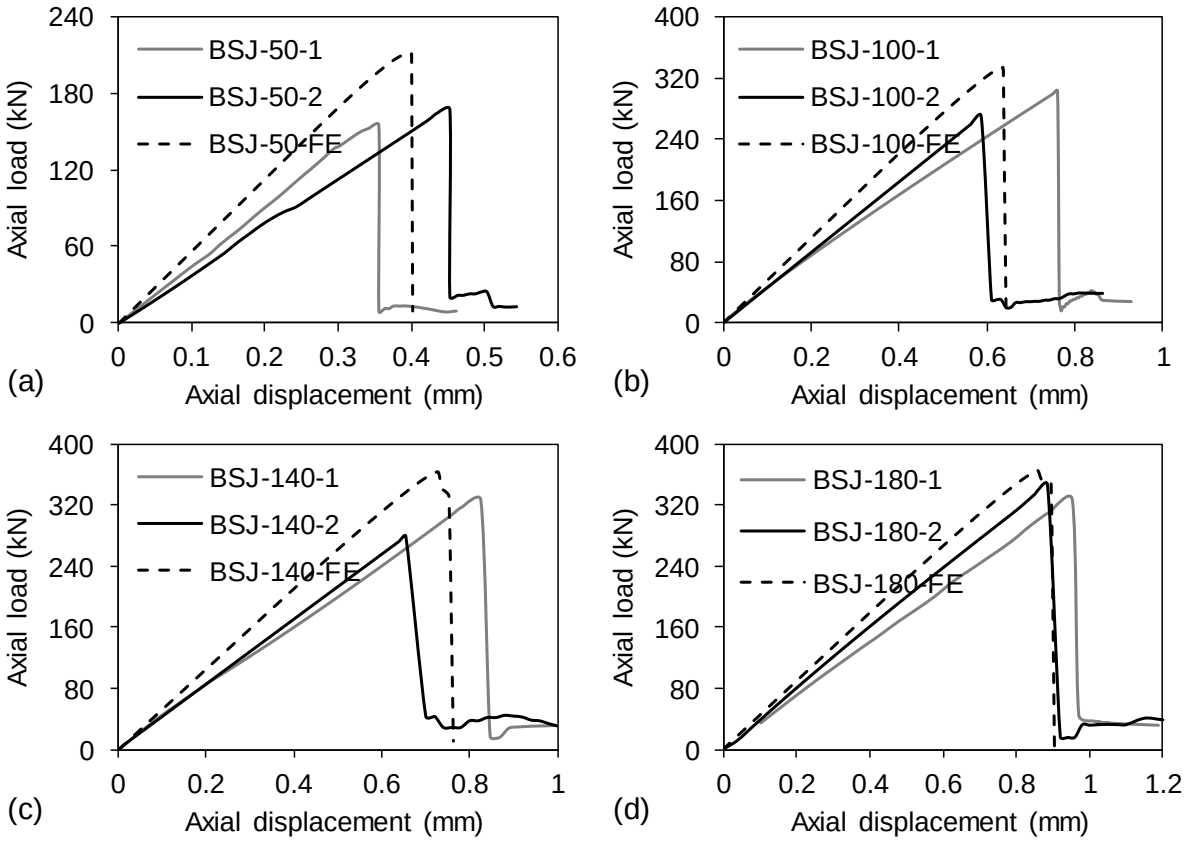

Figure A.2. Load-displacement curves of all BSJ specimens (Chapter 4).

A.2. Supplementary Information for Chapter 5

A.2.1. Tensile Strength and Modulus of GFRP Material

The tensile properties of the GFRP material were obtained following ASTM D3039 [A2]. Tensile samples, 250 mm in length and 25 mm in width (nominal dimensions), were cut

from the flat walls of the square tubular section profiles (102×102×9.5 mm) along the fibre direction. Tensile tests were performed using a 100 kN-capacity Instron machine. The loading rate was at 1.5 mm/min crosshead speed. A laser extensometer and strain gauges were used to gauge the tensile elongation of the samples. Five samples were tested; the average longitudinal tensile strength was 330.6 MPa with a standard deviation (std.) of 19.4; the average longitudinal tensile modulus was 25.2 GPa with a std. of 1.3. The fibre breakage failure and representative tensile stress-strain curves are presented in Figure A.3.

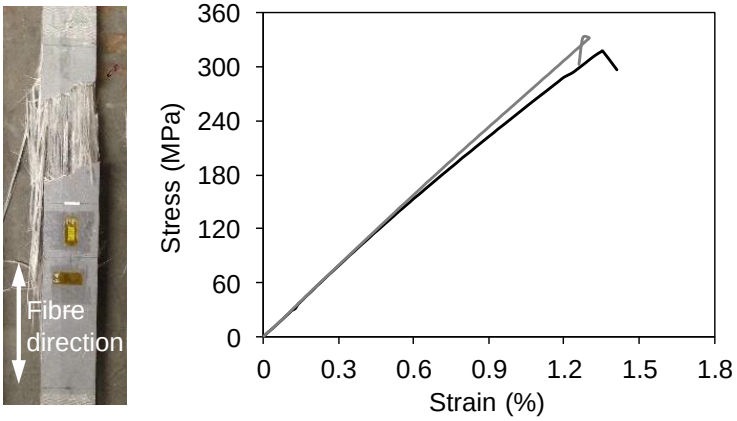

Figure A.3. Failure and representative tensile stress-strain curves of longitudinal samples from the GFRP profile.

A.2.2. In-Plane Shear Strength and Modulus of GFRP Material

The in-plane shear properties of the GFRP material were obtained using the 10° off-axis tensile test [A3]. The samples, cut at a 10° off the fibre direction from the flat walls of the GFRP profiles, were 250 mm in length and 25 mm in width (nominal dimensions, same as in the tensile test). Three strain gauges were attached on each sample as shown in Figure A.4: at 0°, 45° and 90° off the tensile direction. The tensile tests were performed on a 100 kN capacity Instron Machine. The tensile displacement was applied at a crosshead speed of 1.5 mm/min. The 10° shear stress τ_{10} was calculated by

$$\tau_{10} = -\frac{F}{2A} sin(2\theta) \quad \text{(A.1)}$$

where F = tensile force measured by the Instron machine;

A = measured cross section area of the sample;

θ = angle between the fibre direction and the tensile force direction = −10°.

The 10° shear strain γ_{10} was calculated using the strain values from the strain gauges:

$$\gamma_{10} = \frac{\varepsilon_{90} - \varepsilon_0}{2} sin(2\theta) + \frac{1}{2}[2\varepsilon_{45} - (\varepsilon_0 + \varepsilon_{90})cos(2\theta)] \quad \text{(A.2)}$$

where ε_0, ε_{45}, ε_{90} = strain from the strain gauge along the 0°, 45° or 90° direction.

Shear failure occurred along the fibre direction as shown in Figure A.4. Representative shear stress-strain (τ_{10}-γ_{10}) curves are presented in Figure A.4. From the testing of five samples, the average in-plane shear strength was 27.6 MPa with a std. of 1.7; the average shear modulus was 3.0 GPa with a std. of 0.3.

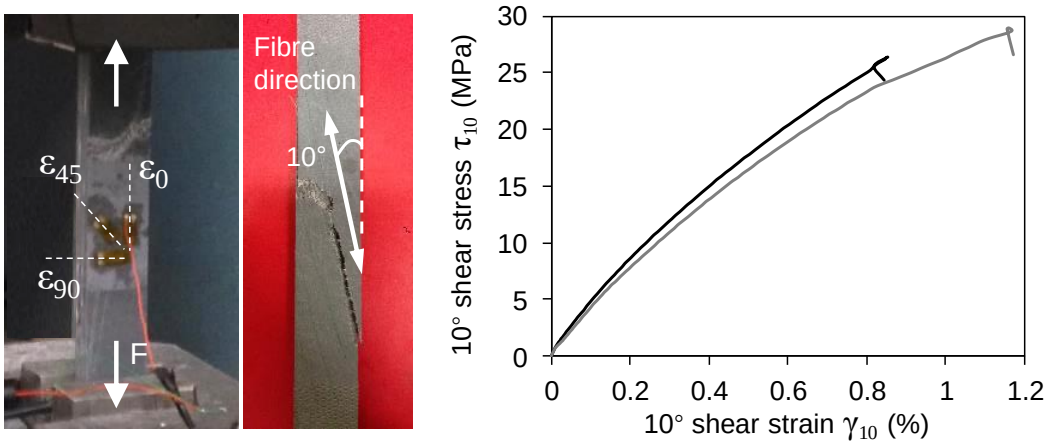

Figure A.4. Failure and representative in-plane shear stress-strain curves of 10° tensile samples from the GFRP profile.

A.2.3. Interlaminar Shear Strength of GFRP Material

The interlaminar shear strength of the GFRP material was determined using the short beam three-point bending test as per ASTM D2344 [A4]. Samples 57 mm in length (six times the nominal thickness) and 19 mm in width (twice the nominal thickness) were from the flat walls of the GFRP profiles along the fibre direction. The three-point bending tests were carried out on an Instron Machine with a 50 kN-capacity load cell. The span length between the rollers was always adjusted to four times of the measured thickness of the sample (Figure A.5). The mid-span load was applied at a crosshead speed of 1 mm/min. The interlaminar shear failure and representative load-displacement curves are shown in Figure A.5.

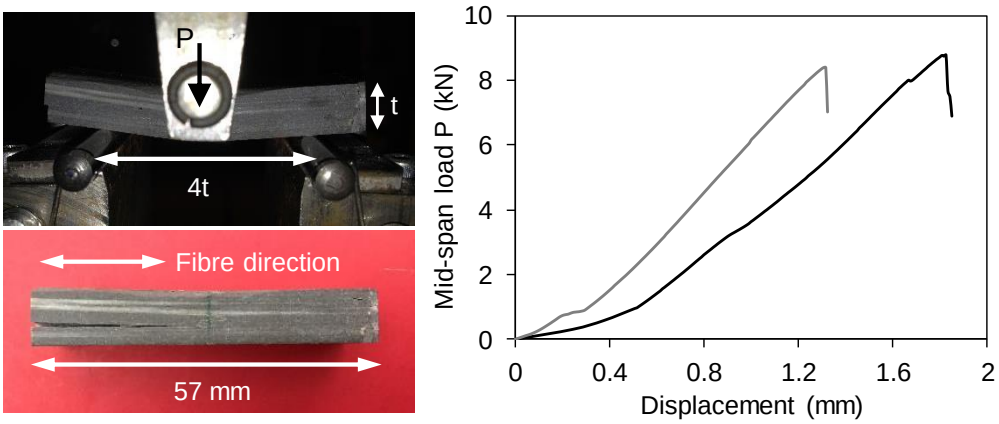

Figure A.5. Failure and representative load-displacement curves of short beam bending tests on the GFRP samples.

The interlaminar shear strength τ_{int} was calculated by Eq. (A.3). Five samples were tested, resulting in an average interlaminar shear strength of 31.2 MPa with a std. of 1.9.

$$\tau_{int} = 0.75 \times \frac{P_{max}}{bt} \tag{A.3}$$

where P_{max} = maximum value of mid-span load;

b = measured width of the sample;

t = measured thickness of the sample.

A.2.4. Flexural Strength and Modulus of GFRP Material

The flexural strength and modulus of the GFRP material were obtained following ASTM D7264 [A5]. Samples 80 mm in length and 20 mm in width (nominal dimensions) were cut from the flat walls of the GFRP profiles along the transverse direction. Flexural tests were performed on the transverse samples because the samples were too short for the available tensile testing rigs. A span-to-depth ratio of no lower than 16:1 is recommended by ASTM D7264, but the 80 mm-long transverse samples were the longest that could be cut from the 102×102×9.5 mm profile. The three-point bending tests were performed on an Instron machine with a 5 kN-capacity load cell. The span between the rollers was 70 mm as shown in Figure A.6. The mid-span deflection δ was gauged by a laser extensometer. The mid-span load P was applied at a crosshead speed of 1 mm/min. The beam samples failed due to tensile failure of the resin matrix at the bottom soffit. Representative load-displacement curves are presented in Figure A.6.

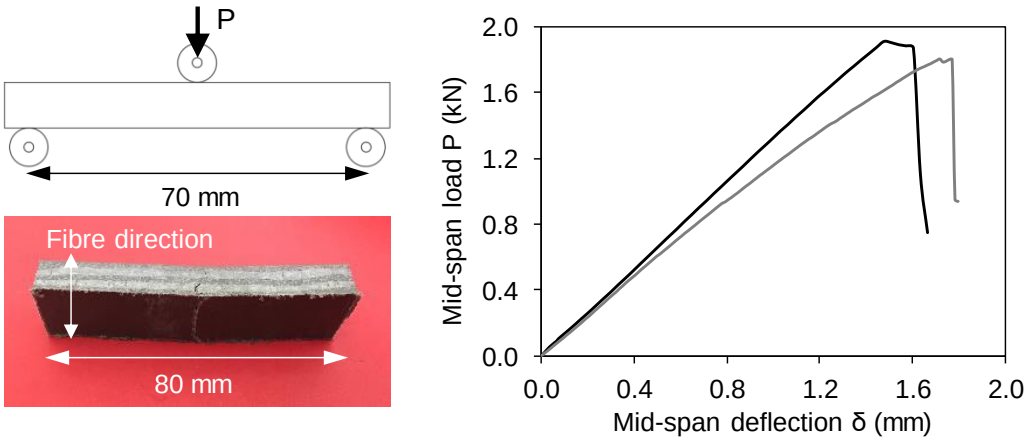

Figure A.6. Failure and representative load-displacement curves of transverse flexural tests on the GFRP samples.

The transverse flexural strength $\sigma_{t,flex}$ was calculated by

$$\sigma_{t,flex} = \frac{3P_{max}L}{2bt^2} \tag{A.4}$$

where P_{max} = maximum value of mid-span load P;

L = span length = 70 mm;

b = measured width of the sample;

t = measured thickness of the sample.

The transverse flexural modulus $E_{t,flex}$ was calculated by Eq. (A.5). From the testing of five samples, the average transverse flexural strength was 88.5 MPa with a std. of 6.5.

$$E_{t,flex} = \frac{L^3 m}{4bt^3} \tag{A.5}$$

where m = slope of the load-deflection (P-δ) curve.

A.2.5. Material Properties of Steel Flange-Plates

The material properties of the steel were characterised using the same method and sample size as described in Section A.1.1. A representative tensile stress-strain curve of the steel samples is presented in Figure A.7. Three samples were tested to obtain the material properties summarised in Table 5.2.

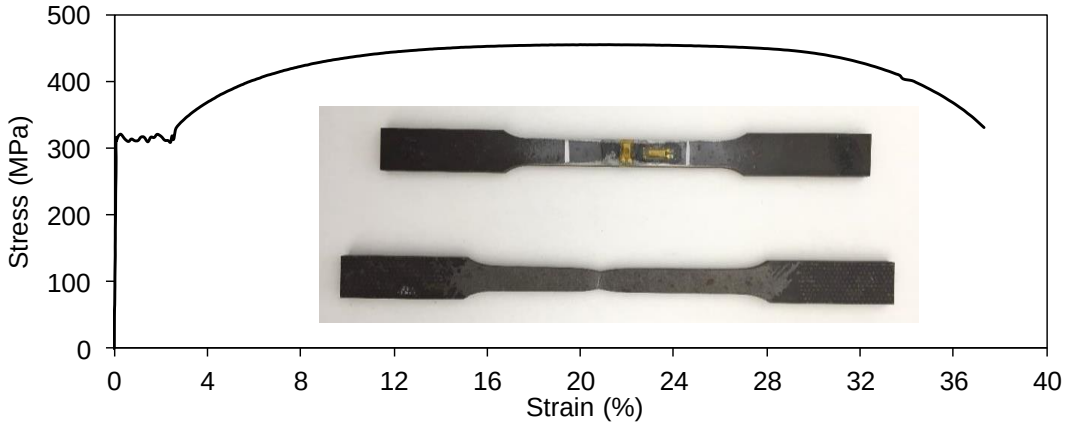

Figure A.7. A representative tensile stress-strain curve of samples from the steel flange-plate (Chapter 5).

A.2.6. Tensile Strength and Modulus of Sikadur-330 Adhesive

Tensile tests were performed on samples of the Sikadur-330 adhesive following ASTM D368 [A6]. The adhesive was cast into a dog-bone shape using Teflon moulds. The adhesive samples were cured under room temperature for two weeks, same as the bonded sleeve joint assemblies (Section 2.1 of Chapter 5). The nominal dimensions of the moulded adhesive samples are shown in Figure A.8 (nominal thickness was 5 mm). The tensile tests were performed using an Instron machine with a 5 kN-capacity load cell. Tensile displacement was applied at a crosshead speed of 0.5 mm/min. Two strain gauges were attached on each sample – one along the tensile direction and the other along the transverse direction. The output of the strain gauges was used for measuring the tensile strain and for calculating the Poisson's ratio. Representative tensile stress-strain curves of the adhesive samples were presented in Figure A.8. From the testing of four samples, the average tensile strength was 32.2 MPa with a std. of 2.5; the average elastic modulus was 4.25 GPa with a std. of 0.29. On the manufacturer's datasheet, the Sikadur-330 adhesive is reported with a tensile strength of 30 MPa and an elastic modulus of 4.5 GPa [A7].

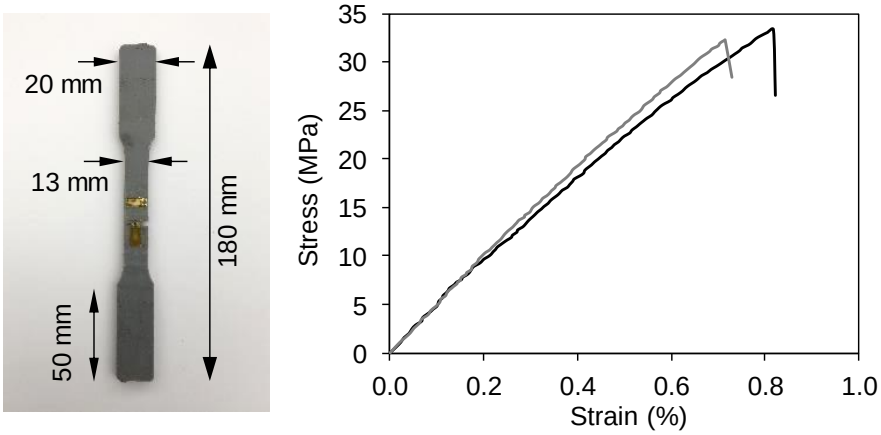

Figure A.8. Nominal dimensions and representative tensile stress-strain curves of the Sikadur -330 adhesive samples (Chapter 5).

A.2.7. Mode I Critical Fracture Energy of Sikadur-330 Adhesive

The mode I critical fracture energy of the Sikadur-330 adhesive was determined through notched beam bending test following ASTM D5045 [A8]. The adhesive was cast into a notched beam-shape using Teflon moulds. The adhesive samples were cured under room temperature for two weeks, same as the bonded sleeve joint assemblies (Section 2.1 of Chapter 5). Figure A.9 shows the nominal dimensions of the moulded adhesive samples and the three-point bending setup; nominally, the width of the samples was one half of the depth. A razor blade was slid across and saw into the notch tip to initiate a sharp crack; the crack length a indicated in Figure A.9 was inclusive of this sharp crack. The bending tests were performed on an Instron machine with a 2 kN-capacity load cell. The displacement of the loading nose, at 0.1 mm/min crosshead speed during the tests, was gauged by a laser extensometer. Representative load-displacement (P-u) curves of the bending test were presented in Figure A.9. To correct for the displacement caused by the indentation of the loading nose, an indentation test was also conducted using a non-notched beam and the same setup except that the two lower rollers were pressed together to minimize the span length. The load and displacement of the indentation test were denoted P_i and u_i.

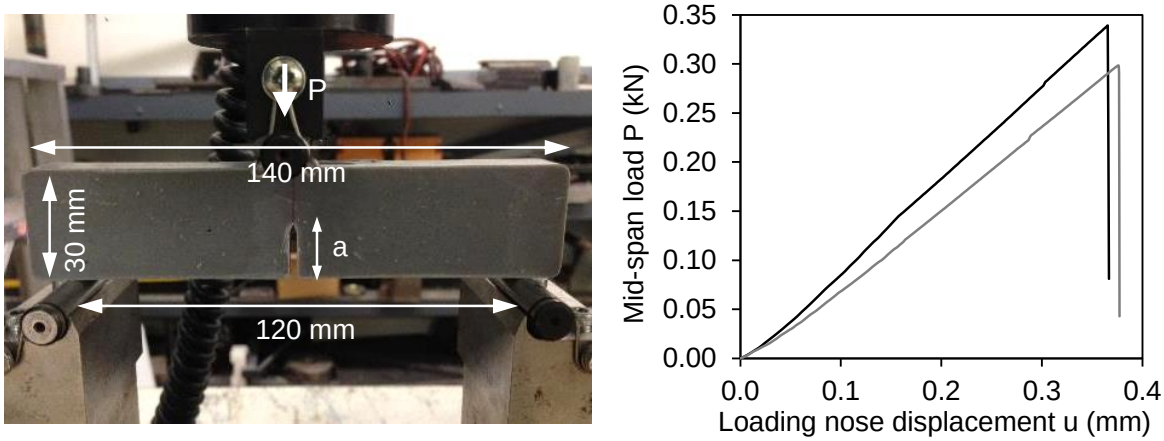

Figure A.9. Nominal dimensions and representative load-displacement curves of notched beam bending tests on the Sikadur-330 adhesive samples.

The mode I critical fracture energy G_I^{cr} was calculated by Eq. (A.6). Five samples were tested, resulting in an average G_I^{cr} of 0.887 kN/m with a std. of 0.067.

$$G_I^{cr} = \frac{\eta_e(U - U_i)}{B(W - a)} \tag{A.6}$$

where B = measured width of the beam sample;

W = depth of the beam sample = 30 mm;

a = total crack length;

U = area under the bending test P-u curve up to P_{max} of the bending test;

U_i = area under the indentation test P_i-u_i curve up to P_{max} of the bending test;

η_e is a function of a/W, which can be looked up from Table 1 of ASTM D5045 [A8].

A.3. Supplementary Information for Chapter 6

A.3.1. Compressive Strengths and Moduli of GFRP Material

In Chapter 6, the same batch of pultruded GFRP profiles was used as in Chapter 5. Compressive tests following ASTM D695 [A9] were further conducted to obtain the compressive strengths and moduli. Rectangular prism samples were cut from the flat walls of the 102×102×9.5 mm GFRP profiles. The samples were nominally 22 mm in height, 22 mm in width and 9.5 mm in thickness. Compressive tests were carried out in the fibre direction and in the transverse direction. The compressive tests were performed on a 100 kN-capacity Instron machine at a crosshead speed of 0.5 mm/min. The compressive shortening of the samples during the tests was measured by a laser extensometer. Failures and representative compressive stress-strain curves were presented in Figure A.10. Five samples were tested for each loading direction. In the fibre direction, the average compressive strength was 307.7 MPa with a std. of 4.0; the average compressive modulus was 23.77 GPa with a std. of 5.46. In the transverse direction, the average compressive strength was 127.9 MPa with a std. of 7.6; the average compressive modulus was 8.78 GPa with a std. of 2.37.

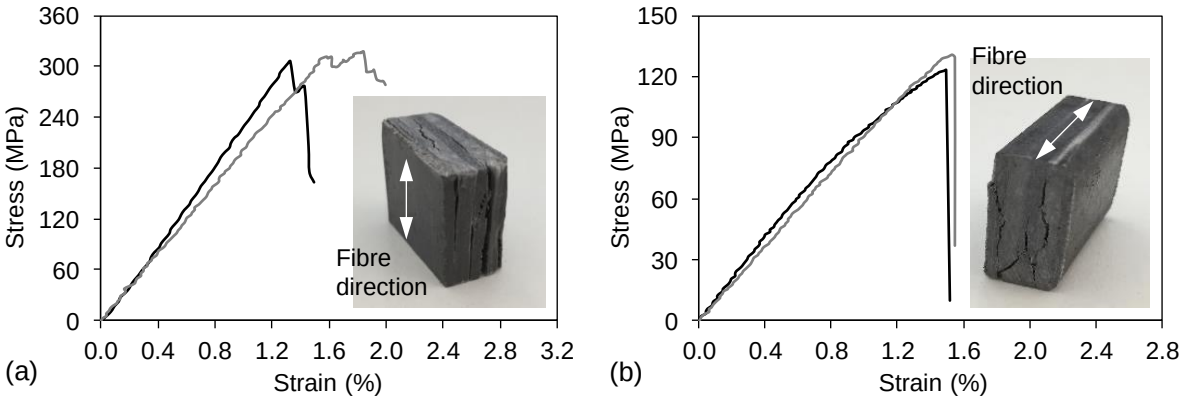

Figure A.10. Failures and representative compressive stress-strain curves of samples from the GFRP profile: (a) compression in the fibre direction; (b) compression in the transverse direction.

A.3.2. Material Properties of Steel Flange-Plates

The material properties of the steel were characterised using the same method and sample size as described in Section A.1.1. A representative tensile stress-strain curve of the steel samples is presented in Figure A.11. Three samples were tested to obtain the material properties summarised in Table 6.2.

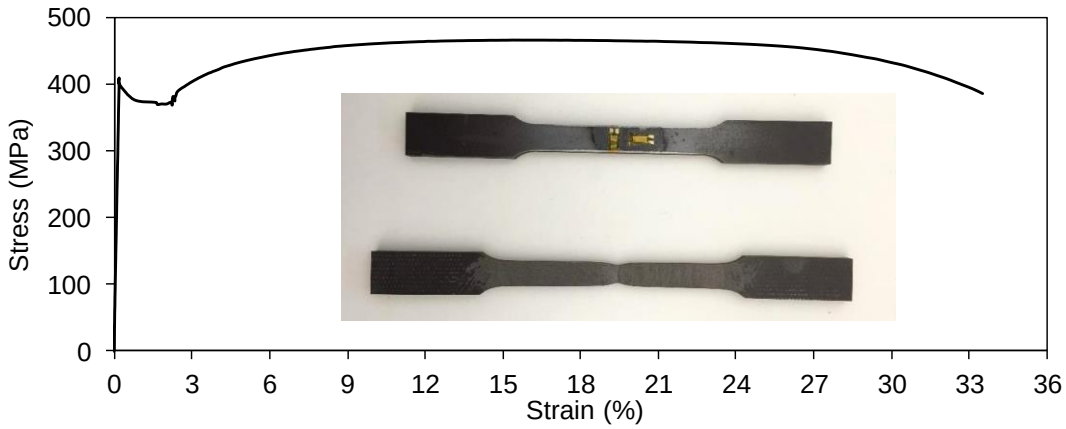

Figure A.11. A representative tensile stress-strain curve of the steel flange-plate (Chapter 6).

A.3.3. Tensile Strength and Modulus of Sikadur-330 Adhesive

The tensile strength and modulus of the Sikadur-330 adhesive were characterised using the same method and sample size as described in Section A.2.5. Representative tensile stress-strain curves of the adhesive samples are presented in Figure A.12. Five samples were tested to obtain an average tensile strength of 33.7 MPa with a std. of 2.2, and a tensile modulus of 4.09 GPa with a std. of 0.13.

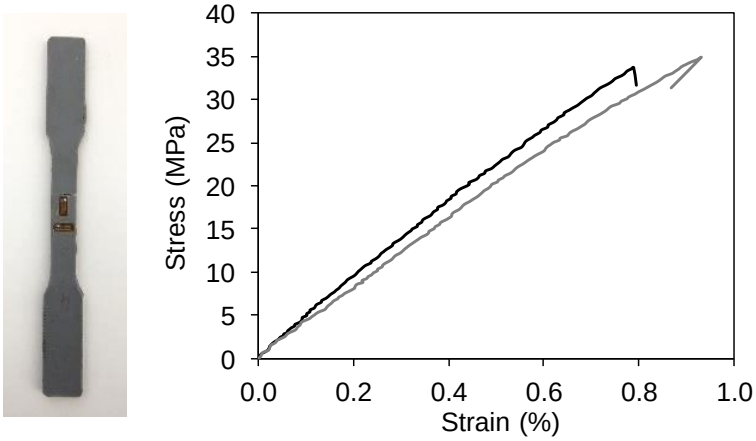

Figure A.12. Representative tensile stress-strain curves of the Sikadur-330 adhesive samples (Chapter 6).

A.4. References

A1. ASTM International. Standard Test Methods and Definitions for Mechanical Testing of Steel Products. ASTM A370-10. West Conshohocken, PA., 2010.

A2. ASTM International. Standard Test Method for Tensile Properties of Polymer Matrix Composite Materials. ASTM D3039. West Conshohocken, PA., 2014.

A3. Lee S, Munro M, Scott R. Evaluation of three in-plane shear test methods for advanced composite materials. Composites. 1990;21(6):495-502.

A4. ASTM International. Standard Test Method for Short-Beam Strength of Polymer Matrix Composite Materials and Their Laminates. ASTM D2344. West Conshohocken, PA., 2016.

A5. ASTM International. Standard Test Method for Flexural Properties of Polymer Matrix Composite Materials. ASTM D7264. West Conshohocken, PA., 2015.

A6. ASTM International. Standard Test Method for Tensile Properties of Plastics. ASTM D638-10. West Conshohocken, PA., 2010.

A7. Sika Limited. Product Datasheet: Sikadur®-330, 2-part epoxy impregnation resin. Hertfordshire, U.K., 2014.

A8. ASTM International. Standard Test Methods for Plane-Strain Fracture Toughness and Strain Energy Release Rate of Plastic Materials. ASTM D5045-99. West Conshohocken, PA., 2007.

A9. ASTM International. Standard Test Method for Compressive Properties of Rigid Plastics. ASTM D695-15. West Conshohocken, PA., 2015.

– This marks the end of the thesis –